U.S. Department of
Transportation

**Federal Railroad
Administration**

Side Impact Test and Analyses of a DOT-117 Tank Car

Office of Research,
Development
and Technology
Washington, DC 20590

DOT/FRA/ORD-19/13

Final Report
May 2019

REPORT DOCUMENTATION PAGE	*Form Approved* *OMB No. 0704-0188*

1. AGENCY USE ONLY (Leave blank)	2. REPORT DATE May 2019	3. REPORT TYPE AND DATES COVERED Technical Report – September 28, 2016

4. TITLE AND SUBTITLE Side Impact Test and Analyses of a DOT-117 Tank Car	5. FUNDING NUMBERS DTFR53-11-D-00008 Task Order 008 TTCI-11-033
6. AUTHOR(S) Przemyslaw Rakoczy[1], Michael Carolan[2], Travis Gorhum[1], Shaun Eshraghi[2]	

7. PERFORMING ORGANIZATION NAME(S) AND ADDRESS(ES)

[1]Transportation Technology Center, Inc.
55500 DOT Road
Pueblo, CO 81001

[2]Volpe National Transportation Systems Center
55 Broadway
Cambridge, MA 02142

8. PERFORMING ORGANIZATION REPORT NUMBER

9. SPONSORING/MONITORING AGENCY NAME(S) AND ADDRESS(ES)

U.S. Department of Transportation
Federal Railroad Administration
Office of Railroad Policy and Development
Office of Research, Development and Technology
Washington, DC 20590

10. SPONSORING/MONITORING AGENCY REPORT NUMBER

DOT/FRA/ORD-19/13

11. SUPPLEMENTARY NOTES

COR: Francisco Gonzalez, III

12a. DISTRIBUTION/AVAILABILITY STATEMENT This document is available to the public through the FRA website.	12b. DISTRIBUTION CODE

13. ABSTRACT

The Federal Railroad Administration (FRA) conducted a side impact test on a U.S. Department of Transportation (DOT)-117J100W (DOT-117) tank car at the Transportation Technology Center (TTC) to evaluate the performance of the tank car under dynamic impact conditions and to provide data for the verification and refinement of a computational model. The tank car was filled with water to approximately 95 percent of its volume and sealed, but not pressurized. The tank car was impacted at 13.9 mph by a 297,125-pound ram car with 12-inch by 12-inch ram head fitted to the ram car. The ram car impacted the tank center; it deformed and cracked the external jacket, but did not puncture the tank's shell.

The Volpe National Transportation Systems Center (Volpe Center) performed pre-test finite element (FE) modeling to estimate the overall response of the tank to the impact. This pre-test models gave results in good agreement with the test results. The post-test FE models were updated to include the actual material behavior and to better represent the test setup. The post-test FE results were in even better agreement with the test results than the pre-test estimates.

The modeling and testing performed in this program demonstrated the ability of the fluid response of an impacted tank car to dominate the general force-displacement response, underscoring the importance of modeling the fluid-structure interactions with appropriate techniques. The test data is intended to be used to better understand the shell impact performance of the new specification DOT-117 tank car. The validated FE model can be used to examine additional impact scenarios beyond the tested scenario.

14. SUBJECT TERMS Impact test, DOT-117 tank car, tank car performance, tank car, transportation safety	15. NUMBER OF PAGES 166
	16. PRICE CODE

17. SECURITY CLASSIFICATION OF REPORT Unclassified	18. SECURITY CLASSIFICATION OF THIS PAGE Unclassified	19. SECURITY CLASSIFICATION OF ABSTRACT Unclassified	20. LIMITATION OF ABSTRACT

NSN 7540-01-280-5500

Standard Form 298 (Rev. 2-89)
Prescribed by ANSI Std. 239-18
298-102

METRIC/ENGLISH CONVERSION FACTORS

ENGLISH TO METRIC

LENGTH (APPROXIMATE)

1 inch (in) = 2.5 centimeters (cm)
1 foot (ft) = 30 centimeters (cm)
1 yard (yd) = 0.9 meter (m)
1 mile (mi) = 1.6 kilometers (km)

AREA (APPROXIMATE)

1 square inch (sq in, in^2) = 6.5 square centimeters (cm^2)
1 square foot (sq ft, ft^2) = 0.09 square meter (m^2)
1 square yard (sq yd, yd^2) = 0.8 square meter (m^2)
1 square mile (sq mi, mi^2) = 2.6 square kilometers (km^2)
1 acre = 0.4 hectare (he) = 4,000 square meters (m^2)

MASS - WEIGHT (APPROXIMATE)

1 ounce (oz) = 28 grams (gm)
1 pound (lb) = 0.45 kilogram (kg)
1 short ton = 2,000 pounds (lb) = 0.9 tonne (t)

VOLUME (APPROXIMATE)

1 teaspoon (tsp) = 5 milliliters (ml)
1 tablespoon (tbsp) = 15 milliliters (ml)
1 fluid ounce (fl oz) = 30 milliliters (ml)
1 cup (c) = 0.24 liter (l)
1 pint (pt) = 0.47 liter (l)
1 quart (qt) = 0.96 liter (l)
1 gallon (gal) = 3.8 liters (l)
1 cubic foot (cu ft, ft^3) = 0.03 cubic meter (m^3)
1 cubic yard (cu yd, yd^3) = 0.76 cubic meter (m^3)

TEMPERATURE (EXACT)

[(x-32)(5/9)] °F = y °C

METRIC TO ENGLISH

LENGTH (APPROXIMATE)

1 millimeter (mm) = 0.04 inch (in)
1 centimeter (cm) = 0.4 inch (in)
1 meter (m) = 3.3 feet (ft)
1 meter (m) = 1.1 yards (yd)
1 kilometer (km) = 0.6 mile (mi)

AREA (APPROXIMATE)

1 square centimeter (cm^2) = 0.16 square inch (sq in, in^2)
1 square meter (m^2) = 1.2 square yards (sq yd, yd^2)
1 square kilometer (km^2) = 0.4 square mile (sq mi, mi^2)
10,000 square meters (m^2) = 1 hectare (ha) = 2.5 acres

MASS - WEIGHT (APPROXIMATE)

1 gram (gm) = 0.036 ounce (oz)
1 kilogram (kg) = 2.2 pounds (lb)
1 tonne (t) = 1,000 kilograms (kg)
= 1.1 short tons

VOLUME (APPROXIMATE)

1 milliliter (ml) = 0.03 fluid ounce (fl oz)
1 liter (l) = 2.1 pints (pt)
1 liter (l) = 1.06 quarts (qt)
1 liter (l) = 0.26 gallon (gal)
1 cubic meter (m^3) = 36 cubic feet (cu ft, ft^3)
1 cubic meter (m^3) = 1.3 cubic yards (cu yd, yd^3)

TEMPERATURE (EXACT)

[(9/5) y + 32] °C = x °F

QUICK INCH - CENTIMETER LENGTH CONVERSION

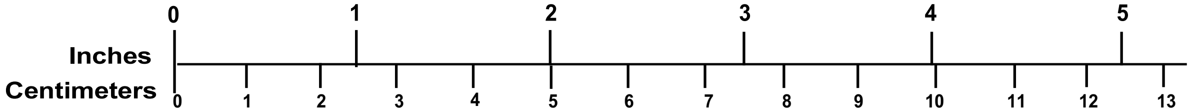

QUICK FAHRENHEIT - CELSIUS TEMPERATURE CONVERSIO

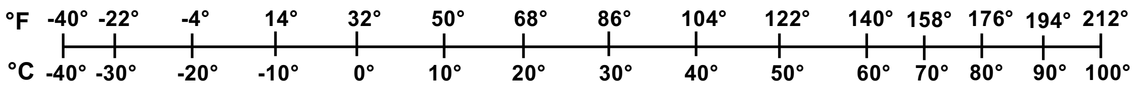

For more exact and or other conversion factors, see NIST Miscellaneous Publication 286, Units of Weights and Measures. Price $2.50 SD Catalog No. C13 10286

Updated 6/17/98

Acknowledgements

The authors of this report gratefully acknowledge the technical assistance of the Volpe National Transportation Systems Center and Transportation Technology Center, Inc. (TTCI) senior engineers David Jeong, Benjamin Perlman, and Nicholas Wilson. The operations and instrumentation test team was led by Dwayne Smith and David Williams at TTCI. Additionally, discussions with Francisco González, III, Program Manager of the Federal Railroad Administration's (FRA) Office of Research, Development and Technology and Karl Alexy, Deputy Associate Administrator of FRA's Office of Railroad Safety were valuable in developing this testing program.

The authors wish to thank Kathi Kube who provided several photographs of the test that are used in this report.

Contents

Illustrations

Tables

Executive Summary

The test and analyses described in this report supports the overall objective of the U.S. Department of Transportation's (DOT) Federal Railroad Administration (FRA) research program to improve transportation safety for tank cars. This report documents the combined efforts of Transportation Technology Center, Inc. (TTCI) and the Volpe National Transportation Systems Center (Volpe) to test and analyze the side impact puncture performance of a DOT-117J100W (herein referred to as DOT-117) tank car. TTCI conducted a side impact test on the DOT-117 tank car on September 28, 2016, at the Transportation Technology Center in Pueblo, CO, to evaluate the performance of the tank car and to provide data for the verification and refinement of a computational model. All test requirements were met. Volpe performed both pre-test and post-test analyses of the impact response to evaluate, validate, and improve the puncture modeling capabilities.

The tank car was filled with water to approximately 95 percent of its volume. It was then sealed but not pressurized, leaving the 5 percent outage at atmospheric pressure. The test was intended to strike the car at a speed that was high enough to result in significant damage to the tank, but would not result in puncture to the tank's shell. Pre-test modeling had estimated a puncture range of between 13 and 14 mph. Based on these results, the target test speed was 13.5 mph +/- 0.5 mph. The tank car was impacted by a 297,125-pound ram car traveling 13.9 mph. A 12-inch by 12-inch ram head fitted to the ram car impacted the tank center. The impact deformed and cracked the external jacket but did not puncture the tank's shell.

Pre-test finite element (FE) modeling was used to estimate the overall response of the tank to the impact, including the force-displacement response. Pre-test material behavior for the TC128 shell of the car was developed based on data provided by the car's manufacturer from tensile tests conducted on the plates used to manufacture the tested car. The pre-test model provided very good agreement with the overall force-displacement behavior, indentation shape, and internal pressures measured during the tank car test.

After the test, material coupons were cut from the tank car shell and subjected to tensile testing. The material characterization indicated the actual tank car material had a higher ductility than the pre-test material model, and higher than that of any previously tested tank car. The post-test model was updated to include the actual material behavior, and to reflect the geometry of a concrete slab beneath the car that was struck during the test. The post-test model was re-run at the test speed and found to continue to be in very good agreement with the test measurements.

The DOT-117 model can achieve an excellent level of agreement with the measured quantities and observed behaviors from the test. The validated model can be used to examine additional impact scenarios beyond the tested scenario. While not undertaken as a part of the model validation process described in this report, this model could be used to investigate modifications to the test setup on the estimated puncture speed of the DOT-117.

1. Introduction

The Federal Railroad Administration (FRA) continues its research to provide the technical basis for rulemaking on enhanced and alternative performance standards for tank cars and review of new and innovative designs that are developed by the industry and other countries. In support of this ongoing research, full-scale tests are necessary to provide the technical information to validate modeling efforts and to inform regulatory activities. These tests evaluated the crashworthiness performance of tank cars used in the transportation of hazardous materials. This report documents the analyses and test results for a side impact test performed on a U.S. Department of Transportation (DOT) 117 tank car. This report describes the model development and pre-test estimates, comparisons of the test and analyses, and the subsequent post-test analyses performed to reflect the actual material of construction and test conditions.

1.1 Background

In recent years, significant research was conducted to analyze and improve the impact behavior and puncture resistance of railroad tank cars. Ultimately, the results of this research will be used by the government regulatory agencies in the United States and Canada (i.e., FRA and Transport Canada [TC], respectively). These results will be used to establish performance-based testing requirements and to develop methods to evaluate the crashworthiness and structural integrity of different tank car designs when subjected to a standardized shell impact scenario. A performance-based requirement for tank car head impact protection has already been defined within the current regulations [1].

Tests and associated analyses were performed to evaluate the crashworthiness performance of tank cars. The tests and analyses evaluated designs that comply with current regulations as well as innovative new designs that have improved puncture resistance. FRA is currently working closely with key industry stakeholders to use the information being generated from these programs to revise and refine the construction, design, and use of tank cars.

On May 1, 2015, FRA and the Pipeline and Hazardous Materials Safety Administration (PHMSA) announced new requirements for high-hazard flammable trains (HHFT) in "Enhanced Tank Car Standards and Operational Controls for High-Hazard Flammable Trains" [2]. Part of the new requirements are enhanced standards for new and existing tank cars used in HHFTs. This rulemaking created a new DOT-specification tank car, referred to as the DOT-117 tank car. The specifications require that the DOT-117 tank shells be constructed out of 9/16-inch steel, with 11-gauge sheet metal jackets, 1/2-inch thick head shields on the ends of the tanks, and improved valves over previous designs.

This report documents the analyses and test results for a side impact test performed on a DOT-117 tank car. This report describes the model development and pre-test estimates, comparisons of the test and analyses, and the subsequent post-test analyses performed to reflect the actual material of construction and test conditions.

1.2 Objectives

The objective of the test was to quantify the deformation mode, impact load-time history, and puncture resistance of a tank car in a side impact. Moreover, the impact conditions were developed so that the side impact test is: (a) safe, (b) repeatable, and (c) analyzable. Also, the test conditions were similar to the impact tests previously performed on a DOT-111 [4] and a DOT-112 tank cars for a direct comparison [5]. This allows a comparison between the results of the DOT-111, DOT-112, and DOT-117 impact tests.

The objective of the analyses was to provide estimates of the tank car impact response both for pre-test planning and for validation of tank car impact and puncture modeling capabilities.

1.3 Scope

This report includes a discussion of developing and executing the finite element (FE) models for this program; including modeling the tank car steel, modeling the water within the tank, and modeling the gas phase. This report presents the test results, discusses the execution of the test, and summarizes the overall results of the test. Discussion of the post-test modeling adjustments is included in this report. Finally, this report presents a comparison between the test measurements and the model results.

This report does not include any results from further analyses using the DOT-117 tank car model, such as impact conditions outside of the conditions of the test. While this report refers to previously performed shell impact tests on tank cars with a different specification, no comparison of results from different tests are included within the scope of this report. Research into the puncture resistance of tank cars is ongoing, and such further simulations or comparisons may be considered in future work.

1.4 Overall Approach

Due to the difficult-to-control variables of testing, such as wind speed, unknown weld qualities, and the inherent variability of material behavior even within a single plate, there is no such thing as a certain test outcome. It is more useful to frame the discussion of test planning in terms of likelihood of puncture. In an ideal test, the target test speed would be chosen to fall somewhere in the shaded range in Figure 1, where puncture is possible, but not certain.

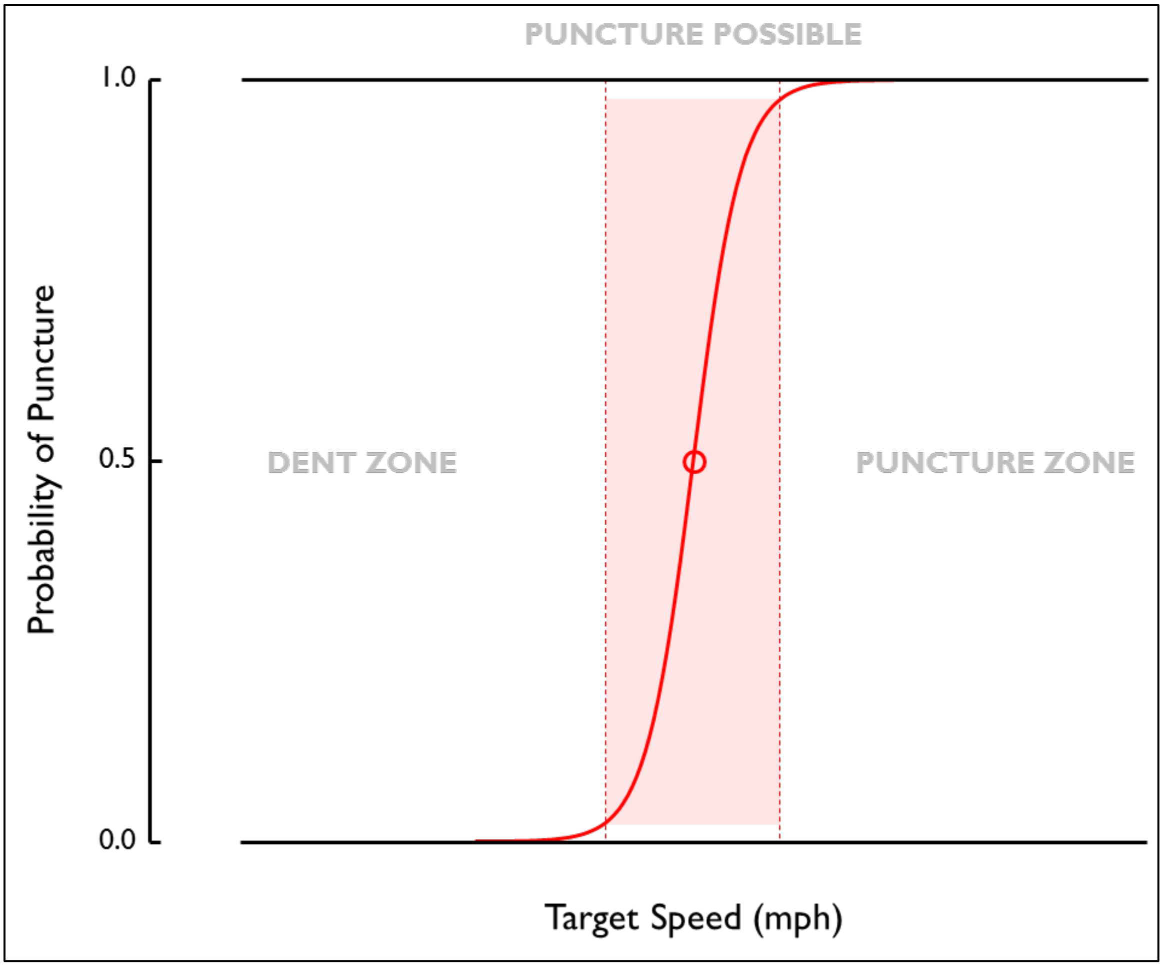

Figure 1. Schematic Illustrating Probability of Puncture Versus Impact Speed

The value of a test can be increased by targeting an impact speed that is very close to the threshold speed between where the tank car punctures and where it does not puncture. If the tested tank speed is close to this threshold speed, regardless of whether or not the tank punctures, the data that is collected can be extremely valuable for both model validation and for estimating the threshold puncture speed under the given impact conditions. From a practical standpoint of test execution, the ideal range of test speeds provides a practical target to maximize the value of the test. One potential target for maximizing the value of the test data could be to run a test in which the impactor is brought to a complete stop at the instant the tank punctures. Such a test would be an experimental demonstration of the threshold puncture speed, as all the ram car's initial kinetic energy has been transferred into the tank car at the same instant that the tank car reaches the limit of its capacity. An incrementally slower test would have been a non-puncture test, and an incrementally faster test would have exceeded the capacity of the tank car to resist puncturing.

In the same spirit, making a blanket statement as to the superiority of a puncture test or a non-puncture test does not provide for a useful discussion without considering proximity to the theoretical threshold puncture speed. As the test speed moves further from the center of the puncture threshold range, the value of the test data decreases. Neither a test that causes catastrophic damage to the tank car structure nor a test that scarcely creates a dent would be an effective tool for evaluating the puncture resistance of the car. These tests also would not provide much utility for model validation, evaluating the relative impact resistance offered by different tank car designs, or for evaluating new or novel methods of simulating impacts. The extremely unlikely-to-puncture case does not provide enough information to assess the model sufficiently to make a comparison, and the overwhelmingly likely-to-puncture case can result in a mode of tank failure that does not truly represent the way tank cars experience puncture near their puncture/non-puncture thresholds.

The highly nonlinear force response of an impacted tank car makes extrapolation or interpolation of test results to attempt to calculate the threshold speed between puncture and non-puncture problematic. The uncertainty of an interpolation or extrapolation increases when the test speed is either significantly higher or significantly lower than the threshold speed. Thus, if test results are obtained at speeds far away from the theoretical threshold puncture speed, the threshold puncture speed will not be known with a high degree of certainty.

A test that punctures the tank, but does not leave the impactor with an excessive amount of residual kinetic energy can be used to verify that a model captures both the overall response of the tank car and the puncture modeling techniques defined for the materials of the car. However, achieving this outcome can be extremely challenging. If a test is planned to be run at slightly above the threshold puncture speed, the threshold puncture speed is typically estimated from pre-test models. If the pre-test model predicts a higher threshold puncture speed than the tank car actually possesses, then a test that is planned to be performed at the threshold puncture speed may in fact be an excessively fast test. While the energy absorbed by the tank up to the point of puncture in the test can be used to estimate the energy necessary to cause puncture, this estimate becomes less reliable as the actual impact speed gets further from the threshold puncture speed. At the same time, if the pre-test model is overly conservative, then a test that is planned for just below the threshold puncture speed on the basis of a conservative model may in fact result in an impact speed that is well below the threshold puncture speed.

The overall approach followed in this program of testing and analyses is presented in Figure 2. This flowchart presents a schematic view of the approach followed by Volpe National Transportation Systems Center (Volpe) in its model development and by Transportation Technology Center, Inc. (TTCI) in developing and executing the test plans. This flowchart illustrates the collaboration between both Volpe and TTCI throughout the testing and modeling process, all of which was coordinated with FRA. For example, the instrumentation placement described in the testing plan was used to guide requests for corresponding results in the FE model. The model results could then be used to estimate the magnitude of the response (such as pressure or displacement) that the instrumentation would experience at that location. If necessary, the instrumentation in the test plan could have been updated to account for the expected response from the model.

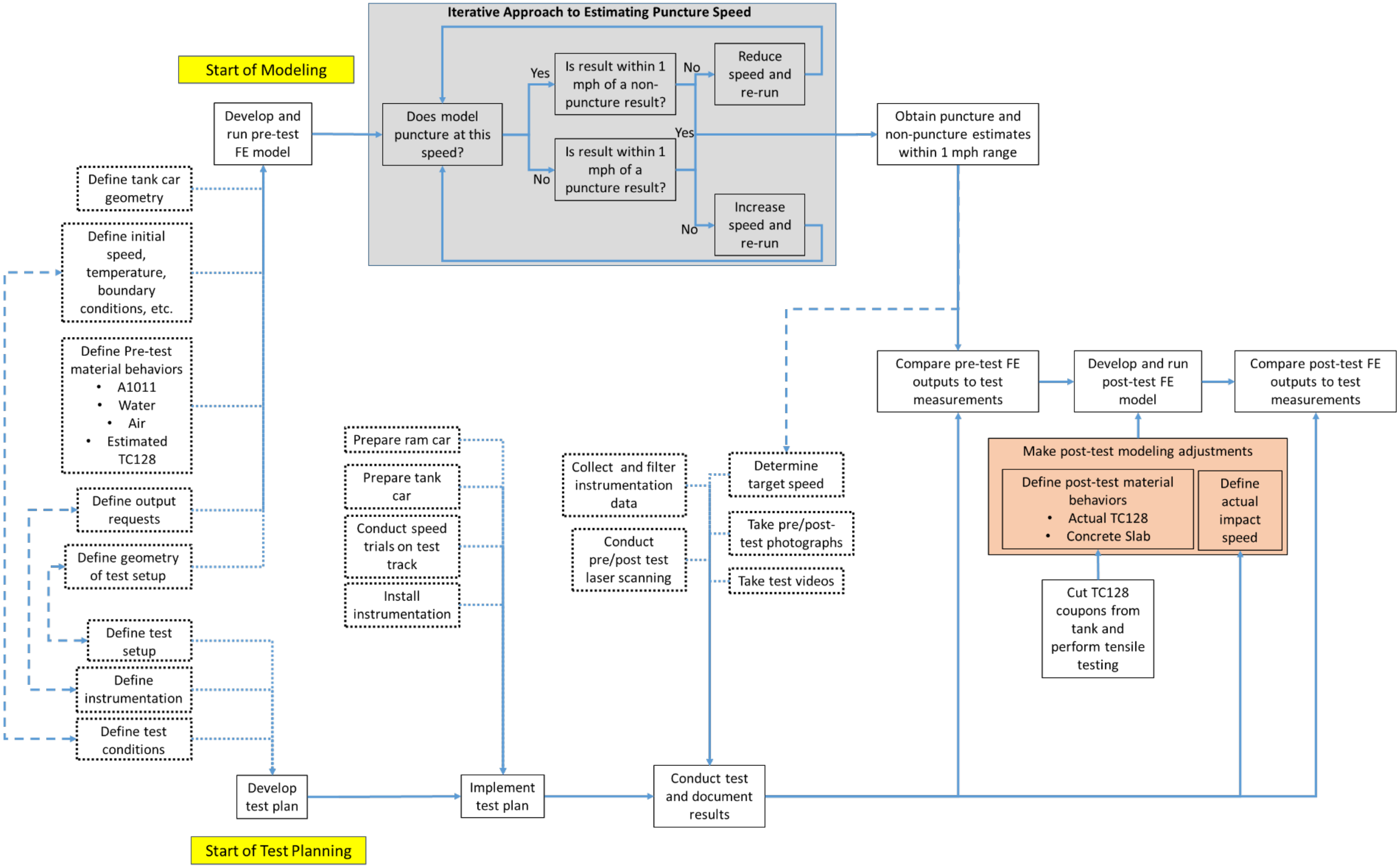

Figure 2. Flowchart Summarizing Overall Modeling and Testing Approach

Prior to the test itself, further collaboration involving Volpe, TTCI, and FRA occurred on determining the target test speed based on the model estimates, the desired outcome of the test, and such factors as ambient conditions (e.g., wind speed influencing actual impact speed) at the time of the test. After the test, material coupon test data from the TC128 shell of the car and the measured test speed were used to update the pre-test model to reflect the actual test conditions. Finally, the post-test model results and the test measurements are compared to one another.

1.5 Organization of the Report

Section 1 of this report includes the introduction, a description of the objectives and scope of the report, and a description of the organization of the report.

Section 2 describes the tank car undergoing testing and analysis, and describes the shell impact test setup.

Section 3 describes the instrumentation used during the test and its placement. This description includes discussion of the cameras used to capture the impact event.

Section 4 presents the results of the test. These results include a description of the actual conditions of the impact, a description of the test itself, and a summary of the measured test data.

Section 5 describes the development of the FE models used in this program. This section describes the geometry used in the model, the different material models developed, and modeling techniques used in the pre-test and post-test models.

Section 6 presents test measurements alongside the corresponding estimates from the pre-test FE models.

Section 7 presents test measurements alongside the corresponding estimates from the post-test FE models.

Section 8 includes a summary of the report, and contains concluding remarks.

Appendix A describes the positions of the cameras and targets used in the test.

Appendix B contains the full set of test data. Appendix B also contains the material data measured during the tensile coupon tests for the TC128 steel making up the car's shell.

Appendix C contains a full set of comparisons between test measurements and FE estimates. This appendix contains comparisons for pre-test models at two different impact speeds, for the post-test model using the actual TC128 behavior and a rigid ground slab, and for the post-test model using the actual TC128 behavior and a simple, deformable ground.

Appendix D describes the geometry and mesh on each part used in the FE models.

Appendix E contains a description of the modeling techniques that were used in both the pre-test and post-test FE models.

Appendix F contains a description of how each material behavior was developed in the FE models.

2. Test Conditions

2.1 Tank Car

The DOT-117 tank car is a non-pressurized tank car used in North America to carry flammable liquids, such as crude oil or ethanol. The DOT-117 specification is the newest specification tank car to be authorized for service in the United States. This specification was created in 2015 through PHMSA's HM-251 final rule [2]. At the time of the test (September 28, 2016), no DOT-117 tanks cars had been known to be involved in a derailment, and thus no data existed from field experience on the puncture resistance of cars of such design. While this test involved the evaluation of one specific DOT-117 tank car, the intent of the test was to allow the results to be more broadly applicable to all DOT-117 tank cars.

The test was performed on a DOT-117J tank car equipped with head protection and thermal protection enclosed in an exterior jacket. This car was constructed in 2015, and was tested new and never used in service. The tank is built from two cylinders slightly inclined toward the bottom and seamed at the center. The 9/16-inch thick tank car shell is constructed with TC-128 Grade B steel and had an outer diameter of 10 feet. Full height, 0.50-inch thick head shields are constructed with the American Society for Testing and Materials (ASTM) A572 Grade 50 steel. The tank car shell is wrapped in a 0.50-inch ceramic blanket for thermal protection and covered by an 11 gauge steel jacket made of ASTM A1011 SS GR 36. The pressure relief valve (PRV) installed on this car had a start-to-discharge pressure of 75 psi.

The drawing for the tank general arrangement is shown in Figure 3.

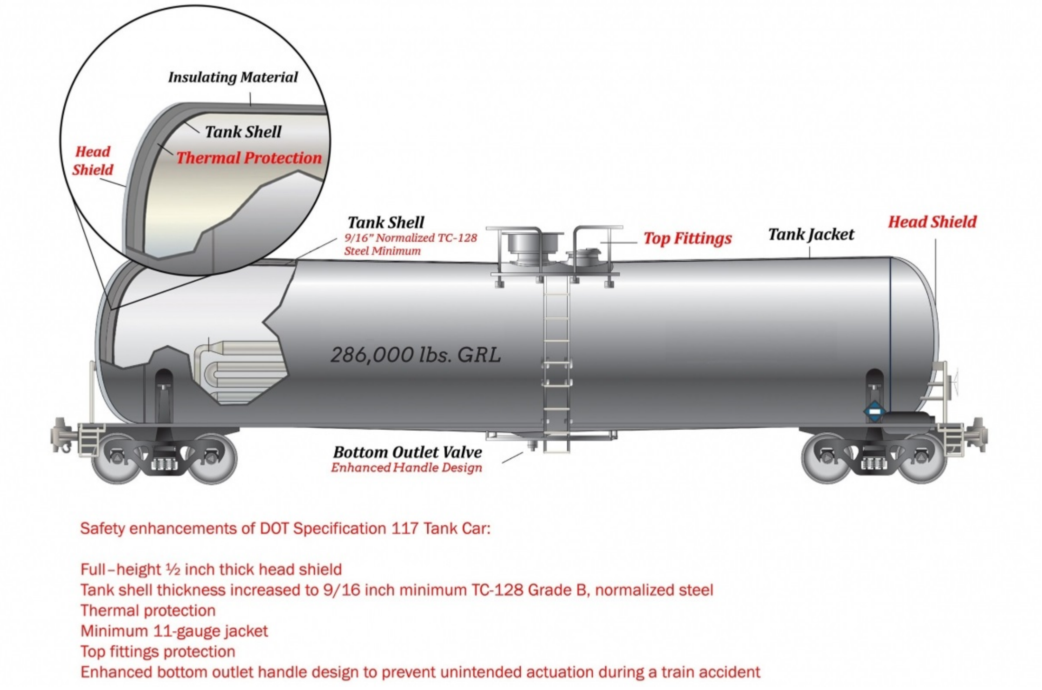

Figure 3. DOT-117 Tank Car Design Specification [24]

The capacity of the car was reported in two sources as slightly different values. The builder's specification listed its full water capacity as 30,100 gallons. The car itself had a stenciled capacity of 30,130 gallons. While these two values represent a small difference in tank capacity, a difference in tank capacity introduces uncertainty into determination of the actual outage volume. In particular, when filling the car to achieve a small outage, the uncertainty in outage volume can be on the same order of magnitude as the desired outage itself. The outage for the test condition was obtained using the loading procedure described in Section 2.

While the car was not modified to enhance its crashworthiness or puncture resistance prior to the test, the car was modified to permit it to be evaluated in the standard impact setup used in previous side-impact tests. Due to the shell sloping downward toward its center, there was very little clearance between the housing protecting the bottom outlet valves and the concrete slab between the rails at the test site. The portion of piping that stuck out below the housing was removed prior to the test, as the intent of the test was to evaluate the tank's puncture resistance, not the shear strength of the piping. The ladders on the sides of the car, used to reach the manway, were also removed prior to the test to reduce the gap between the wall and the tank to the minimum.

2.2 Test Setup

The side impact test was performed on September 28, 2016, at the TTC in Pueblo, CO. The test was performed by sending a ram car into the side of a tank car that was mounted on skids and backed by a rigid impact barrier, as Figure 4 shows.

Figure 4. Target Tank Mounted on Support Skids

Figure 5 (a) shows the two skids oriented parallel to the track with one end against the impact barrier that the tank car was placed on. Four sections of I-beams were welded to the tank car and skids for the attachment, as Figure 5 (b) shows. This test configuration was designed to minimize the ram car rollback and allow the tank car on the skids to slide on the steel plates during the impact. The tank car with skids attached was placed on 1-inch steel plates. For this test, the steel plates were placed on plywood to provide clearance between the center of the car and the concrete slab.

(a) Support skids **(b) Welded I-beam connection**

Figure 5. Tank Support Skid System

The DOT-117 tank car is equipped with a bottom valve protection structure, shown in Figure 6; because of low clearance at the center of the tank, the support skid plates were placed on several plywood sheets to raise the tank car off the ground. Additionally, the bottom outlet valve extension that projected from the protective housing was removed before the test.

Figure 6. Tank Car's Bottom Valve Protection Structure

The tank car jacket and shell were not modified in any way. The tank car's ladders would have interfered with the impactor on one site and the impact wall on the other, therefore, they were removed before the test.

The sloped geometry of this tank car keeps empty volume at both ends even when filled full at the manway. These volumes are not accessible from the car's exterior when the car is filled and cannot be measured. Thus, the test team decided to use an outage measurement gauge installed and calibrated by the car manufacturer. The corresponding distance between the top of the tank and water level outage was also calculated by a volume model of the tank using a nominal geometry from the manufacturing drawings. The tank car was filled with water up to approximately 95 percent of the volume. The manway lid was sealed, but no additional pressure was introduced to the tank car. This is similar to a loaded crude oil tank car in service condition.

This car has never been loaded in service and was in factory new condition at the time of the test. Therefore, it is anticipated that there was no preexisting damage.

The indenter was positioned to align with the mid length and mid height of the target tank car as closely as possible. The ram car is a modified flat car with an 8-foot ram installed on the leading end. This ram car was used in previous tank car tests and has a shortened tank attached to the ram end. Figure 7 shows the ram car. For this test, a 12-inch by 12-inch indenter with 1.0-inch radii on the edges and corners was used. The same indenter was used in the impact test of the DOT-111 tank car, the DOT-112 tank car, and the DOT-105 tank car in the past [4] [5] [6]. Additionally, this large indenter was expected to result in a considerable amount of fluid motion (i.e., "sloshing") during the test, requiring careful modeling of the lading to be able to capture this motion. Figure 8 and Figure 9 show the 12-inch by 12-inch indenter attached to the ram car and aligned with tank car. The ram car was weighed before the test to confirm the actual weight. The measured weight was 297,125 pounds.

Figure 7. Ram Car and Head

Figure 8. Ram Arm with 12-Inch by 12-Inch Indenter

Figure 9. Ram Arm with 12-Inch by 12-Inch Indenter Aligned with Center of the Tank Car

3. Test Instrumentation

3.1 Overview

The test configuration and instrumentation were all consistent with the specifications of the test implementation plan [8]. Table 1 is a list of all instrumentation used for this test. Additional descriptions of the various types of instrumentation are provided in the following subsections.

Table 1. Instrumentation Summary

Type of Instrumentation	Channel Count
Accelerometers	11
Speed Sensors	2
Pressure Transducers	12
String Potentiometers	10
Total Data Channels	35
Digital Video	7 cameras (including 3 high speed cameras)

3.2 Ram Car Accelerometers and Speed Sensors

The local acceleration coordinate systems are defined relative to the ram car. Positive x, y, and z directions are forward, left, and up relative to the lead end of the ram.

Three triaxial accelerometers were mounted on the longitudinal centerline of the ram car at the front, rear, and near the middle of the car. Two uniaxial accelerometers were mounted on the left and right sides of the car to supplement recording of longitudinal acceleration. The positions of these accelerometers are illustrated in Figure 10. A summary of the ram car accelerometer types and positions are provided in Table 2.

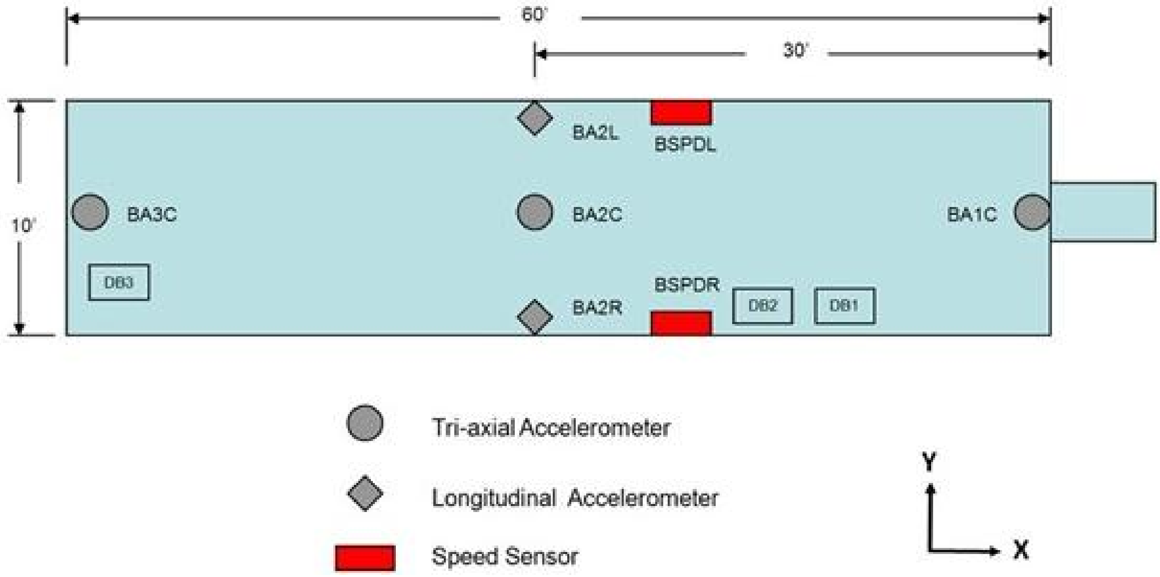

Figure 10. Ram Car Instrumentation

Table 2. Ram Car Accelerometers

Channel Name	Sensor Description	Range
BA1CX	Leading End, Centerline, X Accel	200 g
BA1CY	Leading End, Centerline, Y Accel	100 g
BA1CZ	Leading, Centerline, Z Accel	200 g
BA2LX	Middle, Left Side X Accel	100 g
BA2CX	Middle, Centerline, X Accel	50 g
BA2CY	Middle, Centerline, Y Accel	50 g
BA2CZ	Middle, Centerline, Z Accel	50 g
BA2RX	Middle, Right Side X Accel	100 g
BA3CX	Trailing End, Centerline, X Accel	200 g
BA3CY	Trailing End, Centerline, Y Accel	100 g
BA3CZ	Trailing End, Centerline, Z Accel	200 g

Speed sensors were mounted on both sides of the ram car to provide accurate measurement of the car velocity within 2 feet of the impact point. The speed sensors were reflector based light sensors, which used reflectors on the ground separated by a known distance in conjunction with light sensors mounted on the car that triggered as the car passed over the reflector. The last reflector was positioned to align with the sensor when the ram head was within a few inches of the impact point. The time interval between passing the reflectors was recorded, and speed was calculated from distance and time. A handheld radar gun was also used to take supplemental speed measurements.

3.3 Tank Car String Potentiometers and Pressure Transducers

The local displacement coordinate systems (except for the tank head) are defined relative to the tank car. Positive x, y, and z directions are forward, left (away from the wall), and up relative to the B-end of the tank car. Tank head displacements are positive toward the impact wall.

Six string potentiometers were used to measure the tank crush displacements around the immediate impact zone during the test. Five measured the dent formation of the tank at the tank center and at locations 24 inches and 48 inches to either side of the impact point. The sixth string potentiometer measured the vertical deformations of the tank at the center (aligned with the impact point). Four additional string potentiometers were used to measure the tank motions. The string potentiometers were attached to each of the tank skids and to the center of the tank heads at either end of the car. Fixed anchor positions were established so that these measurements were limited to the longitudinal motions of the tank head and skid movements. One string potentiometer was mounted outside of the pressure relief valve to measure if and when the valve was open. Table 3 provides a list of all string potentiometers inside and outside the tank car. Figure 11 and Figure 12 show their placement.

Table 3. Tank Car String Potentiometers

Area	Location	Axis	Channel Name	Range (inches)
Impact Area	A-end – 48-inch offset	Y	TD1Y	40
Impact Area	A-end – 24-inch offset	Y	TD2Y	50
Impact Area	Center	Y	TD3Y	50
Impact Area	Center	Z	TD3Z	40
Impact Area	B-end – 24-inch offset	Y	TD4Y	50
Impact Area	B-end – 48-inch offset	Y	TD5Y	40
Tank Head	A-end	Y	TDAend	50
Tank Head	B-end	Y	TDBend	50
Skid	A-end	Y	TDAskid	50
Skid	B-end	Y	TDBskid	50
PR Valve	PR Valve (Exterior)	Z	TDRV	10

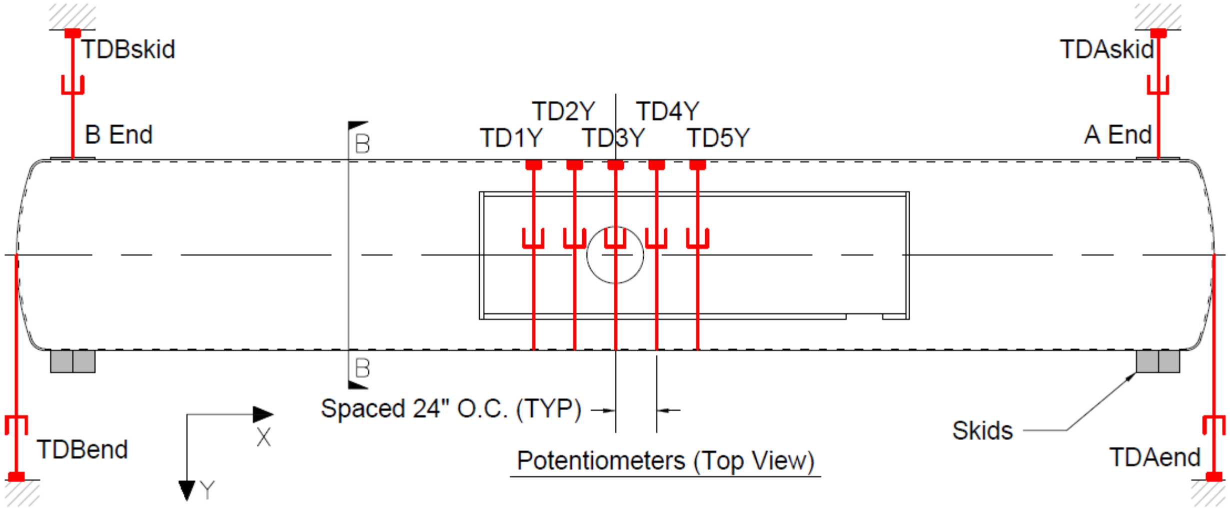

Figure 11. Tank Car String Potentiometers (Top)

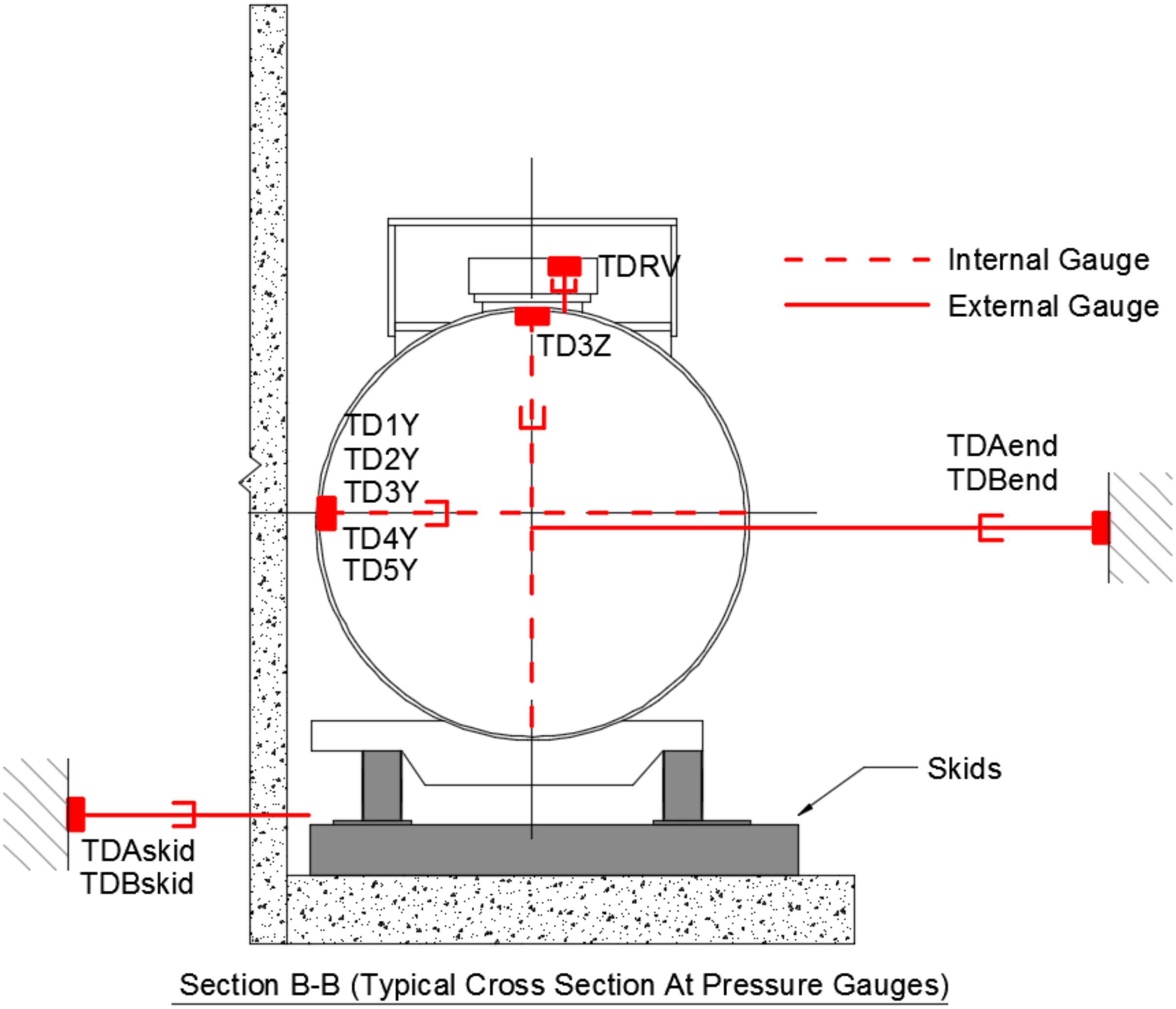

Figure 12. Tank Car String Potentiometers (Side)

An array of 12 pressure transducers was set up within the tank to record the pressure pulse through the lading. These were mounted in three sections on the sides and bottom of the tank. Table 4 provides a list of all pressure transducers used inside the tank car. Figure 13 and Figure 14 show their placement.

Table 4. Tank Car Pressure Transducers

Location	Channel Name	Sensor Description	Range (psi)
A Top	TP1000	A-End Top Pressure	300
A Back wall	TP1090	A-End Back Wall Pressure	300
A Front wall	TP1270	A-End Front Wall Pressure	300
A Floor	TP1180	A-End Floor Pressure	300
M Top	TP2000	Mid-length Top Pressure	300
M Back wall	TP2090	Mid-length Back Wall Pressure	300
M Front wall	TP2270	Mid-length Front Wall Pressure	300
M Floor	TP2180	Mid-length Floor Pressure	300
C Back wall	TP3090	Center Back Wall Pressure	300
C Floor	TP3180	Center Floor Wall Pressure	300
C Front wall	TP3270	Center Front Wall Pressure	300
C Top	TPMH	Outage Pressure in the Manway	500

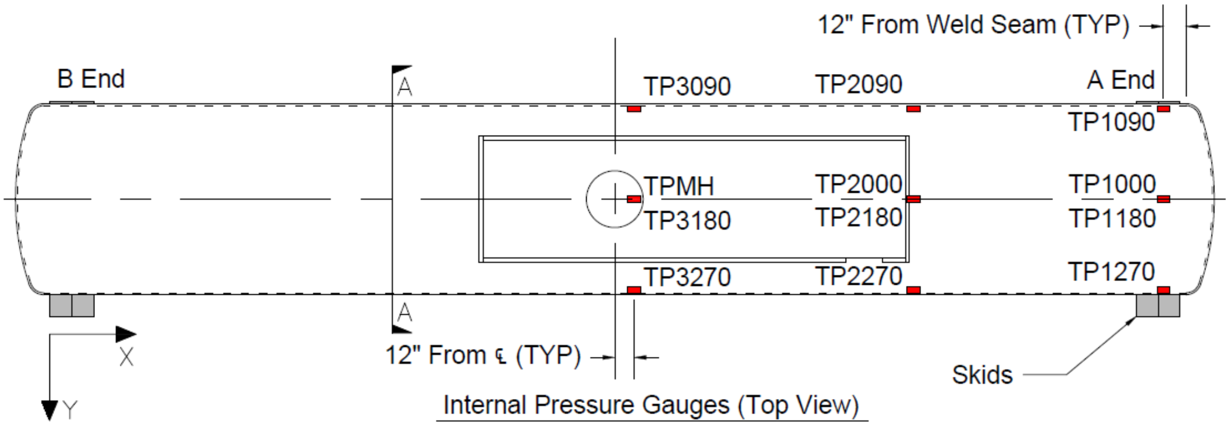

Figure 13. Tank Car Pressure Transducers (Top)

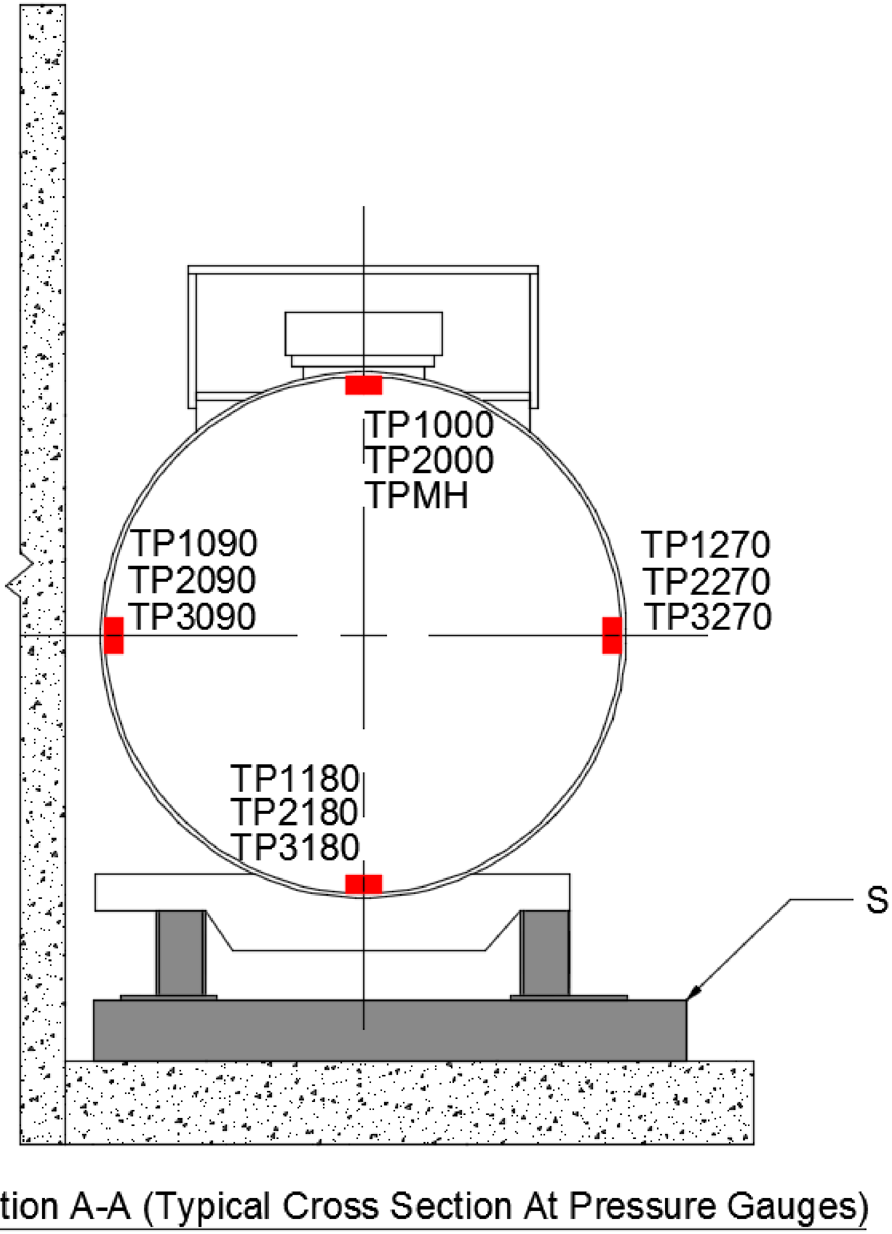

Figure 14. Tank Car Pressure Transducers (Side)

3.4 Real Time and High-Speed Photography

Three high-speed and four real time high definition video cameras were used to document the impact event. All high-speed cameras used were crashworthy and rated for peak accelerations of 100 g. The ram car, the protective panel, and the impact barrier were painted with flat light gray. The tip of the indenter was painted red. High contrast targets were applied to the ram car, the indenter, and the protective panel. Appendix A contains a schematic of the locations of the cameras and positions of the targets.

3.5 Data Acquisition

A set of 8-channel battery-powered onboard data acquisition systems was used to record the data from the instrumentation mounted on the ram car. These systems provided excitation to the instrumentation, analog anti-aliasing filtering of the signals, analog-to-digital conversion, and recording of each data stream. A similar set of ground-based data acquisition systems was used to record data from the pressure transducers on the tank car.

The data acquisition systems were GMH Engineering Data BRICK Model III units. Data acquisition complied with the appropriate sections of SAE J211 [3]. Data from each channel was anti-alias filtered at 1,735 Hz, then sampled and recorded at 12,800 Hz. Data recorded on the data bricks was synchronized to the time zero at initial impact. The time reference came from closure of the tape switches on the front of the test vehicle. Each data brick is ruggedized for shock loading up to at least 100 g. Onboard battery power was provided by GMH Engineering 1.7 Amp-hour 14.4 Volt NiCad Packs. Tape Switches, Inc., model 1201-131-A tape switches provided event initial contact.

Software in the data bricks was used to determine zero levels and calibration factors rather than relying on set gains and expecting no zero drift. The data bricks were set to record 1 second of data before initial impact and 4 seconds of data after initial impact.

4. Results

4.1 Test Conditions

As described in Sections 2.1 and 2.2, this test was a side impact on a DOT-117 tank car, performed on September 28, 2016. The test involved a 13.9 mph side impact by a structurally rigid 297,125-pound ram car with a 12-inch square impactor head into the side of the tank car, backed by a rigid impact barrier. The test tank car was filled to approximately 95 percent capacity with water to simulate standard commodity lading volume of a DOT-117 tank car, and it was sealed but not pressurized above atmospheric pressure.

At the time of the test, the ambient conditions included a wind speed of 11 mph south and an air temperature of 70 °F.

4.2 Details of Test

Pre-test simulations estimated a puncture speed range of 13 to 14 mph, on the basis of estimated material properties. The target speed for the test was 13.5 mph, in the center of this speed range. Regardless of whether the tank punctured or remained intact, one objective in choosing this target test speed was to ensure the actual impact speed was close to the threshold puncture/non-puncture speed. Section 6 contains a discussion of the pre-test simulations used to help select the target test speed. The actual calculated impact speed from the speed sensors was 13.9 mph.

The indenter created a permanent deformation, but did not puncture the tank car. Figure 15 shows the impact area after the test.

Figure 15. Tank Car after the Impact (Impact Side)

After impact, the ram car rebounded and stopped due to the activated airbrake. Since the tank car did not puncture, both the DOT-117 and the impactor rebounded from the wall following the impact. The tank car was measured to have rebounded by 10 inches on one end of the impact wall and 14 inches on the other side. Figure 16 shows the post-test position of the tank car relative to the supporting wall. The bottom outlet housing went inside the pit and struck the concrete slab and caused some damage.

Figure 16. Post-test Position of Tank Car (Wall Side)

The impact caused two vertical tears on the external jacket. These tears corresponded to the two vertical edges of the impactor. The jacket did not experience a horizontal tear. Thus, the impactor did not fully penetrate the jacket. Following a post-test examination of the tank car in its final resting position, a portion of the jacket was cut away from the tank. This allowed the jacket damage to be examined from the interior and allowed the damage to the tank itself to be directly observed. The damage to the jacket as viewed from the interior (i.e., the side that was toward the thermal protection) is shown in Figure 17. The directional notations indicate the position of each of the four edges when the jacket segment had been installed on the tank car. The “west” and “east” sides of the impacted zone are the two sides that had been vertically oriented during the test, and are the locations of the two vertical tears in the jacket. Figure 17 shows the jacket consisted of two partially overlapping sheets in the vicinity of the impact. Each of the vertical tears occurred on a portion of the jacket without any overlap (i.e., where the jacket was made of a single sheet).

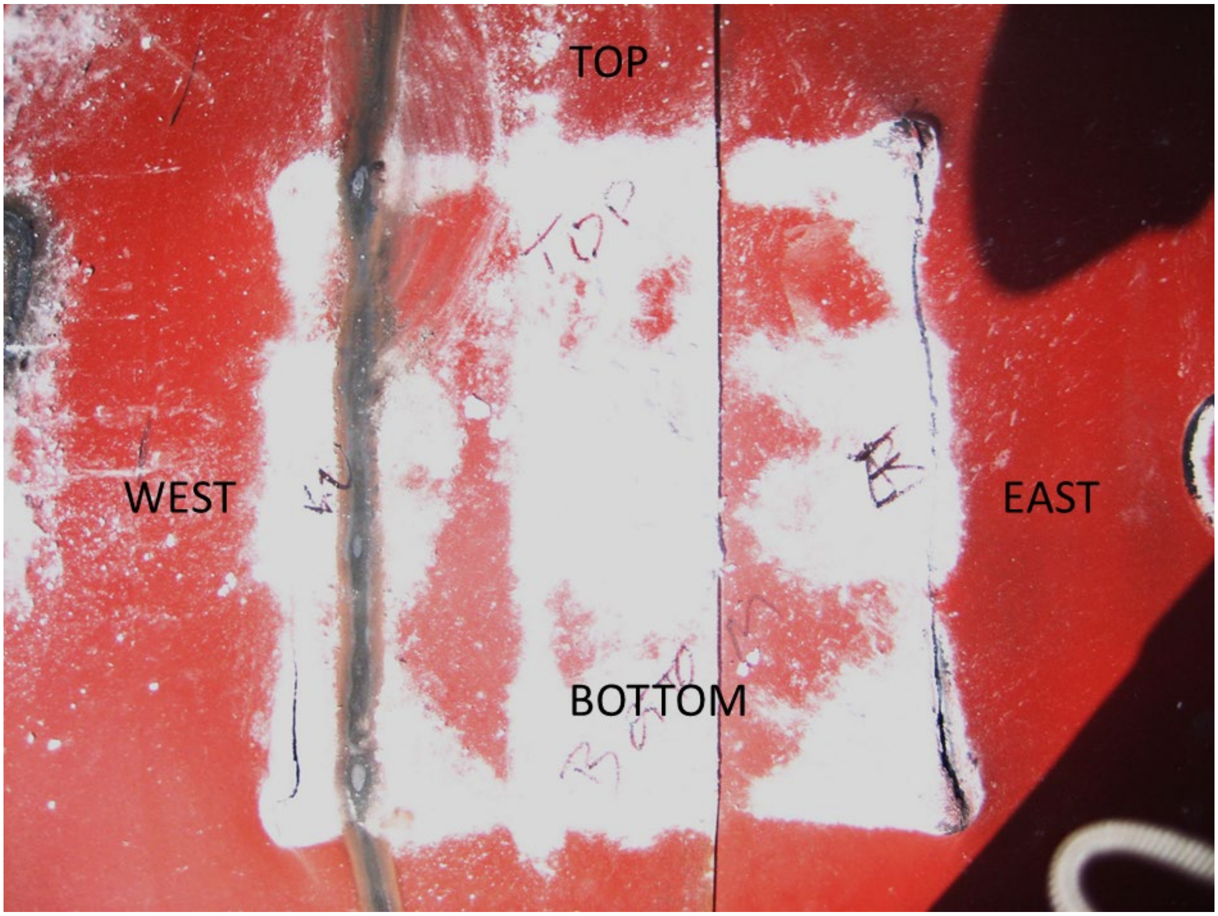

Figure 17. Interior View of Impact Zone on Jacket

Figure 18 shows the indentation of the tank car after impact. Figure 19 shows the interior jacket and area of the removed exterior jacket section.

Figure 18. Tank Car Indentation—Post Impact

Figure 19. Tank Car Indentation—After Removing Jacket and Insulation Section

Following the test, TTCI performed a non-destructive testing (NDT) examination of the interior of the tank itself using a fluorescent magnetic particle technique. This examination did not reveal any cracks or tears to the interior surface of the tank. A photograph of the impact zone taken from within the tank is shown in Figure 20. In this figure, the location of the upper left corner of the impactor is visible in the upper-right side of the image. The weld seam joining two shell rings is also apparent in this figure.

Figure 20. Interior of Impact Zone, Post-Test

4.3 Laser Scanning

TTCI scanned approximately an 8-foot by 8-foot surface of the tank car in the impact zone. Scans were performed before the test on the tank jacket and after the test on the shell. Therefore, there is approximately 0.5 inch of preexisting gap between the scans. Figure 21 shows a comparison of cross-sections at the impact of both scans aligned using reference points located on the tank car. The maximum permanent (plastic) deformation on the impact surface is approximately 22 inches. This indentation is smaller than the permanent deformation recorded by the internal string potentiometer of 28 inches. This is because the string potentiometer measures reduction of the tank shell diameter between the impact point and contact with the wall. Therefore, it includes deformation on both sides of the tank car.

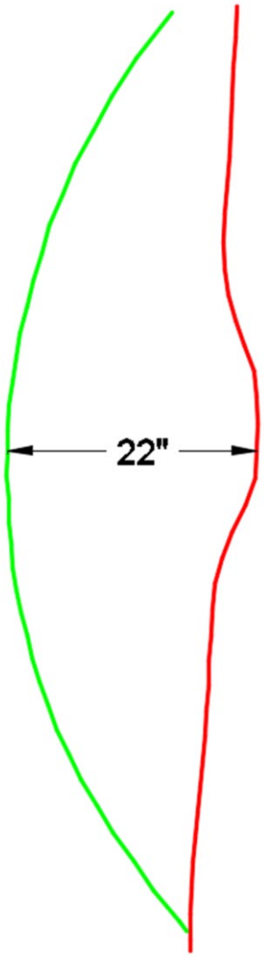

Figure 21. Comparison of Pre-Test and Post-Test Surface Scans—Cross-Section at the Impact

4.4 Measured Data

The data collected in the test was processed (offset corrections, filtering, etc.) initially by TTCI and provided to Volpe for comparison with the results of the analyses. The offset adjustment procedure ensures that the data that is plotted and analyzed contains only impact-related accelerations and strains and excludes electronic offsets or steady biases in the data. In order to determine the necessary offset, the data collected before impact was averaged. This offset was then subtracted from the entire data set for each channel. This post-test offset adjustment was independent of, and in addition to, the pre-test offset adjustment made by the data acquisition system.

The post-test filtering of the data was accomplished with a phaseless four-pole digital filter algorithm consistent with the requirements of SAE J211 [3]. A 60 Hz channel frequency class (CFC) filtering was applied for the filtered acceleration data shown in this report. A brief summary of the measured data is provided in this section. Appendix B contains the plots of filtered data from all transducers.

The longitudinal acceleration of the ram car was one of the primary measurements in the test, and multiple accelerometers were used on the ram car to capture this data. The ram car acceleration data was used to derive the impact energy, deceleration of the ram car, and contact forces between the ram and target tank car. The ram car average longitudinal acceleration history from all the ram accelerometers is shown in Figure 22.

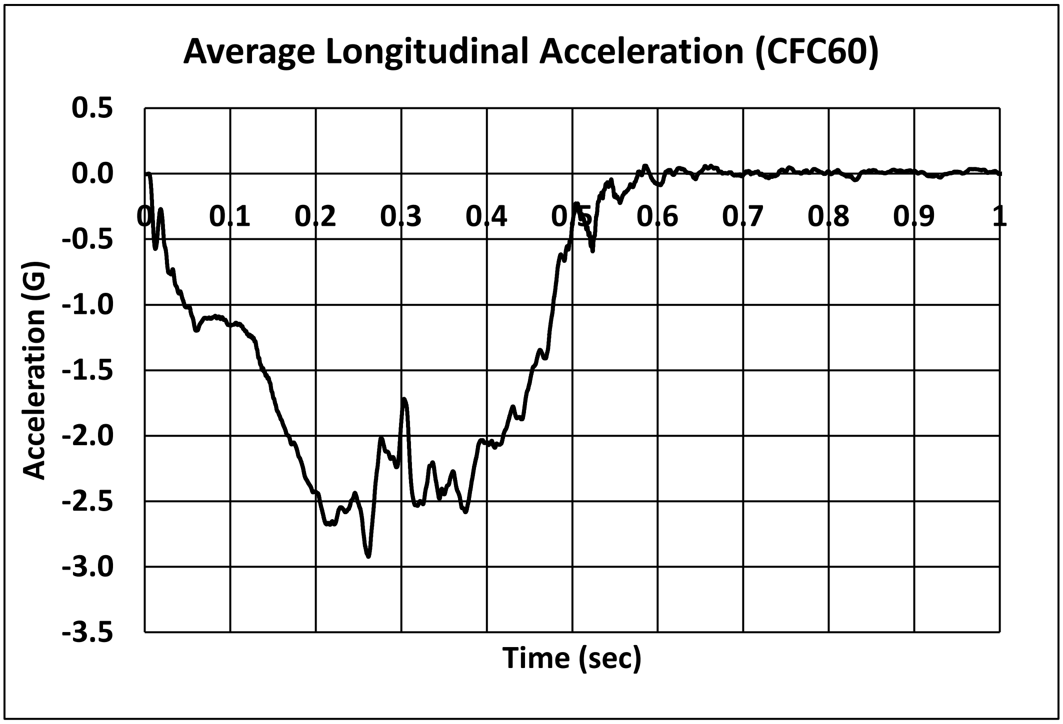

Figure 22. Longitudinal Acceleration Data (Averaged)

The ram car velocity history in the test can be calculated by integrating the average longitudinal acceleration of the ram car and using the impact speed measurement as an initial condition. Contact forces between the ram and target tank car can be calculated as a product of the average acceleration and mass of the ram. Figure 23 shows both the force-time and velocity-time histories, where negative velocity is speed of rebounded ram car. The ram car came to a stop (0 mph) at approximately the same time as the second peak in the force data. Since the tank car did not puncture, the total impact energy of 1,910,800 foot-pounds was absorbed.

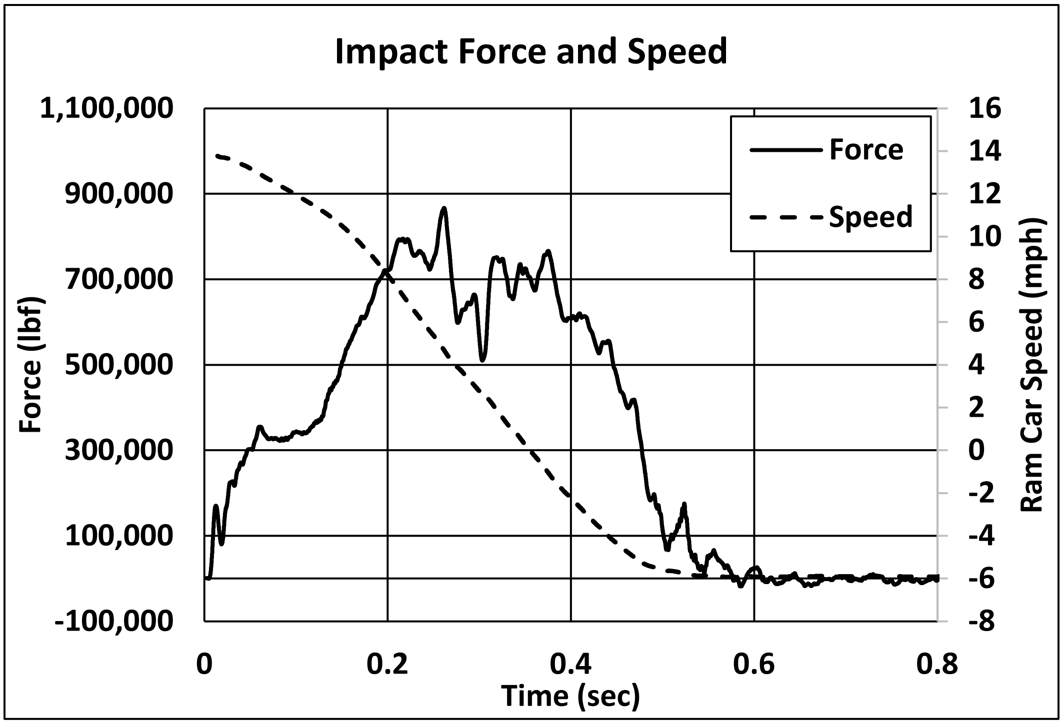

Figure 23. Impact Force and Ram Car Speed

Another significant impact response measured in the test was the effects of the internal pressure as the tank indentation formed and reduced the volume of the tank. The tank was initially unpressurized relative to atmospheric pressure. However, the tank was filled to an approximately 5 percent outage volume with water. Water can be approximated as incompressible for the impact behavior. As a result, the small air volume in the outage, initially at one atmosphere, was compressed as the dent formation reduced the tank volume and the internal pressure rapidly increased. As described in Section 3.3, pressure transducers were mounted at several locations in the tank within the water and within the air volumes.

Figure 24 shows pressure data from the center of the tank car (transducers TP3090, TP3180, TP3270, and TPMH). TP3270 was mounted on the front wall at the location of impact and was damaged during the test. Also, TP3180 showed a high increase in pressure around 0.2 seconds after the initial impact that is not believed to be true. This short duration pressure peak could have been caused by a cable being pulled by the deforming tank shell, except for the questionable pressure spike the comparison of pressure data shows that the pressure was dominated by the average hydrostatic pressure developed from the denting and volume change. However, there were additional dynamic pressures caused by the sloshing motions of the water in the tank that caused additional local pressure variations.

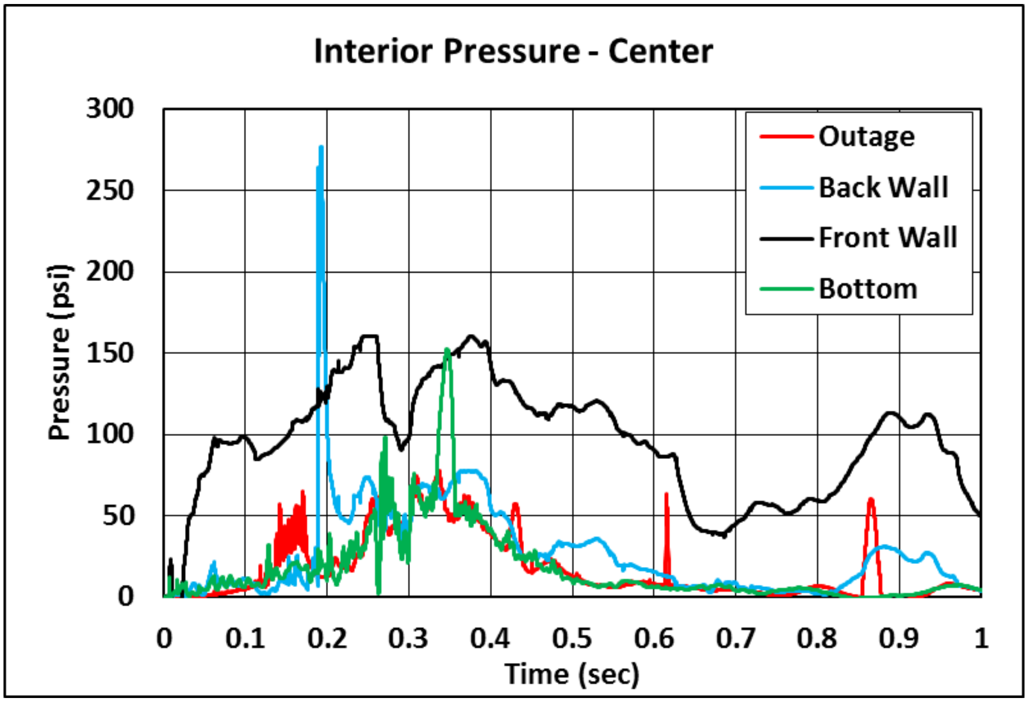

Figure 24. Pressure Data Measured at the Center of the Tank Car

The remaining quantitative measurements made of the tank impact behavior were displacement histories recorded with string potentiometers. These included both internal tank deformations and external tank movements at both ends of the tank. Layout of the string potentiometers is described in Section 3.3.

The measured displacements for the tank internal string potentiometers (TD1Y through TD5Y) are shown in Figure 25. Note that the longitudinal tank crush at the centered string potentiometer location exceeded the limit of the instrumentation, and the test traces max out at approximately 47 inches. Overall, the data shows consistent measurements of the tank deflections, with the largest deflection at the impact and reduced displacements at distances further from the center of the impact indentation.

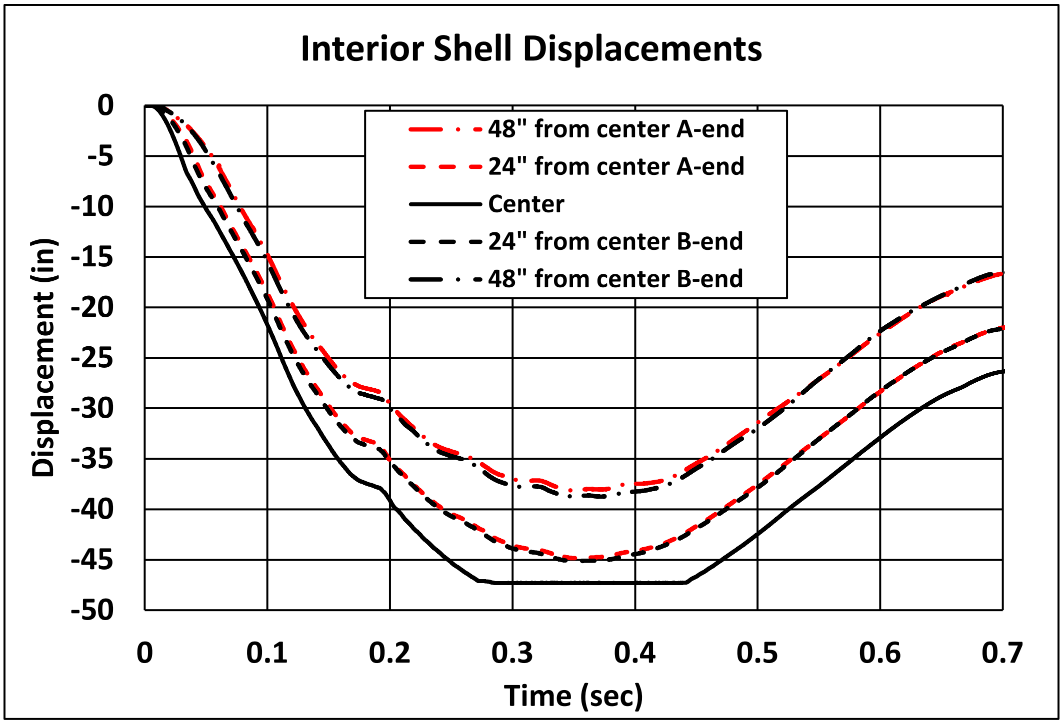

Figure 25. Internal Displacements

The measured displacements for the tank end external string potentiometers are shown in Figure 26 and Figure 27. The displacements of the car end were significantly delayed from the motions in the impact zone and little displacement is seen for the first 150 milliseconds of the response. Note that the measurements of the car end head displacements and the skid displacements were nearly identical and the response was very symmetric between the A-end and B-end of the tank until rebound occurred approximately 0.3 seconds after the impact.

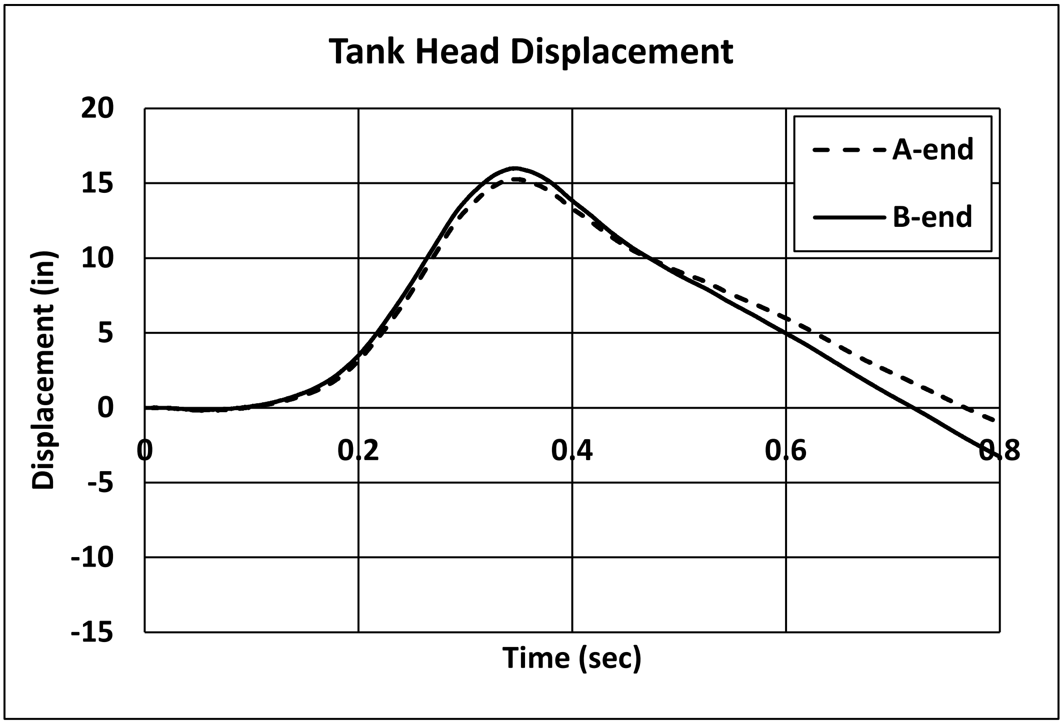

Figure 26. External Displacements—Tank Car Heads

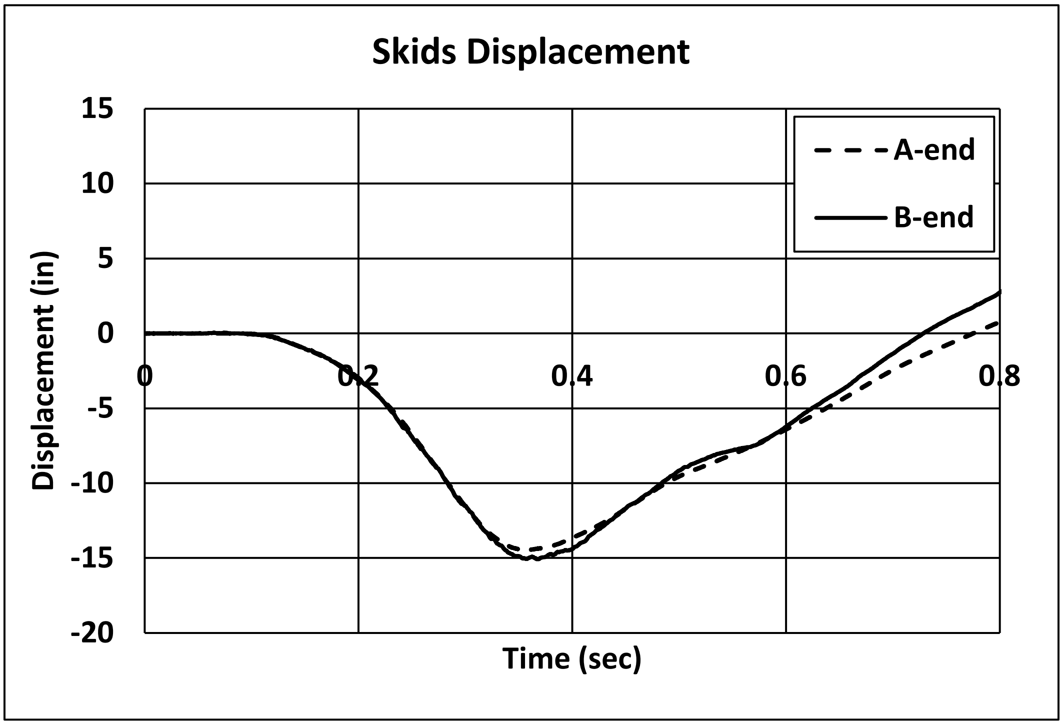

Figure 27. External Displacements—Skids

5. FE Model Development

FE models of the DOT-117 tank car were used before the test to help estimate the desired impact speed. Volpe developed the FE models, which incorporated and expanded upon several modeling techniques that had been used during simulations of previous tank car impact tests [4] [5] [6] [7]. The DOT-117 model required definition of the tank car geometry, geometry of the impact setup (e.g., impact wall, impactor, ground, etc.), definition of boundary conditions, constraints, initial conditions, and development of several material models. Additionally, modeling techniques, such as element types, mesh sizes, and fluid/structure interactions were selected.

The models were developed using the Abaqus/CAE preprocessor and executed in Abaqus/Explicit [9]. Abaqus/Explicit is a commercially available, general purpose nonlinear FE solver capable of simulating dynamic impacts involving complex material behaviors such as plasticity and puncture. The Abaqus software also includes several modeling techniques to represent the water and air phases of the lading, permitting these two parts to be modeled explicitly. The simulation techniques used in the DOT-117 model included modeling an elastic-plastic material response for the tank and jacket, ductile failure implementation of the Bao-Wierzbicki (B-W) triaxiality-based damage initiation model, and modeling of the water and air phases within the tank [10]. Following the test, the model underwent several adjustments to obtain better agreement between the test results and the FE results.

The purpose of the pre-test models was to provide estimates of the speed range where puncture could be expected to occur. In an ideal pre-test model, the actual yield strength, ultimate strength, ductility, and the shape of the plastic stress-strain response would be known, and used as inputs to the model. Prior to this test, this tank's material properties could not be known without excising coupons from the tank. Yield strength, ultimate strength, and ductility data were provided by the manufacturer of the tank car for the plates that were used to manufacture the shells of several DOT-117 cars in the same production run as the tested car. However, this data did not include the actual plastic stress-strain responses. Additionally, the data were measured from the as-received plates prior to any heat treatment, mechanical rolling, or welding necessary to fabricate the shell of the tank car. In the absence of additional material data, the plate data were used in conjunction with material behavior measured in previous tests to define the pre-test material behaviors required by the FE model. The development of the pre-test material responses is described in detail in Appendix F.4.1.

The impact conditions for the test, and therefore the FE model, were chosen specifically to permit comparison between this test and the 2013 test of a DOT-111 tank car and the 2014 test of a DOT-112 tank car [4] [5]. As previously described, the 12-inch by 12-inch impactor was used in this DOT-117 impact test and in the DOT-111 and DOT-112 impact tests.

The air and water phases of the lading were modeled using two different modeling techniques. Previously, a smoothed particle hydrodynamics (SPH) modeling approach was used to model the air phase of the DOT-112 test, and a Lagrangian (brick) formulation was used for the water phase [5]. An April 2016 DOT-105 impact test was modeled using a hydraulic cavity modeling approach for the water phase, and a pneumatic cavity modeling approach for the pressurized air phase [6]. For the DOT-117 test, the water phase was modeled using Lagrangian elements, while the air phase was modeled using the same pneumatic cavity approach as in the 2016 DOT-

105 tank car test. The Lagrangian approach to modeling water is described more fully in Appendix F5, and the pneumatic cavity approach to modeling air is described more fully in Section 5.3.4.

Following the test, several changes were introduced to the pre-test model to improve its agreement with the test results. The TC128 material behaviors in the post-test model were updated based on the results of tensile tests performed on the actual material of the tested car. The post-test model was run at the measured test speed of 13.9 mph. Based on pre-test measurements, the geometry of the rigid wall and ground in the post-test model were updated to more accurately reflect the test setup. Additionally, post-test models were run with both a rigid and deformable representation of the ground. The post-test model was run with a smaller mass scaling factor than the pre-test models, as a longer runtime was acceptable in post-test modeling. In the post-test model with the deformable ground, the geometry of the jacket was modified to reflect the overlap of two jacket segments at the impact zone. Finally, in the post-test model with deformable ground the areas of refined mesh on the tank and jacket were enlarged in the post-test model to ensure that the model was not artificially limited in its ability to simulate puncture.

5.1 Overview of Models

The pre-test and post-test FE models are made up of geometry representing the different components in the test setup, material parameters describing the behavior of the materials making up the car and its lading, and numerous constraints, boundary conditions, and loads describing the conditions of the test. As a part of both the pre-test and post-test modeling studies, non-puncture models were developed along with puncture-capable models. Non-puncture models featured simplified material behaviors, where the tank and jacket featured only elastic-plastic material responses, but not ductile failure behaviors. As the material definitions were not capable of simulating puncture, coarser meshes were used on the non-puncture models in the impact zone in the interest of reducing model runtime. The non-puncture models were useful for investigating several parameters, including fluid behaviors, before implementing any new behavior in the more complex puncture models.

In addition to featuring more complex material definitions, capable of simulating element degradation and removal, the puncture-capable models featured refined meshes on the tank and jacket in the areas of contact with the impactor. For the tank, this refined area was meshed using solid elements, while the much thinner jacket featured a refined shell mesh. The majority of the FE results presented in this report were obtained using puncture-capable models. A small number of non-puncture results are presented in Appendix F5, describing several different approaches to modeling water that were investigated during the pre-test modeling phase.

All models (pre-test, post-test, puncture-capable, and non-puncture) used a half-symmetric condition, with a vertical-longitudinal symmetry plane at the centerline of the tank car to reduce the size of the model. The tank geometry was simplified, and structures such as the bolster were omitted. These simplifications have a relatively minor effect on the impact response of the tank under the test conditions. The pre-test model is shown in Figure 28. The assembly of the pre-test model was similar to that of the post-test model, except that the pre-test model used a flat ground while ground in the post-test model incorporated a pit that was present in the test setup.

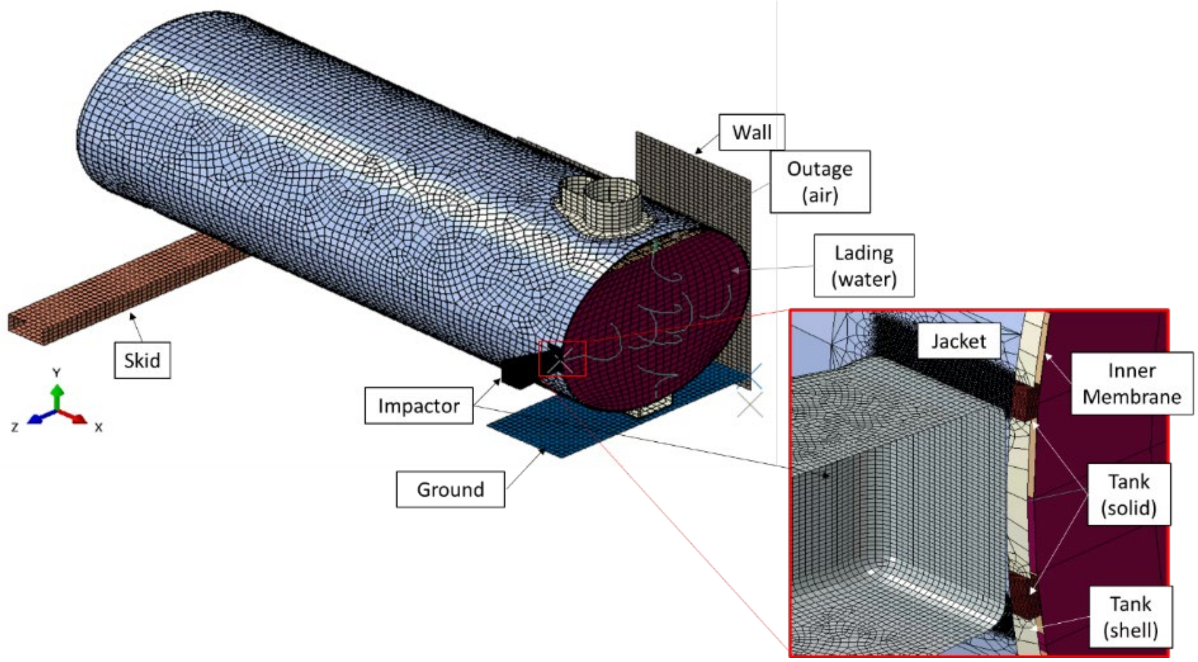

Figure 28. Annotated Pre-Test FE Model with Rigid Ground

5.2 Summary of the Assembly

The parts making up the model can generally be divided into three categories: rigid bodies, deformable bodies made of steel, and deformable bodies made of other materials. As the model was half-symmetric, the part weights in the FE model generally correspond to half of the weight of the actual tested geometry. The exception to this is the skid, as the skid exists entirely to one side of the symmetry plane. Therefore, the full weight of the skid is included in the model.

Table 5 contains a summary of the parts making up the FE model used in the pre-test puncture simulations. This table contains the weight of the part in the model, as well as the weight of the full part (2x model weight) for applicable parts. Due to adjustments made between this model and the post-test models, the meshes and part weights were slightly different in the post-test models. A full description of each part in the pre-test and post-test models can be found in Appendix D.

Table 5. Summary of Parts in Pre-test FE Model

Type of Part	Part Name	Number of Elements	Part Weight (in model) lbf	Part Weight (full) lbf
Rigid Bodies	Impactor	14,827	148,562.7	297,125.4
Rigid Bodies	Rigid Wall	1,728	-	-
Rigid Bodies	Skid	1,324	11,200	11,200
Rigid Bodies	Ground	643	-	-
Deformable, Steel	Jacket	41,172	5,857.4	11,714.8
Deformable, Steel	Tank (Shell Elements)	11,949	21,195.4	42,390.8
Deformable, Steel	Tank (Solid Elements)	40,152	5.9	11.8
Deformable, Non-steel	Internal Membrane	14,327	325.37	650.74
Deformable, Non-steel	Water	45,530	119,996.1	239,992.2

From this table, the total weight of the parts in the FE model corresponding to the entire DOT-117 (so, twice the weight in the half-symmetric model) would be approximately 317,200-pound force. This weight exceeds the 286,000-pound weight limit for a DOT-117 tank car in service. The single heaviest part in both the FE model and the test setup is the water within the tank car. Water was used in the test to account for both the mass and the dynamic effects of a fluid-filled tank car. However, the DOT-117 tank car would typically be used to carry flammable liquids such as ethanol or crude oil. As it is neither safe not practical to run an impact test using ethanol or crude oil within the tank car, water is used as an analogue. This also simplifies the pre-test and post-test FE modeling, as the mechanical properties of water are well-documented in publicly available sources.

Pure ethanol has a specific gravity of approximately 0.79 (at 70 °F, the test temperature) [25]. Crude oil is a more complicated substance to compare, as the term refers to a wide variety of substances that can vary greatly in chemical components and physical properties. However, specific gravities of 0.8–0.83 were found for light crude oils at temperatures slightly below the test temperature [26] [27]. Thus, if the tested DOT-117 tank car had been filled with the type of commodity typically carried within such a car, it would weigh approximately 40,000 to 50,000 lbf less than the water-filled tank car configuration.

5.3 Material Behaviors in FE Models

Three material definitions were used in both the pre-test and post-test FE models without adjustment: A1011 steel, an internal membrane, and air. The material properties for water were adjusted in the post-test model to match the properties at the temperature of the water in the test. A fifth material, TC128 steel, was modeled using different properties in the pre-test and post-test models. The material properties input to the FE models are summarized in this section. Complete descriptions of the development of the A1011 and TC128 steel characterizations are given in Appendix F3 and Appendix F4, respectively. A post-test model including a material characterization of the concrete slab that was struck by the bottom outlet housing was also developed. The development of the concrete model is described in Appendix F6.

5.3.1 Membrane

An artificial surface was modeled within the tank to define the limits of the pneumatic cavity modeling the outage, which is described in Appendix D7. Since this surface does not correspond to any physical structure within the tank, modeling techniques were chosen to minimize the increase in either mass or stiffness introduced into the model by the membrane.

The membrane part was meshed using surface elements for the portion of the part along the interior of the tank, and with membrane elements for the portion of the part that defined the interface between the water and the outage within the tank. Surface elements do not have a defined thickness or material behavior. Thus, these elements must be constrained to elements with these properties defined to prevent the surface elements from unconstrained distortion. The surface elements were attached to the mid-plane surface of the tank using a tied constraint (see Appendix E6).

Additionally, a membrane material was defined for the internal surface that divided the gas phase of the lading from the liquid phase. This membrane was modeled as having the same mass density of steel to avoid the minimum time increment becoming dominated by the artificial material in the membrane. The material properties of the membrane are summarized in Table 6.

Table 6. Material Properties Defined for Membrane Material

Density	0.00073499 lbf-s^2/inch
Modulus of Elasticity	30,000 psi

5.3.2 A1011 Steel

The outer jacket was made of A1011 steel for the tested DOT-117 tank car. The material properties defined for the A1011 material were derived from the Applied Research Associates, Inc. final report “Detailed Puncture Analyses of Various Tank Car Designs: Final Report – Revision 1” [7]. A full description of the development of the material parameters is provided in Appendix F3. These parameters are summarized in Table 7.

Table 7. Summary of Material Parameters for A1011 Steel

Parameter	Value
Modulus of Elasticity	3×10^7 psi
Plasticity	Piecewise nonlinear (see Appendix F3)
Poisson's Ratio	0.3
Mass Density	7.35×10^{-4} lbf-s^2/inch
Damage Initiation	B-W Envelope (see Appendix F3)
Damage Progression	Linear, 1,500 in-lbf/in^2
Mesh Implementation	0.04 inch Fully Integrated Shell (S4) Elements

5.3.3 Water

The DOT-117 tank car was being tested with a fairly small (5 percent) outage, and with the outage initially at atmospheric pressure. These conditions are similar to the test conditions used in a previous test of a DOT-112 tank car [5]. The DOT-112 test results indicated the need to model the lading in such a way that the sloshing and pressure increase of the outage could be properly captured. Thus, the water within the DOT-117 tank was explicitly modeled with a mesh, rather than the hydraulic cavity simplification employed in the simulation of the 2016 DOT-105 impact test [6]. While representing the water with an explicit mesh would lead to an increased simulation runtime, it was expected to better capture the complex fluid behaviors anticipated during the test.

The water filling the tank was modeled using an equation-of-state (EOS) model within Abaqus. The pre-test finite element analysis (FEA) used physical properties of water that were previously defined for an impact test of a DOT-112 tank car [5]. The post-test FEA used physical properties at the actual impact temperature of 70 °F. The differences between pre-test and post-test behaviors are small for the properties used in the model. Additionally, both the pre-test and post-test models made use of a "pressure cutoff" feature within the FE software. This feature limited the maximum tensile stress the water could support to 0 psi, effectively limiting the water from experiencing any tensile stresses. The physical parameters used to describe the water are shown in Table 8.

Table 8. Material Behaviors Defined for Water

Parameter	Value Input to Pre-Test Model	Value Input to Post-Test Model
Mass Density (lbf-s^2/in/in^3)	9.42294×10^{-5} [5]	9.40043×10^{-5} [11]
Speed of Sound (in/s)	56,064 [5]	58,421 [12]
Dynamic Viscosity (lbf-s^2/in^2)	2.24×10^{-7} [5]	1.42×10^{-7} [13]
Cutoff Pressure (psi)	0	

Several non-puncture simulations were used to guide the selection of mesh type and element size to capture the liquid response. These results are discussed in Appendix F5.

5.3.4 Air

The gas phase of the lading was modeled as air at an initial pressure of 1 atmosphere, as this was the desired internal pressure for the tank car during the test. Within Abaqus, the air within the outage was modeled as an ideal gas, using a pneumatic cavity modeling technique. This modeling technique requires a surface to be defined that encloses the cavity, with a reference point defined within this cavity to which initial temperature and pressure can be assigned. The initial pressure and temperature are discussed further in Appendix E9. The pneumatic cavity approach models the entire cavity with a single average pressure and average temperature value, each of which can vary with time. Thus, by using this technique, the air pressure within the model can change as the volume of the tank changes due to the impact. The modeling inputs defined for the air phase of the model are summarized in Table 9.

Table 9. Material Behaviors Defined for Air

Parameter	Value Input to Pre-Test and Post-Test Models	Reference
Universal Gas Constant (R) $\frac{in \cdot lbf}{mol \cdot K}$	73.583	[14]
Molecular Weight (MW) $\frac{\frac{lbf \cdot s^2}{in}}{mol}$	1.654×10^{-4}	[15]

The molar specific heat for air was calculated according to Equation 1.

Equation 1. Calculation of Molar Specific Heat

$$C_{pmolar} = C_p \times MW$$

Values for the specific heat capacity of air (C_p) were obtained from published values [16]. Table 10 shows the calculated values for molar specific heat at different temperatures that were defined as inputs to the FE models in the unit system used in the FE models.

Table 10. Molar Specific Heat for Air

Temperature (K)	C_{pmolar} $\frac{in \cdot lbf}{mol \cdot K}$
250	257.2
300	257.7
350	258.5
400	259.7

5.3.5 TC128 Steel

One purpose of this test was to subject the tank car to a moderately high speed impact that was close to the threshold speed between a puncture and a non-puncture outcome. While it was known from the certificate of construction that the tank was manufactured from TC128 Grade B steel, the actual plastic stress-strain response and elongation at failure would not be known until coupons could be excised from the tank car shell and subjected to tensile testing. As a means of developing a pre-test material model, the manufacturer of the car to be tested provided data on the yield strength, ultimate strength, and elongation at failure for the plates making up several DOT-117 cars from the same production period, including the test car. The average properties obtained from the manufacturer-provided plate data are summarized in Table 11.

Table 11. Average Material Properties for Plates Used to Construct DOT117 Shells

Average Yield Strength	62,062.5	psi
Average Ultimate Strength	88,854.17	psi
Average % Elongation in 8"	21.56667	%

Based on previous material modeling efforts for tank cars performed by Volpe, a pre-test TC128 elastic-plastic material response was developed that agreed with the properties of the manufacturer-provided plates [5] [6]. The process for developing the plastic stress-strain response is described more fully in Appendix F4. The material properties for the pre-test TC128 material are summarized in Table 12.

Table 12. Summary of Material Parameters for Pre-Test TC128

Parameter	Value
Modulus of Elasticity	3.26×10^7 psi
Plasticity	Piecewise nonlinear (see Appendix F4)
Poisson's Ratio	0.3
Mass Density	7.35×10^{-4} lbf-s^2/inch
Damage Initiation	B-W Envelope from Test 2 (see Appendix F4)
Damage Progression	Exponential, 700 in-lbf/in^2
Mesh Implementation	0.081 inch Fully Integrated Brick (C3D8) Elements (7 elements through coupon thickness)

In addition to requiring a plastic stress-strain response, the pre-test FE model required that a damage initiation envelope and damage progression behavior be defined, as described in

Appendix F4. report for a previous impact test of a DOT-105 tank car (Test 2) was used with the DOT-117 pre-test material response [7].

The nominal stress-strain response obtained from the tensile coupon simulation for the pre-test TC128 is shown in Figure 29. Additionally, the average yield strength, average ultimate strength, and average elongation from the manufacturer-provided plate data are plotted on this figure as a means of evaluating the nominal coupon response's level of agreement.

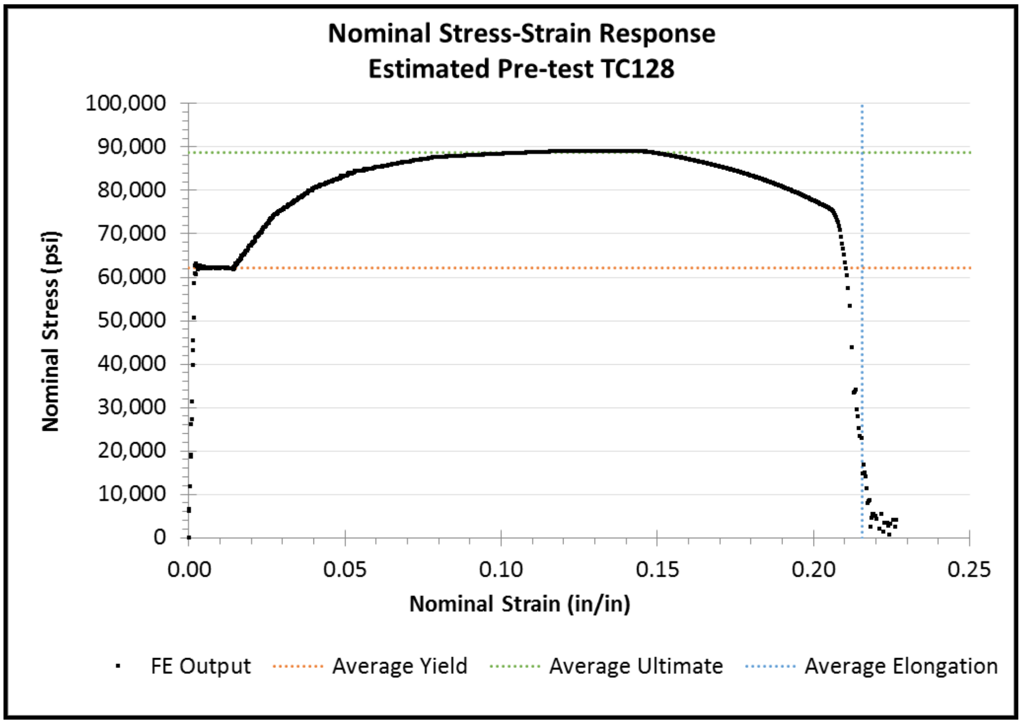

Figure 29. Nominal Stress-Strain Response from Estimated Pre-Test TC128 Behavior

Figure 30 plots the damage initiation envelope that was used in both Test 2 and the pre-test material model for the DOT-117 test.

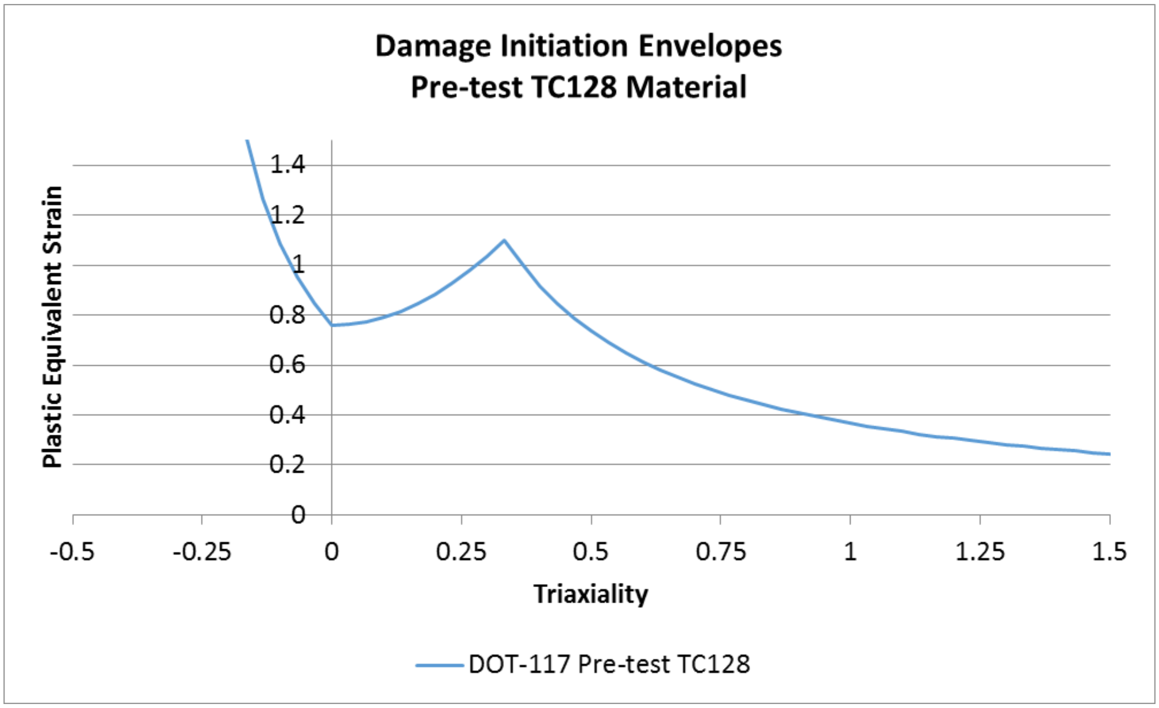

Figure 30. Damage Initiation Envelope for Pre-Test TC128 Material

After the test, material coupons were cut from undamaged areas of the tested DOT-117 and subjected to tensile testing. The post-test TC128 behavior is described in Section 5.5.2.

5.3.6 Concrete

A concrete material model was developed to investigate the effects of allowing the ground slab that was struck by the bottom outlet protection housing to deform. The concrete material properties were based on properties given in an Abaqus example problem [17]. The development of the concrete model is described in Appendix F6. The concrete material properties are summarized in Table 13.

Table 13. Summary of Material Parameters for Concrete

Parameter	Value
Modulus of Elasticity	4.5 x 10^6 psi
Dilation Angle	36.31°
Compression Hardening	Piecewise nonlinear (see Appendix F6)
Tension Stiffening	Piecewise nonlinear (see Appendix F6)
Poisson's Ratio	0.2
Mass Density	2.49 x 10^{-4} lbf-s^2/inch

5.4 Modeling Techniques Common to Pre-Test and Post-Test Models

In addition to the geometry making up the models, a series of constraints, loads, initial conditions, and boundary conditions were applied to the model to approximate the loading and support conditions expected during in the test. These techniques were generally common to both the pre-test and post-test FE models. Appendix E contains a detailed discussion of these techniques.

5.5 Modeling Techniques Adjusted Between Pre-Test and Post-Test Models

Several modeling techniques were adjusted in the post-test models, on the basis of either re-examining the model or the outcome of the test. These modeling techniques and their adjustments are described in this section.

The modeling changes were implemented incrementally, resulting in two distinct post-test models. The first post-test model featured the same meshes as in the pre-test model, an updated rigid ground geometry, updated initial position of the tank car, TC128 material properties based on the actual TC128 making up the tested tank car, and ran at the measured test speed but with a reduced mass scaling factor. This model is referred to as the post-test model with the rigid ground.

Based on the results of the post-test model with the rigid ground, a second post-test model was created that incorporated further refinements. In addition to the adjustments made to the post-test model with the rigid ground, this second post-test model featured a deformable concrete ground (replacing the rigid ground in the first post-test model), updated meshes in the puncture zones of the tank and jacket, and a representation of the area of the jacket with overlapping jacket sheets. This model is referred to as the post-test model with the deformable ground.

This section summarizes each of the changes made between the pre-test and post-test models.

5.5.1 Ground and Wall Geometry

During pre-test preparations at the TTC, it became apparent that there would be very little clearance between the bottom fittings protection on the tank car and the concrete slab located between the rails at the impact wall. TTCI placed plywood sheets under the skids to increase the clearance between the bottom of the tank and the skid, and exposed piping outside of the protective housing was removed prior to the test. Even with these measures, the distance between the bottom of the protective housing and the ground slab was only approximately 4.25 inches at the time of the test, as shown in Figure 31.

Figure 31. Pre-Test Vertical Clearance of Bottom Protection (Photo Courtesy of Kathi Kube)

The pre-test FE model included a rigid ground slab located 4 inches below the bottom outlet protection of the tank car. However, the actual ground slab was not a continuous plane, but contained a pit. During test preparations, the leading edge of the protective housing was measured to be approximately 17 inches in front of the leading edge of the pit. Thus, if the protective housing made contact with the ground and then pushed back by more than 17 inches during the test, the housing could fall into the pit, eliminating the vertical constraint imposed by the ground slab. The housing and pit are shown in Figure 32.

Figure 32. Pre-Test Positions of Bottom Protection and Pit (left) and Measurement from Leading Edge of Pit to Leading Edge of Bottom Protection (right)

Review of the test videos and post-test inspection of the test site showed the protective housing made contact with the ground, slid backward, entered the pit, and tore out a portion of the concrete when the tank rebounded from the wall. The post-test condition of the concrete slab and the housing are shown in Figure 33.

Figure 33. Post-Test Positions of Bottom Housing and Pit Viewed from Front (left) and Rear (right)

Due to the evidence of interaction between the protective housing and the pit, the post-test model was updated to include a rigid ground slab that featured the pit. A simplified updated geometry featured a rigid ground plane 4.25 inches below the bottom housing of the tank car that dropped off into a pit 17 inches behind the leading edge of the protective housing. The ground geometry used in this post-test FE model is shown in Figure 34.

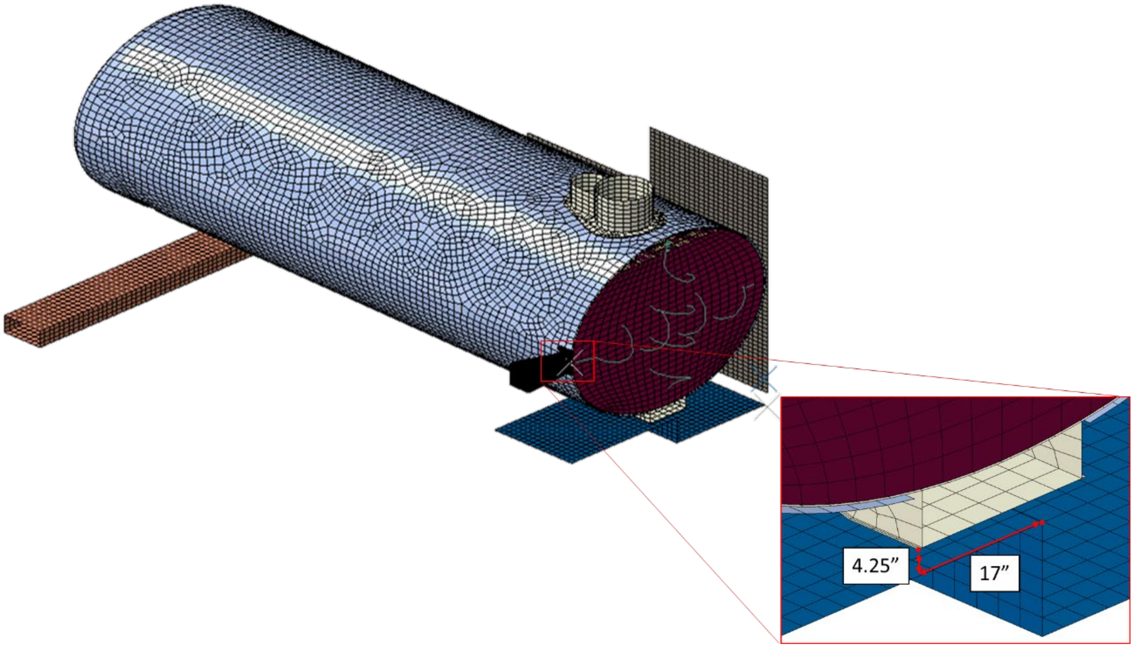

Figure 34. Rigid Ground Geometry used in Post-Test FE Model

A second post-test model featuring a deformable ground geometry was also created. This model was intended to determine whether it was necessary for the concrete slab to be able to deform in response to the strike from the bottom outlet protection. This was considered an important feature to investigate, as the slab in the test experienced fracture and had several chunks break off. The geometry of the post-test model with the deformable ground is shown in Figure 35.

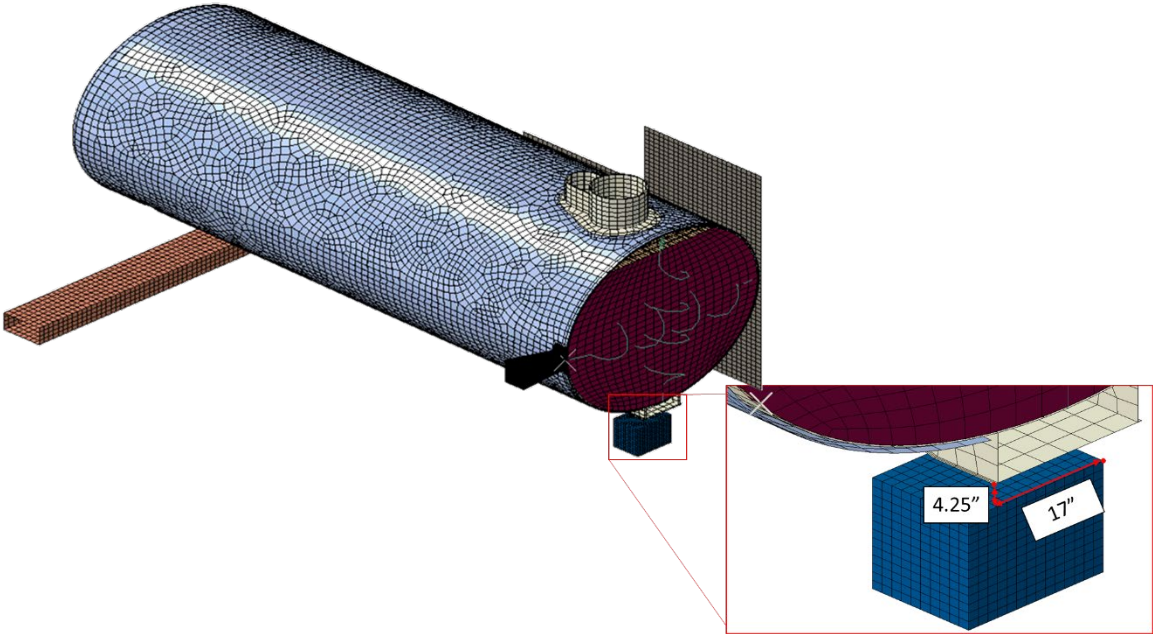

Figure 35. Deformable Ground Geometry used in Post-Test FE Model

Additionally, during the pre-test documentation of the test setup, the DOT-117 tank car was observed to not be uniformly resting against the impact wall. While the pre-test FE models featured the jacket initially in contact with the rigid wall, the post-test models incorporated a 1-inch offset between the outside of the jacket and the impact wall to better reflect the actual test setup, seen in Figure 36.

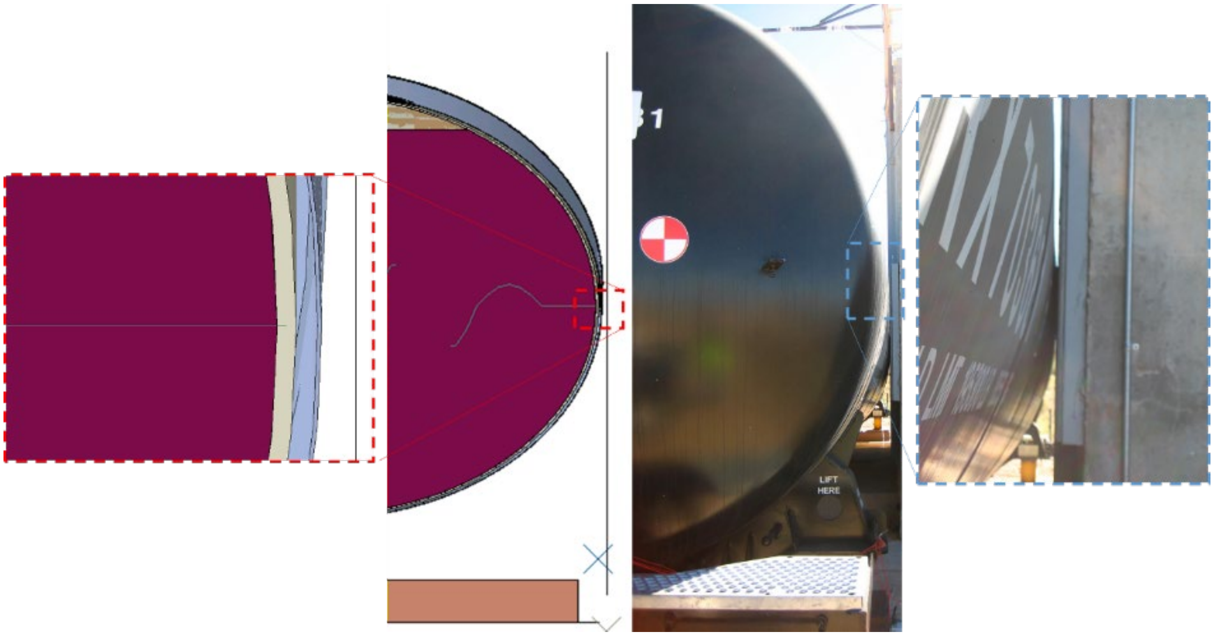

Figure 36. Gap Between Tank and Wall in Post-Test FEA (left) and Test (right)

5.5.2 Material Behaviors

Following the test, coupons were cut from the shell and subjected to tensile testing. The results of the coupon tests were used to develop the post-test TC128 material response, referred to as *actual TC128.* The process of developing the plastic stress-strain response in the format required by Abaqus, and the process of developing the ductile failure initiation and progression parameters are discussed in Appendix F4.

Figure 37 contains a plot of the nominal stress-strain response of the actual TC128 alongside the estimated pre-test TC128 response. From this figure, it is apparent that the actual TC128 featured a decreased yield strength, but an increased ductility compared to the pre-test material response. However, it is important to note that the pre-test TC128 results shown in this figure are derived from FE results of an 8-inch gage length coupon, and the post-test results in this figure are taken from tensile test measurements using 2-inch gage length coupons. The significant difference in elongation can be attributed to the use of different gage lengths between the pre-test and post-test material characterizations. However, the difference in strength between the pre-test estimate (based on plate data) and the actual post-test material is not attributable to using coupons of different sizes.

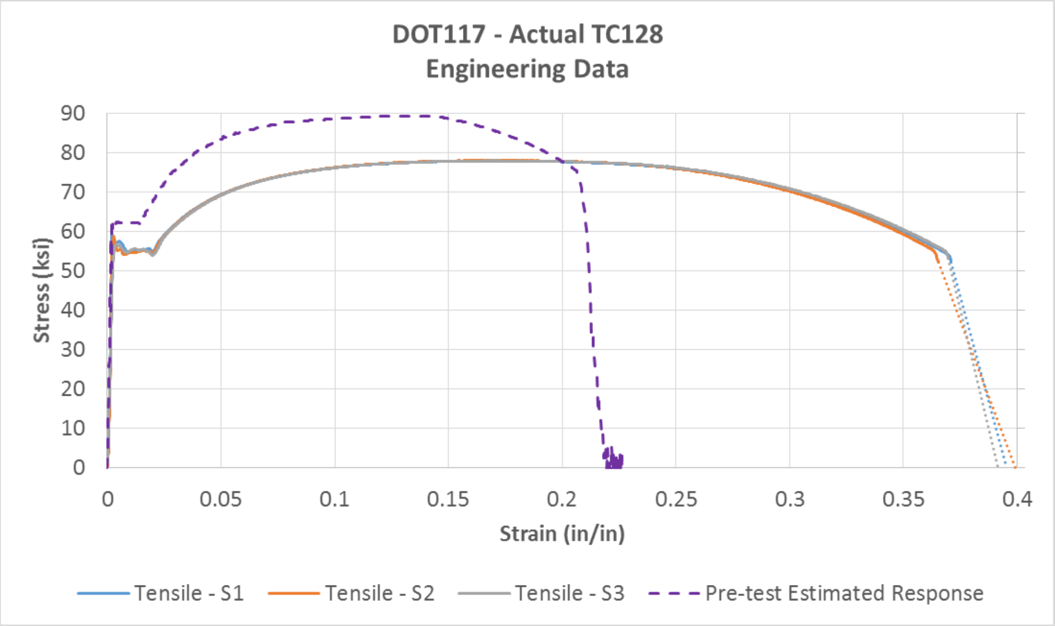

Figure 37. Nominal Stress-Strain Characteristics from FE Simulations of Pre-Test and Post-Test TC128 Varieties

Figure 38 contains a plot of the damage initiation envelopes of the actual TC128 material alongside the pre-test TC128 response. For triaxialities greater than approximately 0.45, the actual test material was found to have a damage initiation envelope that is very similar to the Test 2 envelope that was used in the pre-test modeling. As is discussed in Appendix F4, the damage initiation envelope developed for the actual TC128 material has its cusp at a calculated value, whereas the pre-test material model has its cusp forced to occur at a triaxiality of one-third.

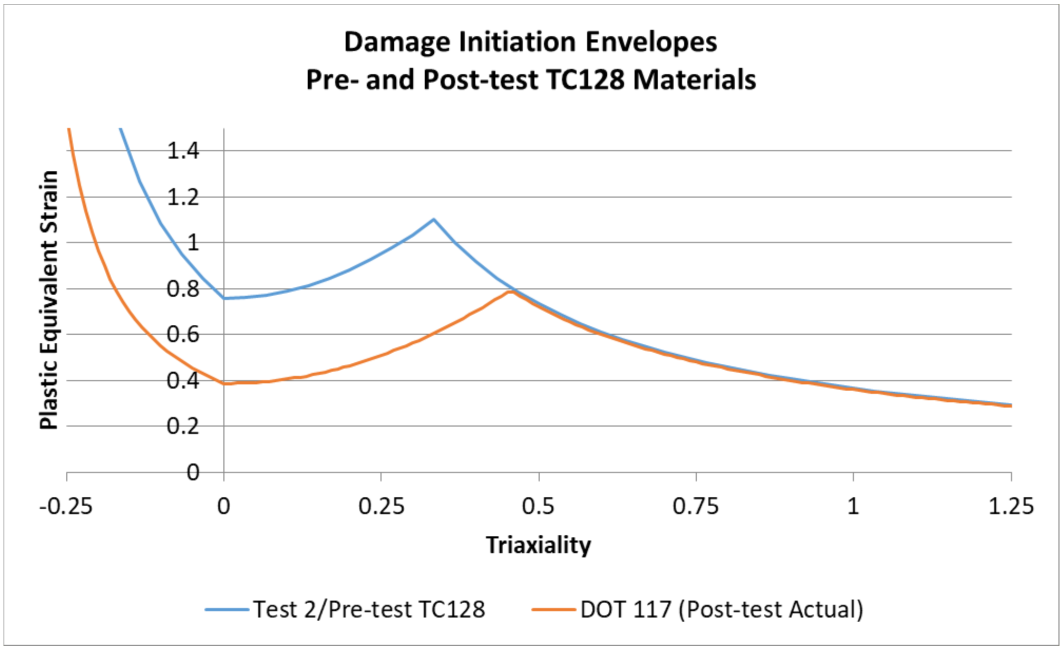

Figure 38. Damage Initiation Envelopes for all TC128 Materials

In addition to modifying the TC128 material in the tank, two other materials were adjusted or created in the post-test FE models. A concrete material behavior was defined in the post-test model to represent the deformable slab that was struck by the bottom outlet protection during the test. The development of this material behavior is described in Appendix F6. Additionally, the material properties used to model the water within the tank were updated to reflect the properties at the measured test temperature of 70 °F. The updated water material properties are described in Section 5.3.3.

5.5.3 Mass Scaling

The pre-test puncture-capable models used a mass scaling factor of 1 x 10^{-6} seconds. The post-test FEA used a reduced mass scaling factor of 5 x 10^{-7} seconds. In the pre-test modeling, it was more critical to reduce the runtime of the model to permit iterative modeling to be performed, but in the post-test modeling a longer runtime was more acceptable. Using a larger mass scaling target time will speed up the model's runtime, but will also result in a larger amount of mass being added to the smallest elements to bring up the minimum time increment. If these elements are in a localized area, such as the impact zone, the additional mass has the potential to affect the puncture response of the tank car.

5.5.4 Test Speed

The post-test FE models were run at the actual test speed as determined from the speed traps, which was 13.9 mph.

5.5.5 Refined Mesh in Impact Zone

In both the pre-test and post-test puncture models, a region of highly refined mesh was defined on the jacket and the solid patch of the tank to allow the model to experience puncture, should the damage initiation envelope be exceeded during the impact. The meshes on these two parts were carefully chosen to match the element size and element type used in simulating the material coupon tests for each respective material.

Although the 13.9 mph test did not puncture the tank, it was important to the model validation that the post-test model be *capable* of puncturing. If the post-test model were run at the test speed, and the model punctured, then the model would be known to be conservative compared to the test. However, if the post-test model did not puncture, it was important to establish that this behavior was accurately modeled. If the post-test model was created in such a way that puncture was either not possible, or puncture was not likely because of an unjustified assumption, then the model's validity would be more questionable.

The solid patch on the tank, and the refined shell mesh on the jacket were examined during the post-test modeling. The first post-test model used the same tank and jacket mesh as the pre-test modeling, but with an updated rigid ground geometry. In the solid patch, there was unreasonable distortion of the solid elements involved in the shell-to-solid coupling. This indicates that the shell-to-solid coupling may have been located in an area of distortion too extreme to be accurately captured by the shell-to-solid coupling simplification. Additionally, the jacket was known to tear in the test. It was important that the FE model include a large enough refined patch of elements on the jacket to ensure that the tearing initiated in the center of this patch, and not to be too close to the transition to the coarser mesh.

The second post-test model featured a deformable concrete slab under the tank. This post-test model also featured an expanded solid element patch and an expanded refined mesh in the jacket. These two changes increased the runtime of the post-test model compared to the pre-test models, but were considered important factors in the determination of whether the post-test model experienced puncture. This post-test model also featured a zone of elements in the center of the impact zone on the jacket that had twice the thickness of the jacket, to more accurately represent the region of overlap between jacket sheets observed in the tested jacket (as previously shown in Figure 17).

The extents of the solid patch in the pre- and post-test FE models are described in Appendix D6. The jacket geometry and meshes are described in Appendix D4.

6. Comparison of Test Response to Pre-Test Analysis

One of the intended uses of the pre-test models was to assist in test planning by estimating the range of impact speeds over which puncture would be likely to occur. The model was run using an iterative approach to attempt to determine a speed that would cause puncture without resulting in an excessive amount of residual energy in the impactor at the time of puncture. After using this iterative approach, the model was found to puncture at a speed of 14 mph, but to resist puncturing at a speed of 13 mph. The target speed for the test was chosen to be 13.5 mph on the basis of these results. Thus, a test run at 13.5 mph was in the range of speeds where puncture was a possible outcome, but not the only likely outcome. The range of expected test speeds was +/-0.5 mph around the target speed, or 13 to 14 mph.

The pre-test modeling results for each of these two impact speeds are compared to the test results in this section. In general, there was very good agreement between the pre-test FEA results and the measurements made during the test. The complete set of comparisons between pre-test FEA and test results can be found in Appendix C.

During post-test examination of the data, it was apparent that the acceleration-time data experienced a lag after triggering, but before a significant deceleration was measured. The triggers on both the ram car and the DOT-117's jacket were offset from their respective surfaces by placing 0.5-inch pieces of plywood between each trigger and the surface to which it was attached. Assuming that the instrumentation was activated the instant the two triggers made contact, this time would correspond to a zero-time when the ram and jacket were still 1-inch away from one another. Based on the measured test speed of 13.9 mph, a 1-second gap would take 0.004 seconds to close. For all test results presented in this section, the time has been offset by 0.004 seconds to account for the test instrumentation triggering when the ram surface was still approximately 1-inch away from making contact with the jacket.

The impact force versus impactor travel is compared between each of the pre-test FE models (13 mph and 14 mph) and the test measurements in Figure 39. While the FE model used a rigid impactor with a single acceleration-time history, the ram car in the test featured five longitudinal accelerometers. Unless otherwise specified in this section of the report, the test force reported is the average of the five longitudinal accelerometer channels. Additionally, both the test and FE forces reported in this section were filtered using a CFC60 filter [3].

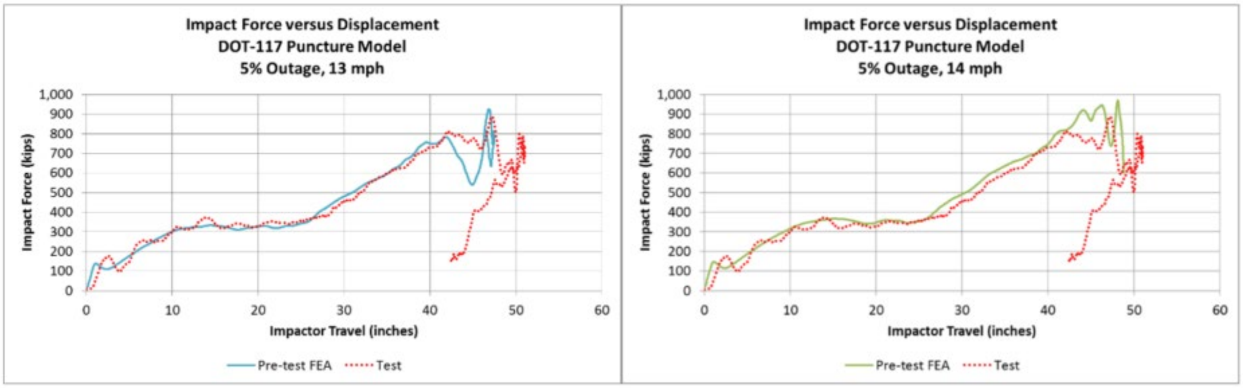

Figure 39. Force-Displacement Responses from Pre-Test FEA at 13 mph (left) and 14 mph (right), Compared to Test Results

Both the 13 mph and 14 mph models showed a similar shape to the test measurements. The models did a good job of capturing the overall response of the test, including the changes-in-slope to the response as the impactor deformed the tank car and pushed it back against the wall. The test measurements indicated a larger maximum indentation than either model. The 13-mph pre-test model was run at a lower speed than the test (13.9 mph) and thus, imparted less kinetic energy to the tank. The 14-mph pre-test model resulted in puncture of the tank car, whereas the test did not puncture the tank car at a slightly lower speed.

Figure 40 shows two comparison plots of air pressure for the 13 mph and 14 mph pre-test models compared to the test data. For each FE result, the air pressure is plotted as the average air pressure in the outage. For the test data, the average air pressure is plotted. During review of the test data, one of the pressure transducers in the outage (TP2000) appeared to measure pressures that were dramatically higher than the other pressure transducers. Therefore, the average pressure values plotted in this section exclude channel TP2000. The data results from this channel are shown in Appendix B2.

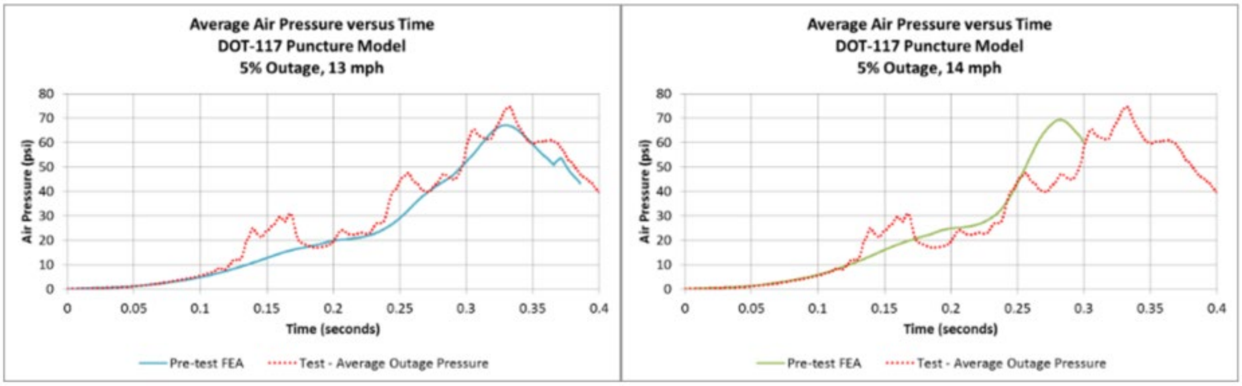

Figure 40. Air Pressure-Time Responses from Pre-Test FEA at 13 mph (left) and 14 mph (right), Compared to Test Results

Figure 41 contains plots comparing the internal string potentiometer measurement at the center of the car against the 13 mph and 14 mph pre-test FE model results. During the test, the string potentiometer at this location reached its measurement limit, resulting in the horizontal line seen after approximately 0.27 seconds. In both pre-test FE models, the model captures the general shape of the test response, including a change-in-slope measured just before 0.2 seconds during the test.

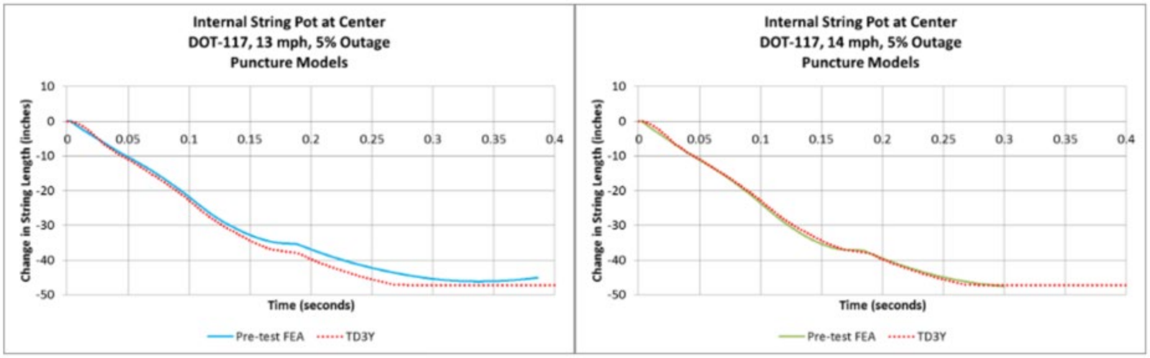

Figure 41. Change in Center String Potentiometer Length for Pre-Test FEA at 13 mph (left) and 14 mph (right), Compared to Test Results

Figure 42 contains plots comparing the vertically oriented internal string potentiometer measurements at the center of the car against the 13 mph and 14 mph pre-test FE model results. Both the 13 mph and 14 mph pre-test models exhibited good agreement with the test results in terms of the overall shapes of the curves, and the general magnitudes of the responses. The test measurements indicated a larger change-in-length than either model. This difference may be due to the existence of a pit in the ground under the tested car, which would have allowed an increase in vertical travel of the bottom outlet protective structure. Both pre-test FE models used a flat ground plane without any pit, which would have inhibited the ability of the model to ovalize to the same degree as the test.

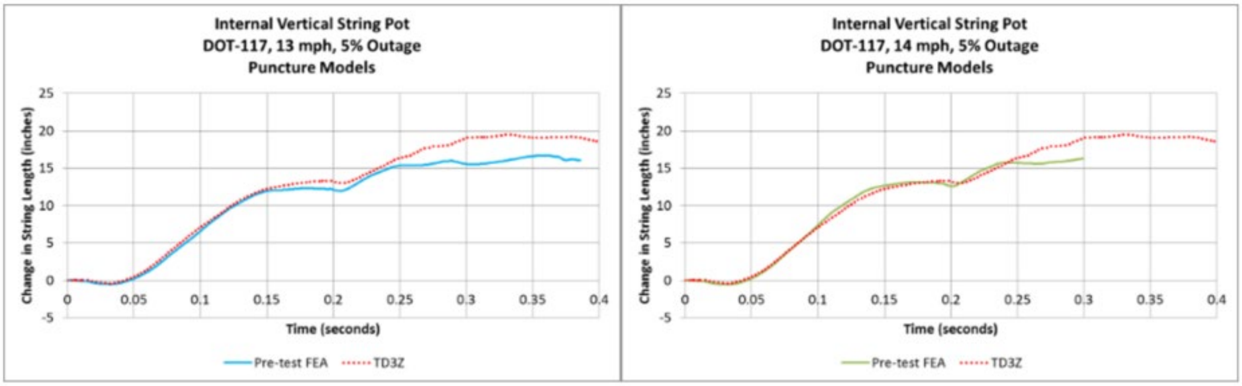

Figure 42. Change in Vertical String Potentiometer Length for Pre-Test FEA at 13 mph (left) and 14 mph (right), Compared to Test Results

Table 14 presents a summary of the level of agreement between the peak measurements from the pre-test FEA at 13 mph and the test. The pre-test FE results from the 13 mph simulation were in good qualitative (shape) and quantitative (magnitude) agreement for the values compared with the test data. For many of the displacement results, the pre-test FEA estimated a value below the test measurements. This outcome is consistent with this pre-test model being run at 0.9 mph below the test speed.

Table 14. Comparison of Peak Results from Pre-Test FEA at 13 mph and Test Results (13.9 mph)

	Pre-Test FEA 13 mph	Test 13.9 mph	Percent Difference
Longitudinal Acceleration	-3.1 g	-3.0 g	4.7%
Impact Force	925.8 inches	883.8 inches	4.7%
Displacement at Peak Force	46.9 inches	47.3 inches	-0.9%
48-inch Offset String Potentiometer	-36.1 inches	-38.1 inches	-5.3%
48-inch Offset String Potentiometer	-36.1 inches	-38.7 inches	-6.7%
24-inch Offset String Potentiometer	-41.5 inches	-44.8 inches	-7.4%
24-inch Offset String Potentiometer	-41.5 inches	-45.1 inches	-8.0%
Center String Potentiometer	-46.2 inches	-47.3 inches	-2.3%
Vertical String Potentiometer	16.7 inches	19.5 inches	-14.3%
Skid String Potentiometer	-11.7 inches	-14.4 inches	-19.2%
Skid String Potentiometer	-11.7 inches	-15.1 inches	-22.6%

	Pre-Test FEA 13 mph	Test 13.9 mph	Percent Difference
Head String Potentiometer	-14.4 inches	-15.3 inches	-5.9%
Head String Potentiometer	-14.4 inches	-16.0 inches	-10.2%
Average Air Pressure	67.1 psi	74.6 psi	-10.0%

Table 15 presents summary of the level of agreement between the peak measurements from the pre-test FEA at 14 mph and the test. The pre-test FE results from the 14 mph simulation were in good qualitative (shape) and quantitative (magnitude) agreement for the values compared with the test data. For many of the displacement results, the pre-test FEA estimated a value below the test measurements. This outcome is consistent with this pre-test model being run at a speed high enough to cause puncture of the model. The impactor in the model punctured the tank and thus, limited further deformation of the tank in those areas that were instrumented in the test.

Table 15. Comparison of Peak Results from Pre-Test FEA at 14 mph and Test Results (13.9 mph)

	Pre-Test FEA 14 mph	Test 13.9 mph	Percent Difference
Longitudinal Acceleration	-3.3 g	-3.0 g	9.8%
Impact Force	970.0 kips	883.8 kips	9.8%
Displacement at Peak Force	48.1 inches	47.3 inches	1.8%
48-inch Offset String Potentiometer	-36.6 inches	-38.1 inches	-4.0%
48-inch Offset String Potentiometer	-36.6 inches	-38.7 inches	-5.5%
24-inch Offset String Potentiometer	-42.0 inches	-44.8 inches	-6.3%
24-inch Offset String Potentiometer	-42.0 inches	-45.1 inches	-7.0%
Center String Potentiometer	-47.7 inches	-47.3 inches	0.8%
Vertical String Potentiometer	16.3 inches	19.5 inches	-16.4%
Skid String Potentiometer	-8.2 inches	-14.4 inches	-43.0%
Skid String Potentiometer	-8.2 inches	-15.1 inches	-45.4%
Head String Potentiometer	-12.9 inches	-15.3 inches	-15.6%
Head String Potentiometer	-12.9 inches	-16.0 inches	-19.4%
Average Air Pressure	69.4 psi	74.6 psi	-7.0%

7. Comparison of Test Response to Post-Test Analysis

Following the test, the pre-test FE model was updated to include the actual material properties, to better reflect the support provided by the rigid wall and ground, to ensure puncture capability was adequately modeled, and to be run at the measured impact speed of 13.9 mph. Two post-test models were executed. The first model replaced the flat, rigid ground slab beneath the car with a rigid ground slab based on the geometry of the test setup, including a pit. The second post-test model used a simplified concrete material response to model the ground slab as a deformable body. Further details on the changes made in each post-test model were provided in Section 5.5. The post-test modeling results for this impact speed are compared to the test results in this section. In general, there was excellent agreement between the post-test FEA results and the measurements made during the test, with better agreement seen between the model including the deformable ground than the model using the rigid ground.

7.1 Post-Test Model with Rigid Ground

The post-test FE model with rigid ground experienced puncture at the test speed of 13.9 mph, with a small (~1.5 mph) residual impactor speed. This small residual speed indicated that the energy to cause puncture of the model was only slightly exceeded by the impact energy. The complete set of comparisons between post-test FEA and test results can be found in Appendix C3.

The impact force versus impactor travel is compared between the post-test FE model with rigid ground and the test measurements in Figure 43. While the FE model used a rigid impactor with a single acceleration-time history, the ram car in the test featured five longitudinal accelerometers. Unless otherwise specified in this section of the report, the test force reported is the average of the five longitudinal accelerometer channels. Additionally, both the test and FE forces reported in this section were filtered using a CFC60 filter [3].

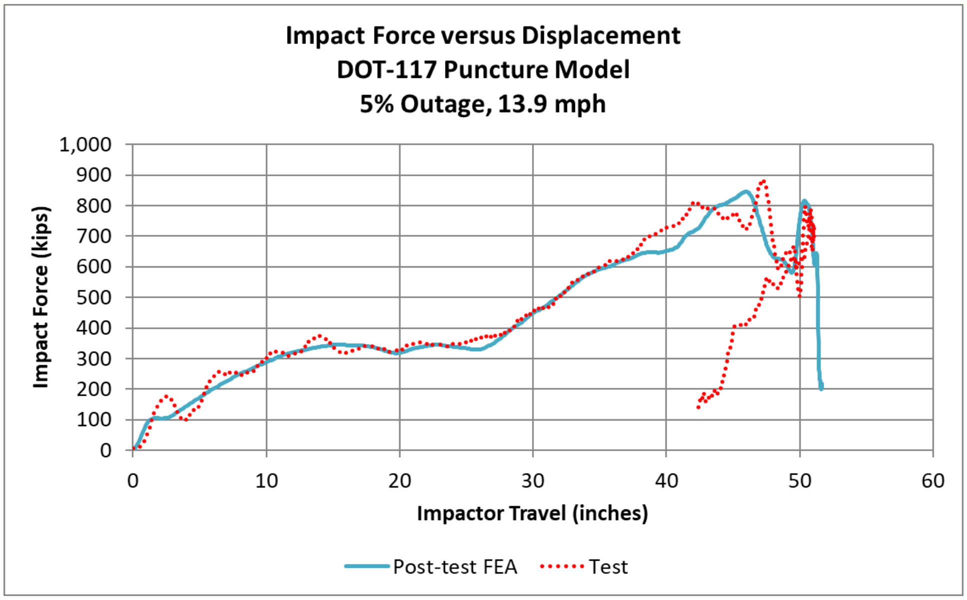

Figure 43. Force-Displacement Responses from Post-Test FEA with Rigid Ground and Test

The post-test model shows excellent qualitative agreement with the overall shape of the test measurements. The model does a very good job of capturing the response of the test, including the changes-in-stiffness of the response as the impactor deformed the tank car, pushed it back against the wall, and deformed it. The model and the test both experienced a dip in force after approximately 45 inches of impactor travel, likely the result of the fluid sloshing within the tank. The model also experienced peak forces that are in good agreement with the test for both timing and magnitude. The model nearly stops the impactor before experiencing puncture, whereas the test completely stopped the impactor without puncturing.

Overall, the FE model did a good job of capturing the response of the fluid during the test. Figure 44 shows side and front section views of the tank at three times. The top row corresponds to t=0, the initial position of the model. The center row corresponds to t=0.175 seconds, midway through the impact event. The bottom row corresponds to t=0.33 seconds, after the time of puncture. As can be seen in the bottom frame of this figure, the bottom outlet protective housing has fallen into the pit in the ground by the end of the impact event.

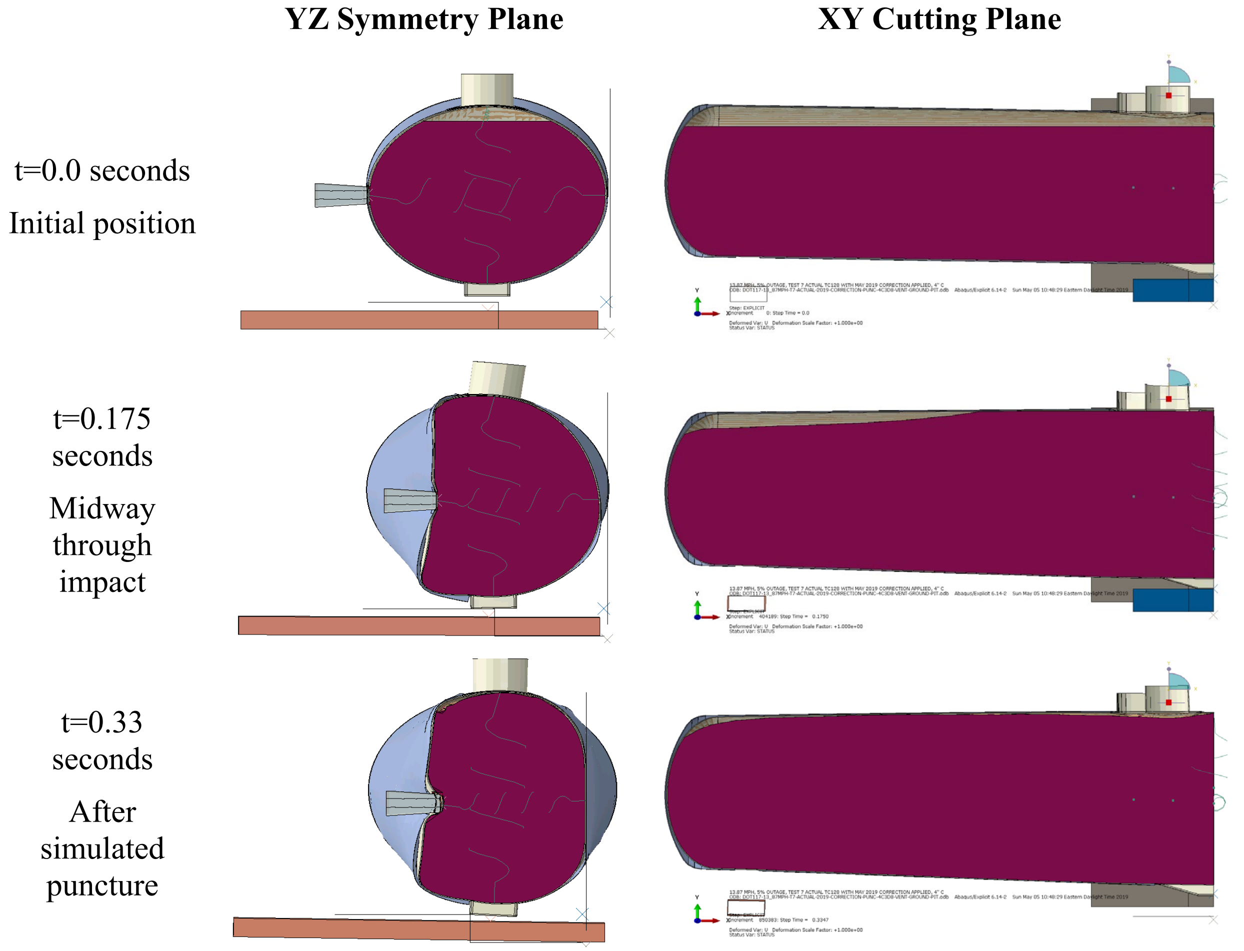

Figure 44. Impact Progression, Post-Test FE Model with Rigid Ground

Figure 45 shows a comparison plot of air pressure for the post-test model and the test data. For the FE result, the air pressure is plotted as the average air pressure in the outage. For the test data, the average air pressure is plotted. During review of the test data, one of the pressure transducers in the outage (TP2000) appeared to measure pressures that were dramatically higher than the other pressure transducers. Therefore, the average pressure values plotted in this section exclude channel TP2000. The data from this channel are shown in Appendix B2.

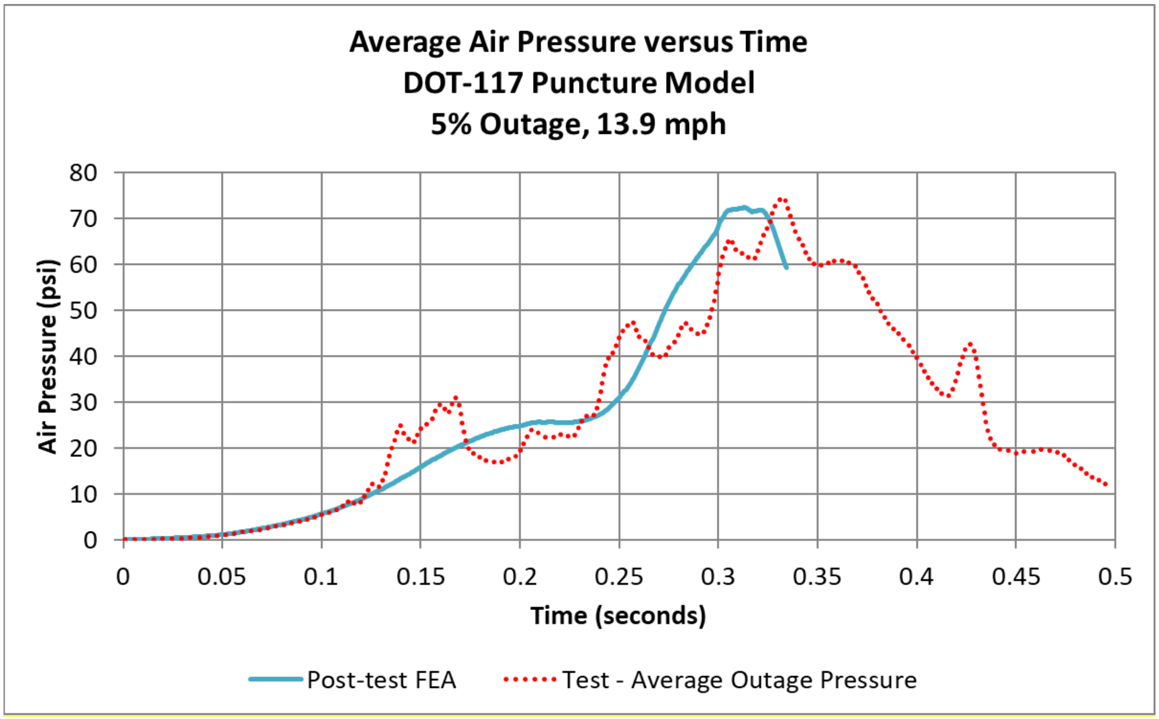

Figure 45. Air Pressure-Time Responses from Post-Test FEA with Rigid Ground and Test

Figure 46 compares the A-end (TDASKID) and B-end (TDBSKID) skid displacements measured during the test to the skid displacement calculated in the post-test FE model. The overall shape of the three responses are similar, however, the puncture of the FE model limits the length of impact time that was simulated. Thus, the FE results do not include the skid behavior measured after the impactor rebounded from the tank car, whereas the test measurements do.

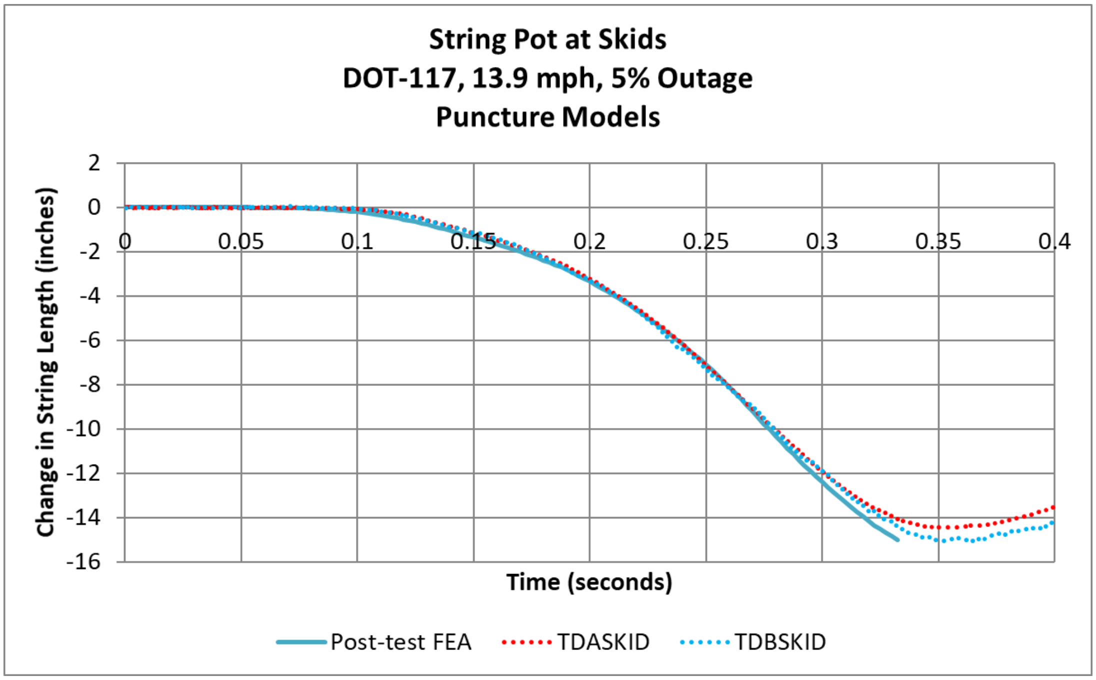

Figure 46. Skid Displacement in Post-Test FEA with Rigid Ground and Test

Figure 47 compares the internal string potentiometer measurement at the center of the car against the post-test FE model results. During the test, the string potentiometer reached its measurement limit, resulting in the horizontal line seen after approximately 0.27 seconds. In the post-test FE model, the model captures the general shape of the test response quite well, including a change-in-slope measured just before 0.2 seconds during the test.

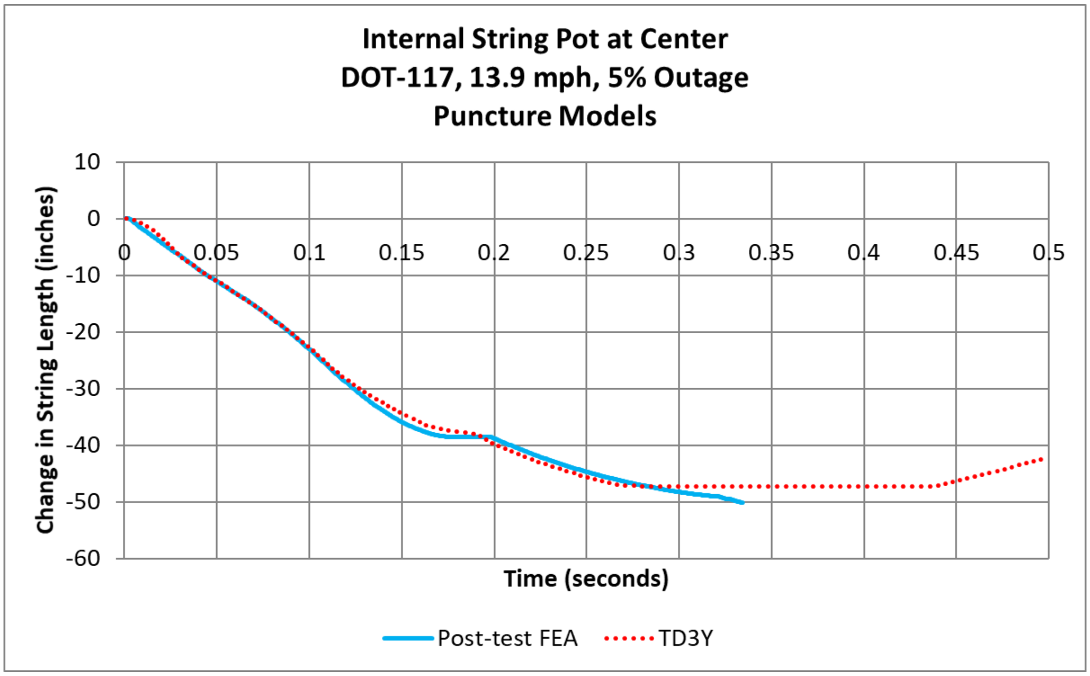

Figure 47. Change in Center String Potentiometer Length for Post-Test FEA with Rigid Ground and Test

Figure 48 compares the vertically oriented internal string potentiometer measurements at the center of the car against the post-test FE model results. The FE model exhibits good agreement with the test results in terms of the overall shapes of the curves and the general magnitudes of the responses.

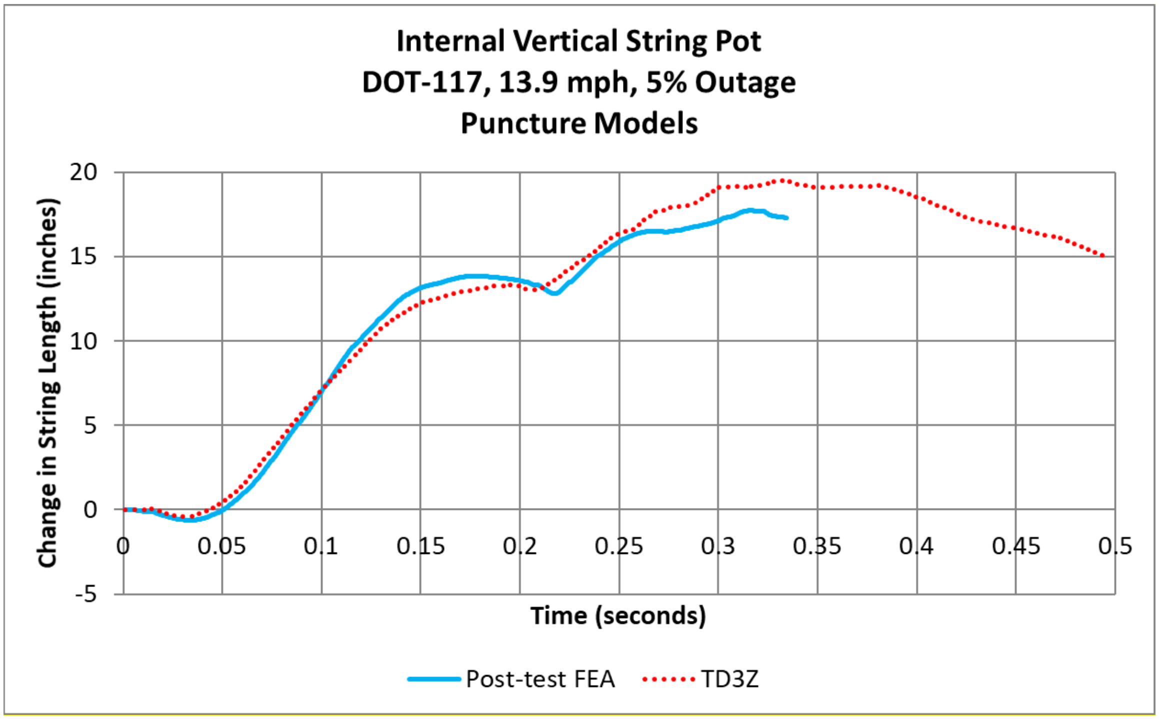

Figure 48. Change in Vertical String Potentiometer Length for Post-Test FEA with Rigid Ground and Test

The complete set of test and post-test FEA results for the model with the rigid ground are compared in Appendix C. Table 16 compares the peak measurements from the test and the corresponding peak value calculated for each output in the post-test FE model. This table also includes a column indicating the difference between the test measurement and FE calculations. The post-test model exhibited agreement that is consistent with the agreement obtained between the pre-test FEA and the test measurements.

Table 16. Comparison of Peak Results from Actual TC128 Post-test Model with Rigid Ground (13.9 mph) and Test Results (13.9 mph)

	Post-test FEA (rigid ground)	Test	Percent Difference
Longitudinal Acceleration	-2.8 g	-3.0 g	-4.3%
Impact Force	845.6 kips	883.8 kips	-4.3%
Displacement at Peak Force	46.0 inches	47.3 inches	-2.8%
Peak Energy Absorbed (1 x 10^6 foot-pounds)	1.89	1.91	-1.0%
48-inch Offset String Potentiometer	-36.6 inches	-38.1 inches	-4.0%
48-inch Offset String Potentiometer	-36.6 inches	-38.7 inches	-5.5%
24-inch Offset String Potentiometer	-42.8 inches	-44.8 inches	-4.5%
24-inch Offset String Potentiometer	-42.8 inches	-45.1 inches	-5.2%
Center String Potentiometer	-50.2 inches	-47.3 inches	6.0%
Vertical String Potentiometer	17.7 inches	19.5 inches	-9.0%
Skid String Potentiometer	-15 inches	-14.4 inches	3.9%
Skid String Potentiometer	-15 inches	-15.1 inches	-0.5%
Head String Potentiometer	-16.2 inches	-15.3 inches	6.4%
Head String Potentiometer	-16.2 inches	-16.0 inches	1.5%
Outage Pressure	72.5 psi	74.6 psi	-3%

Overall, the post-test FE results for the rigid ground model are within 10 percent of the test measurements for every measurement that was compared. It should be noted that the string potentiometer at the center of the tank car in the test reached its measurement limit of approximately 48 inches, and thus it did not capture any further deformations of the car in this location.

Although the post-test FE model experienced a puncture while the test did not, the results indicate that this puncture occurred with very little residual energy in the impactor. The tested car absorbed the total kinetic energy of the impactor at the instant of impact, which was 1.91 million foot-pounds of energy. The total energy under the force-displacement response from the post-test FE model was calculated to be 1.89 million foot-pounds. The energy that was not absorbed by the post-test model prior to puncture is equal to the residual kinetic energy of the impactor. The small residual kinetic energy of the impactor when the model estimates puncture indicates that the initial impact energy of the impactor only slightly exceeded the maximum amount of energy the model could absorb without puncturing.

Figure 49 contains a plot of the impactor speed versus time for both the test and the post-test FEA. There is excellent agreement between the two responses until approximately 0.32 seconds. At this point, the test measurement shows the impactor continues to slow at about the same rate as it had been slowing, while the FEA diverges. The FEA experiences a slower loss of speed starting at this time. This is consistent with the onset of puncture, as the tank car offers less resistance to the impactor's motion. The impactor in the FE model is traveling at approximately

1.5 mph when it diverges from the test measurements. In addition to the energy comparison discussed above, the small residual speed is another indication of the how close the model is to successfully resisting the impactor without puncturing the tank.

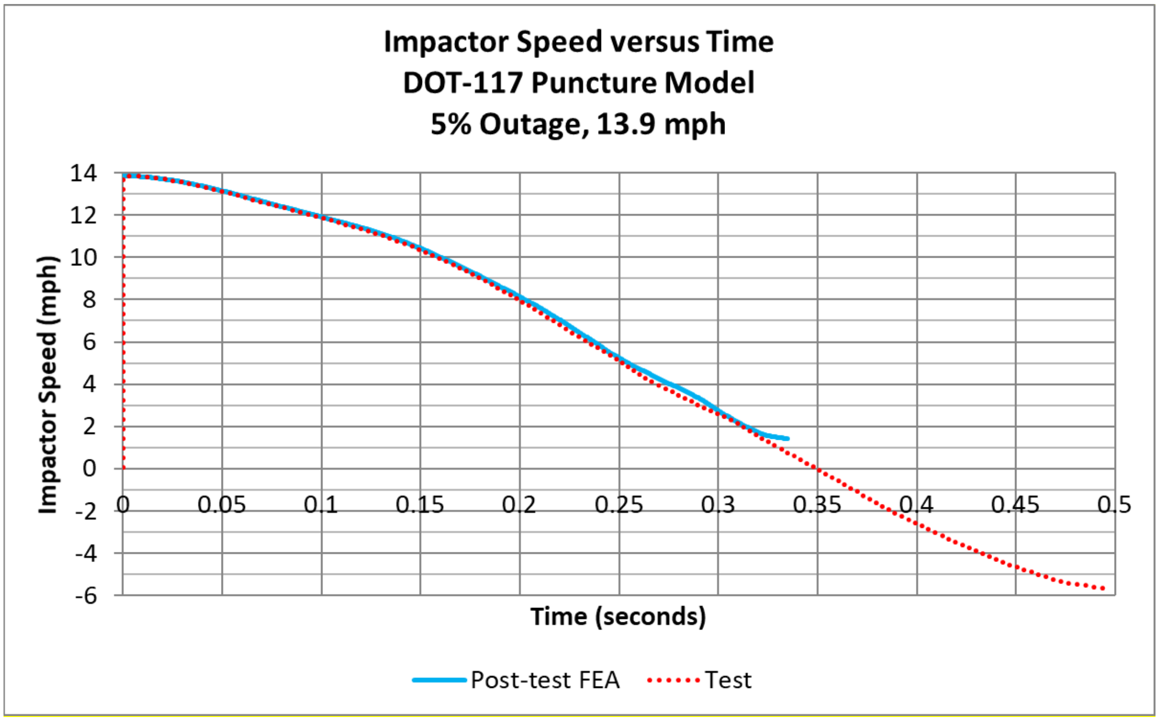

Figure 49. Impactor Speed Versus Time for Post-Test FEA with Rigid Ground and Test

In general, the post-test FE model with the rigid ground exhibited equal or better agreement with the test results compared to the pre-test model (Table 15). Based on the post-test modeling estimating a puncture outcome at the test speed, the post-test model is demonstrated to be conservative. As the residual energy and speed of the impactor at the time of simulated puncture are small, the level of conservatism in the model is expected to be small. Thus, the model indicates that the tested car would be expected to experience puncture with only a small increase in the impact speed, under these test conditions.

7.2 Post-Test Model with Deformable Ground

The post-test FE model with the deformable ground was run for 0.365 seconds of impact time. At that point, the water mesh became highly distorted, and the simulation was terminated. The complete set of comparisons between post-test FEA and test results can be found in Appendix C4. Figure 50 contains a plot of the impactor speed versus time for both the test measurements and the post-test FE model with deformable ground. From this figure, it is apparent that the model has been run until such a time as the impactor is rebounding from the tank at approximately 2 mph. Thus, while the model terminated at approximately 0.365 seconds due to distortion of water elements, the model ran for sufficiently long to bring the impactor to a stop and cause it to rebound from the tank. From this figure, it is also apparent that the model exhibits excellent agreement with the model for the speed versus time histories of the impactor.

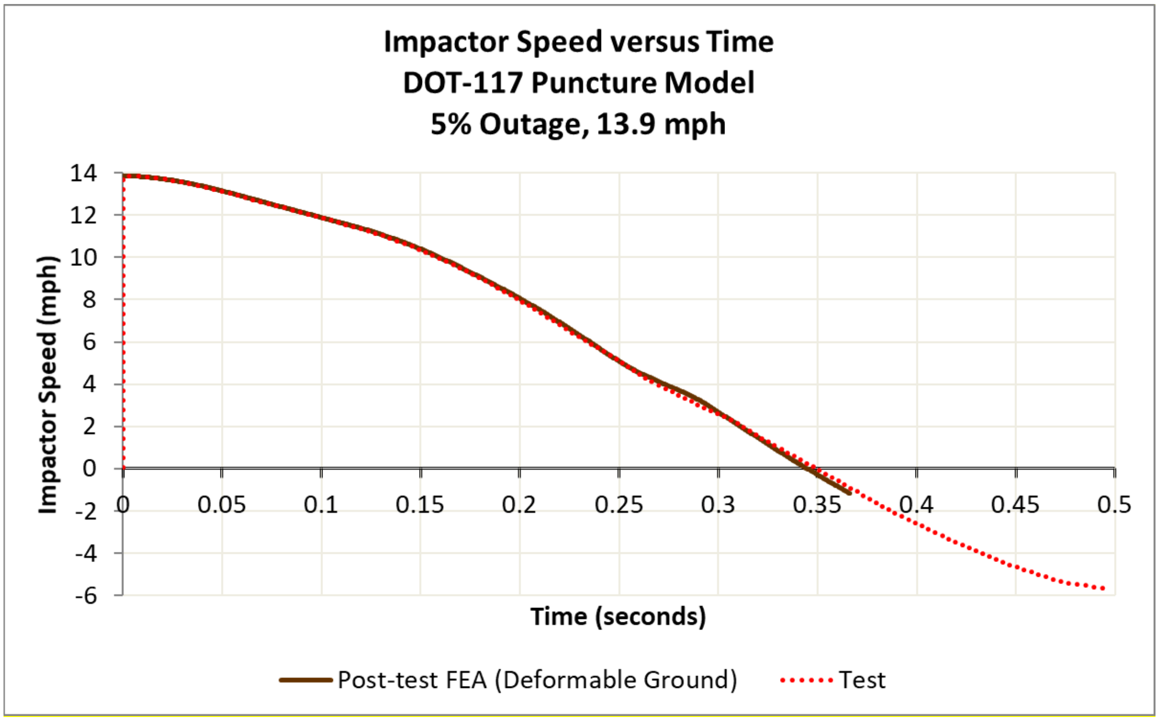

Figure 50. Impactor Speed Versus Time for Post-Test FEA with Deformable Ground and Test

At approximately 0.365 seconds, the impactor was rebounding from the tank. This model experienced a tear in the jacket, but the jacket was not fully punctured. Additionally, elements beneath the corners and sides of the impactor have failed within the solid patch of the tank, but the tank has not fully punctured. This result indicated that the energy to fully puncture the tank, with the impactor continuing to move through the shell, would only slightly exceed the speed of the test.

Figure 51 shows the damaged area of the jacket from the post-test FE model with the deformable ground, with an inset view of the tear under the impactor. This figure has mirrored the symmetric model setup so that the damage to both the left and right sides of the tank are visible. It should be noted in this figure that the extents of the tear reach the edges of the fine mesh under the impactor. However, the mode of tearing is consistent with the actual test (Figure 17), where the jacket tore along the two vertical edges of the impactor.

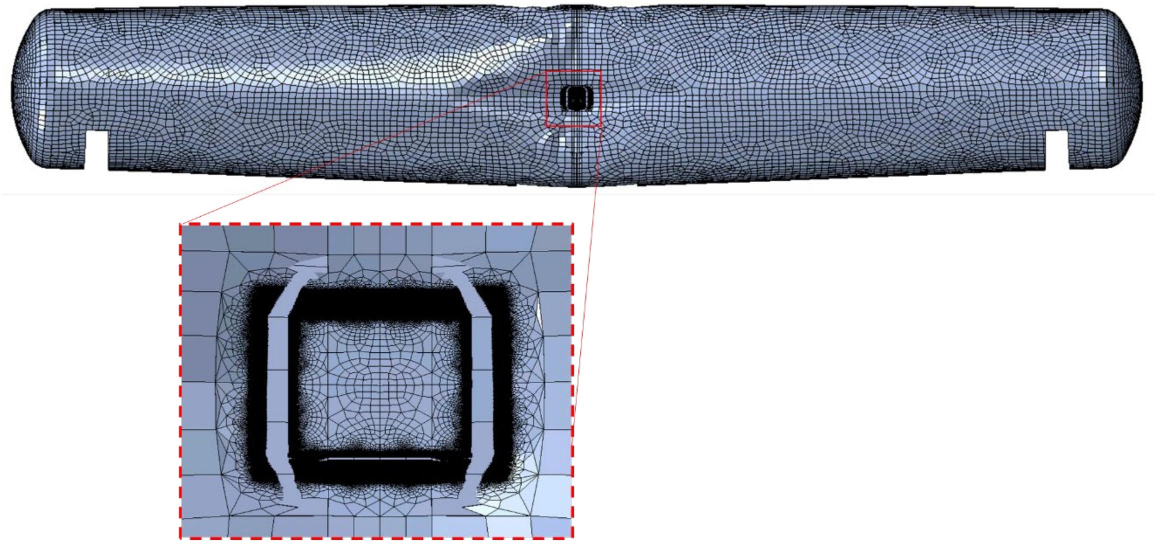

Figure 51. Jacket Damage on Post-Test FE Model with Deformable Ground

Figure 52 shows the deformed shape of the DOT-117 tank at 0.365 seconds of simulated impact time. This figure has mirrored the symmetric model setup so that the damage to both the left and right sides of the tank are visible. An inset image shows the details of the damage to the solid patch of elements beneath the impactor. The failed elements are apparent as gaps in the mesh in this figure, indicating that puncture is imminent in this model for an incrementally higher impact speed.

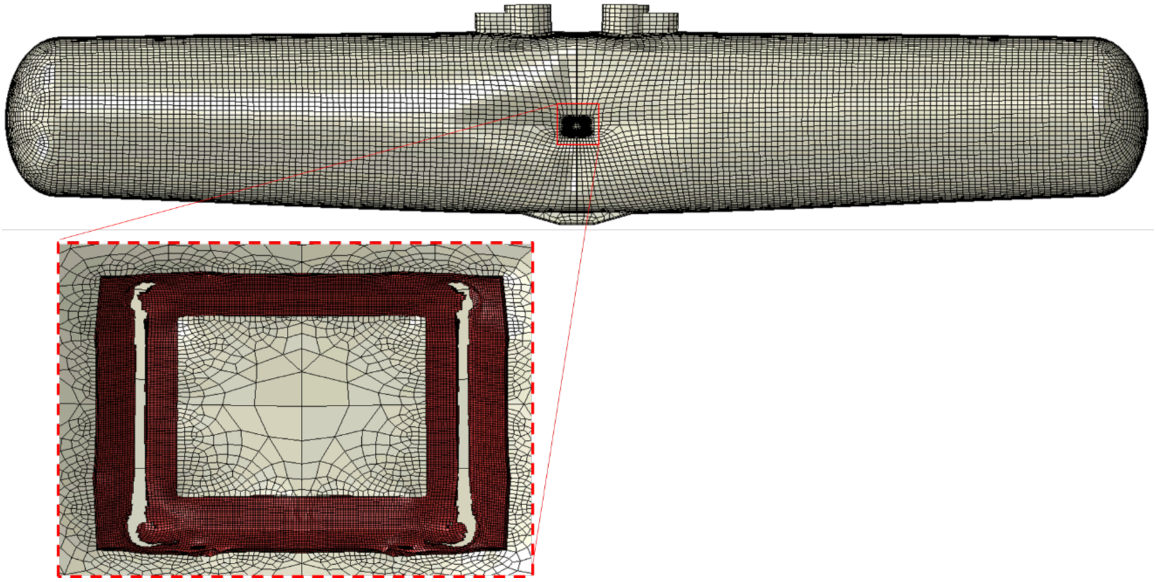

Figure 52. Tank Damage on Post-Test FE Model with Deformable Ground

The impact force versus time is compared between the post-test FE model and the test measurements in Figure 53. While the FE model used a rigid impactor with a single acceleration-time history, the ram car in the test featured five longitudinal accelerometers. Unless otherwise specified in this section of the report, the test force reported is the average of the five longitudinal accelerometer channels. Additionally, both the test and FE forces reported in this section have been filtered using a CFC60 filter [3].

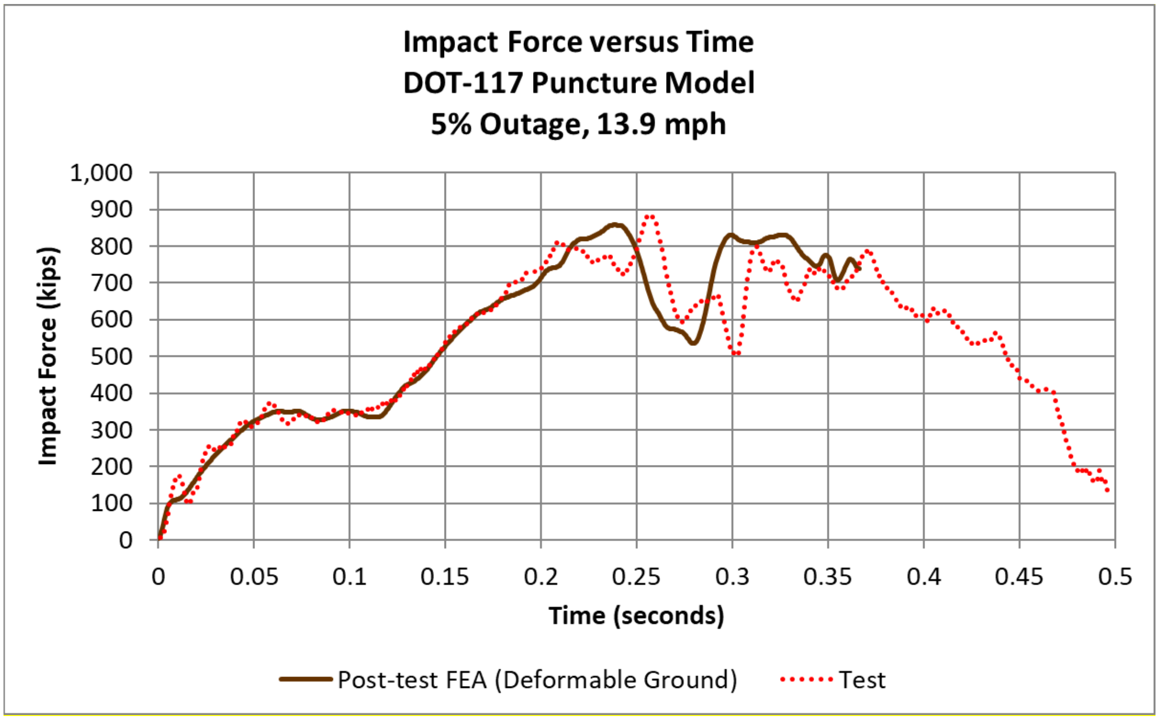

Figure 53. Force-Time Responses from Post-Test FEA with Deformable Ground and Test

The post-test model with the deformable ground shows excellent qualitative agreement with the overall shape of the test measurements. The model did a very good job of capturing the response of the test, including the changes-in-slope to the response as the impactor deformed the tank car and pushed it back against the wall.

The impactor force versus impactor travel from both the test and the post-test FEA with the deformable ground are compared to one another in Figure 54. The model and the test both experienced a dip in force after approximately 45 inches of impactor travel, likely the result of the fluid sloshing within the tank. The model also experiences peak forces that are in good agreement with the test for both timing and magnitude. The impactor is brought to a stop, and has begun to rebound from the tank. The model terminated due to excess fluid distortion after approximately 0.365 seconds of simulation time.

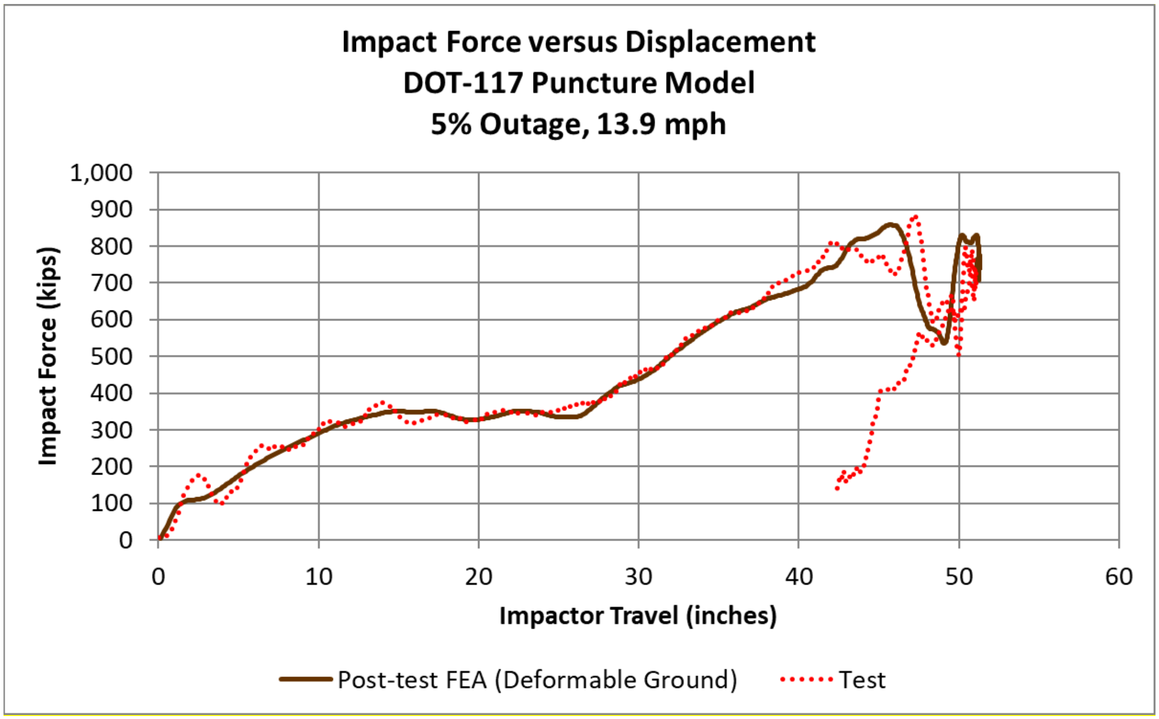

Figure 54. Force-displacement responses from Post-test FEA with Deformable Ground and Test Data

Figure 55 displays a series of frames from the post-test FE model with the deformable ground. Overall, the FE model does captures the response of the fluid during the test. This figure shows side and front section views of the tank at three times. The top row corresponds to t=0, the initial position of the model. The center row corresponds to t=0.175 seconds, midway through the impact event. The bottom row corresponds to t=0.365 seconds, after the time that the impactor began to rebound from the tank. As the bottom frame of this figure shows, the bottom outlet protective housing has caused a significant amount of deformation to the ground slab.

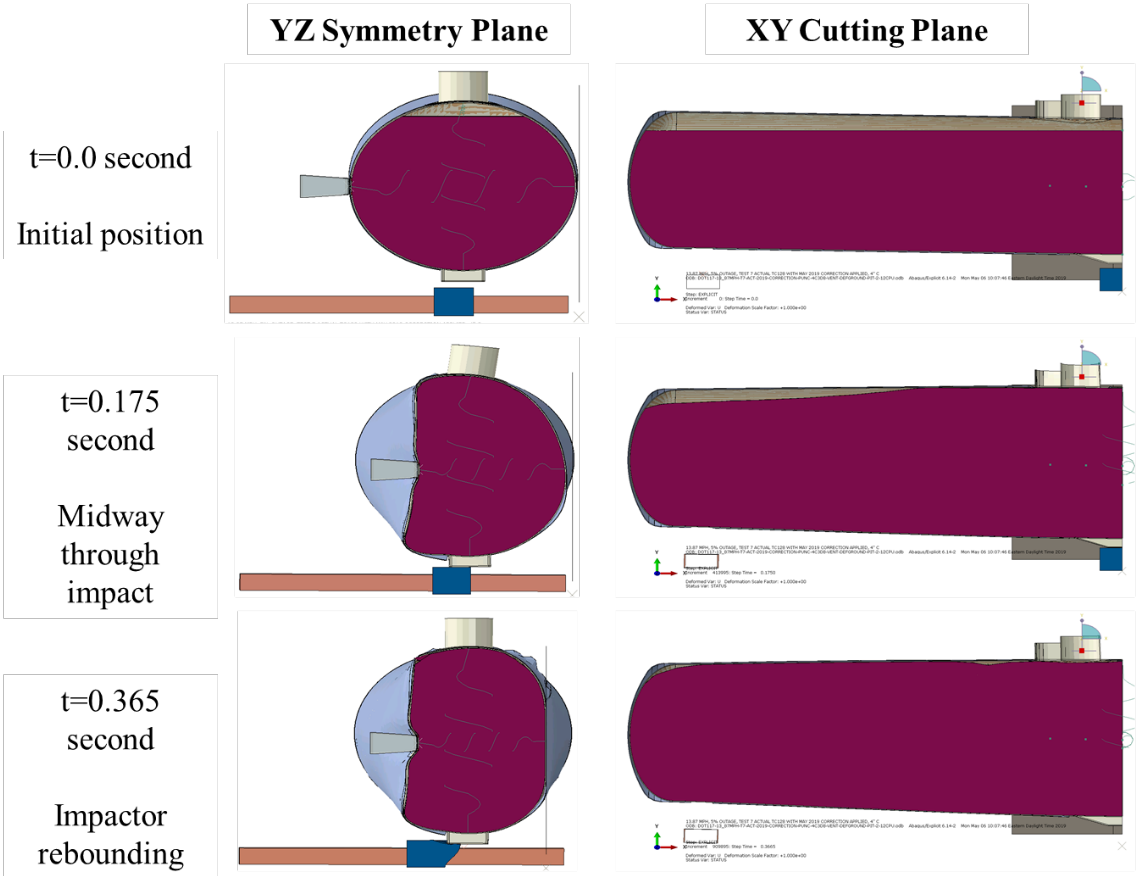

Figure 55. Impact Progression, Post-Test FE Model with Deformable Ground

Figure 56 contains contour plots comparing the indentation in the post-test FE model with the deformable ground at 0.365 seconds of simulated time to the post-test laser-scanned geometry of the tank shell from the test. The two results were aligned in the z (indentation) direction so that the center of the impact zone is aligned at z=0. Negative values indicate z-coordinates of the tank shell between the center of the impact zone and the rigid impact wall, and positive values indicate z-coordinates further from the impact wall than the point of impact. The contours were limited to span the values of measurements from the laser measurement, as increasing the range of contours to include the complete FE model of the tank would result in less resolution in the area of interest surrounding the impact zone.

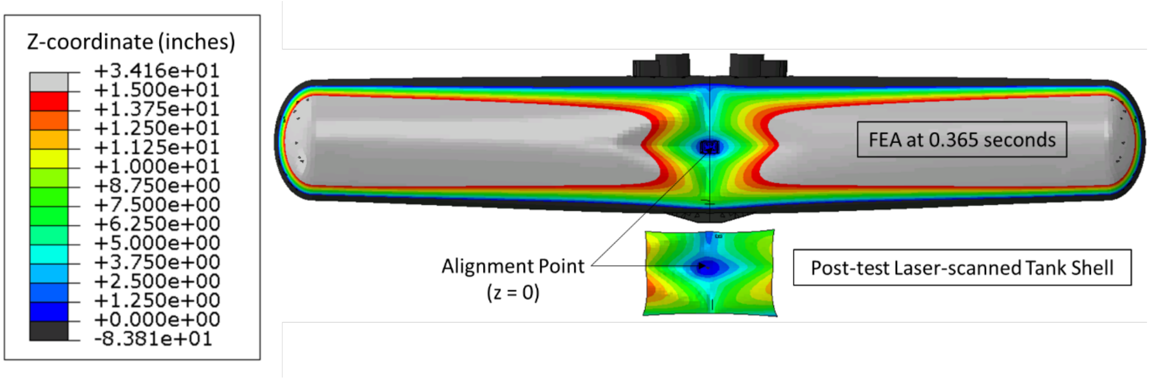

Figure 56. Comparison of Post-Test FE Indentation to Laser Measurements of Test Indentation

Figure 57 compares the air pressure for the post-test model and the test data. For the FE result, the air pressure is plotted as the average air pressure in the outage. The FE pressure plateaus at approximately 0.32 seconds, as the simulated PRV has activated. At the end of the simulation, the air pressure suddenly increases. Shortly after this spike, the water mesh becomes too distorted for the simulation to continue. This spike may be an indication of incipient instability in the lading, and thus be an artifact of the modeling techniques. For the test data, the average air pressure is plotted. During review of the test data, one of the pressure transducers in the outage (TP2000) appeared to measure pressures that were dramatically higher than the other pressure transducers. Therefore, the average pressure values plotted in this chapter exclude channel TP2000. The data values from this channel are shown in Appendix B2.

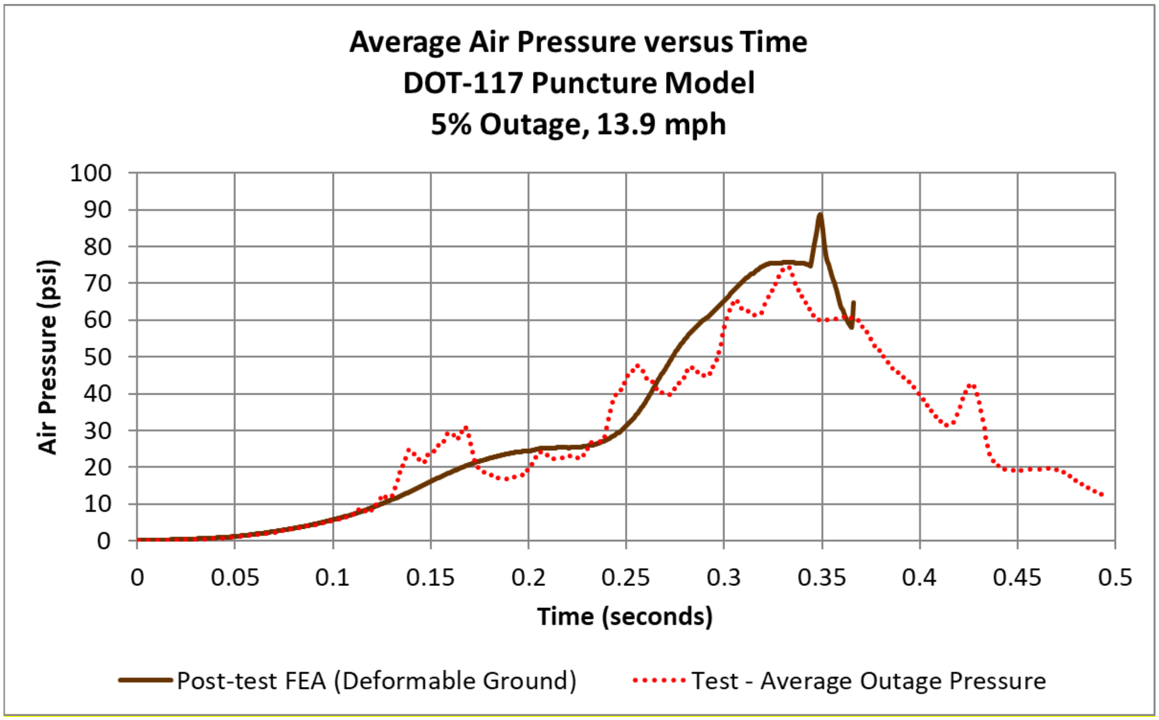

Figure 57. Air Pressure-Time Responses from Post-Test FEA with Deformable Ground and Test

Figure 58 compares the A-end (TDASKID) and B-end (TDBSKID) skid displacements measured during the test and the skid displacement calculated in the post-test FE model. The overall shape of the three responses are similar, however, the puncture of the FE model limits the length of impact time that was simulated. Thus, the FE results do not include the skid behavior measured after the impactor rebounded from the tank car, while the test measurements do include skid behavior.

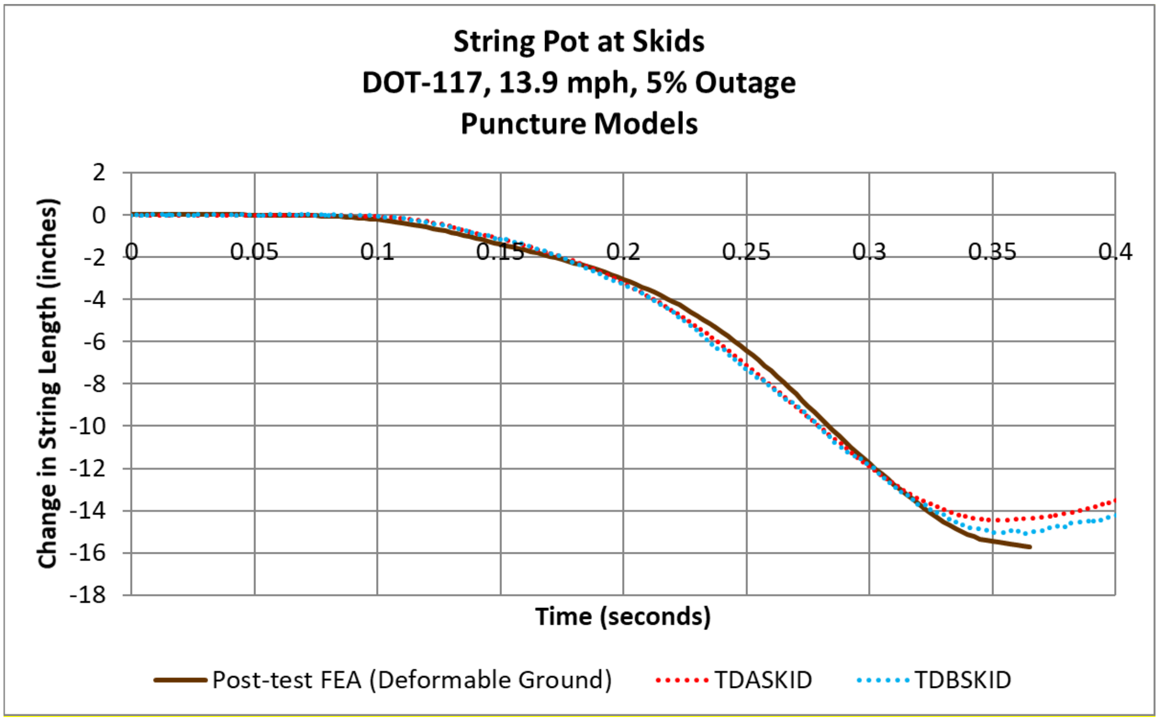

Figure 58. Skid Displacement in Post-Test FEA with Deformable Ground and Test

Figure 59 compares the internal string pot displacements measured during the test and the displacement calculated in the post-test FE model at the center of the tank. The overall shape of the two responses are similar. During the test, the string potentiometer reached its measurement limit, resulting in the horizontal line seen after approximately 0.275 seconds. In the post-test FE model, the model captures the general shape of the test response quite well, including a change-in-slope measured just before 0.2 seconds during the test.

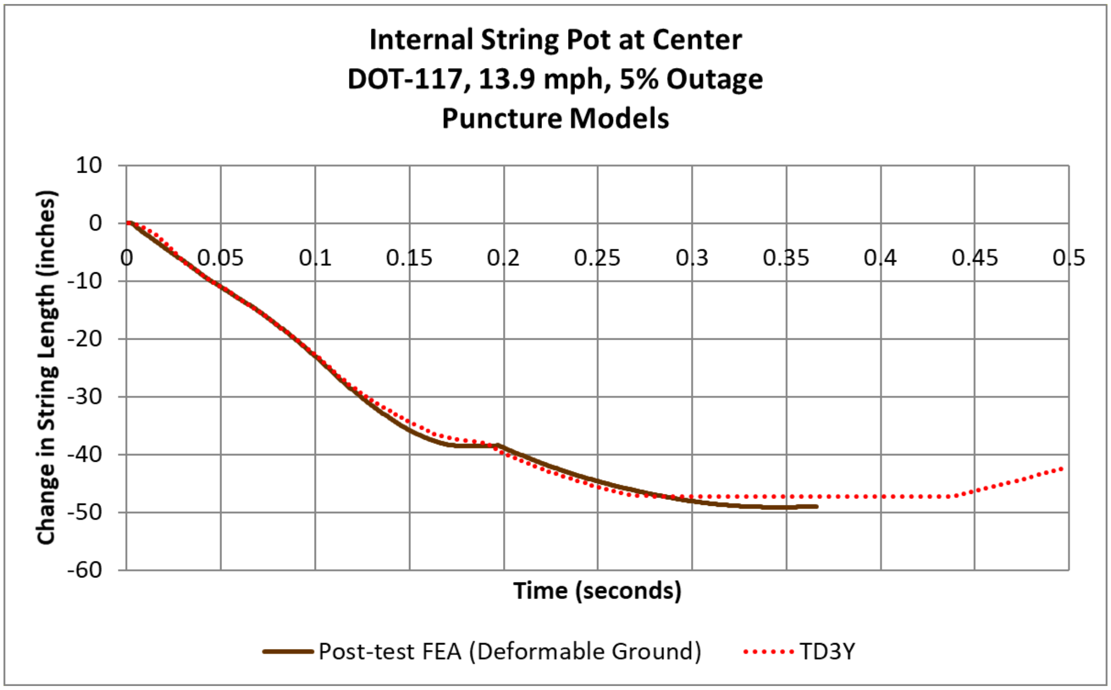

Figure 59. Change in Center String Potentiometer Length for Post-Test FEA with Deformable Ground and Test

Figure 60 compares the vertically oriented internal string potentiometer measurements at the center of the car against the post-test FE model results. The FE model exhibits good agreement with the test results in terms of the overall shapes of the curves and the general magnitudes of the responses.

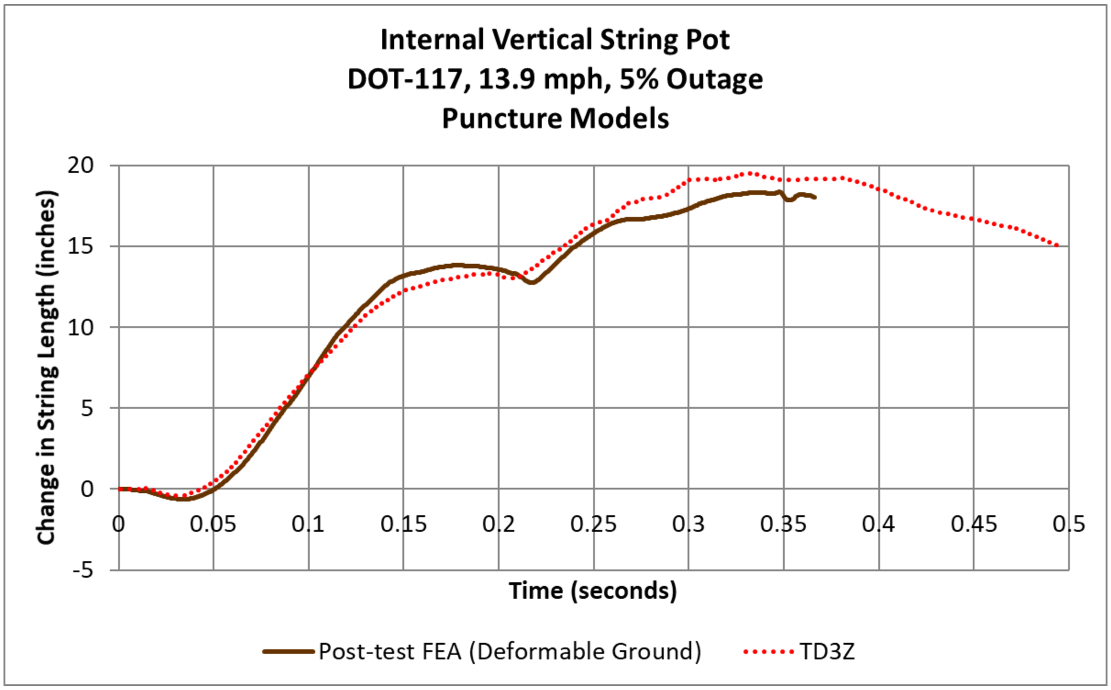

Figure 60. Change in Vertical String Potentiometer Length for Post-Test FEA with Deformable Ground and Test

The complete set of test and post-test FEA results are compared in Appendix C. Table 17 compares the peak measurements from the test and the corresponding peak value calculated for each output in the post-test FE model with the deformable ground. This table also includes a column indicating the difference between the test measurement and FE calculations. The post-test model exhibited excellent agreement with the test measurements.

Table 17. Comparison of Peak Results from Actual TC128 Post-Test Model with Rigid Ground (13.9 mph) and Test Results (13.9 mph)

		Post-Test FEA (deformable ground)	**Test**	**% Difference**
Longitudinal Acceleration	G's	-2.9	-3.0	-2.9%
Impact Force	kips	858.1	883.8	-2.9%
Displacement at Peak Force	inches	45.7	47.3	-3.4%
Peak Energy Absorbed	1 x 10^6 foot-pounds	1.91	1.91	0.1%
48-inch Offset String Potentiometer	inches	-36.7	-38.1	-3.9%
	inches	-36.7	-38.7	-5.4%
24-inch Offset String Potentiometer	inches	-43.3	-44.8	-3.5%
	inches	-43.3	-45.1	-4.1%
Center String Potentiometer	inches	-49.1	-47.3	3.9%
Vertical String Potentiometer	inches	18.3	19.5	-5.9%
Skid String Potentiometer	inches	-15.7	-14.4	8.7%
Skid String Potentiometer	inches	-15.7	-15.1	4.1%
Head String Potentiometer	inches	-15.8	-15.3	3.5%
Head String Potentiometer	inches	-15.8	-16.0	-1.2%
Outage Pressure	psi	88.7	74.6	19%

Overall, the post-test FE results for the deformable ground model are within 10 percent of the test measurements for every measurement that was compared. It should be noted that the string potentiometer at the center of the tank car in the test reached its measurement limit of approximately 48 inches, and thus did not capture any further deformations of the car in this location. It should also be noted that the peak value in air pressure calculated in the model occurs close to the time the water mesh becomes so distorted that the analysis terminates, and thus this value may be a modeling artifact.

Since the post-test FE model experienced the failure of several elements in the tank whereas the test did not experience puncture, the results indicate that the model remains slightly conservative compared to the test. From the model results, it is apparent that a slightly higher impact speed would cause the damage to the solid patch of the tank to spread, causing a complete puncture of the tank. Based on the post-test models estimating element failure at the test speed, where no puncture occurred in the test, the post-test model is demonstrated to be conservative. When the deformable ground is included in the model, the level of conservatism within the model decreases compared to the post-test model with a rigid representation of the ground. Thus, while both post-test models are expected to estimate puncture at a speed below that expected for the actual tank, the model using the deformable ground would be expected to be closer.

8. Conclusion

This report documents the combined efforts of TTCI and Volpe to test and analyze the side impact puncture performance of a DOT-117 tank car. This research supports FRA's tank car research program to provide the technical basis for rulemaking on enhanced and alternative performance standards for tank cars.

The tank car was filled with water to approximately 95 percent of its volume. It was then sealed, but not pressurized above atmospheric pressure. The test was intended to strike the car at a speed high enough to result in significant damage to the tank and possibly puncture the tank's shell. The tank car was impacted by a 297,125-pound ram car traveling at 13.9 mph. A 12-inch by 12-inch ram head fitted to the ram car impacted the tank center. The impact deformed and tore the external jacket and rebounded from the tank without causing a shell puncture.

Pre-test FE modeling was used to estimate the overall response of the tank to the impact, including the force-displacement response. Due to uncertain parameters (e.g., material properties, actual test speed), the pre-test models were intended to bound the range of likely puncture speeds. The model estimated that the tank could puncture after an impact of between 13 mph and 14 mph, depending on the particular properties of the TC128 steel in the car's shell. The pre-test models exhibited reasonably good agreement with the measured force-displacement result from the test. Additionally, the internal pressure-time response and the displacements of the tank measured by string potentiometers were all in very good agreement with the pre-test model estimations.

The FE modeling performed in this effort used an explicit Lagrangian mesh and a simplified pneumatic cavity modeling technique to simulate the water and air responses, respectively. A detailed representation of the water was chosen based on the pre-test assumption that the combination of a small and unpressurized outage would lead to complex fluid sloshing within the tank, requiring a detailed representation in the model. The test measurements confirmed that this modeling approach provided a good representation of the fluid behavior in the tank car.

Several changes were made to the model after the test. Material coupons were cut from undamaged regions of the tested car and subjected to tensile testing. These coupons were used to generate a new material response, which was implemented in the post-test FE model. Additionally, the post-test model was run at the actual 13.9 mph impact speed measured during the test. The geometry of the jacket, ground, and the impact wall were adjusted to better match the actual test setup. Two post-test models were then run at the test speed. The first post-test model used a rigid ground with a pit, and the second post-test model used a simple, deformable concrete ground with a pit.

The post-test model with the rigid ground exhibited excellent agreement with the test measurements. When run at the test speed, this post-test model estimated puncture of the tank car based on the actual material responses. The post-test model is slightly conservative, as evidenced by the small residual speed of the impactor at the time of puncture. In this post-test model, the impactor has slowed to approximately 1.5 mph, whereas the test resulted in the impactor slowing to a complete stop before rebounding from the tank. The model thus estimates puncture at a slightly lower impact speed than would be expected to puncture the car during a future test.

The post-test model with the deformable ground exhibited even better agreement with the test measurements than the post-test model with the rigid ground. When run at the test speed, this model estimated tearing of the jacket and a number of failed elements in the solid patch of the tank while also causing the impactor to come to a full stop and rebound from the tank. This post-test model remains conservative, but is less conservative than the model with the rigid ground.

The absence or presence of a deformable ground does not affect the crashworthiness of a DOT-117 tank car; however, the model results indicate the importance of modeling the test setup in a sufficient amount of detail to make a fair assessment of the model's performance. While the pre-test models demonstrated reasonable agreement with the eventual test measurements, these models used a flat, rigid ground. Better agreement was obtained between the post-test model that used a rigid ground matching the geometry of the ground slab in the test setup than the pre-test models. From the test observations, it was apparent that the deforming tank car had broken several chunks of concrete out of the ground slab. Thus, a post-test model incorporating a simplified concrete material response was also run. This model gave the best agreement between test measurements and FE results.

The DOT-117 model is capable of achieving an excellent level of agreement with the measured quantities and observed behaviors from the test. While not undertaken as a part of the model validation process described in this report, this model could be used to investigate modifications to the test setup on the estimated puncture speed of the DOT-117. For example, the ground slab could be removed entirely to examine what influence the constraint offered by the ground has on the overall puncture speed.

9. References

1. Government Publishing Office. 49 CFR § 179.16. Pipeline and Hazardous Materials Safety Administration, DOT, 2015.
2. Government Publishing Office. Hazardous Materials: Enhanced Tank Car Standards and Operational Controls for High-Hazard Flammable Trains. *Federal Register*, *80*(89), 26644, May 8, 2015.
3. SAE J211/1 Standard. "Instrumentation for Impact Test – Part 1: Electronic Instrumentation." SAE International, Warrendale, PA, 2007.
4. Federal Railroad Administration. "Side Impact Test and Analyses of a DOT 111 Tank Car." Technical Report, DOT/FRA/ORD-15/30: U.S. Department of Transportation, October 2015.
5. Federal Railroad Administration. "Side Impact Test and Analysis of a DOT-112 Tank Car." Technical Report, DOT/FRA/ORD-16/38: U.S. Department of Transportation, December 2016.
6. Carolan, M., and Rakoczy, P. "Side Impact Test and Analyses of a DOT-105 Tank Car." Technical Report, DOT/FRA/ORD-19/12, U.S. Department of Transportation: Federal Railroad Administration, May 2019.
7. Kirkpatrick, S. W. "Detailed Puncture Analyses of Various Tank Car Designs: Final Report – Revision 1." Applied Research Associates, January 2010.
8. Transportation Technology Center, Inc. "Test Implementation Plan for FRA Tank Car Side Impact, Revision 1," September 27, 2016.
9. Abaqus 6.14-2. Dassault Systemes Simulia Corp: Providence, RI, 2014.
10. Bao, Y., Wierzbicki, T. "On fracture locus in the equivalent strain and stress triaxiality space." *International Journal of Mechanical Sciences*, *46*(1), pp. 81–98, 2004.
11. The Engineering Toolbox. "Water – Density, Specific Weight and Thermal Expansion Coefficient."
12. The Engineering Toolbox. "Speed of Sound in Water."
13. The Engineering Toolbox. "Water – Dynamic and Kinematic Viscosity."
14. The Engineering Toolbox. "Universal and Individual Gas Constants."
15. The Engineering Toolbox. "Air – Molecular Weight Composition."
16. Urieli, I. Engineering Thermodynamics. "Specific Heat Capacities of Air," July 26, 2018.
17. Abaqus Example Problems Manual. "Example 2.1.15 Seismic analysis of a concrete gravity dam." Dassault Systemes Simulia Corp: Providence, RI, 2014.
18. Lee, Y. W., Wierzbicki, T. "Quick Fracture Calibration for Industrial Use." Impact and Crashworthiness Laboratory, Report No. 115, August 2004.
19. The Engineering Toolbox. "Air – Altitude, Density, and Specific Volume."

20. United States Board of Geographic Names. Feature Detail Report for: Pueblo Memorial Airport. USGS Geographic Names Information System (GNIS): United States Geologic Survey.

21. U.S Climate Data. Climate Pueblo – Colorado and Weather Averages Pueblo – September.

22. Fort Vale 5. 5" Supaflo Pressure Only Rail Car Relief Valve Data Sheet, 2014.

23. Ohio Medical Corporation. "ACFM vs. SCFM vs. ICFM." Series of Technical White Papers from Ohio Medical Corporation, 560808 Rev. 2.

24. U.S. Department of Transportation, DOT 117 Specification Car. Pipeline and Hazardous Materials Safety Administration.

25. Dortmund Data Bank (DDB). *Liquid Density Calculation by DIPPR105 Equation (Ethanol)*.

26. George, A. K., Singh, R. N., Arafin, S. Equation of State of Crude Oil Samples. *Journal of Petroleum & Environmental Biotechnology*, *4*(162). doi:10.4172/2157-7463.1000162, 2013.

27. Enbridge Pipelines Inc. "2015 Crude Characteristics, No. 46." 2015.

28. Association of American Railroads. *AAR Manual of Standards of Recommended Practices.* Section C. Standard M-1002, 2000. *Specifications for Tank Cars, Appendix M*: Washington, DC.

Appendix A.
Camera and Target Positions

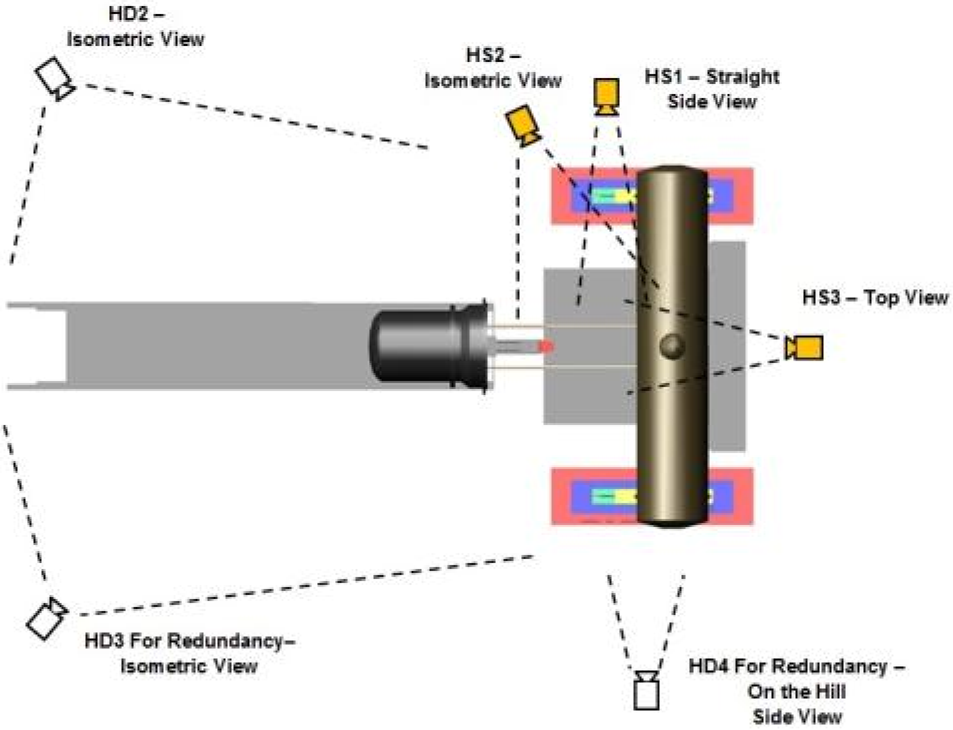

Figure A1. Camera Positions (Top) — High Speed (HS), High Definition (HD)

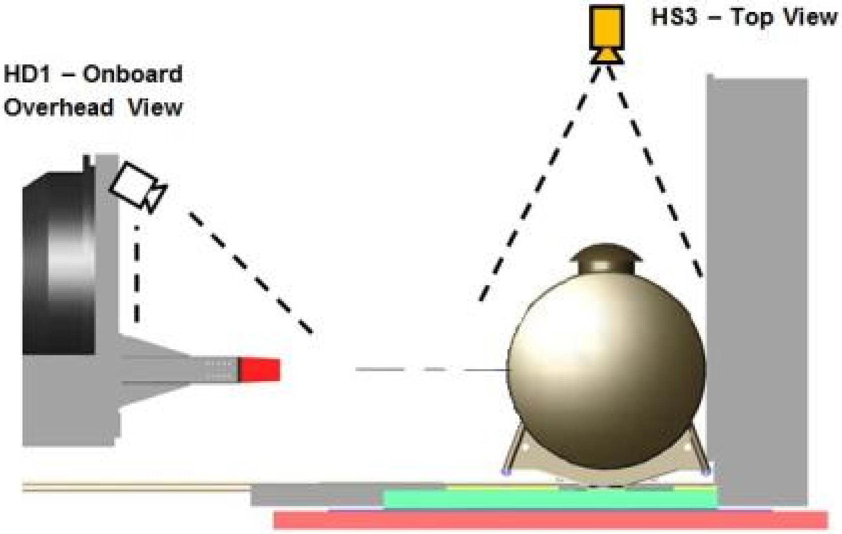

Figure A2. Camera Positions (Side) — High Speed (HS), High Definition (HD)

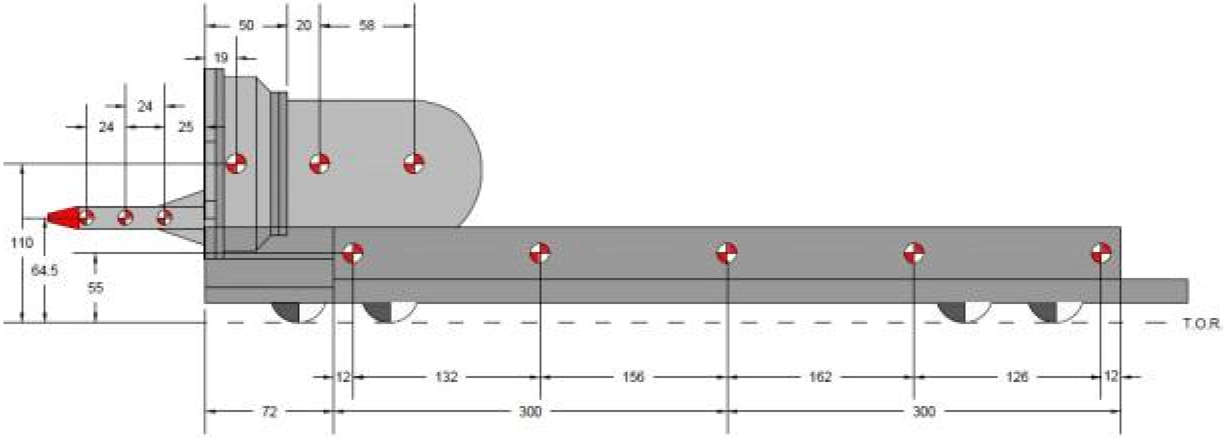

All units in inches

Figure A3. Ram Car Target Positions

Appendix B.
Test Data

This appendix contains raw and filtered test data. The raw accelerations and internal pressures measured on different locations on the impact cart were processed as follows. The test data from -1 second to -0.1 second on each channel were averaged, and this value was subtracted from the test measurements in order to remove any initial offsets in the data. Each channel was then filtered to channel frequency class (CFC) 60, using the procedures given in SAE J211 [3]. Displacement data did not require any filtration.

B1 – Accelerations

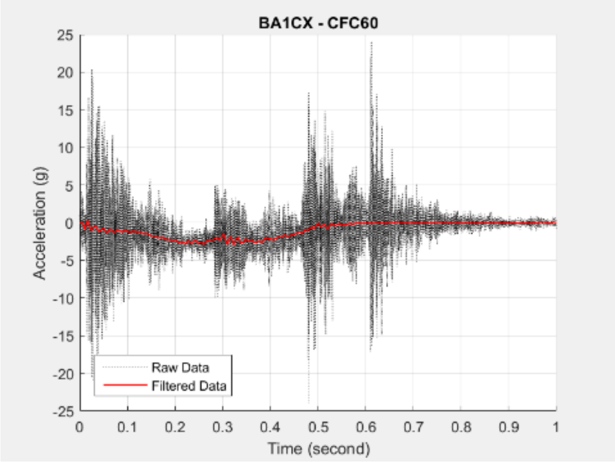

Figure B1. Raw and CFC60 Filtered Acceleration-time Data from BA1CX

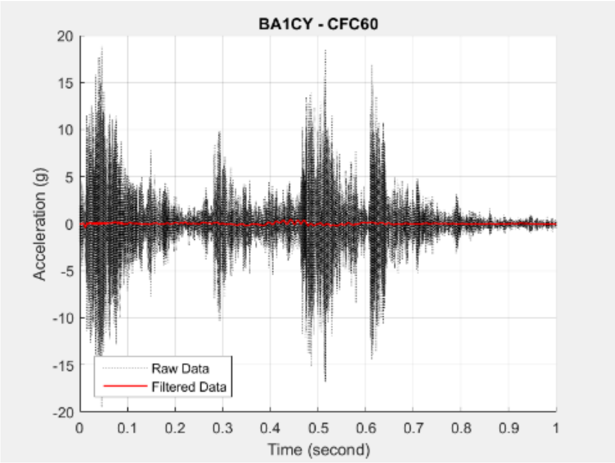

Figure B2. Raw and CFC60 Filtered Acceleration-time Data from BA1CY

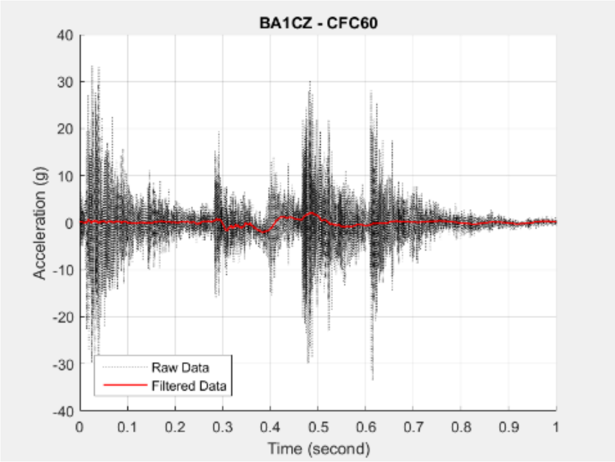

Figure B3. Raw and CFC60 Filtered Acceleration-time Data from BA1CZ

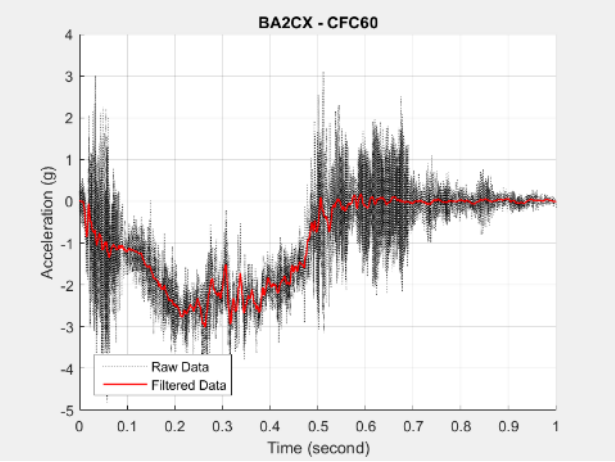

Figure B4. Raw and CFC60 Filtered Acceleration-time Data from BA2CX

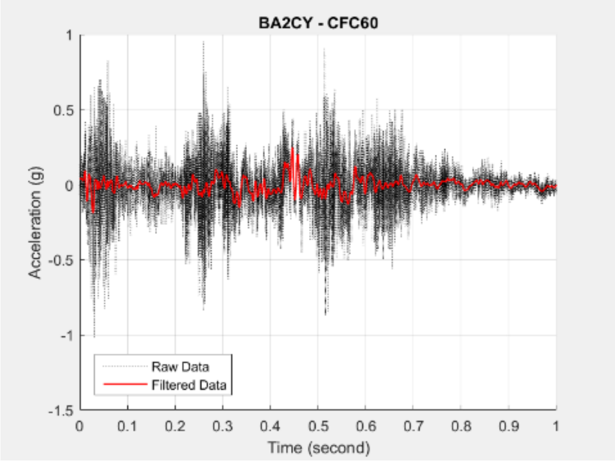

Figure B5. Raw and CFC60 Filtered Acceleration-time Data from BA2CY

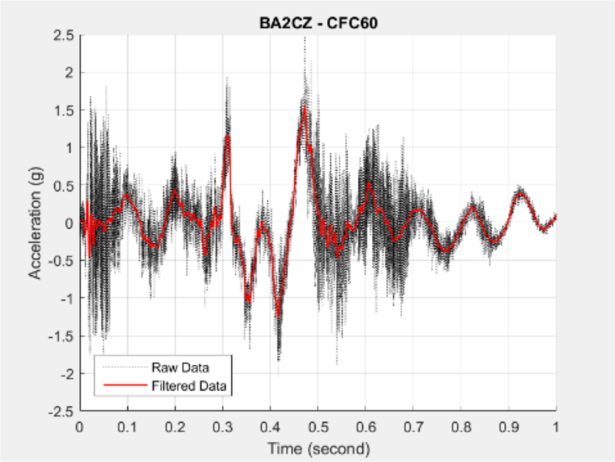

Figure B6. Raw and CFC60 Filtered Acceleration-time Data from BA2CZ

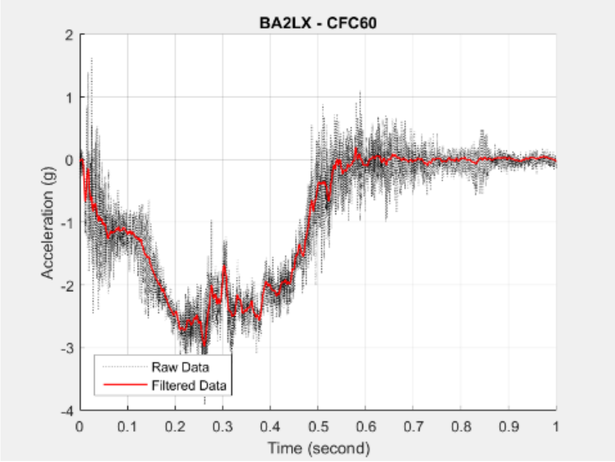

Figure B7. Raw and CFC60 Filtered Acceleration-time Data from BA2LX

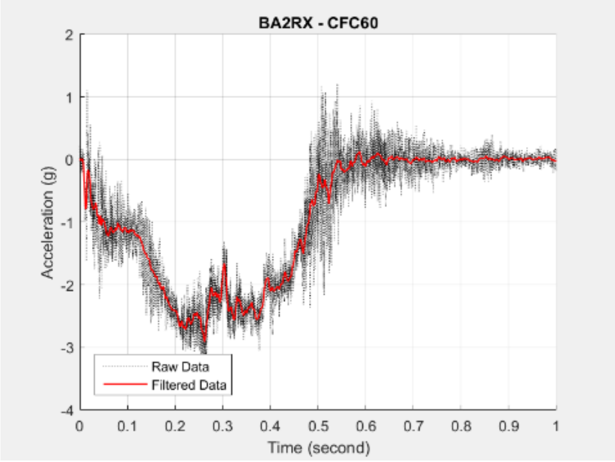

Figure B8. Raw and CFC60 Filtered Acceleration-time Data from BA2RX

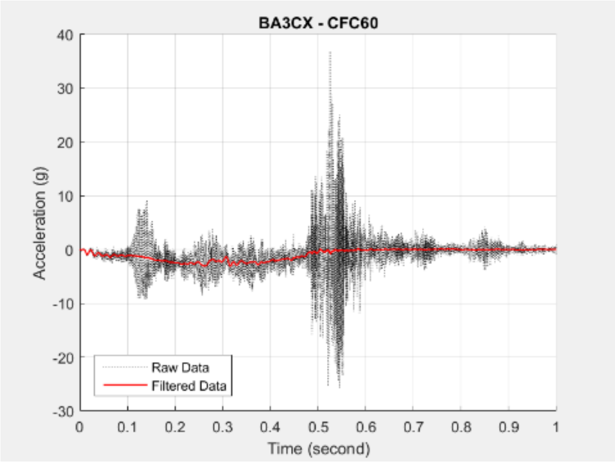

Figure B9. Raw and CFC60 Filtered Acceleration-time Data from BA3CX

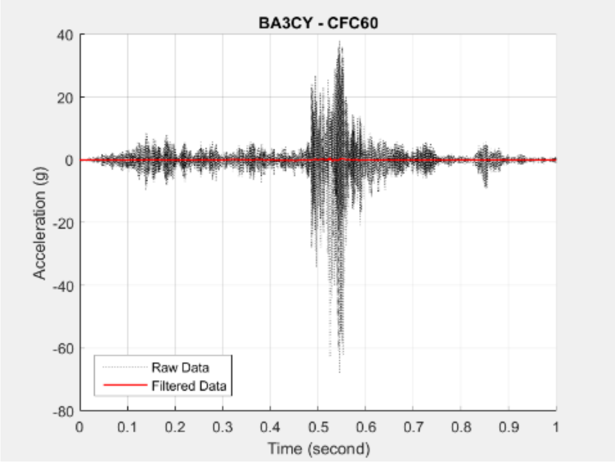

Figure B10. Raw and CFC60 Filtered Acceleration-time Data from BA3CY

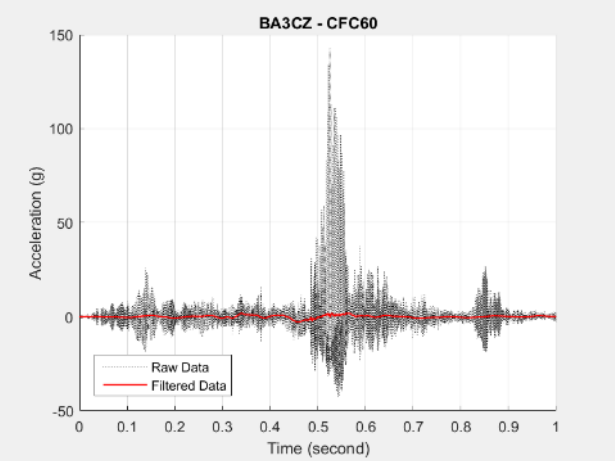

Figure B11. Raw and CFC60 Filtered Acceleration-time Data from BA3CZ

B2 – Pressures

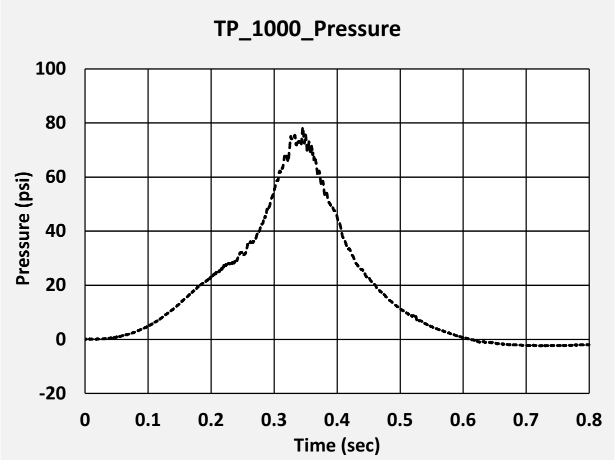

Figure B12. Raw Pressure-time Data from TP1000

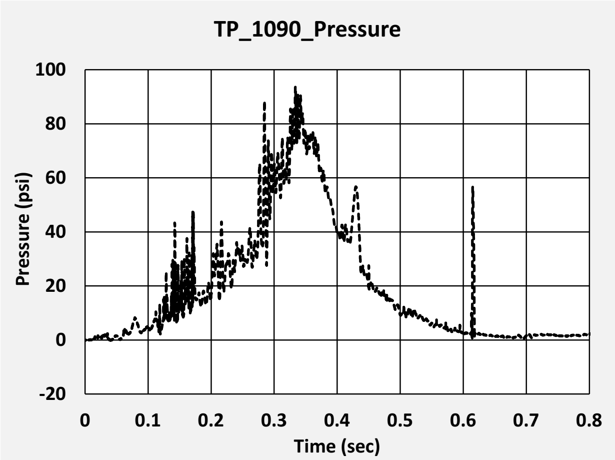

Figure B13. Raw Pressure-time Data from TP1090

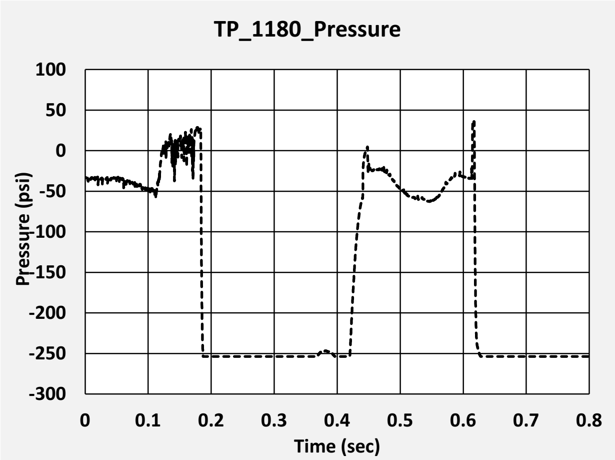

Figure B14. Raw Pressure-time Data from TP1180

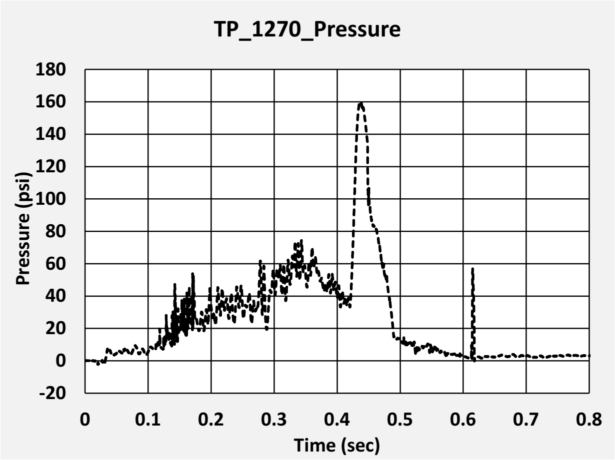

Figure B15. Raw Pressure-time Data from TP1270

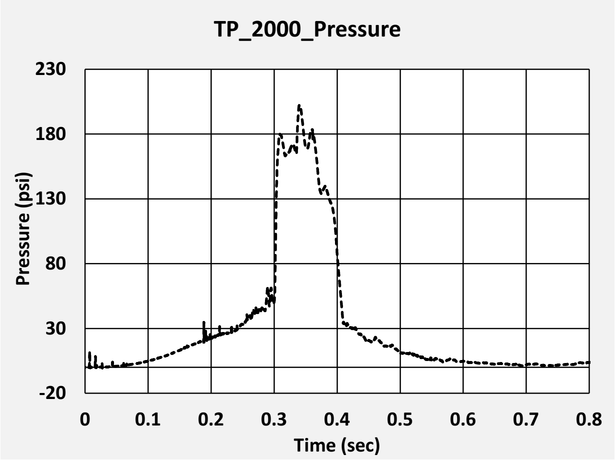

Figure B16. Raw Pressure-time Data from TP1270

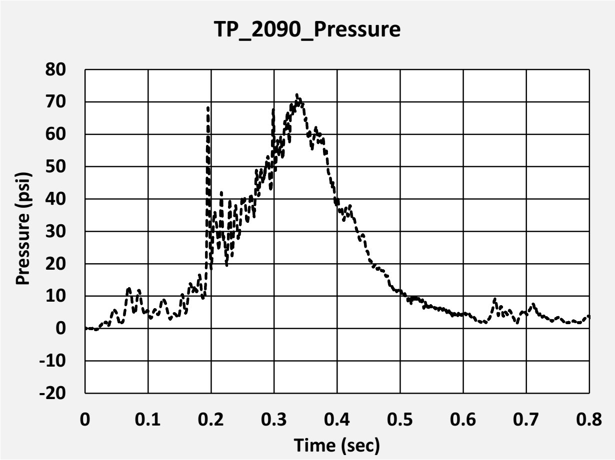

Figure B17. Raw Pressure-time Data from TP2090

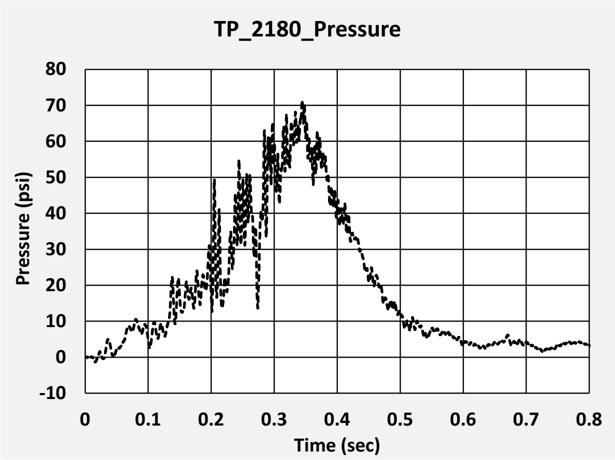

Figure B18. Raw Pressure-time Data from TP2180

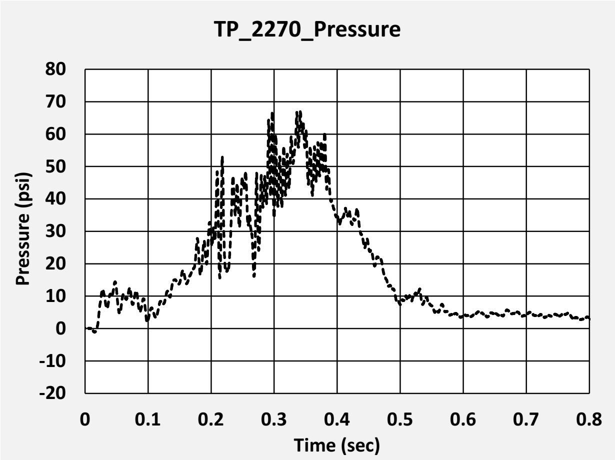

Figure B19. Raw Pressure-time Data from TP2180

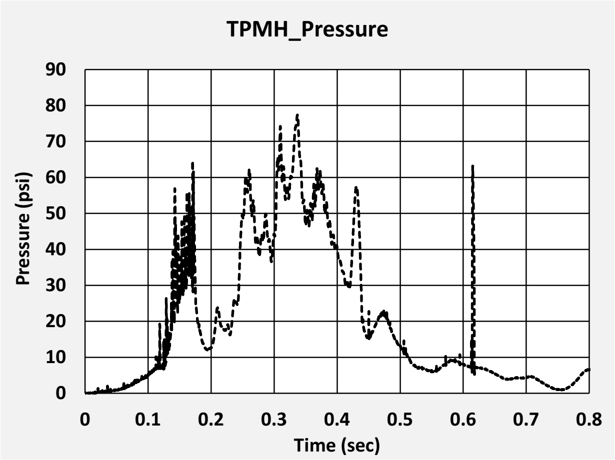

Figure B20. Raw Pressure-time Data from TPMH

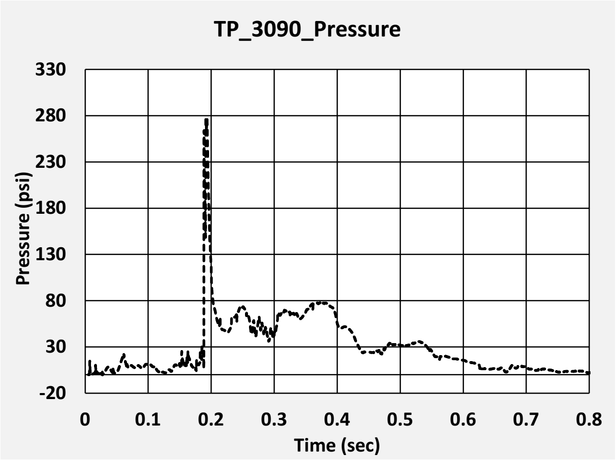

Figure B21. Raw Pressure-time Data from TP3090

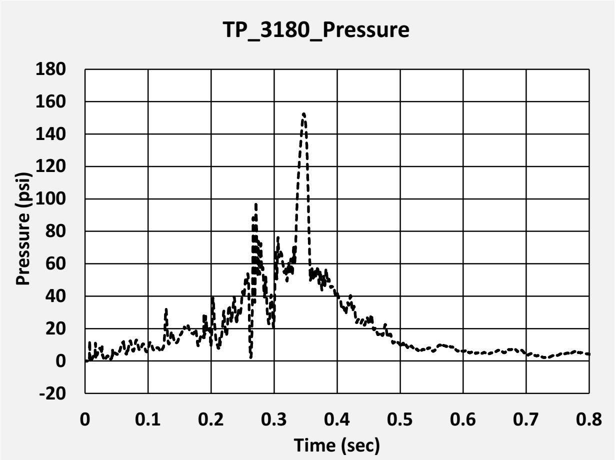

Figure B22. Raw Pressure-time Data from TP3180

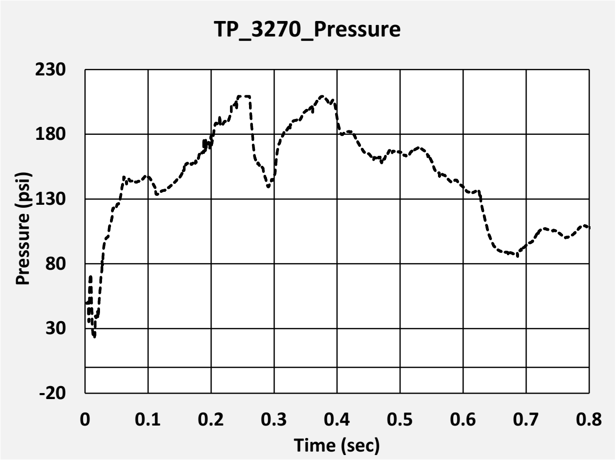

Figure B23. Raw Pressure-time Data from TP3270

B3 – Displacements

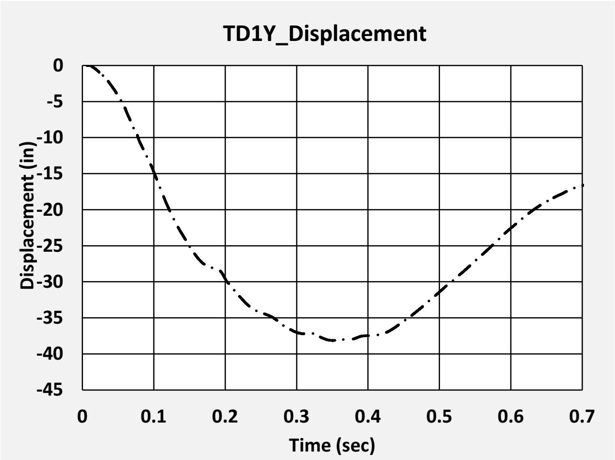

Figure B24. Raw Displacement-time Data from TD1Y

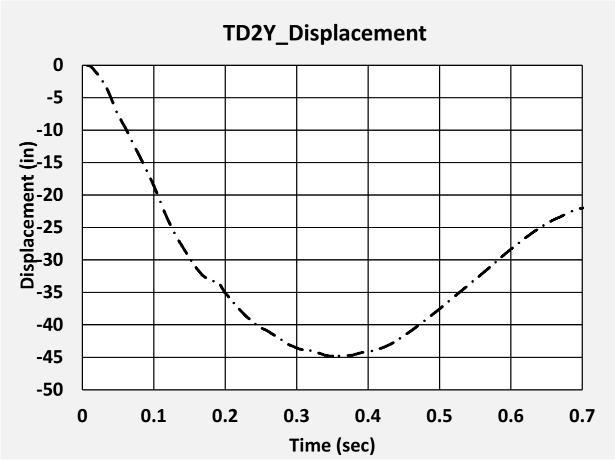

Figure B25. Raw Displacement-time Data from TD2Y

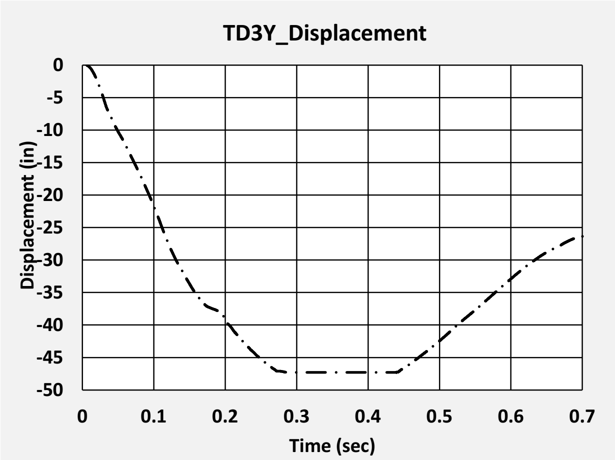

Figure B26. Raw Displacement-time Data from TD3Y

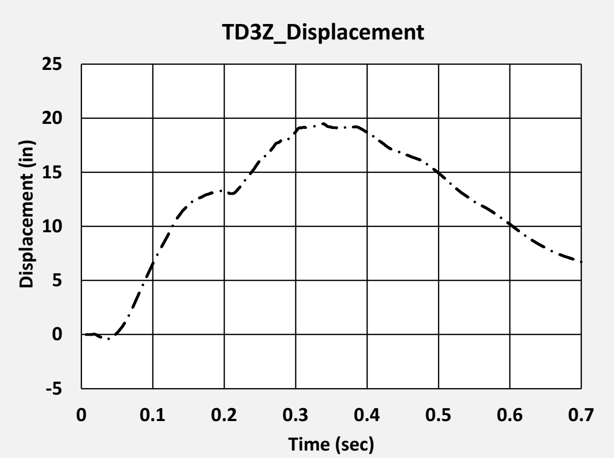

Figure B27. Raw Displacement-time Data from TD3Z

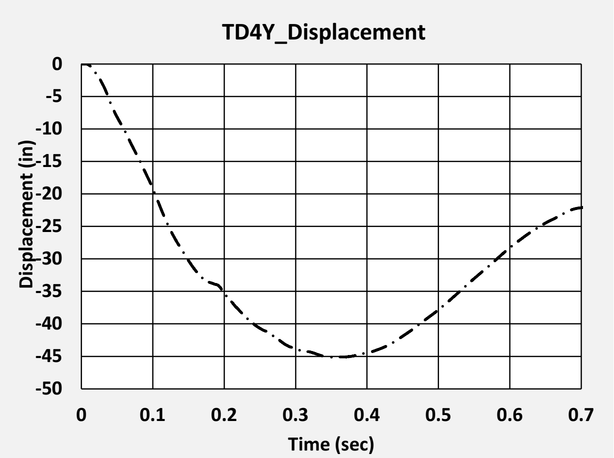

Figure B28. Raw Displacement-time Data from TD4Y

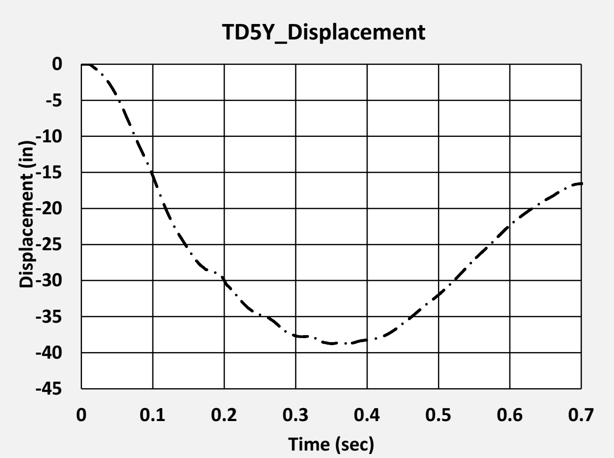

Figure B29. Raw Displacement-time Data from TD5Y

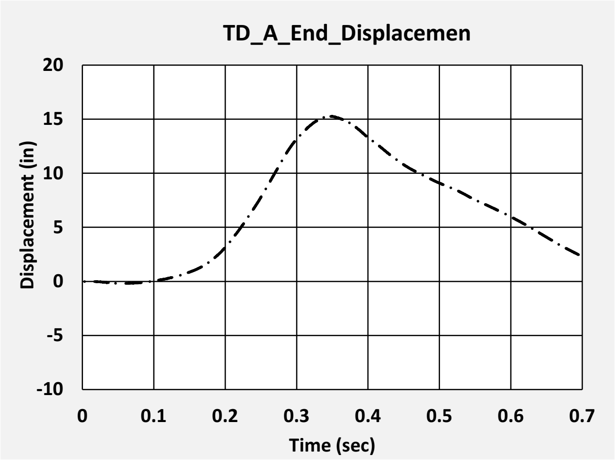

Figure B30. Raw Displacement-time Data from Displacement Transducer on A-End Head

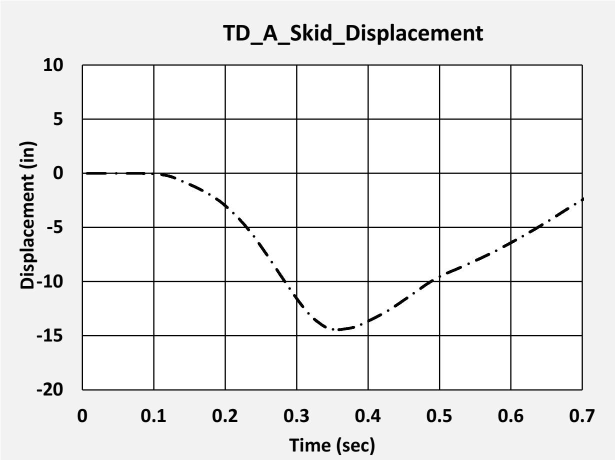

Figure B31. Raw Displacement-time Data from Displacement Transducer on A-End Skid

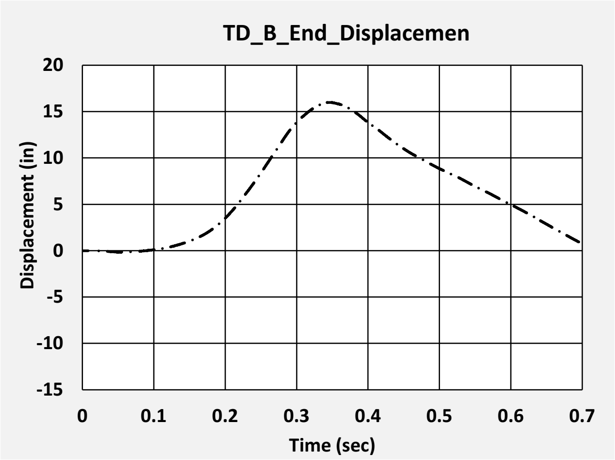

Figure B32. Raw Displacement-time Data from Displacement Transducer on B-End Head

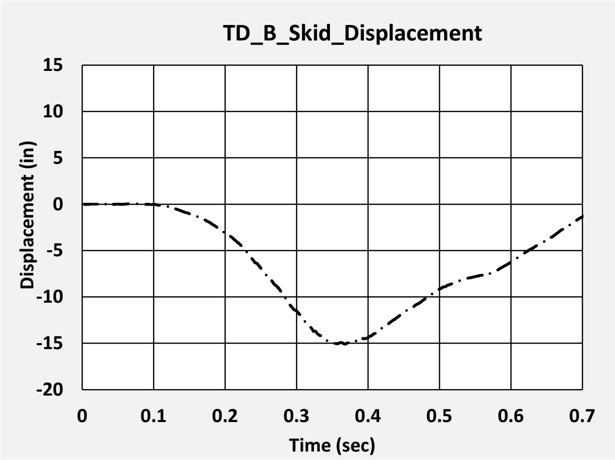

Figure B33. Raw Displacement-time Data from Displacement Transducer on B-End Skid

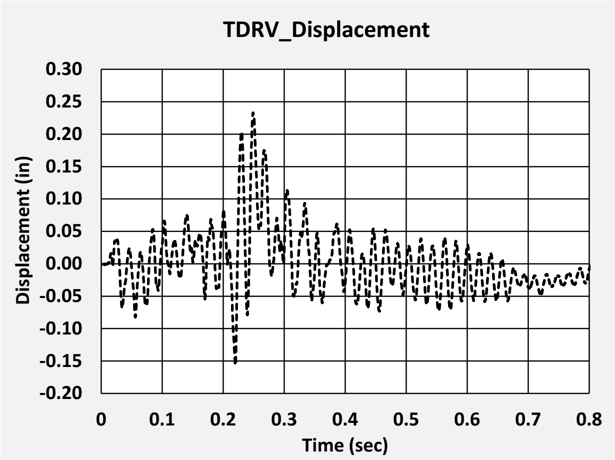

Figure B34. Raw Displacement-time Data from Displacement Transducer on Pressure Relief Valve

B4 – Material Characterization Results

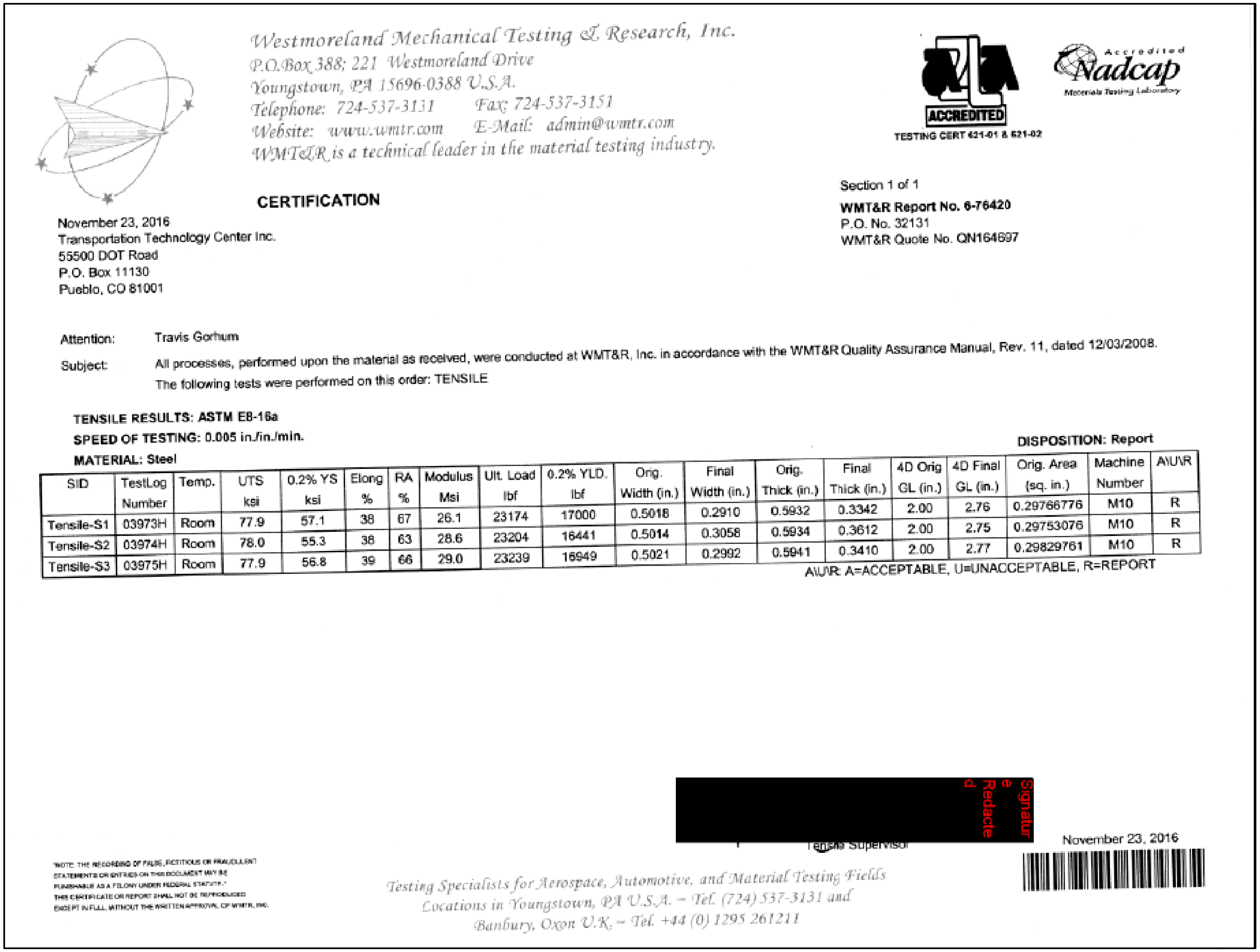

Westmoreland Mechanical Testing & Research, Inc.
P.O.Box 388; 221 Westmoreland Drive
Youngstown, PA 15696-0388 U.S.A.
Telephone: 724-537-3131 Fax: 724-537-3151
Website: www.wmtr.com E-Mail: admin@wmtr.com
WMT&R is a technical leader in the material testing industry.

ACCREDITED
TESTING CERT 621-01 & 621-02

Accredited Nadcap
Materials Testing Laboratory

CERTIFICATION

November 23, 2016
Transportation Technology Center Inc.
55500 DOT Road
P.O. Box 11130
Pueblo, CO 81001

Section 1 of 1
WMT&R Report No. 6-76420
P.O. No. 32131
WMT&R Quote No. QN164697

Attention: Travis Gorhum

Subject: All processes, performed upon the material as received, were conducted at WMT&R, Inc. in accordance with the WMT&R Quality Assurance Manual, Rev. 11, dated 12/03/2008.
The following tests were performed on this order: TENSILE

TENSILE RESULTS: ASTM E8-16a
SPEED OF TESTING: 0.005 in./in./min.
MATERIAL: Steel

DISPOSITION: Report

SID	TestLog Number	Temp.	UTS ksi	0.2% YS ksi	Elong %	RA %	Modulus Msi	Ult. Load lbf	0.2% YLD. lbf	Orig. Width (in.)	Final Width (in.)	Orig. Thick (in.)	Final Thick (in.)	4D Orig GL (in.)	4D Final GL (in.)	Orig. Area (sq. in.)	Machine Number	A\U\R
Tensile-S1	03973H	Room	77.9	57.1	38	67	26.1	23174	17000	0.5018	0.2910	0.5932	0.3342	2.00	2.76	0.29766776	M10	R
Tensile-S2	03974H	Room	78.0	55.3	38	63	28.6	23204	16441	0.5014	0.3058	0.5934	0.3612	2.00	2.75	0.29753076	M10	R
Tensile-S3	03975H	Room	77.9	56.8	39	66	29.0	23239	16949	0.5021	0.2992	0.5941	0.3410	2.00	2.77	0.29829761	M10	R

A\U\R: A=ACCEPTABLE, U=UNACCEPTABLE, R=REPORT

Signature Redacted
Tensile Supervisor

November 23, 2016

*NOTE: THE RECORDING OF FALSE, FICTITIOUS OR FRAUDULENT STATEMENTS OR ENTRIES ON THIS DOCUMENT MAY BE PUNISHABLE AS A FELONY UNDER FEDERAL STATUTE."
THIS CERTIFICATE OR REPORT SHALL NOT BE REPRODUCED EXCEPT IN FULL, WITHOUT THE WRITTEN APPROVAL OF WMTR, INC.

Testing Specialists for Aerospace, Automotive, and Material Testing Fields
Locations in Youngstown, PA U.S.A. – Tel. (724) 537-3131 and
Banbury, Oxon U.K. – Tel. +44 (0) 1295 261211

Figure B35. Page 1 of Material Characterization Report

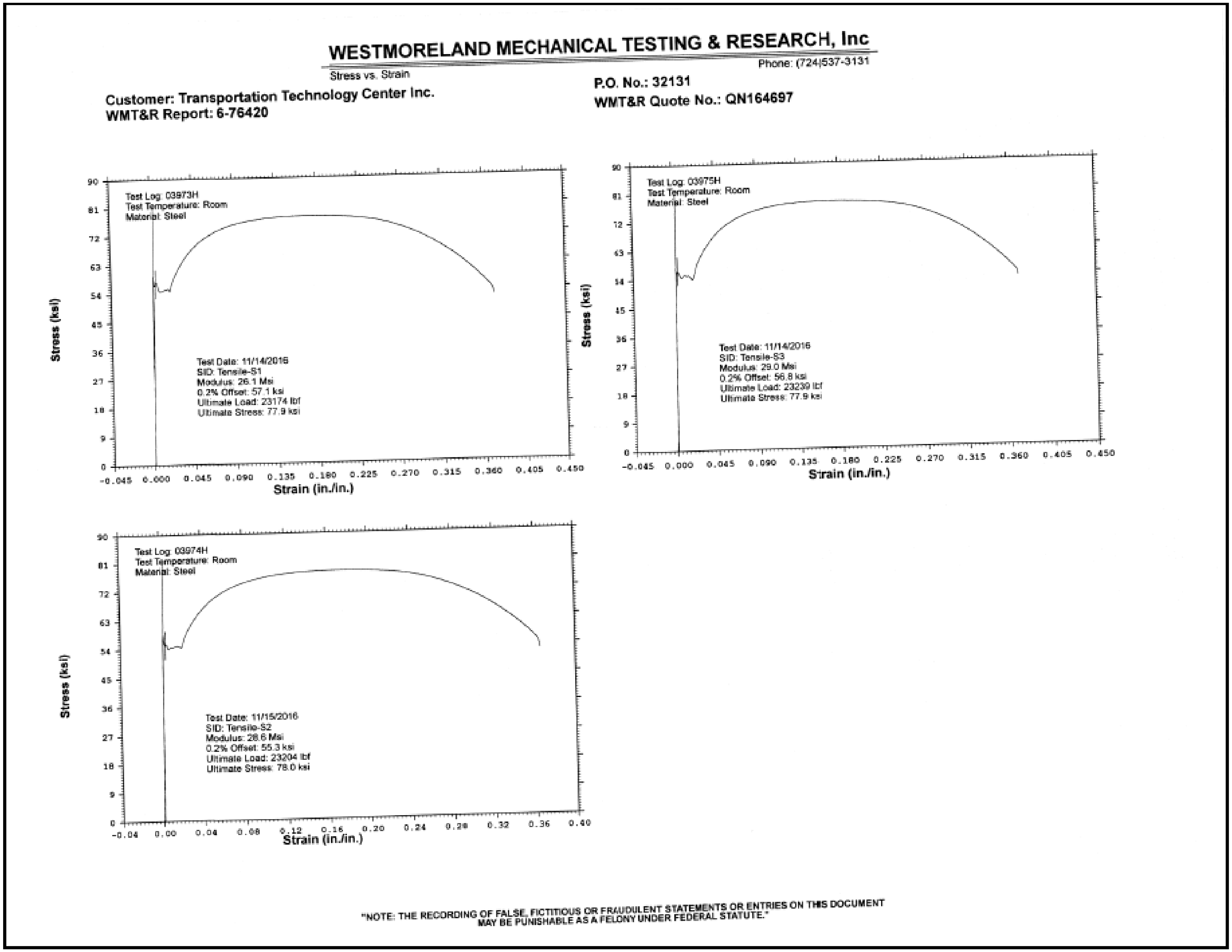

WESTMORELAND MECHANICAL TESTING & RESEARCH, Inc

Phone: (724)537-3131

Stress vs. Strain

Customer: Transportation Technology Center Inc.
WMT&R Report: 6-76420

P.O. No.: 32131
WMT&R Quote No.: QN164697

Test Log: 03973H
Test Temperature: Room
Material: Steel

Test Date: 11/14/2016
SID: Tensile-S1
Modulus: 26.1 Msi
0.2% Offset: 57.1 ksi
Ultimate Load: 23174 lbf
Ultimate Stress: 77.9 ksi

Test Log: 03975H
Test Temperature: Room
Material: Steel

Test Date: 11/14/2016
SID: Tensile-S3
Modulus: 29.0 Msi
0.2% Offset: 56.8 ksi
Ultimate Load: 23239 lbf
Ultimate Stress: 77.9 ksi

Test Log: 03974H
Test Temperature: Room
Material: Steel

Test Date: 11/15/2016
SID: Tensile-S2
Modulus: 28.6 Msi
0.2% Offset: 55.3 ksi
Ultimate Load: 23204 lbf
Ultimate Stress: 78.0 ksi

"NOTE: THE RECORDING OF FALSE, FICTITIOUS OR FRAUDULENT STATEMENTS OR ENTRIES ON THIS DOCUMENT MAY BE PUNISHABLE AS A FELONY UNDER FEDERAL STATUTE."

Figure B36. Page 2 of Material Characterization Report showing Stress-strain Responses from Tensile Tests

Appendix C.
Finite Element Analysis and Test Results

For all test results presented in this appendix, the time has been offset by 0.004 seconds to account for the test instrumentation triggering when the ram surface was still approximately 1-inch away from making contact with the jacket.

C1 – Pre-Test FEA and Test Results—14 mph

The pre-test model run at 14 mph experienced puncture. Thus, the pre-test FE model results presented in the following series of plots end at approximately 0.3 seconds of simulated impact, as that is when the model punctured.

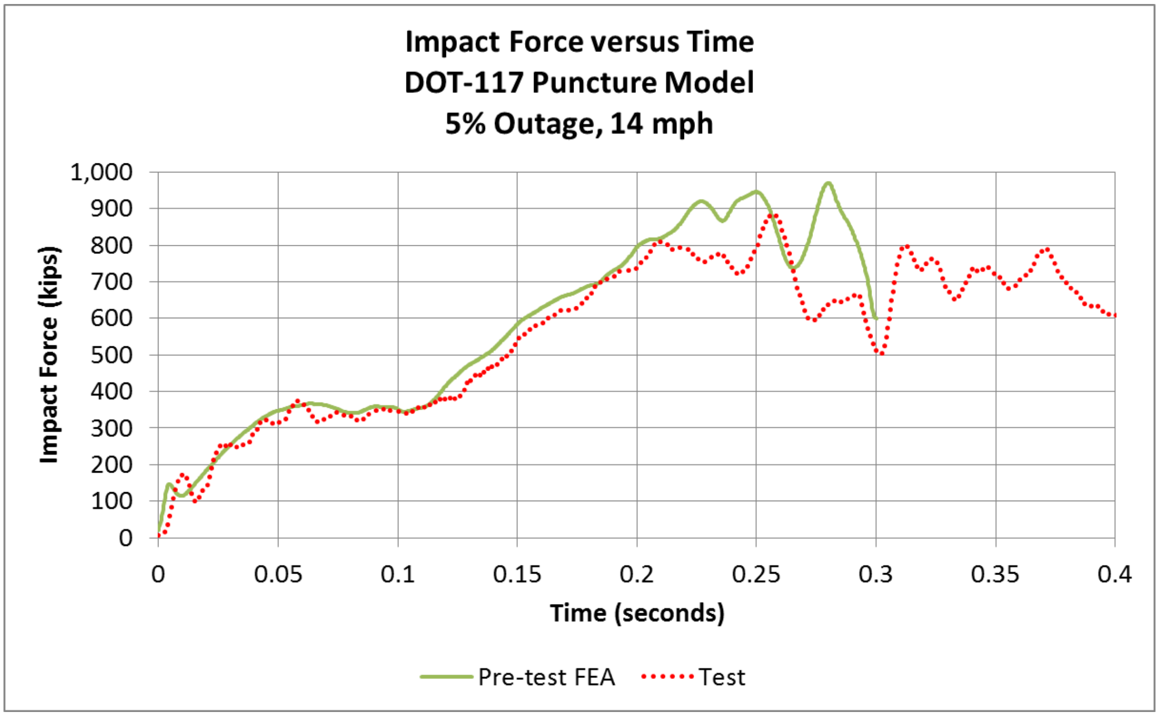

Figure C1. Impact Force Versus Time, 14 mph Pre-Test FEA and Test Data

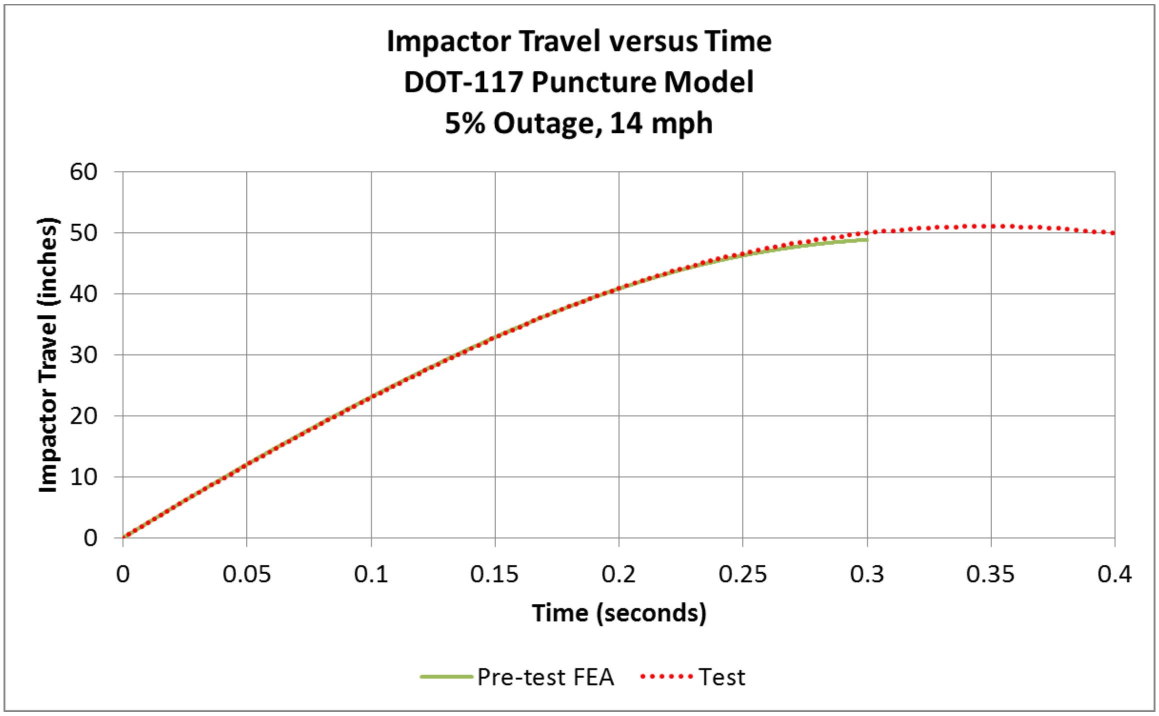

Figure C2. Impactor Travel versus Time, 14 mph Pre-Test FEA and Test Data

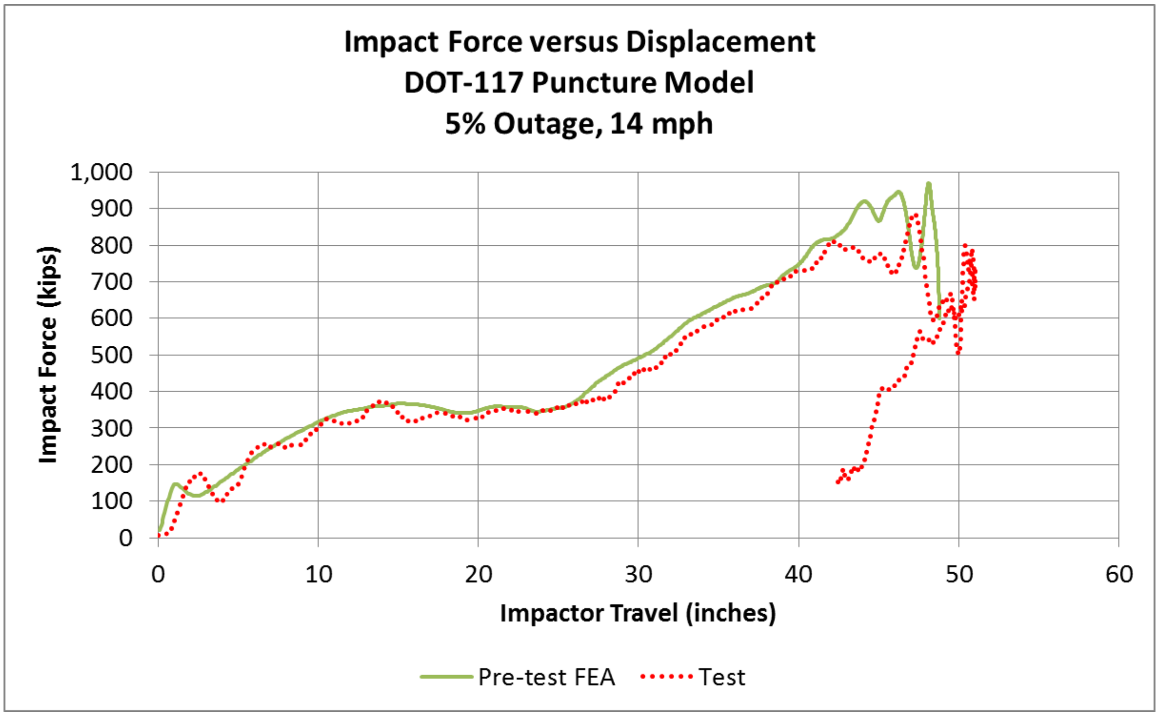

Figure C3. Impact Force Versus Impactor Travel, 14 mph Pre-Test FEA and Test Data

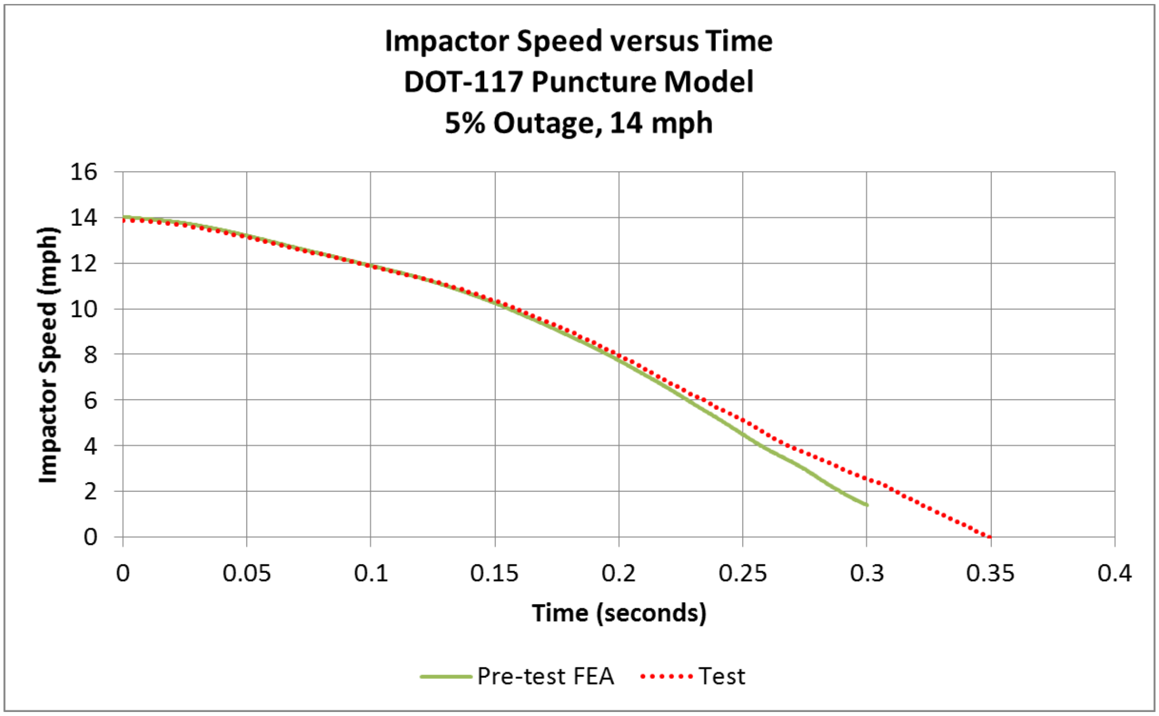

Figure C4. Impactor Speed Versus Time, 14 mph Pre-Test FEA and Test Data

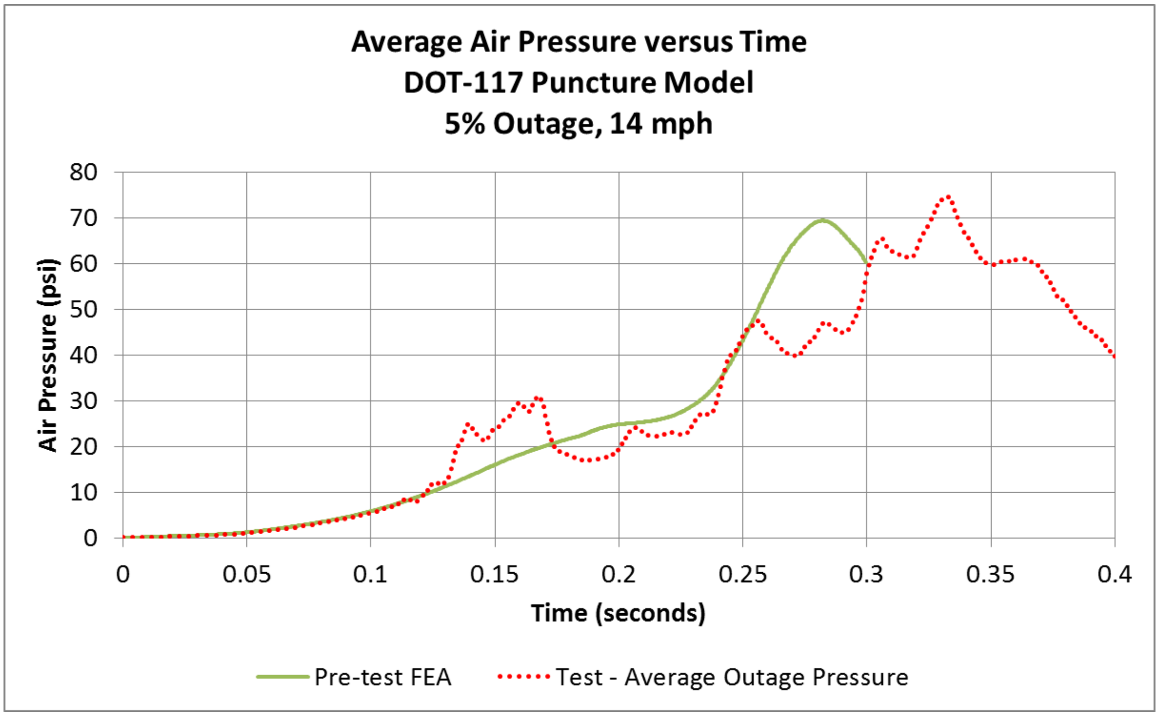

Figure C5. Average Air Pressure Versus Time, 14 mph Pre-Test FEA and Test Data

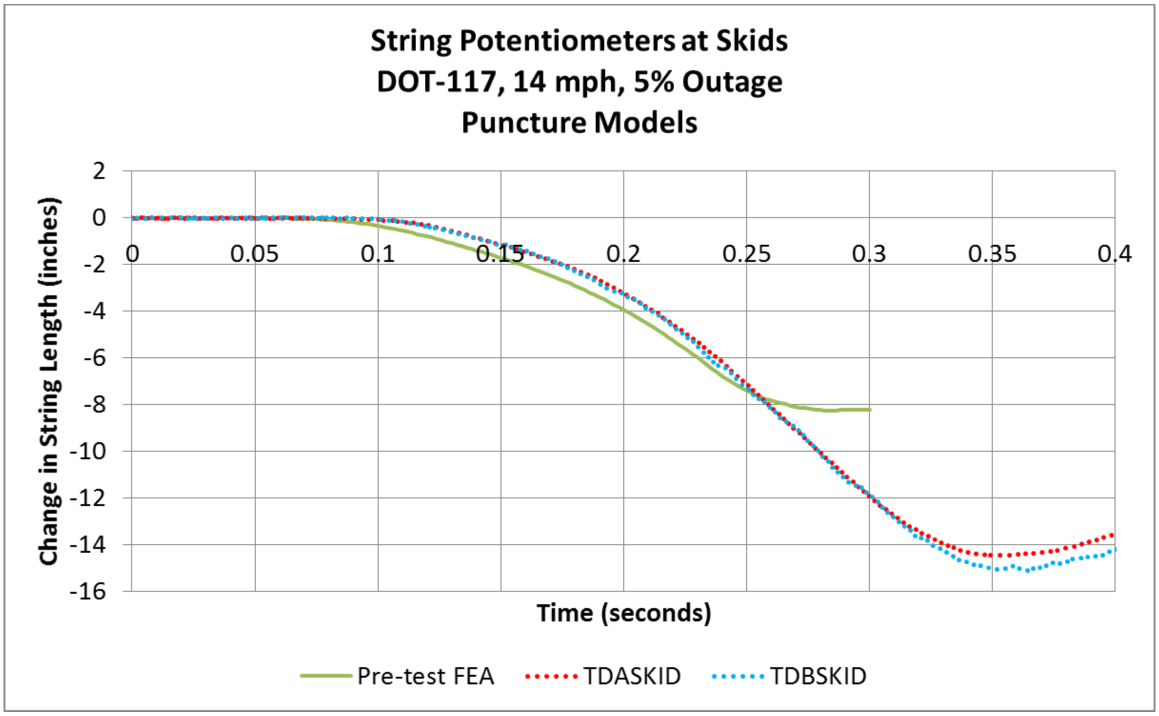

Figure C6. String Potentiometers at Skids, 14 mph Pre-Test FEA and Test Data

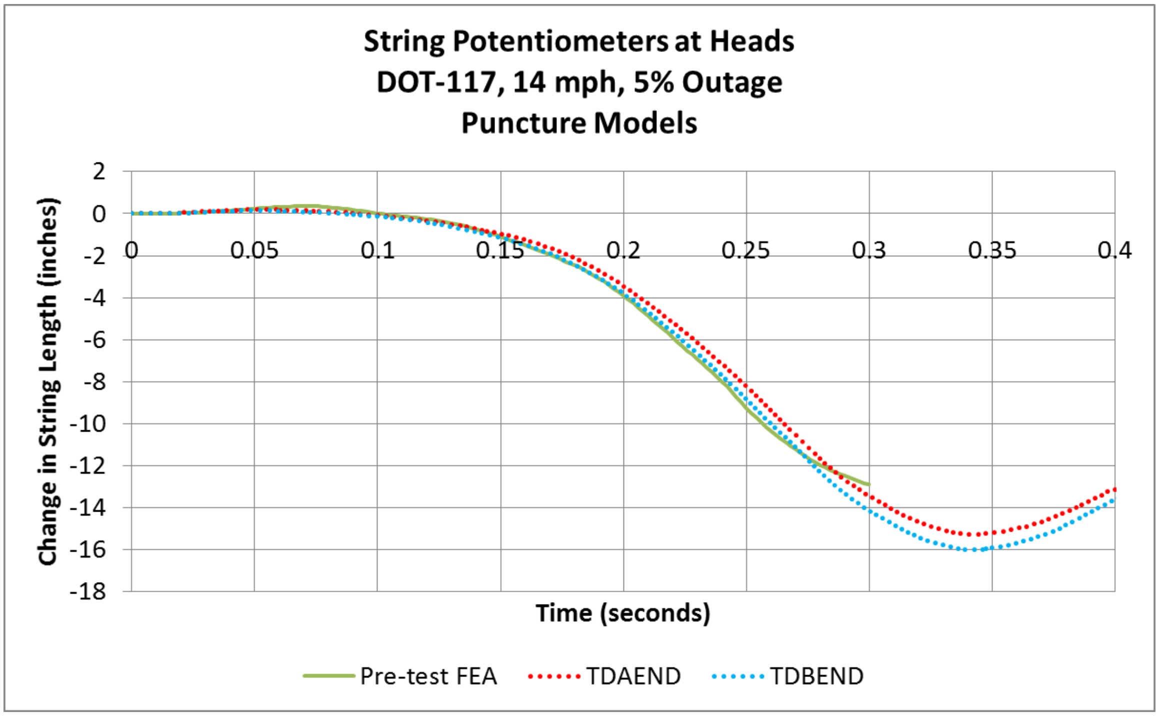

Figure C7. String Potentiometers at Heads, 14 mph Pre-Test FEA and Test Data

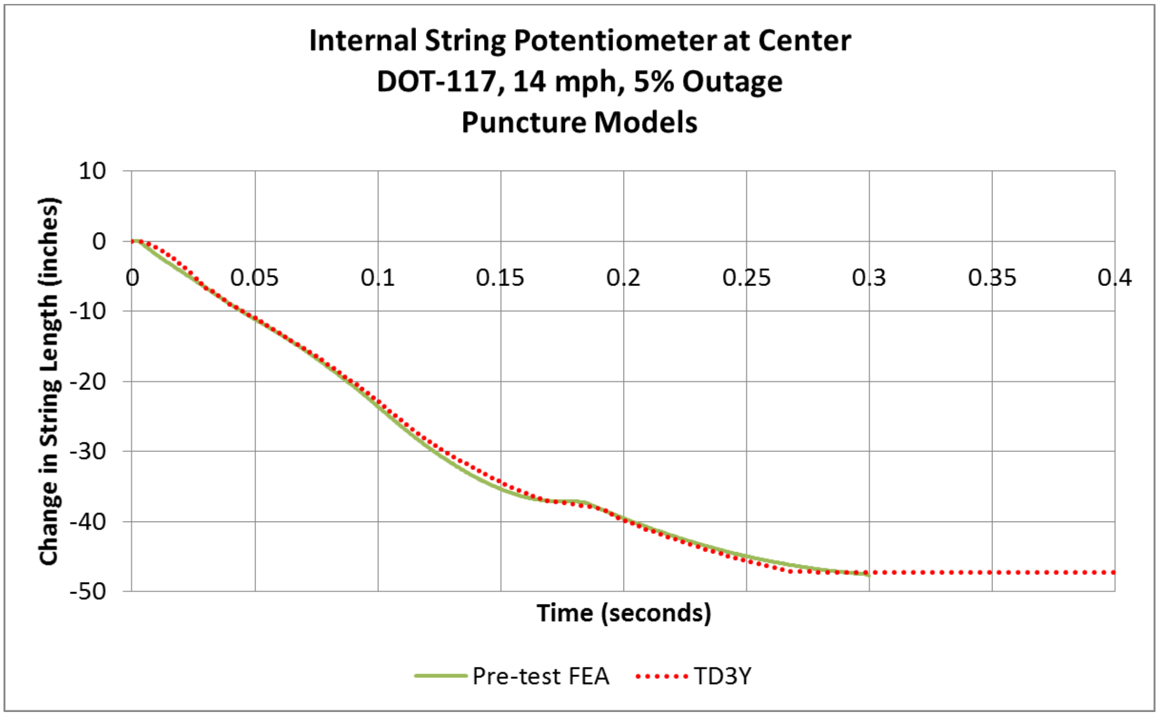

Figure C8. Internal String Potentiometer at Center of Tank, 14 mph Pre-Test FEA and Test Data

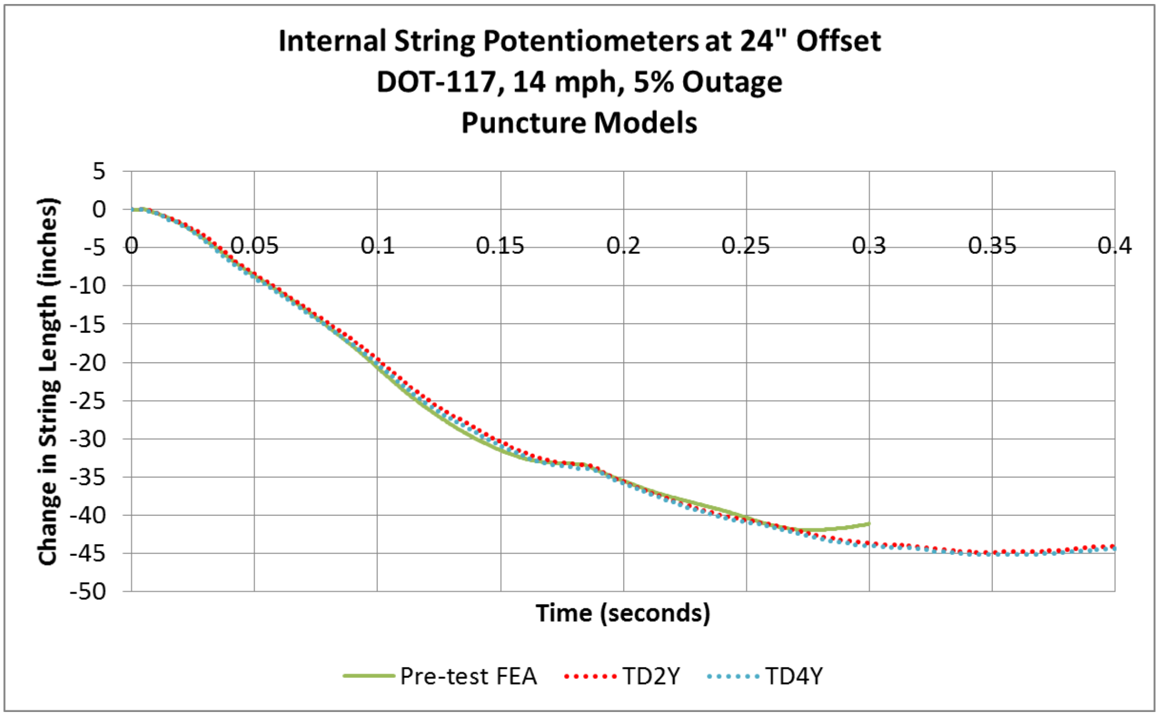

Figure C9. Internal String Potentiometers 24 Inches from Impact, 14 mph Pre-Test FEA and Test Data

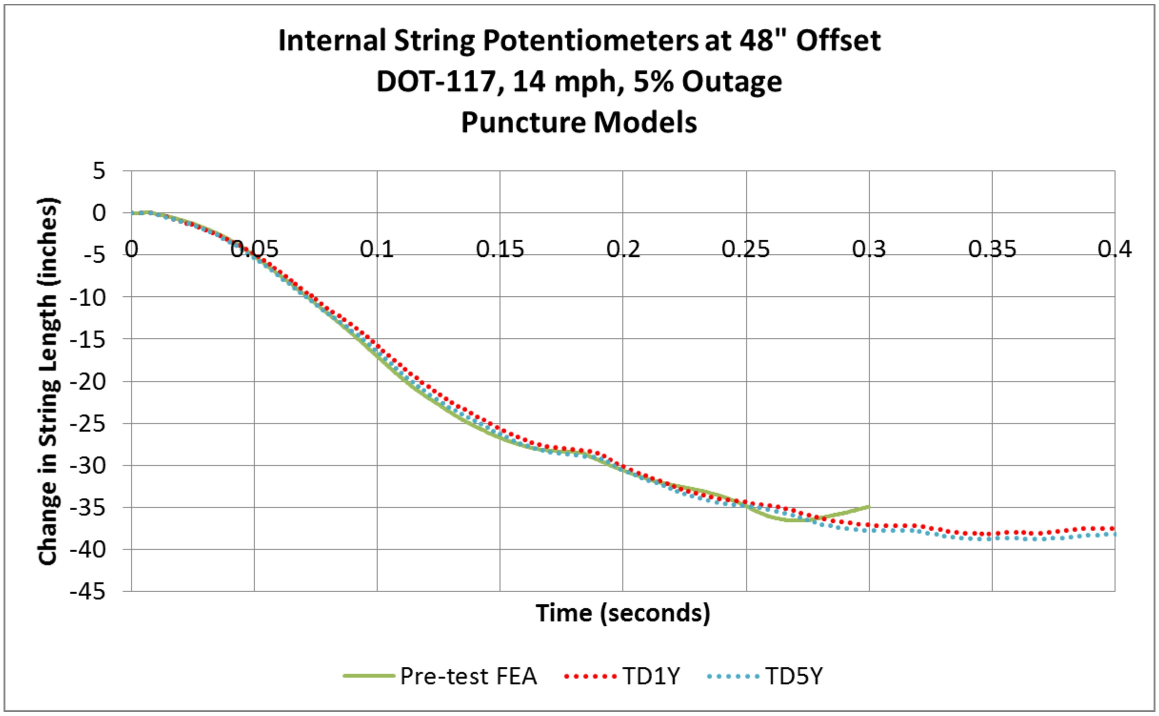

Figure C10. Internal String Potentiometers 48 Inches from Impact, 14 mph Pre-Test FEA and Test Data

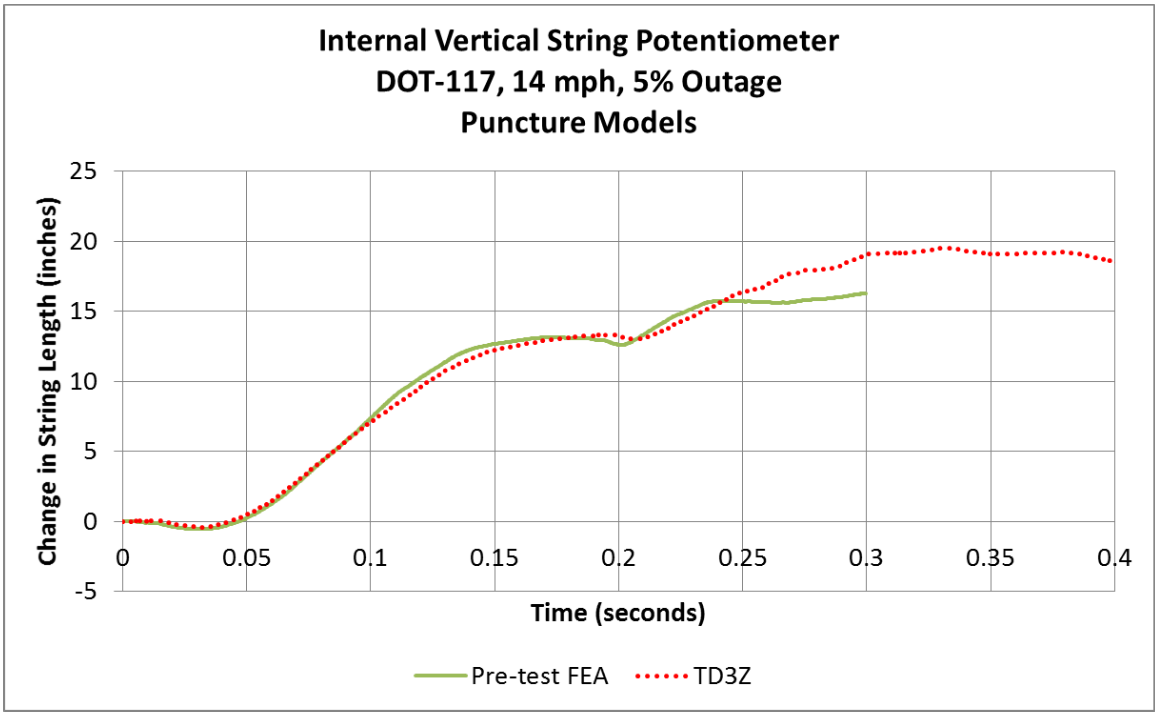

Figure C11. Internal Vertical String Potentiometer, 14 mph Pre-Test FEA and Test Data

C2 – Pre-Test FEA and Test Results—13 mph

The pre-test model run at 13 mph uses the same mesh and material behaviors as in the 14-mph model. Thus, the modeling techniques employed in this model would allow puncture to occur if the impact speed were sufficiently high to result in puncture. However, this model did not result in puncture of the tank itself, only tearing of the jacket.

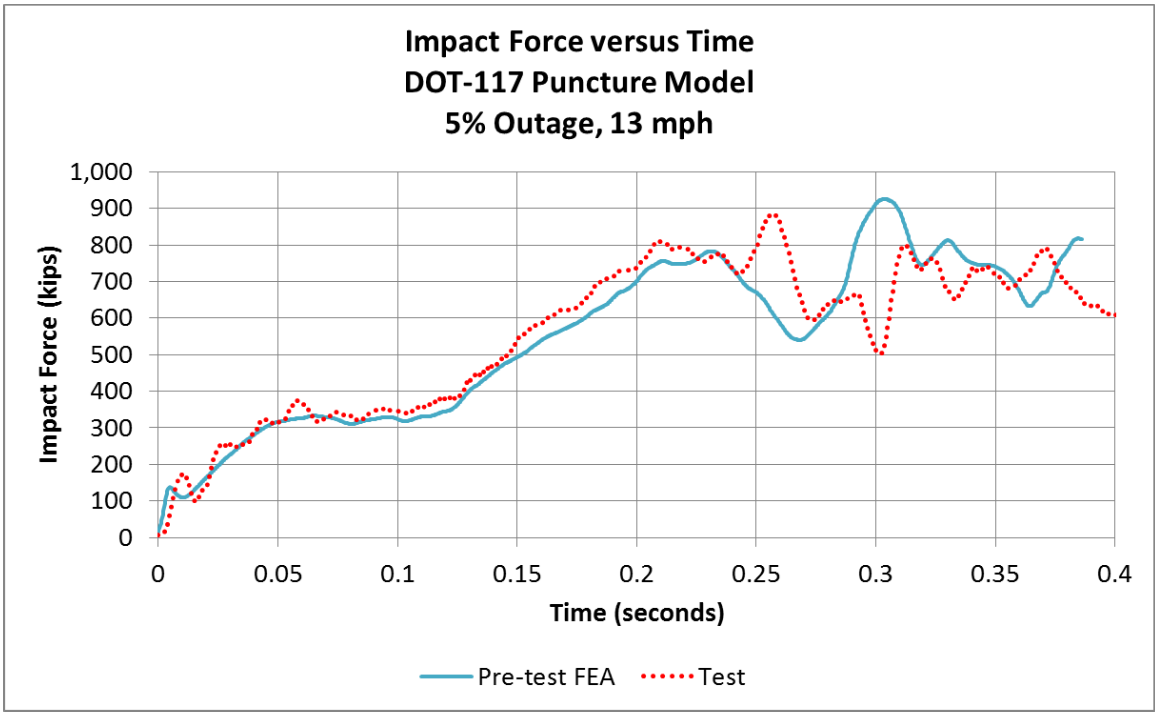

Figure C12. Impact Force Versus Time, 13 mph Pre-Test FEA and Test Data

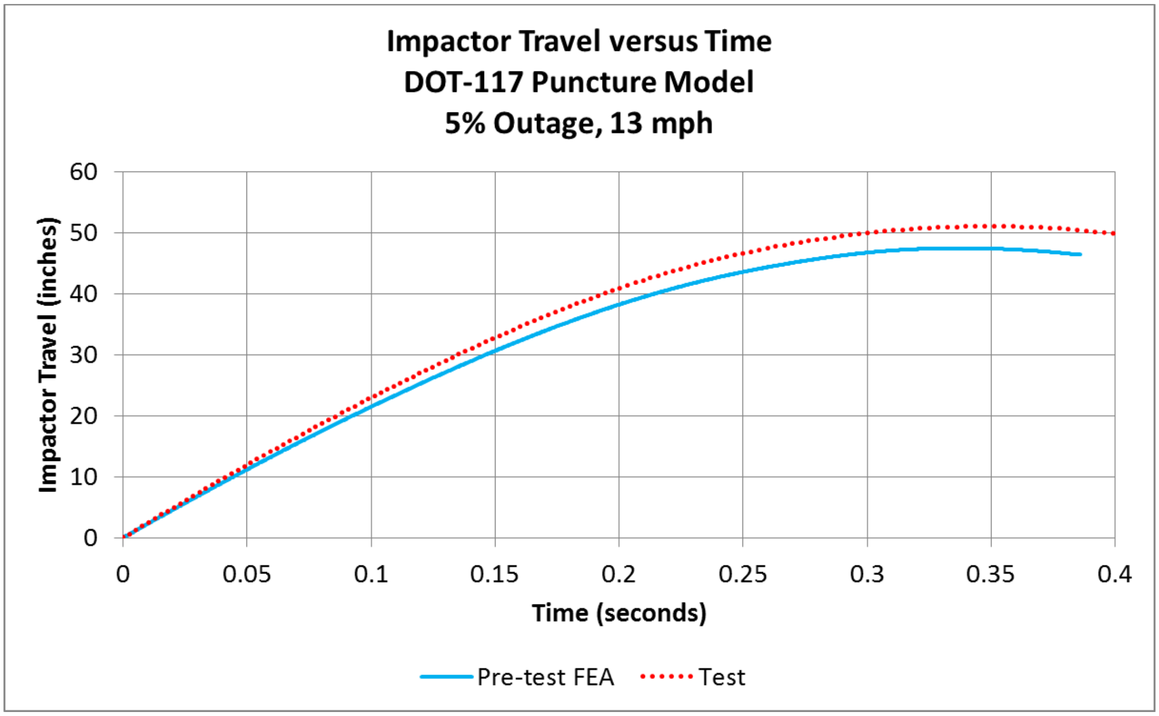

Figure C13. Impactor Travel Versus Time, 13 mph Pre-Test FEA and Test Data

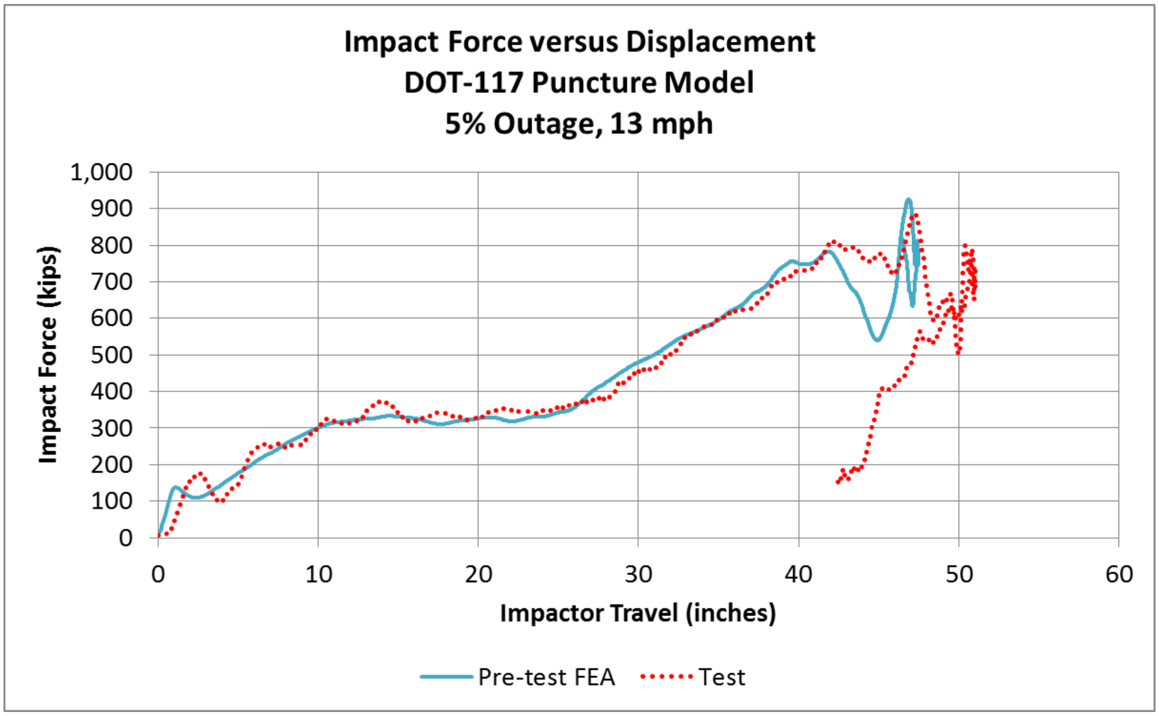

Figure C14. Impact Force Versus Impactor Travel, 13 mph Pre-Test FEA and Test Data

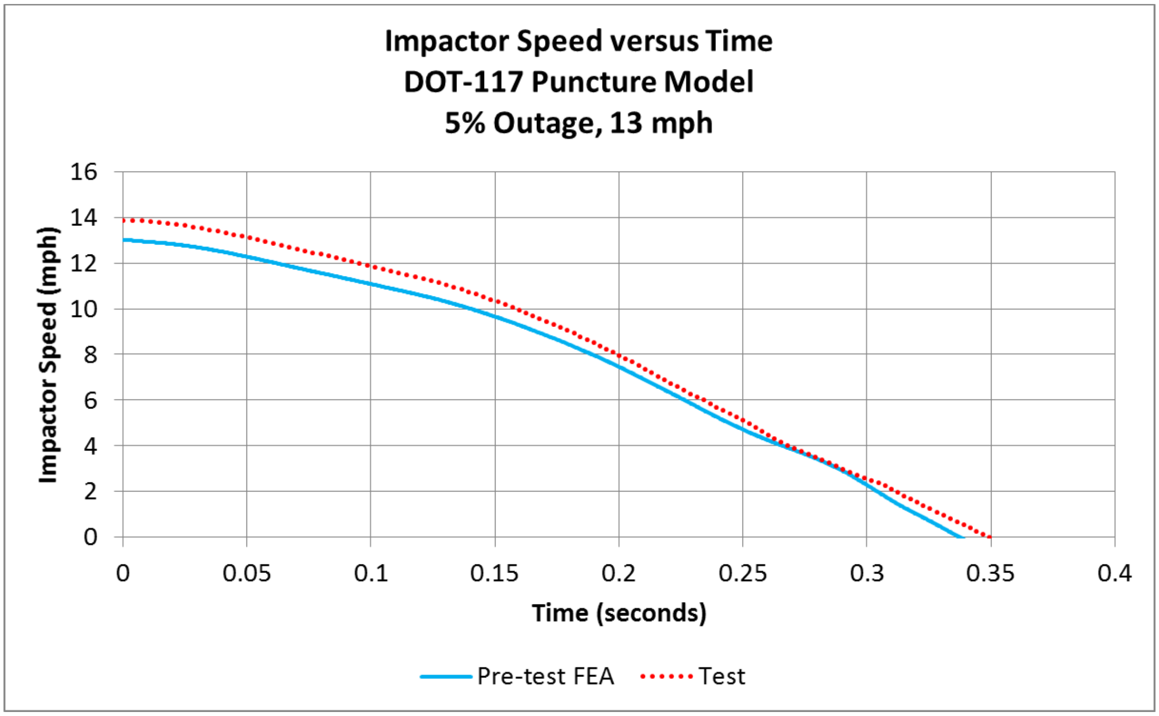

Figure C15. Impactor Speed Versus Time, 13 mph Pre-Test FEA and Test Data

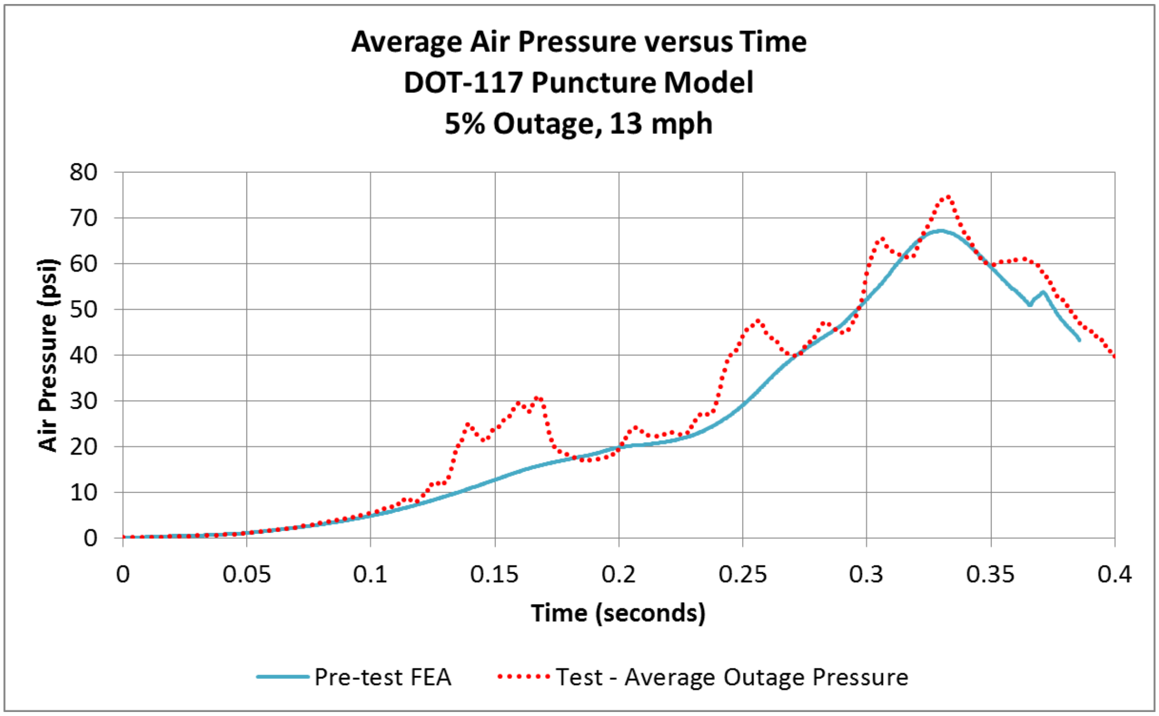

Figure C16. Average Air Pressure Versus Time, 13 mph Pre-Test FEA and Test Data

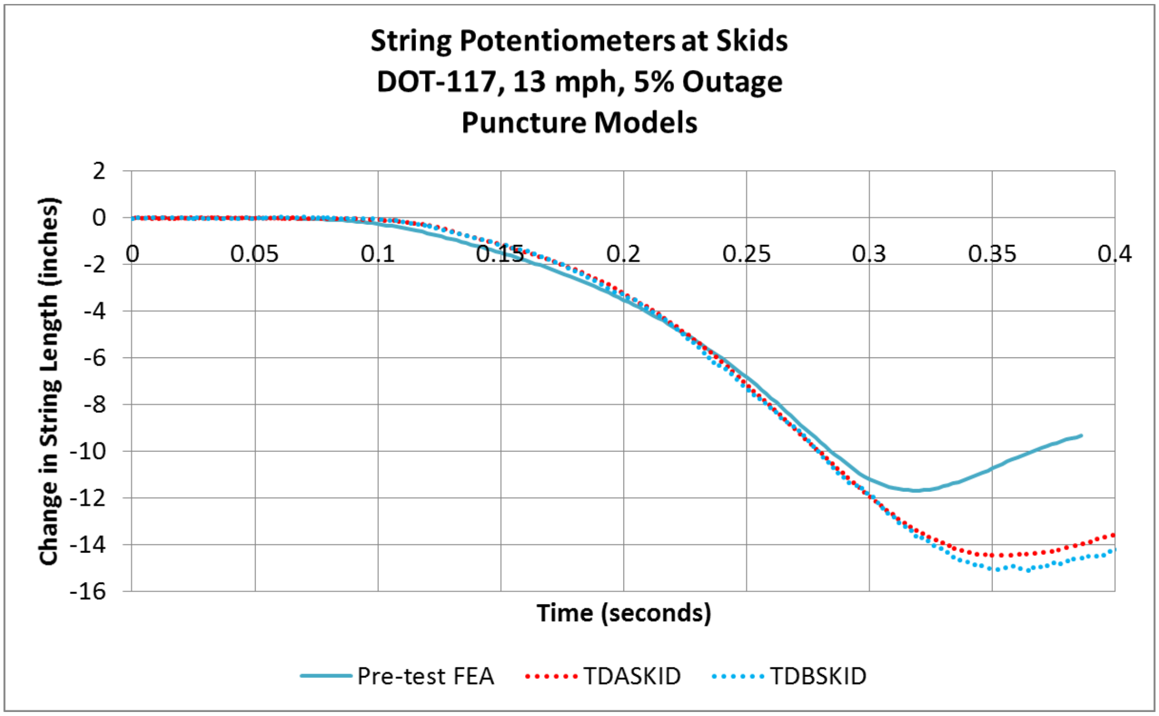

Figure C17. String Potentiometers at Skids, 13 mph Pre-Test FEA and Test Data

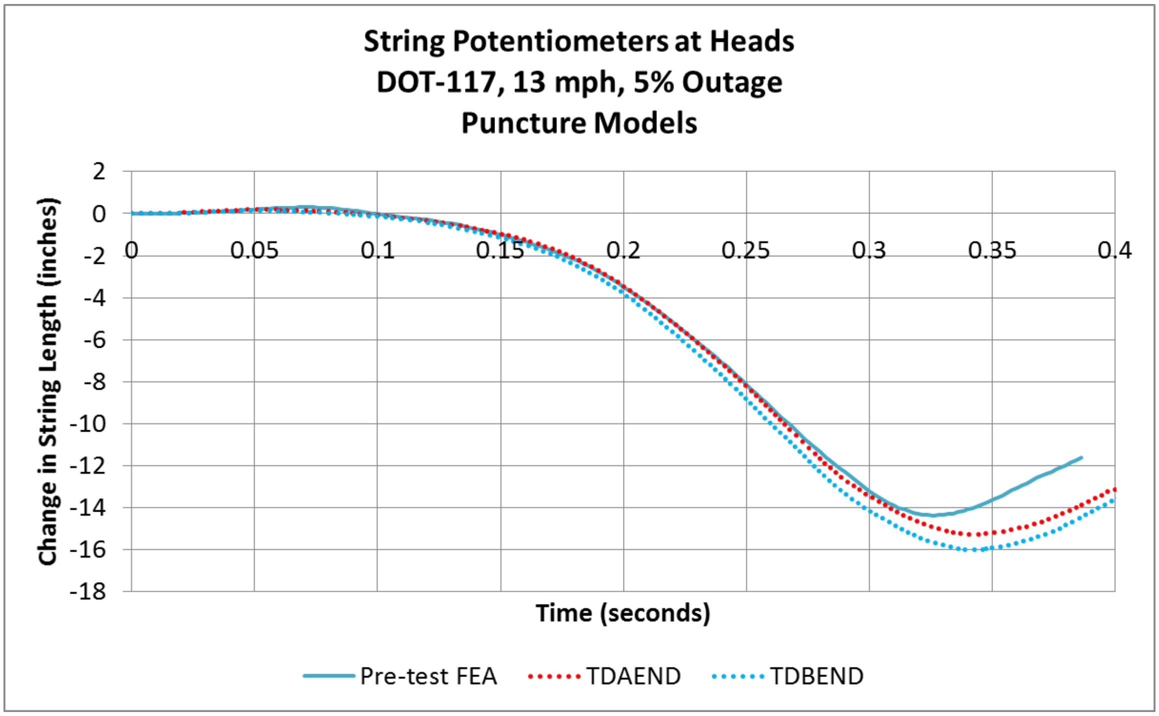

Figure C18. String Potentiometers at Heads, 13 mph Pre-Test FEA and Test Data

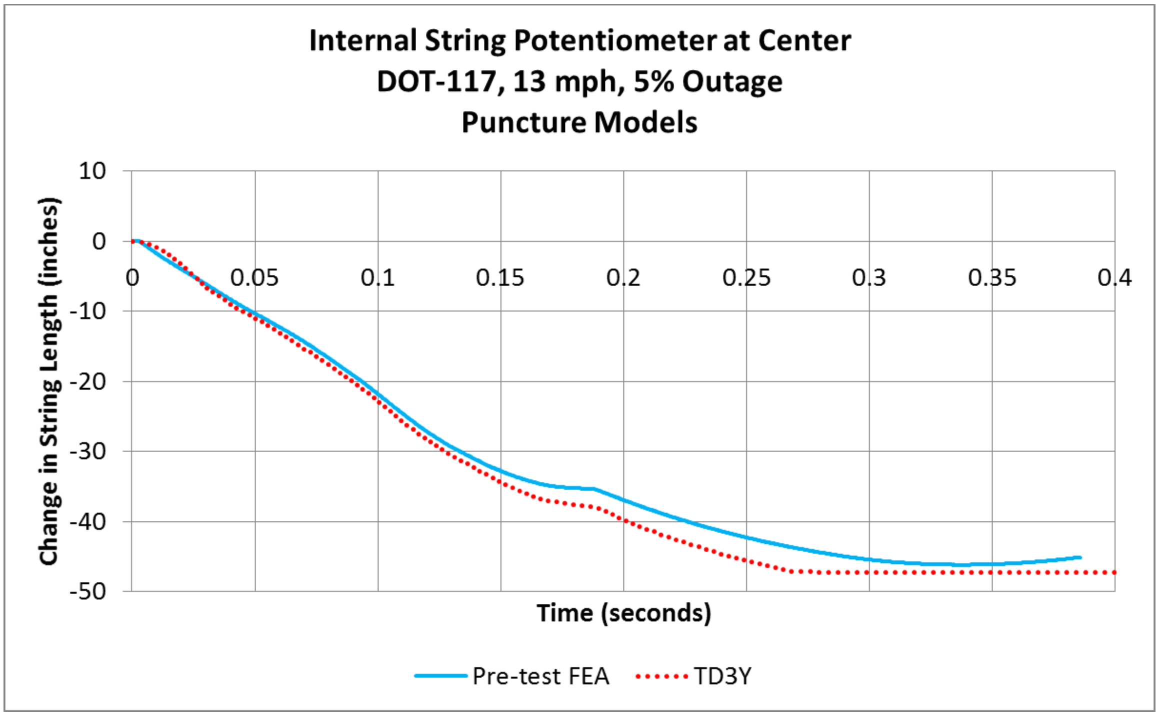

Figure C19. Internal String Potentiometer at Center of Tank, 13 mph Pre-Test FEA and Test Data

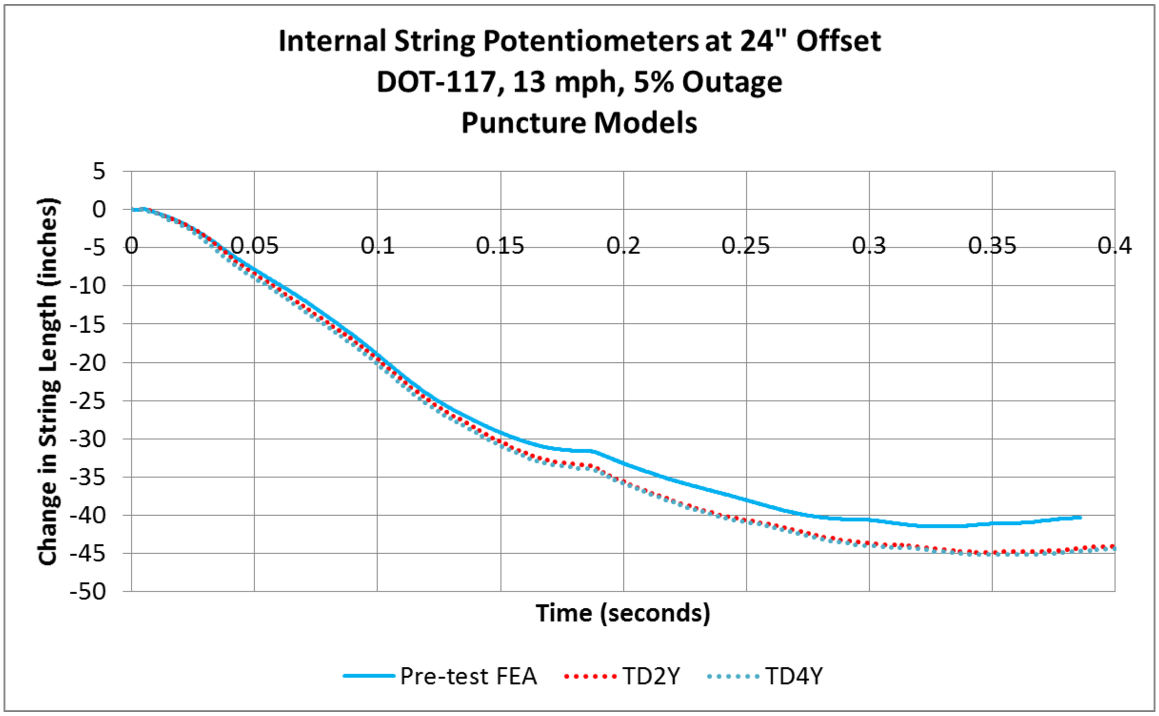

Figure C20. Internal String Potentiometers 24 Inches from Impact, 13 mph Pre-Test FEA and Test Data

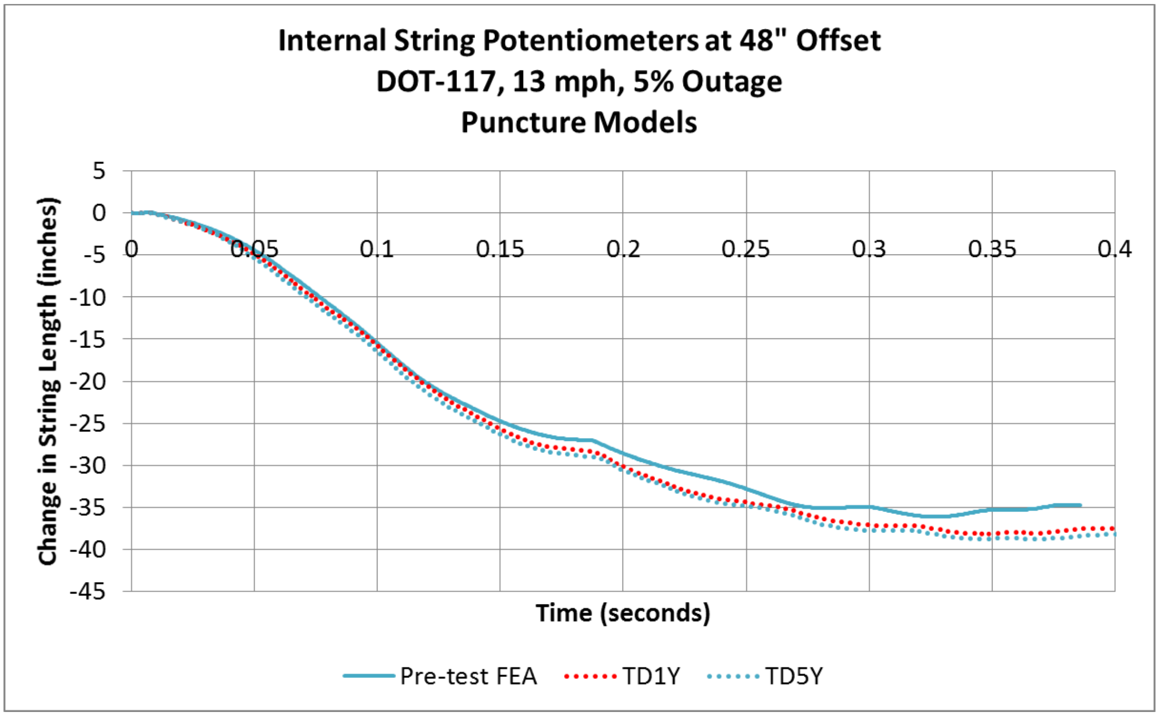

Figure C21. Internal String Potentiometers 48 Inches from Impact, 13 mph Pre-Test FEA and Test Data

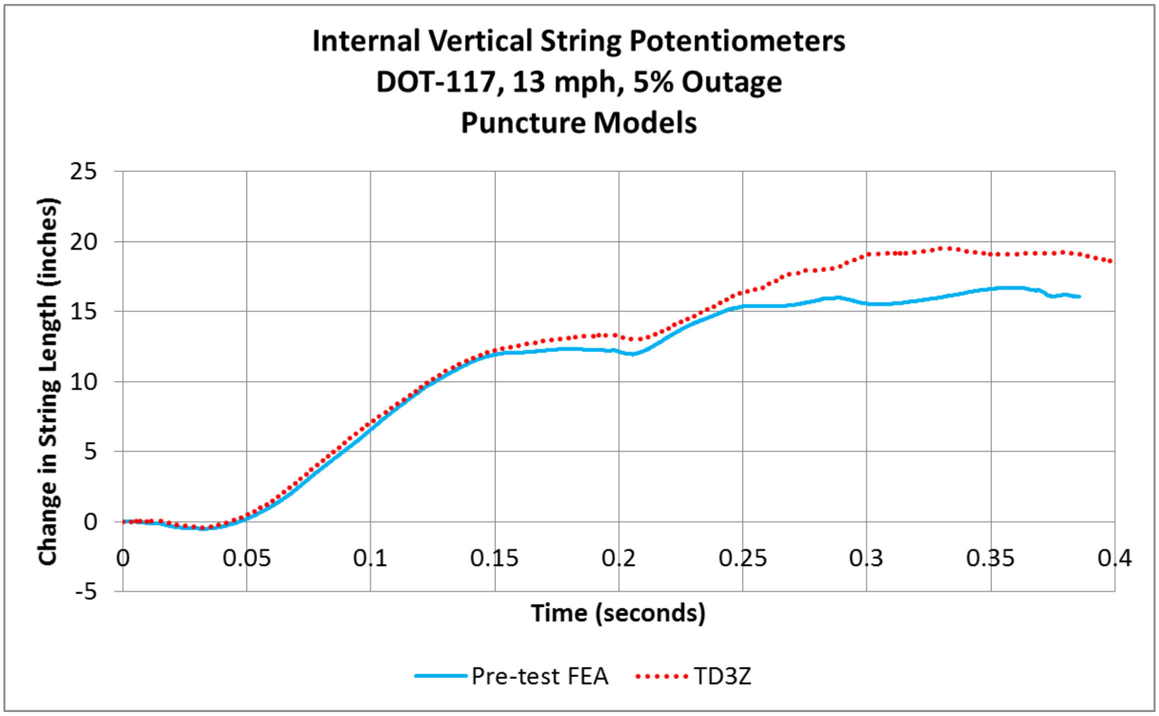

Figure C22. Internal Vertical String Potentiometer, 13 mph Pre-Test FEA and Test Data

C3 – Post-Test FEA and Test Results—13.9 mph (Rigid Ground)

Post-test FEA was run at the speed determined from the speed traps, 13.9 mph. The post-test models were also run using updated material behaviors for both the tank and for the water to better match the test conditions. Finally, the post-test models have a 1-inch gap between the jacket and the rigid wall, and a ground geometry that included the pit in the actual test setup. The results in this appendix are from the post-test model using a rigid representation of the ground slab geometry. The changes implemented in the post-test model compared to the pre-test model are described in Section 5.5. Results derived from accelerometers or pressure transducers have been filtered using a CFC60 filter.

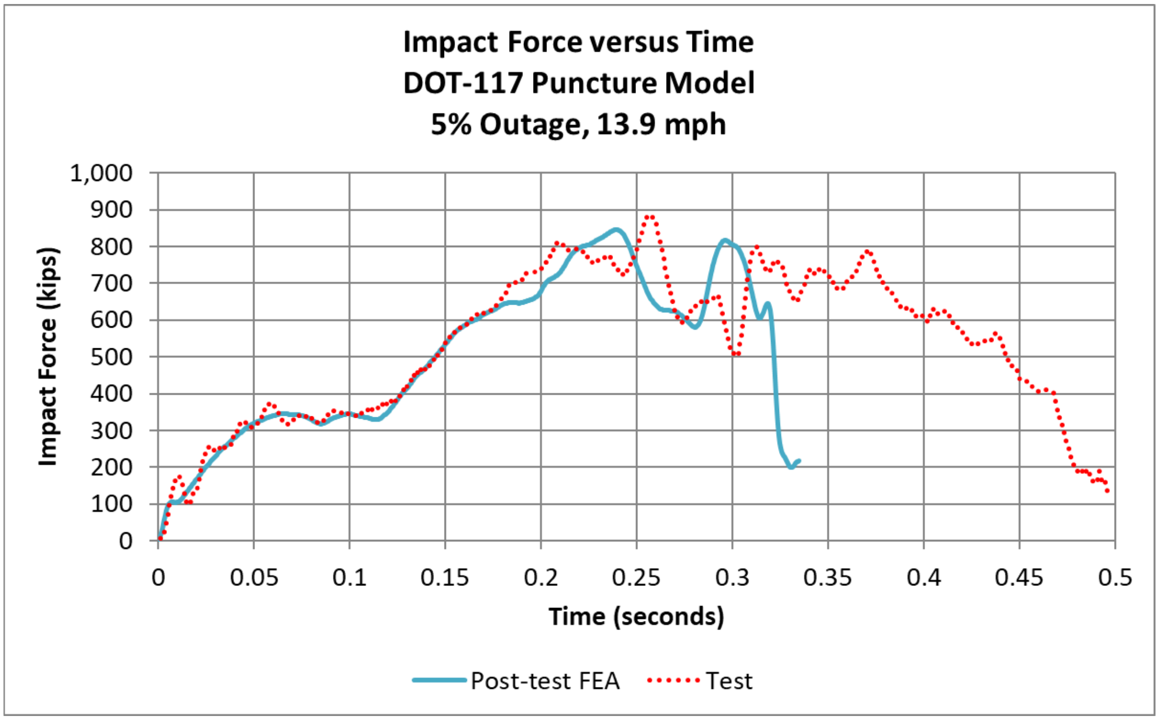

Figure C23. Impact Force Versus Time, Post-Test FEA with Rigid Ground and Test Data

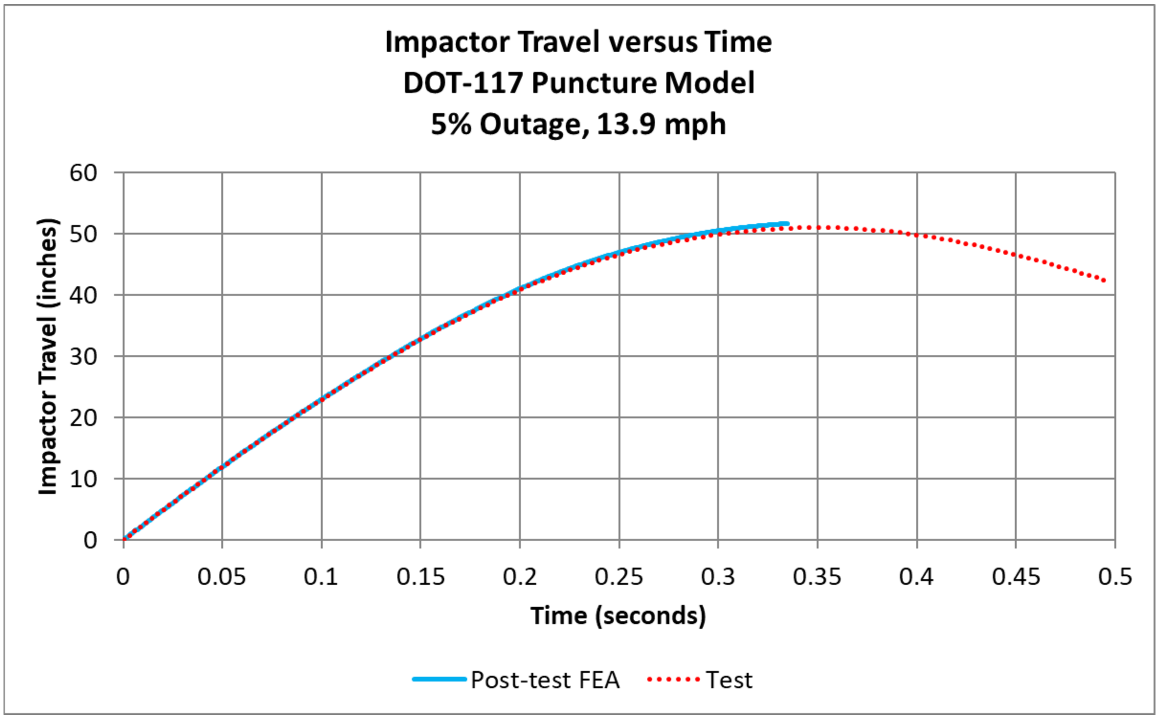

Figure C24. Impactor Travel versus Time, Post-Test FEA with Rigid Ground and Test Data

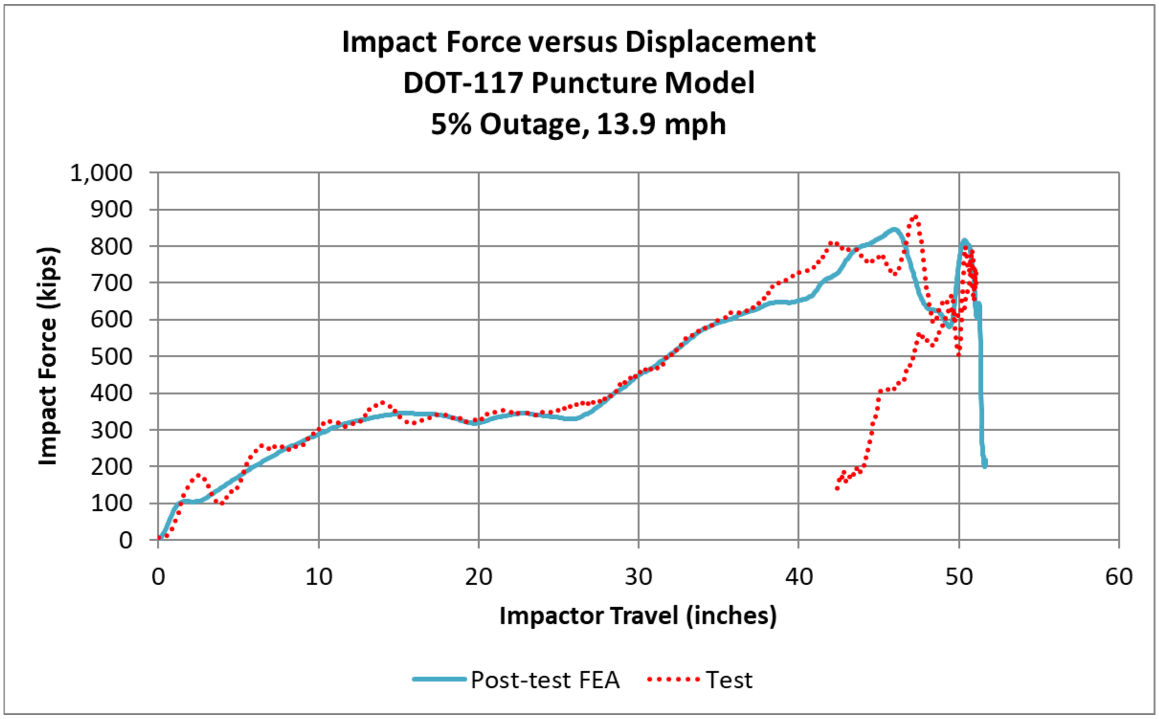

Figure C25. Impact Force Versus Impactor Travel, Post-Test FEA with Rigid Ground and Test Data

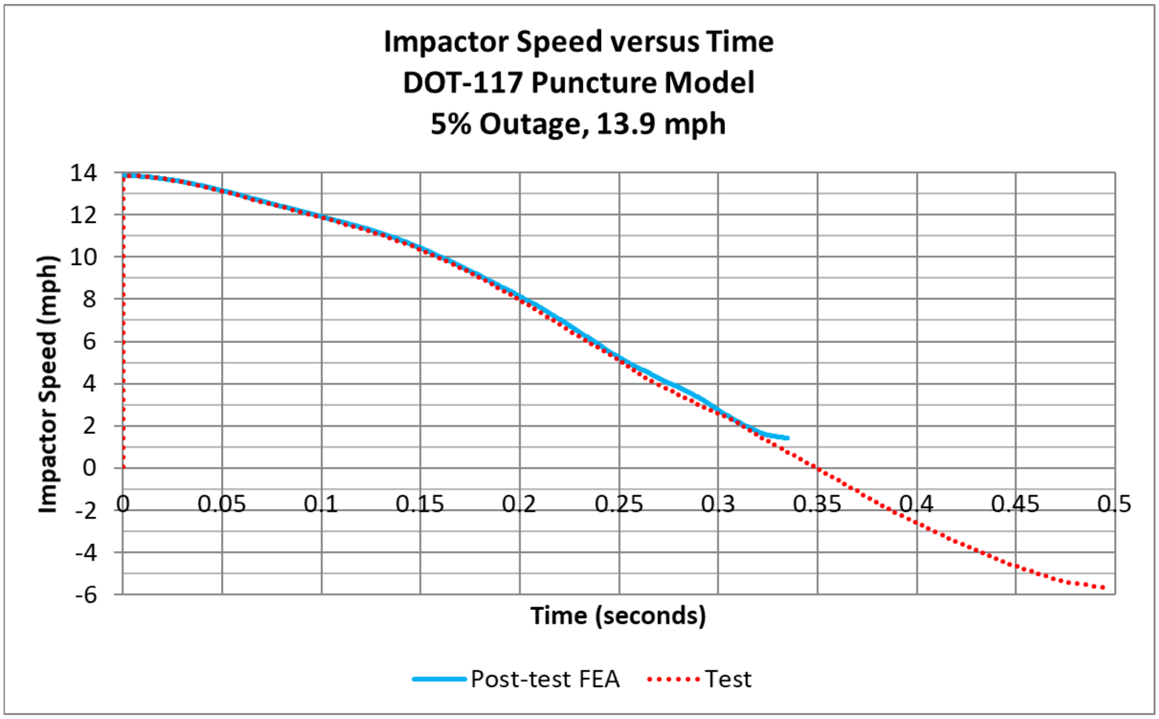

Figure C26. Impactor Speed Versus Time, Post-Test FEA with Rigid Ground and Test Data

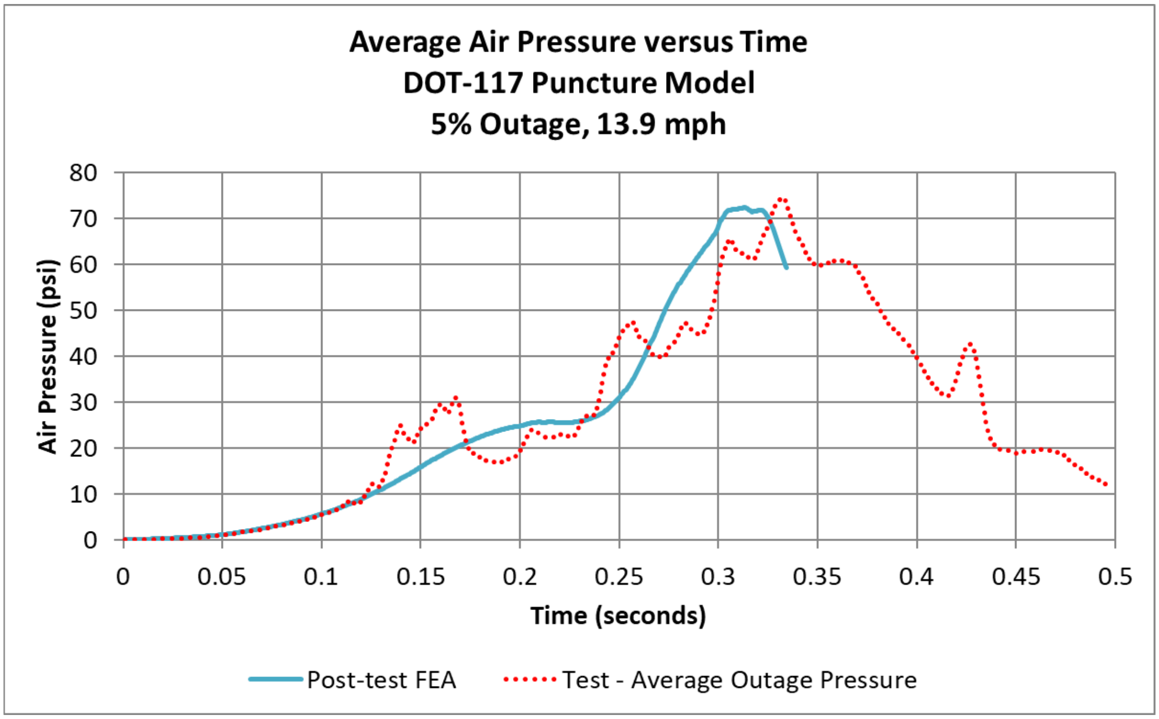

Figure C27. Average Air Pressure Versus time, Post-Test FEA with Rigid Ground and Test Data

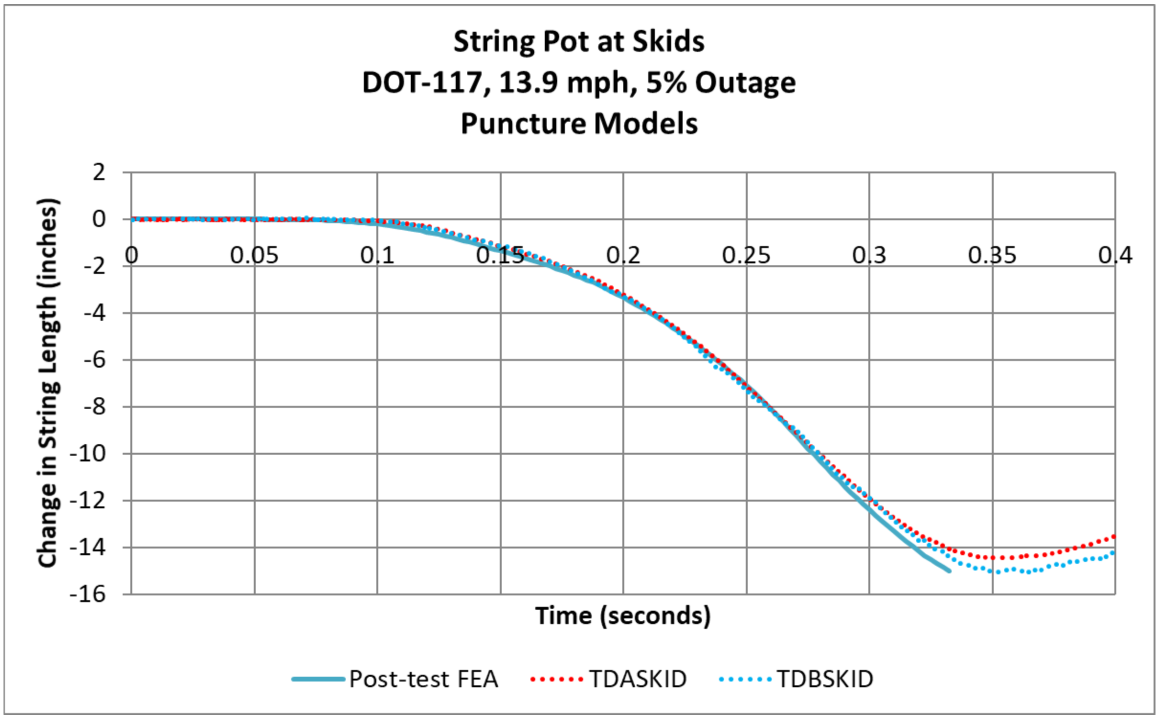

Figure C28. String Potentiometers at Skids, Post-Test FEA with Rigid Ground and Test Data

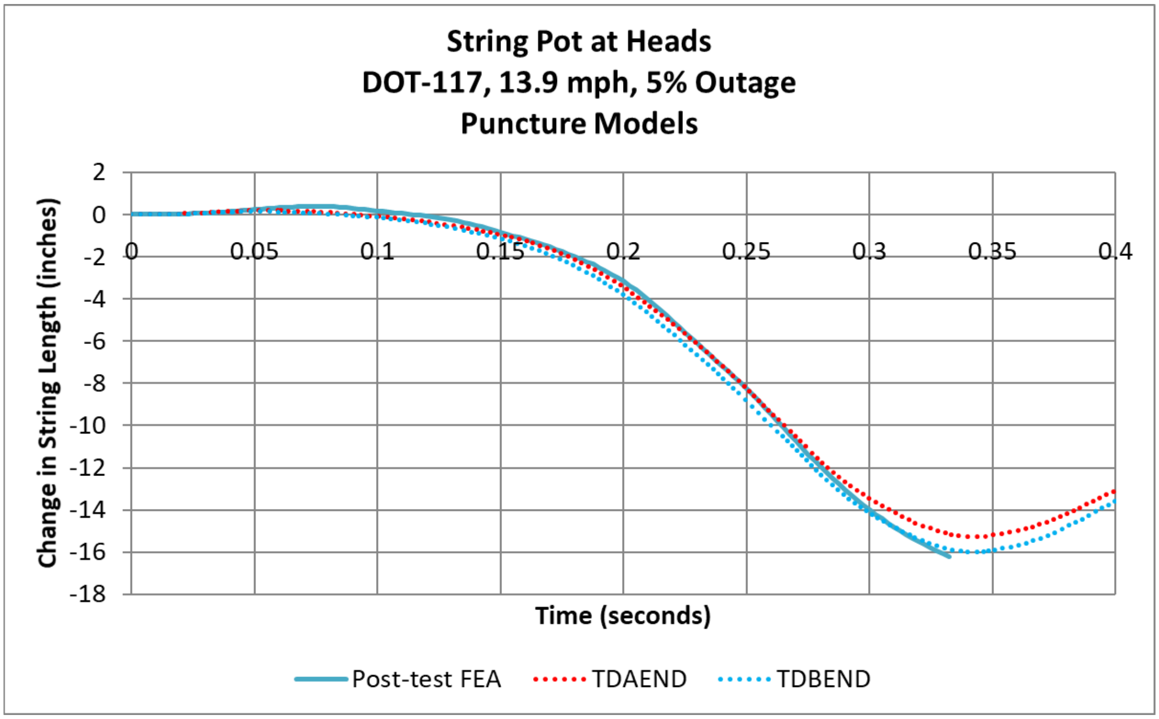

Figure C29. String Potentiometers at Heads, Post-Test FEA with Rigid Ground and Test Data

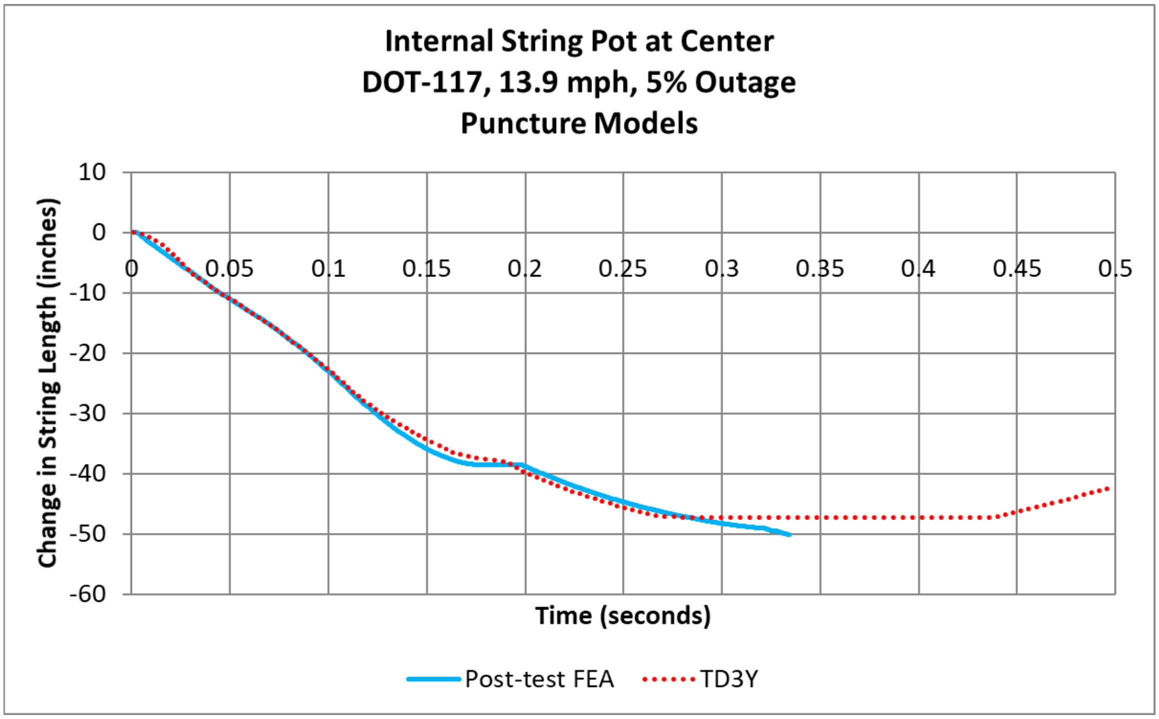

Figure C 1. Internal String Potentiometer at Center of Tank, Post-Test FEA with Rigid Ground and Test Data

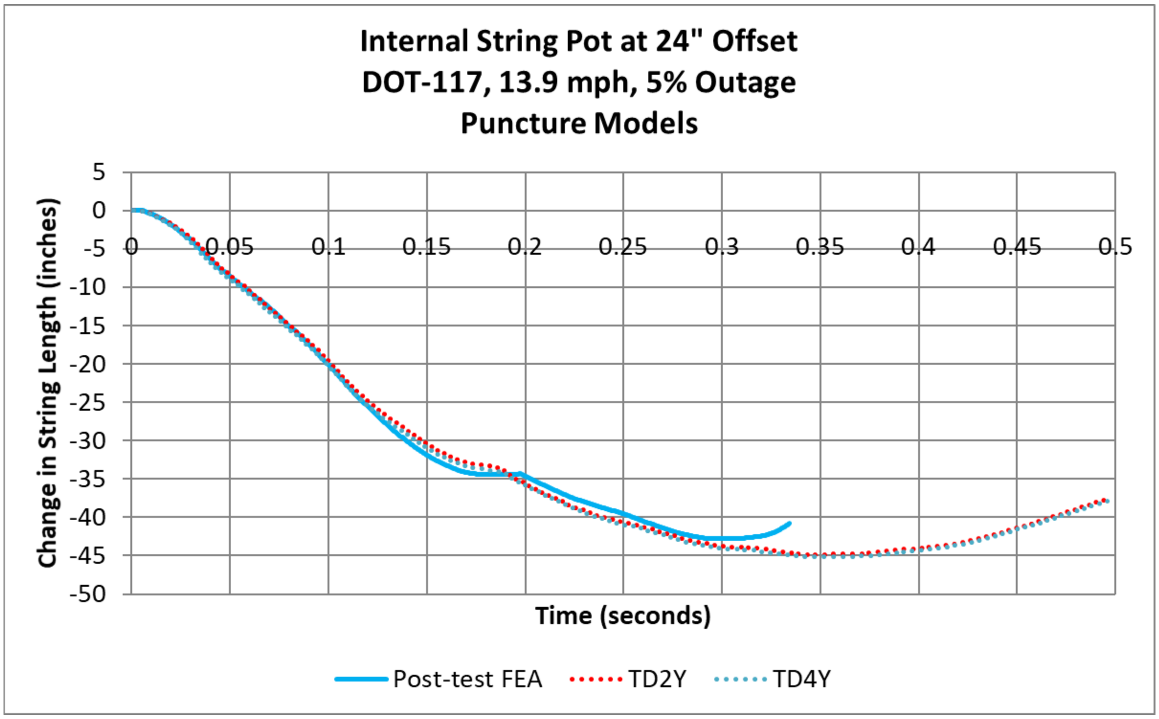

Figure C31. Internal String Potentiometers 24 Inches from Impact, Post-Test FEA with Rigid Ground and Test Data

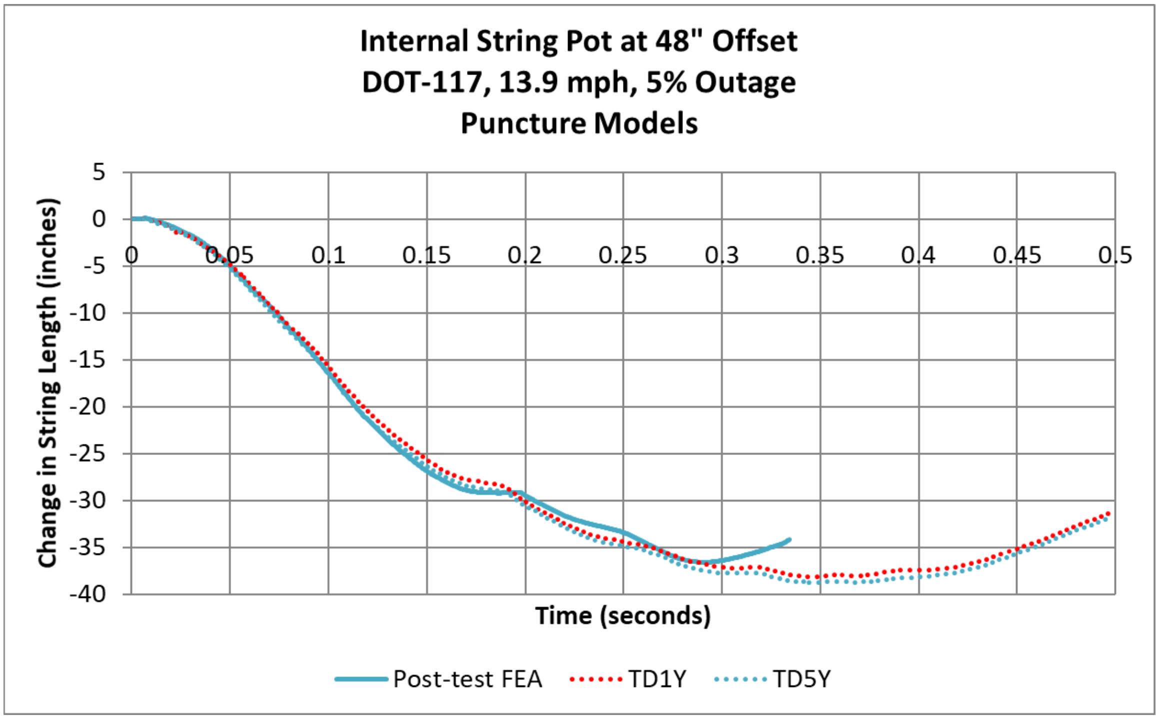

Figure C32. Internal String Potentiometers 48 Inches from Impact, Post-Test FEA with Rigid Ground and Test Data

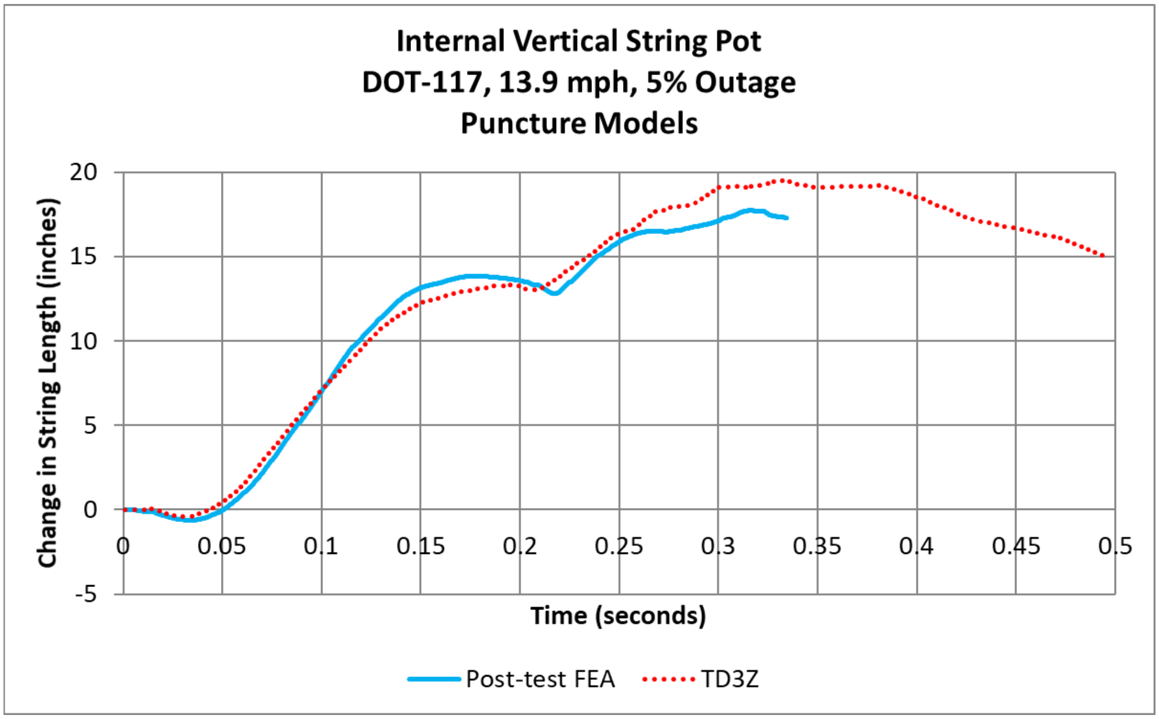

Figure C33. Internal Vertical String Potentiometer, Post-Test FEA with Rigid Ground and Test Data

C4 – Post-Test FEA and Test Results—13.9 mph (Deformable Ground)

Post-test FEA was run at the speed determined from the speed traps, 13.9 mph. The post-test models were also run using updated material behaviors for both the tank and for the water to better match the test conditions. Finally, the post-test models have a 1-inch gap between the jacket and the rigid wall, and a ground geometry that included the pit in the actual test setup. The results in this appendix are from the post-test model using a deformable representation of the ground slab geometry. The model described in this section also has a refined mesh in the impact zone, as well as a jacket geometry that better reflected the overlapping jacket sheets in the impact area. The changes implemented in the post-test model compared to the pre-test model are described in Section 5.5. Results derived from accelerometers or pressure transducers have been filtered using a CFC60 filter.

One hypothesis for the post-test model estimating puncture when the test did not experience puncture concerned the interaction of the bottom outlet protection with the concrete slab and pit at the test wall. While the model described in Appendix C3 included the geometry of the ground and pit, these surfaces were modeled as rigid bodies. The results of the test (see Section 4.2) showed that the tank car damaged the concrete slab and tore out several pieces of concrete. It was hypothesized that modeling a deformable ground slab would result in better agreement between test and model than treating the ground as a rigid body.

Because the properties of the concrete used in the slab are not known, a simplified model was developed based on available information. The material properties used to describe the concrete behavior are summarized in Appendix F6. The purpose of this modeling effort was not to accurately model the deformation behavior of the concrete slab, but to determine whether a deformable slab has a measurable effect on the forces at the impactor.

Previous models had used a membrane thickness of 0.05 inch, but this model experienced membrane distortion and premature termination with this thickness. The membrane thickness was increased to 0.1 inch. However, this model terminated due to distortion of the water mesh. Because the impactor was rebounding from the tank at approximately 2 mph at the time of termination, the model was not re-run to attempt a longer simulated impact.

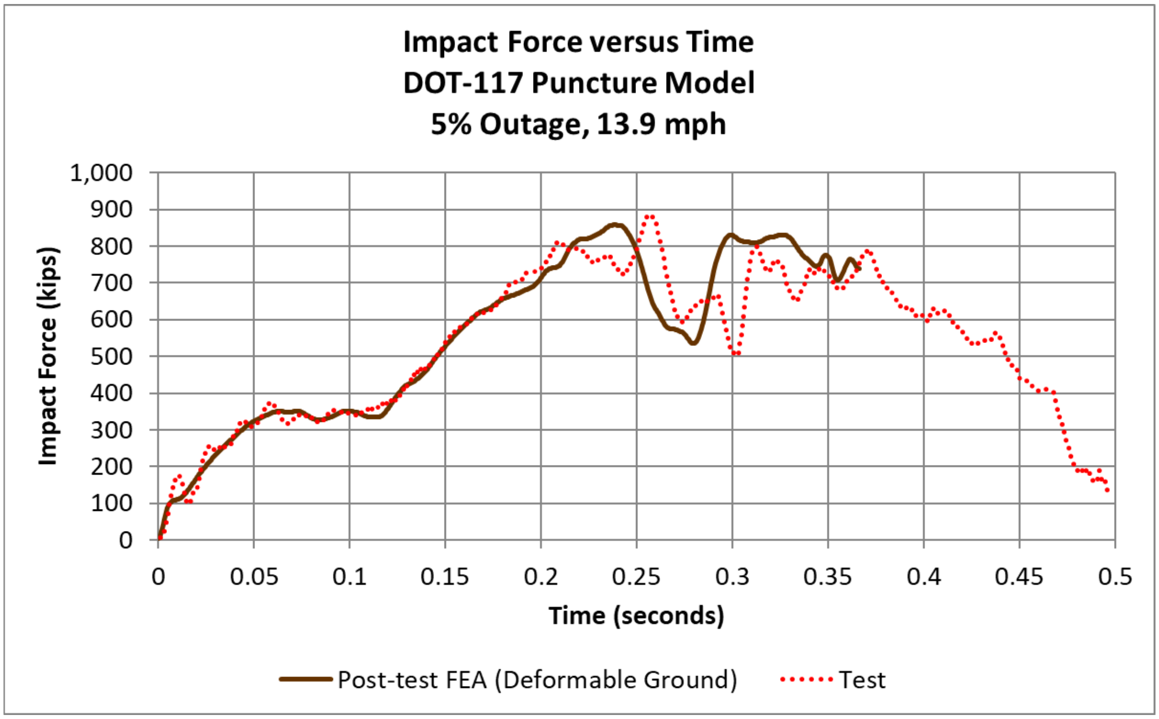

Figure C34. Impact Force Versus Time, Post-Test FEA with Deformable Ground and Test Data

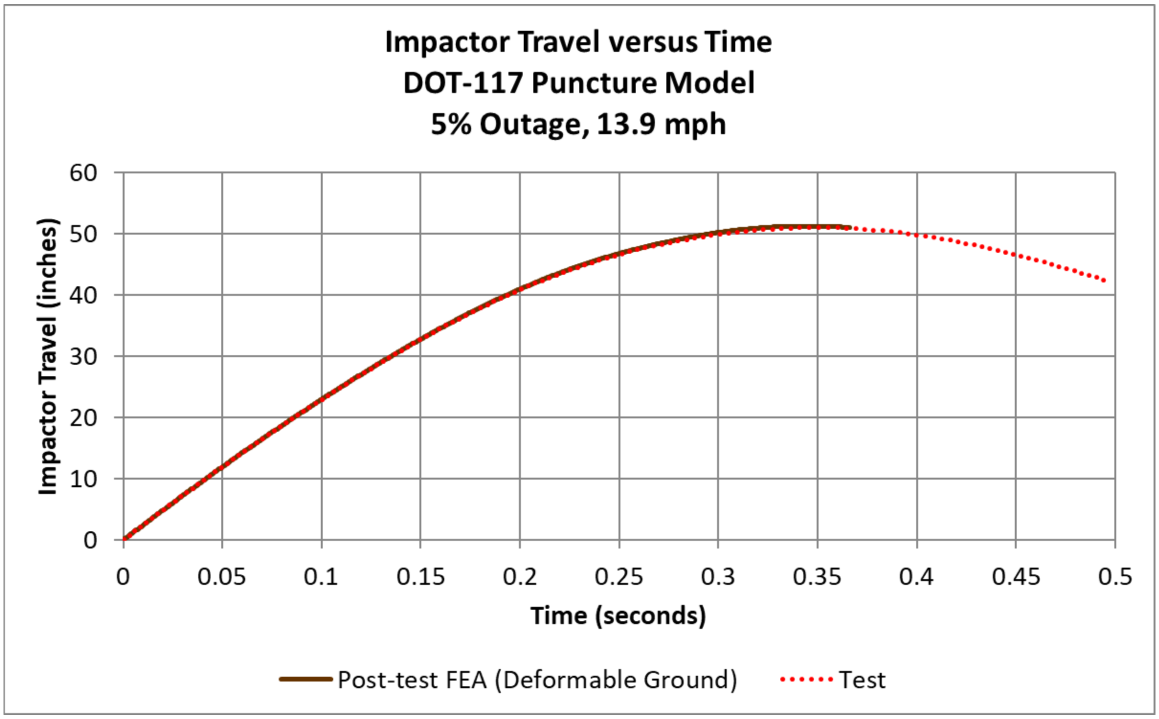

Figure C35. Impactor Travel Versus Time, Post-Test FEA with Deformable Ground and Test Data

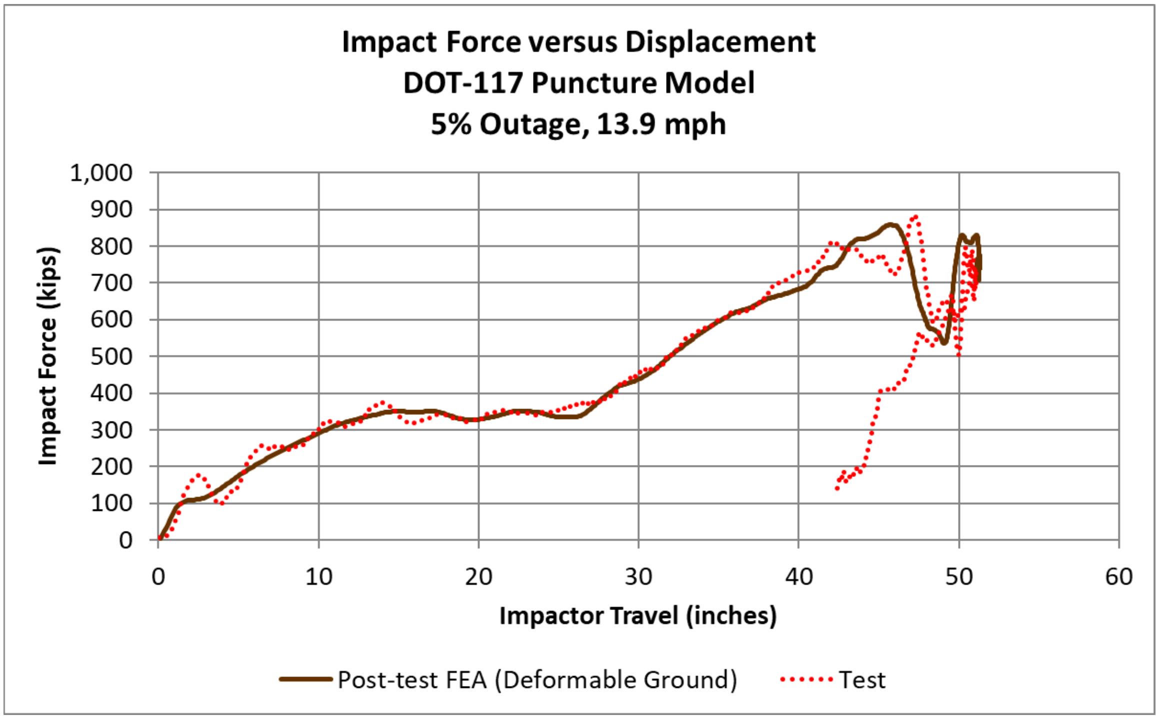

Figure C36. Impact Force Versus Impactor Travel, Post-Test FEA with Deformable Ground and Test Data

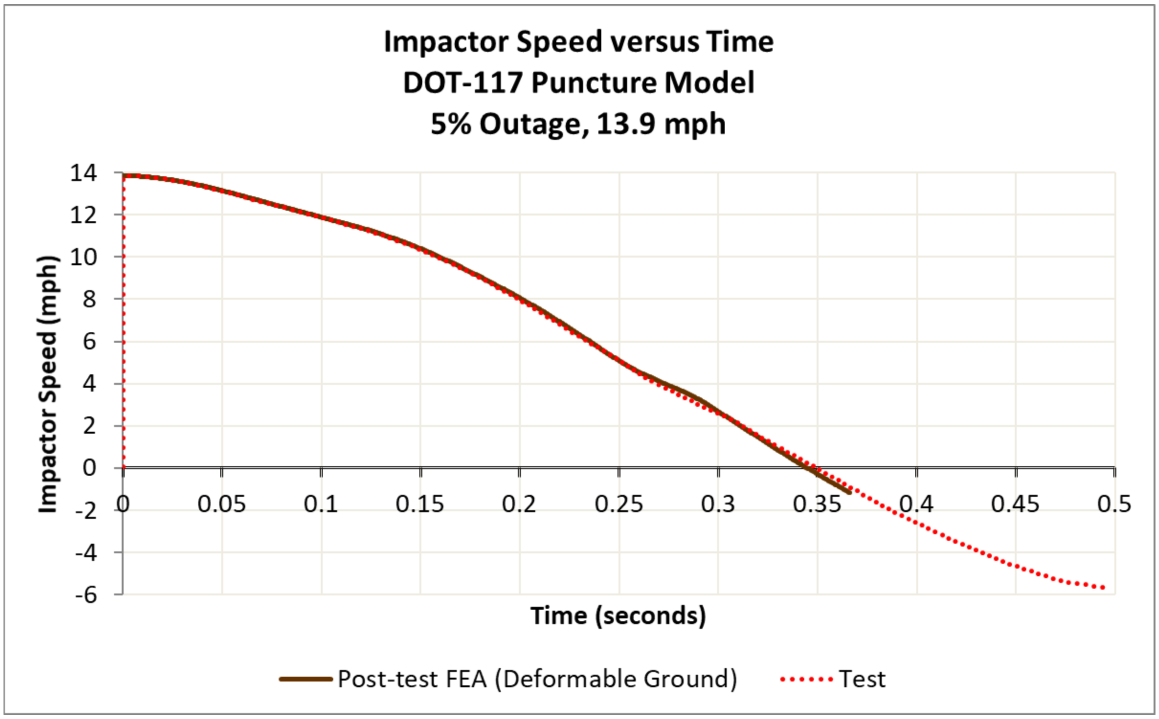

Figure C37. Impactor Speed Versus Time, Post-Test FEA with Deformable Ground and Test Data

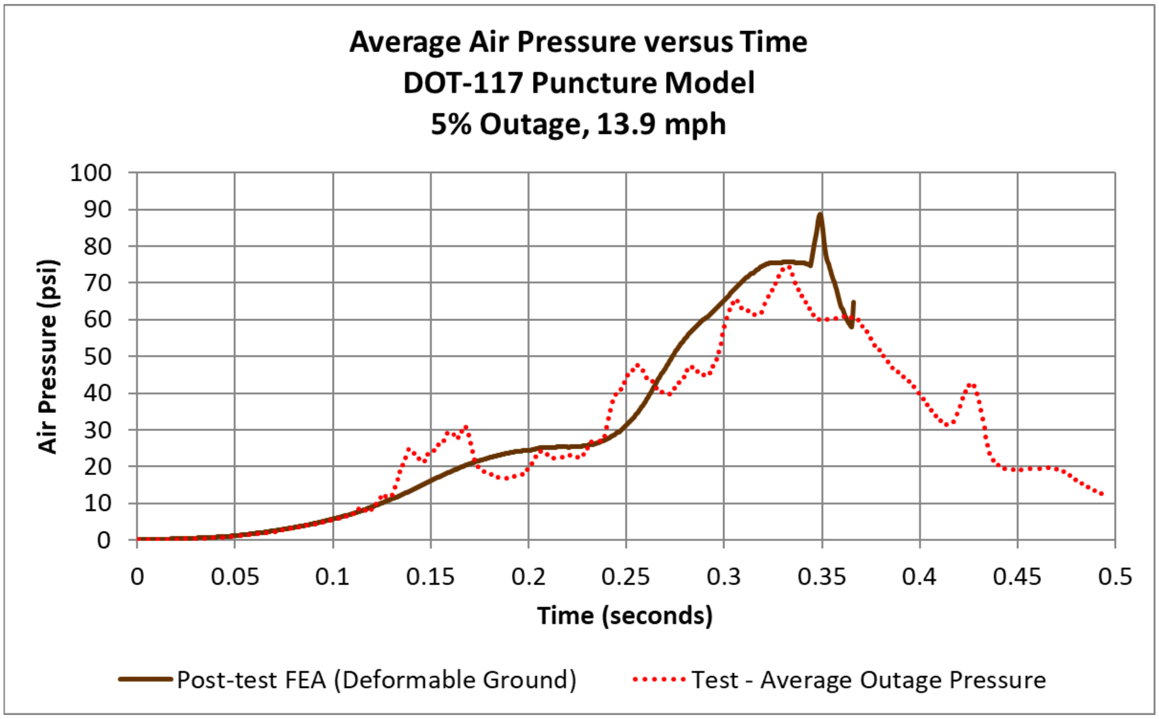

Figure C38. **Average Air Pressure Versus Time, Post-Test FEA with Deformable Ground and Test Data**

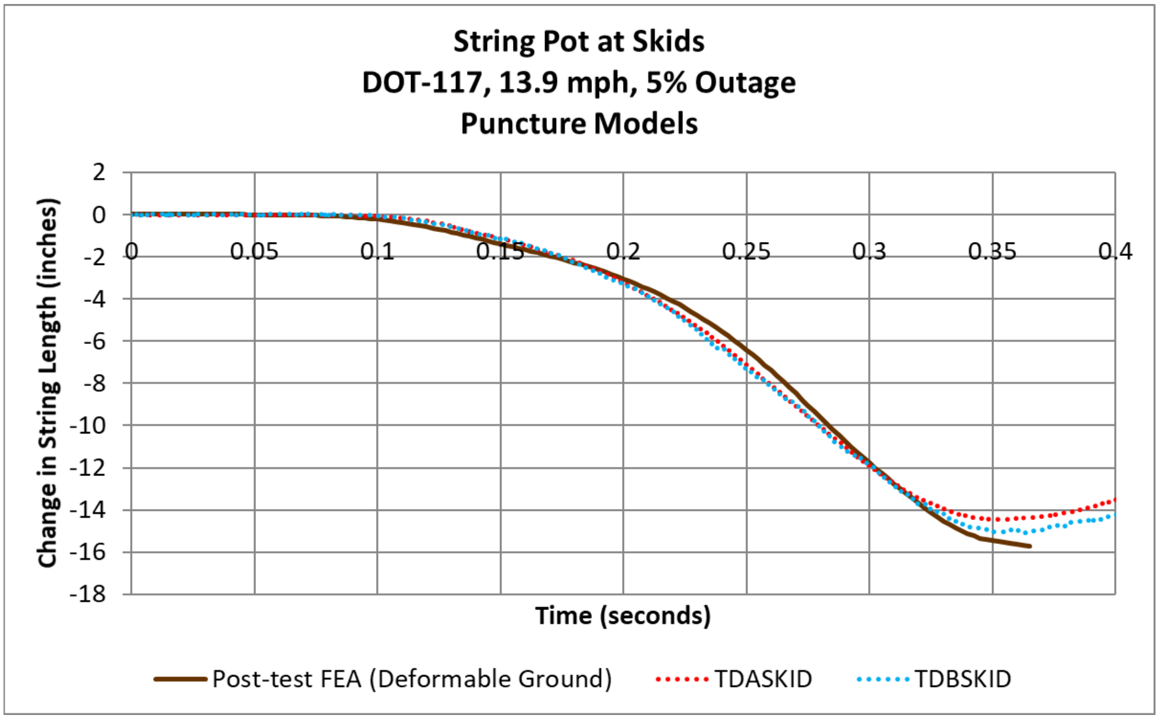

Figure C39. String Potentiometers at Skids, Post-Test FEA with Deformable Ground and Test Data

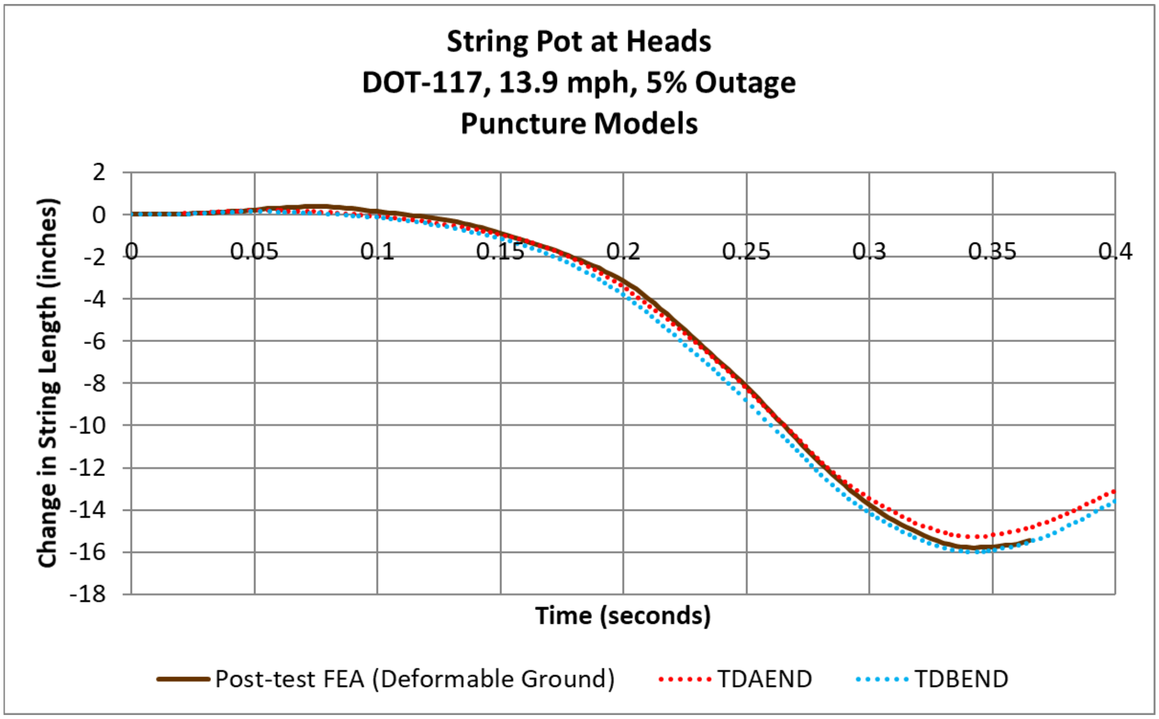

Figure C40. String Potentiometers at Heads, Post-Test FEA with Deformable Ground and Test Data

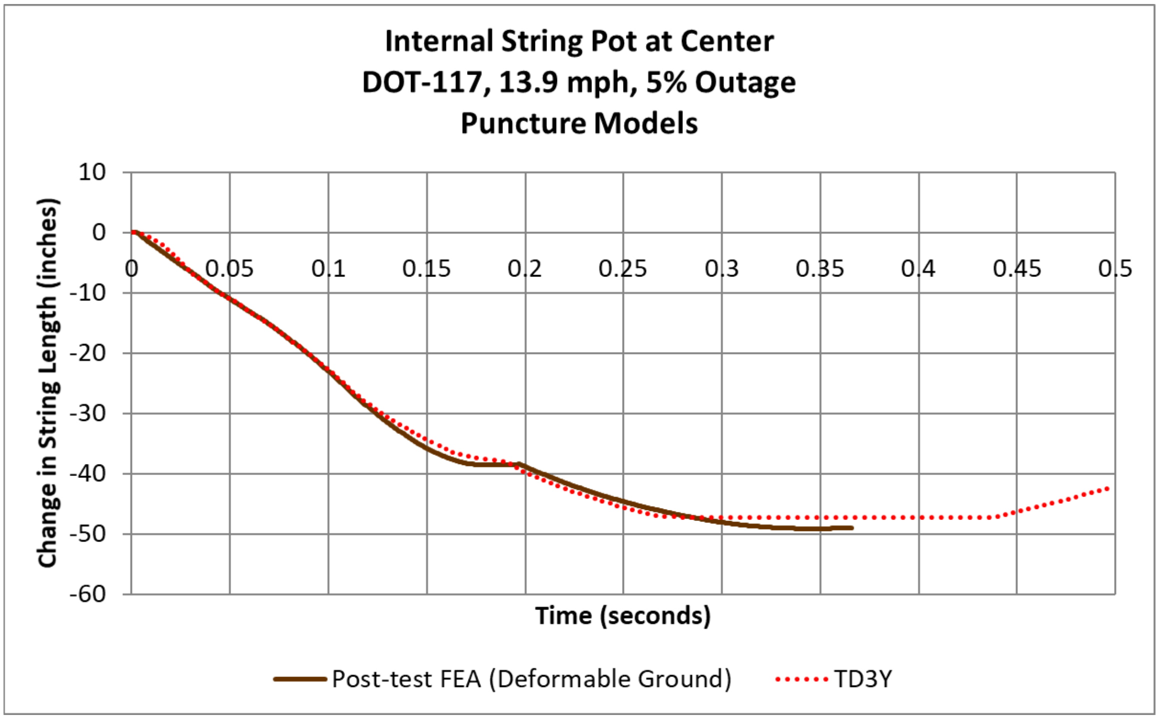

Figure C41. Internal String Potentiometer at Center of Tank, Post-Test FEA with Deformable Ground and Test Data

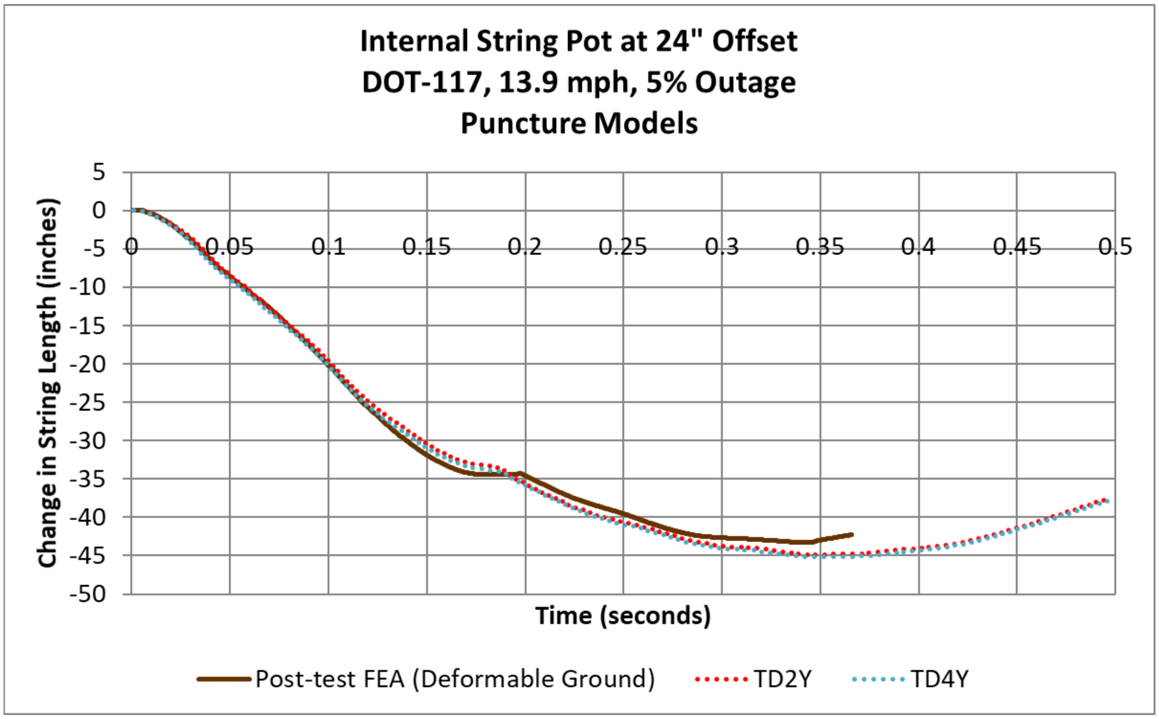

Figure C42. Internal String Potentiometers 24 Inches from Impact, Post-Test FEA with Deformable Ground and Test Data

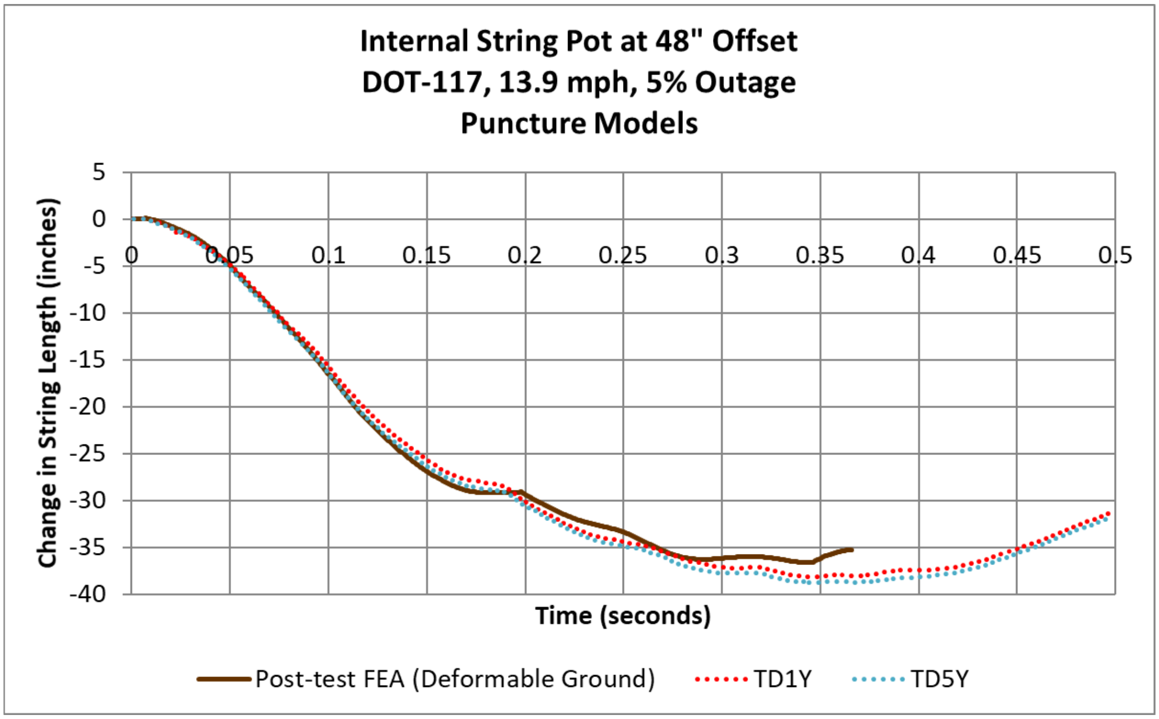

Figure C43. Internal String Potentiometers 48 Inches from Impact, Post-Test FEA with Deformable Ground and Test Data

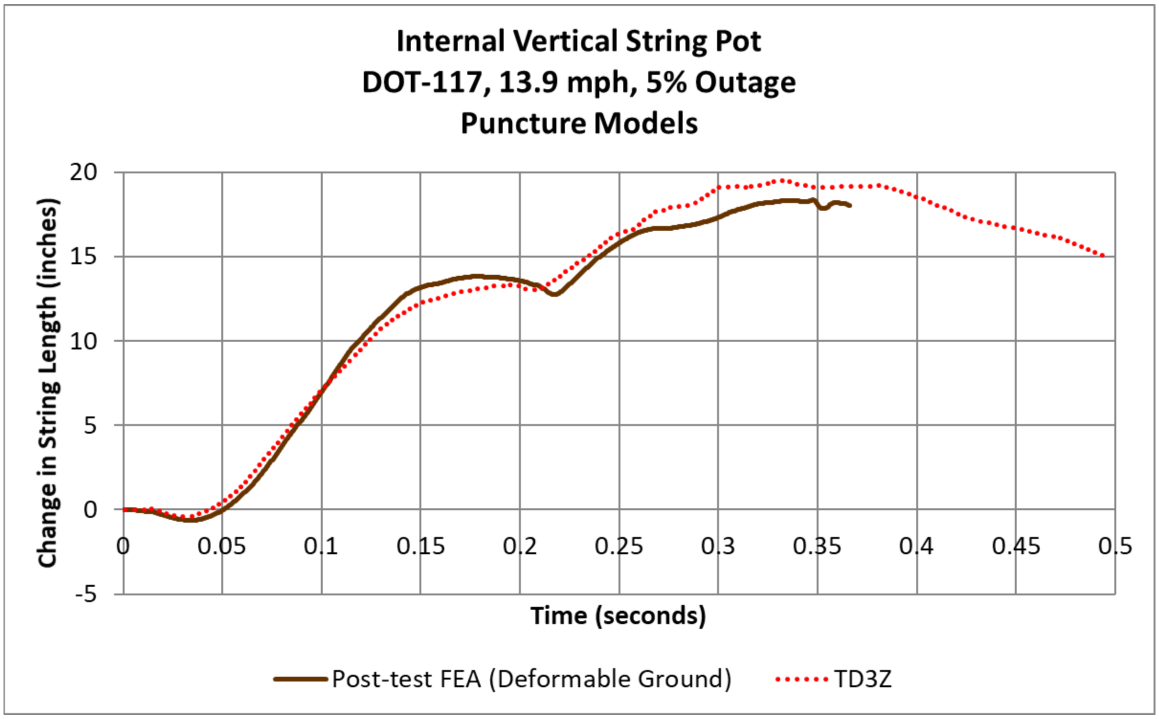

Figure C44. Internal Vertical String Potentiometer, Post-Test FEA with Deformable Ground and Test Data

Appendix D.
Geometry in Pre-Test and Post-Test Finite Element Models

A discussion of each of the parts making up the model is contained in the following paragraphs. Note that for parts that are bisected by the symmetry plane, the values reported in the following tables for mass and number of elements correspond to what was included in the FE model (i.e., half the mass of the physical body during the test).

Rigid parts were used when it was important to include a part for its inertia or for its interaction through contact, but where the deformation of the part could be neglected in the calculations. Four parts were modeled as rigid bodies. The remaining bodies were modeled as deformable bodies.

A summary of the element types used to mesh the model assembly is provided in Table D1.

Table D1. Summary of Element Types from [9]

Element Designation	Description
C3D8	8-node linear brick element for stress and displacement modeling
CONN3D2	Connector element between two nodes or ground and a node
DCOUP3D	Three-dimensional distributing coupling element
M3D3	3-node triangular membrane element
M3D4R	4-node quadrilateral membrane element (reduced integration)
MASS	Point mass
R3D3	3-dimensional, 3-node triangular facet rigid element
R3D4	3-dimensional, 4-node bilinear quadrilateral rigid element
RNODE3D	3-dimensional reference node
S3R	3-node triangular general-purpose shell, finite membrane strains (identical to element S3)
S4	4-node general-purpose shell, finite membrane strains
S4R	4-node general-purpose shell, reduced integration with hourglass control, finite membrane strains
SFM3D3	3-node triangular surface element
SFM3D4R	4-node quadrilateral surface element
SPRINGA	Axial spring between two nodes, whose line of action is the line joining the two nodes. This line of action may rotate in large-displacement analysis.

D1 – Rigid Impactor

The impactor was modeled as a rigid body in the DOT-117 FE models. The simulations used a 12-inch by 12-inch square impactor with 1-inch radii edges around the impact face. The geometry included the impact face and the tapered cone back to the portion of the impactor where the impactor attached to the ram car. Because only the impactor itself was modeled and this model used one-half symmetry, half of the mass of the entire ram car was assigned to the reference node on the impactor. The impactor, both with and without mesh, is shown in Figure D1.

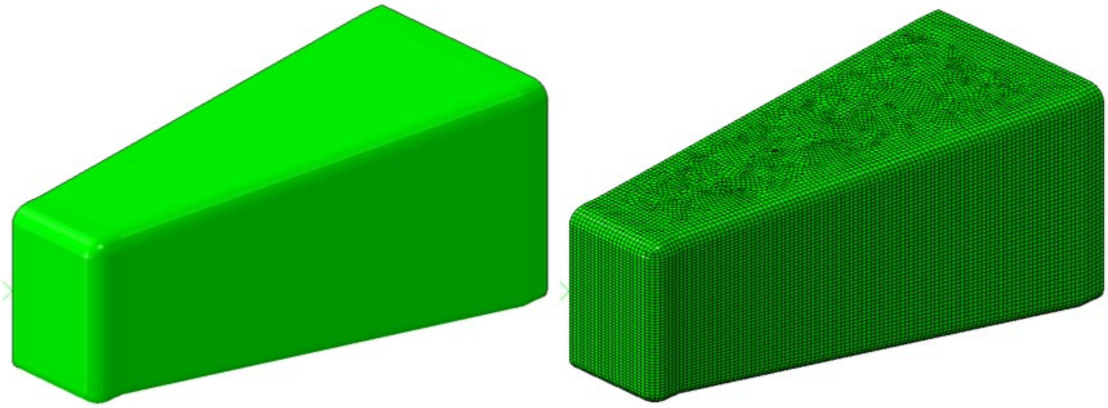

Figure D1. Impactor Geometry (left) and Mesh (right)

Table D2. Properties of Impactor in Pre-Test and Post-Test FE Models

Type of Part	Rigid
Number of Elements	R3D4: 14,623 R3D3: 198 RNODE3D: 5 MASS: 1
Part Weight	148,562.69 lbf

D2 – Rigid Wall

The rigid wall was modeled as a rigid body in the DOT-117 FE model. Because the wall was constrained against motion in any direction, no mass needed to be defined for this part. The wall's geometry and mesh are shown in Figure D2.

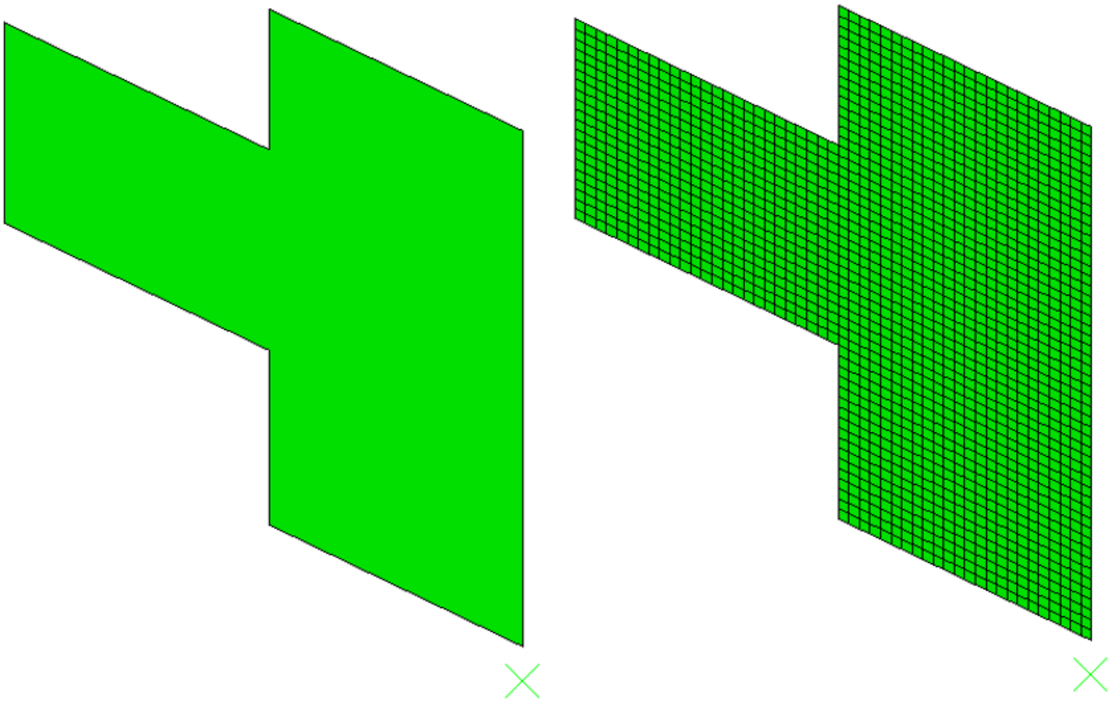

Figure D2. Rigid Wall Geometry (left) and Mesh (right)

Table D2. Properties of Rigid Wall in Pre-Test and Post-Test FE Models

Type of Part	Rigid
Number of Elements	R3D4: 1,724 RNODE3D: 4

D3 – Rigid Skid

The trucks of the tank car were removed prior to the test. The bolster of the car rested directly upon a set of skids, which themselves rested upon steel plates (see Figure 5). The skids were designed to inhibit rigid-body roll of the tank car following rebound from the rigid wall during a test. The skid geometry and mesh are shown in Figure D3. Note that since this part exists entirely to one side of the symmetry plane, the mass and geometric properties correspond to the actual mass and geometry of one full skid.

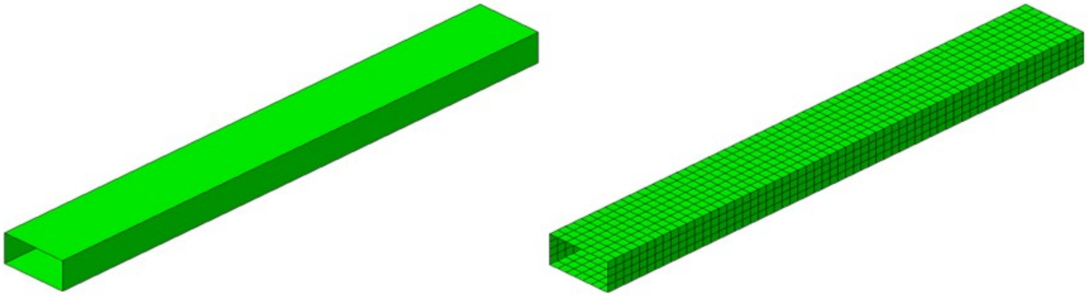

Figure D3. Skid Geometry (left) and Mesh (right)

Table D 1. Properties of Skid in Pre-Test and Post-Test FE Models

Type of Part	Rigid
Number of Elements	R3D4: 1,320 MASS: 2 RNODE3D: 2

The rigid skids used in the test weigh approximately 3,500 pounds each. This mass was included in the model through the use of a point mass at the rigid body reference node of each skid. Since the FE model is a simplified representation of the tank, the model does not include such geometric details as the bolsters, draft sills, draft gear, or couplers, as these features are not expected to play a significant role in the puncture response for an impact near the center of the shell. The masses of these components are included as a second point mass on the skid. For this car, the additional structure at each end of the car was assumed to have a weight of approximately 7,700 pounds. These additional point masses were added to both the pre-test and post-test models without adjustment.

Table D4. Point Masses Added to Skid Reference Point in Models

Component	Approximate Weight (lbf)	Added Mass in Model (lbf*s^2/in)
Skid	3,500	9.06
Draft Sill, Draft Gear, Coupler, Bolster, etc.	7,700	19.92

D4 – Jacket

The jacket was modeled entirely with deformable shell elements. The diameter of the jacket part was 121.3804 inches, representing the mid-plane of the actual jacket. The jacket featured a cutout at its 12 o'clock position to allow the manway to pass through, and a rectangular cutout at the 6 o'clock position to allow the bottom outlet protection to pass through. The majority of the jacket was meshed with quadrilateral, reduced integration (S4R) elements with a 3.5-inch mesh seed. A small number of triangular, reduced elements (S3R) were used to mesh the head. In the area of the jacket that would be contacted by the impactor, the mesh was made up of quadrilateral, full integration (S4) elements with a 0.04-inch mesh seed. The region of refined mesh was C-shaped in the FE model, as the jacket puncture was assumed to initiate around the perimeter of the impactor. Thus, the fine mesh intended to capture puncture only needed to extend around the region that would make contact with the perimeter of the impactor. A transition zone between the fine mesh and the coarse mesh also used full integration elements. Since only half the jacket is included in the FE model due to symmetry, the mass of the jacket in the FE model corresponds to half the mass of the physical jacket.

The post-test jacket model featured two changes from the pre-test jacket model. The post-test jacket featured an expanded refined mesh patch, to ensure that if puncture occurred in the model, the puncture occurred in the refined mesh and not in the transition zone. Post-test examination of the tested jacket revealed an overlap between two jacket sheets in the vicinity of the impacted zone on the tank (see Figure D 4). Thus, the post-test model featured a 3-inch wide band of material in the center of the impact zone that was modeled with twice the thickness of the rest of the jacket.

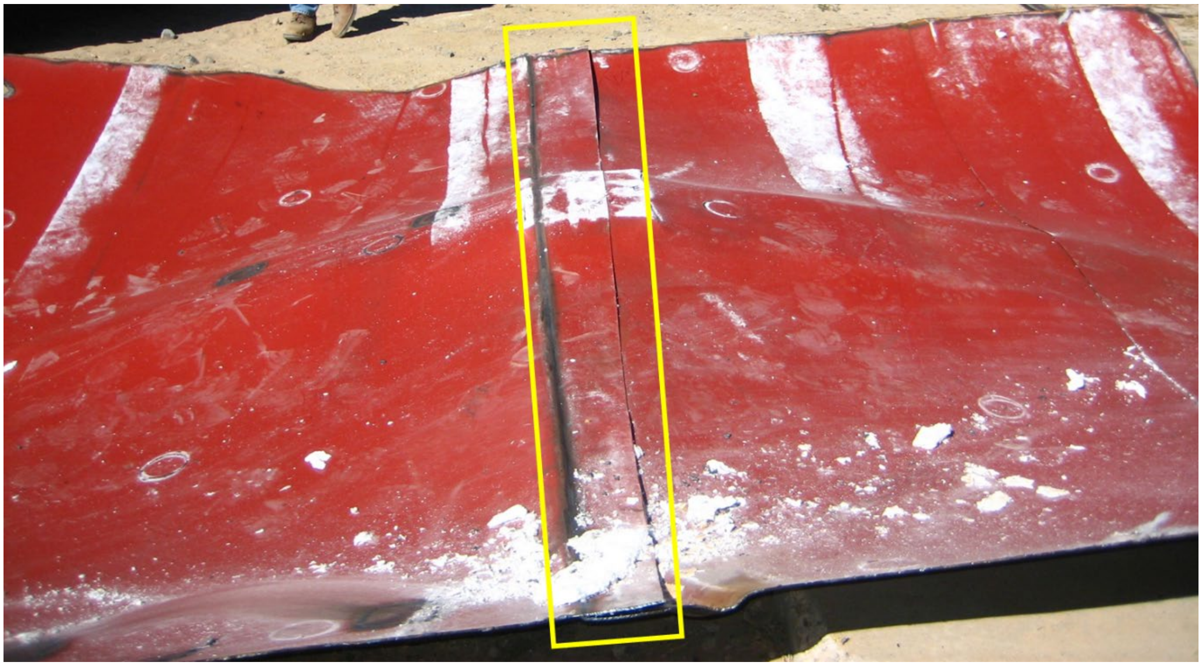

Figure D4. Region of Jacket Overlap in Tested Car

The jacket geometry and mesh for the pre-test FE model are shown in Figure D5, and the geometry and mesh for the post-test FE models are shown in Figure D6.

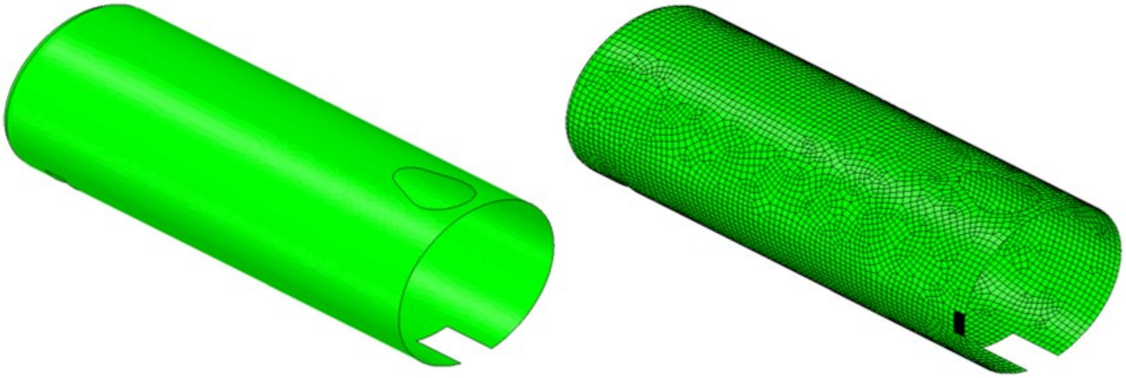

Figure D5. Jacket Geometry (left) and Mesh (right) in Pre-Test FE Model and Post-Test FE Model with Rigid Ground

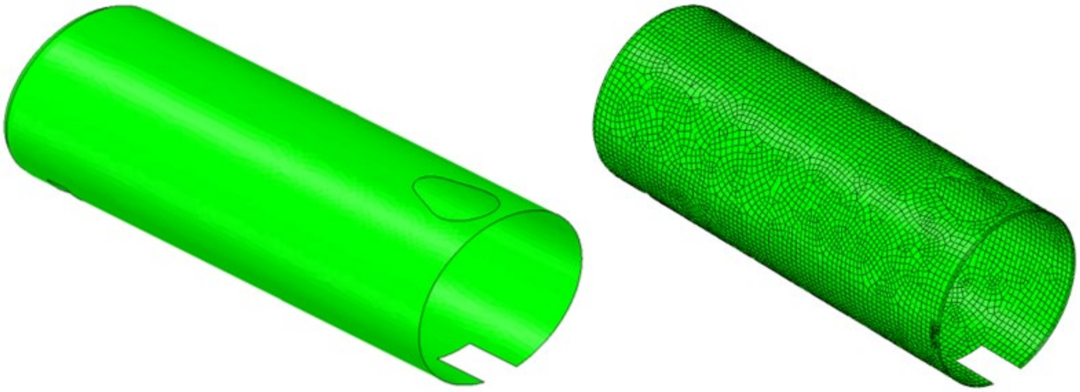

Figure D6. Jacket Geometry (left) and Mesh (right) in Post-Test FE Model with Deformable Ground

The transition between coarse S4R mesh and 0.04 inch S4 mesh in the impact zone is shown in Figure D7 for the pre-test FE model on the left, and the post-test FE model on the right. In this image, different colors denote different types of elements.

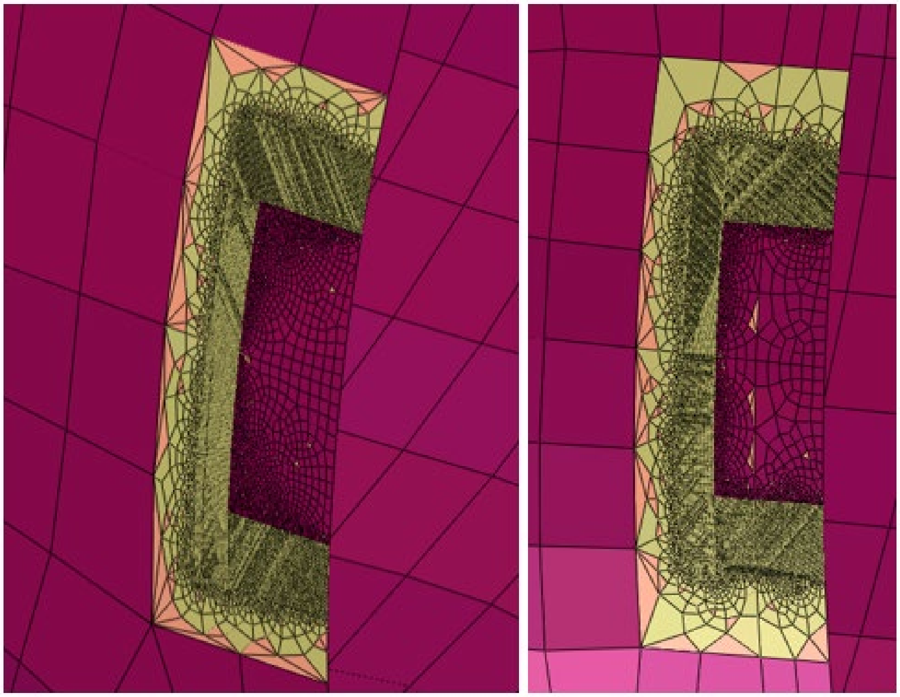

Figure D7. Jacket Mesh in Impact Zone for Pre-Test and Post-Test with Rigid Ground (left) and Post-Test with Deformable Ground (right) FE Models

The properties of the jacket from the pre- and post-test models are summarized in Table D5.

Table D5. Properties of Jacket in Pre- and Post-Test FE Models

	Pre-test FE Model	**Post-test FE Model (Rigid Ground)**	**Post-test FE Model (Deformable Ground)**
Type of Part	Deformable, Shell	Deformable, Shell	Deformable, Shell
Number of Elements	S4R: 11,457 S4: 29,068 S3R: 647	S4R: 11,457 S4: 29,068 S3R: 647	S4R: 10,519 S4: 34,052 S3R: 647
Shell Thickness	0.1196 inch (11 gauge)	0.1196 inch (11 gauge)	0.1196 inch (11 gauge), 0.2392 inch in overlap
Head Thickness	0.5 inch (integrated head shield)	0.5 inch (integrated head shield)	0.5 inch (integrated head shield)
Material(s)	A1011	A1011	A1011
Part Weight	5,857.4 lbf	5,857.4 lbf	5,894 lbf

D5 – Tank—Shell Elements

The commodity tank was modeled using two different techniques. In the impact zone, the tank was modeled using solid "brick" elements. This part is discussed in Appendix D6. Away from the impact zone, the tank was modeled using shell elements. The shell portion of the tank is described in this section. Because only half the tank is included in the FE model due to symmetry, the mass of the tank in the FE model corresponds to half the mass of the physical tank.

Figure D8 shows the shell portion of the tank. This part was globally meshed using quadrilateral reduced integration (S4R) elements with a 3.5-inch mesh seed. At the edges of the impact zone, the mesh was seeded such that each shell element edge would span exactly two solid elements on the impacted patch. The mesh in the region of attachment to the solid plate was meshed using quadrilateral fully integrated (S4) elements. A technique referred to as shell-to-solid coupling was used to attach the solid patch to the edges of the shell mesh on the tank. The shell part of the tank represents the midplane surface of the tank. The shell part has a midplane diameter of 119.437 inches in the model. The models include a small number of S3R elements.

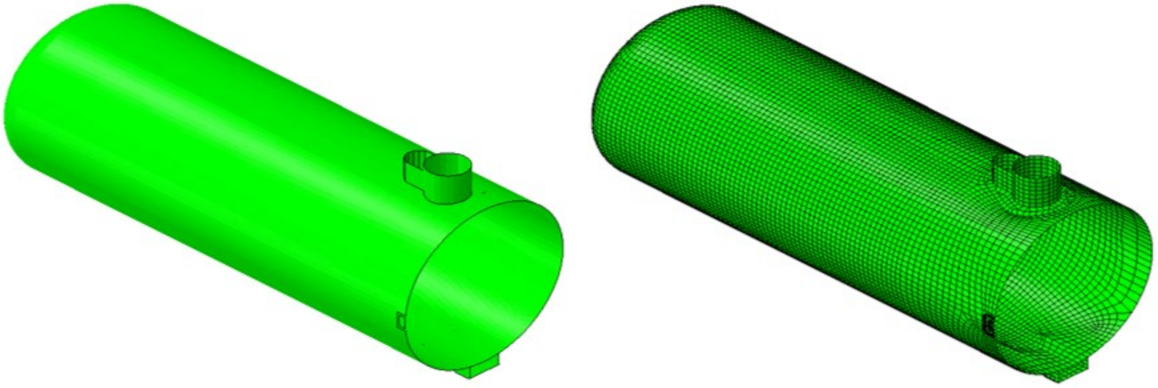

Figure D8. Shell Tank Geometry (left) and Mesh (right)

The pre- and post-test models featured similar geometries. In the post-test model, the solid tank patch was modified slightly to ensure that if puncture occurred, it did not initiate in any of the edges involved in the shell-to-solid coupling. The shell mesh was adjusted slightly to ensure a compatible mesh with the solid part. The shell tank parts in the pre-test and post-test models are summarized in Table D6.

Table D6. Properties of Tank Shell Mesh in FE Models

	Pre-test Model, Post-test Model with Rigid Ground	Post-test Model with Rigid Ground	Post-test Model with Deformable Ground
Type of Part	Deformable, Shell	Deformable, Shell	Deformable, Shell
Number of Elements	S4R: 10,936 S4: 921 S3R: 92	S4R: 10,936 S4: 921 S3R: 92	S4R: 10,962 S4: 877 S3R: 94
Shell Thickness	0.563 inch	0.563 inch	0.563 inch
Head Thickness	0.563 inch	0.563 inch	0.563 inch
Material(s)	Pre-test TC128	Actual TC128	Actual TC128
Part Weight	21,195.39 lbf	21,195.39 lbf	21,194.43 lbf

D6 – Tank – Solid Elements

The commodity tank was modeled using two different techniques. Away from the impact zone, the tank was modeled using shell elements. This part is discussed in Appendix D5. In the impact zone, the tank was modeled using solid brick elements. The solid portion of the tank is described in this section. Since only half the tank is included in the FE model due to symmetry, the mass of the solid portion of the tank in the FE model corresponds to half the mass of the corresponding portion of the physical tank.

Figure D9 shows the solid portion of the tank. The outer height of the part measures approximately 12.25 inches high by 6.125 inches wide in both the pre-test and post-test models. The inner cutout measures approximately 8.5 inches high by approximately 4.5 inches wide in the pre-test model, and 8 inches high by 4 inches wide in the post-test models. The part was meshed using a 0.081-inch mesh seed, resulting in 7 elements through the thickness of the tank shell. The solid portion of the tank was meshed using 8-noded hexahedral “brick” (C3D8) elements. The solid tank mesh was attached to the shell tank mesh along the outer and inner edges using shell-to-solid coupling. The elements along the inner and outer edges of the solid tank that were involved in the shell-to-solid coupling were given the same elastic and plastic material responses as the rest of the solid patch, but did not have damage initiation or failure behaviors defined. This was done to prevent elements involved in the shell-to-solid coupling from being removed from the model, as that could cause the coupling itself to fail.

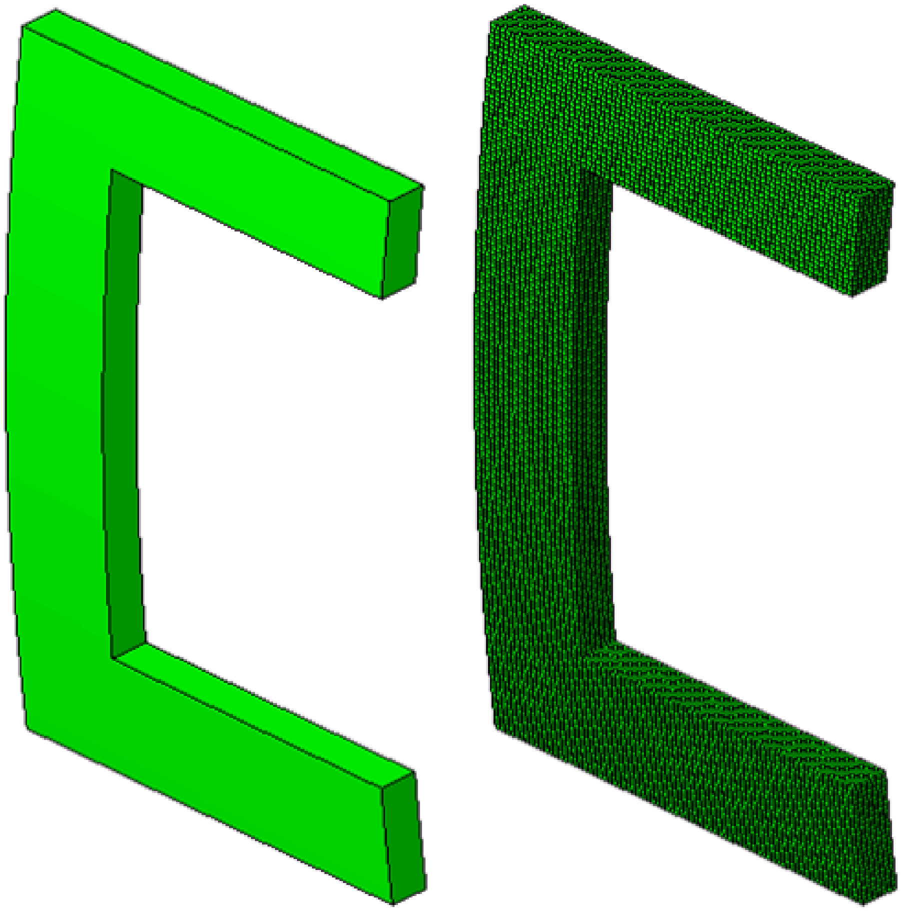

Figure D9. Tank Solid Geometry (left) and Mesh (right)

The properties of the solid tank part are summarized in Table D7 for the pre-test and post-test models.

Table D7. Properties of Tank Solid Mesh in FE Models

	Pre-test Model, Post-test Model with Rigid Ground	Post-test Model with Deformable Ground
Type of Part	Deformable, Solid	Deformable, Solid
Number of Elements	C3D8: 40,152	C3D8: 42,644
Shell Thickness	0.563 inches	0.563 inches
Material(s)	Pre-test TC128	Actual TC128
Part Weight	5.9 lbf	6.9 lbf

D7 – Membrane

The FE model of the DOT-117 tank car included a deformable membrane and surface part that represented the extents of the lading. The gas phase of the contents of the tank was modeled within the tank using a pneumatic cavity. The material properties used to describe the behavior of the air are described in Section 5.3.4, and the material properties used to describe the water are described in Section 5.3.3. In the model, the outage volume was filled with air.

The pneumatic cavity model requires a geometric surface to be defined within the model that defines the boundary of the cavity. Since the tank car model is a half-symmetric model, the cavity is not entirely enclosed within the membrane. In the case of a cavity bisected by a symmetry plane, it is necessary to place the cavity's internal reference point on the symmetry plane.

As discussed in Appendix D5, the shell geometry of the tank represents the mid-plane geometry of the tank. If this geometry were used to define the outer surfaces of the pneumatic cavity, the cavity volume would be too large, since the volume enclosed was based on the mid-plane surface and not on the inner surface of the tank. The membrane part was defined to correspond to the inner surface of the tank's geometry.

The membrane part was meshed using surface elements for the portion of the part along the interior of the tank, and with membrane elements for the portion of the part that defined the interface between the water and the lading within the tank. Surface elements do not have a defined thickness or material behavior. Thus, these elements must be constrained to an element with these properties defined to prevent the surface elements from unconstrained distortion. The surface elements were attached to the mid-plane surface of the tank using a tied constraint. The geometry and mesh of the membrane part are shown in Figure D10.

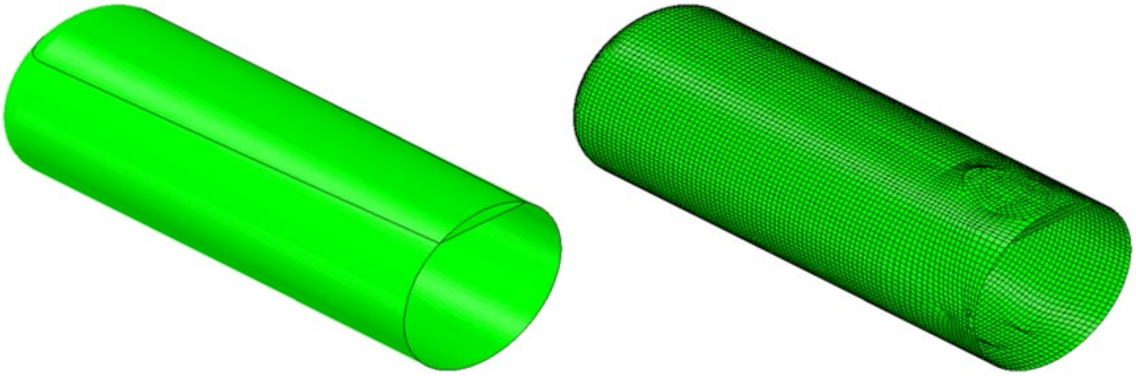

Figure D10. Membrane Geometry (left) and Mesh (right)

Since the portion of the membrane defined to divide the water and air boundary represents geometry that is not physically present within the tank, surface elements would not be suitable for this part. Instead, a membrane element representation was chosen to be as thin and flexible as practical within the model, without causing the model to terminate due to excessively distorted membrane elements. The membrane in the pre-test and post-test models with rigid ground had a thickness of 0.05 inch, whereas the membrane used in the post-test model with deformable ground used a thickness of 0.1 inch. This additional thickness was necessary to prevent membrane distortion from causing the analysis to terminate prematurely.

The particular DOT-117 tank car used in this test featured a sloped shell geometry to facilitate bottom unloading of its lading. This means that a liquid lading at rest will have a horizontal free surface, but the height from this free surface to the interior of the tank at 12 o'clock will increase as the position of interest moves further from the center of the tank. The zero-outage condition for this car is defined as the volume of lading that will fill the tank to the point that lading makes contact with the interior of the tank at the 12 o'clock position, dividing the remaining space within the car into two volumes no longer in communication with one another. The height of the horizontal plane (measured from the 12 o'clock position of the membrane at the symmetry plane, as shown in Figure D11) was adjusted to give the desired outage for this tank.

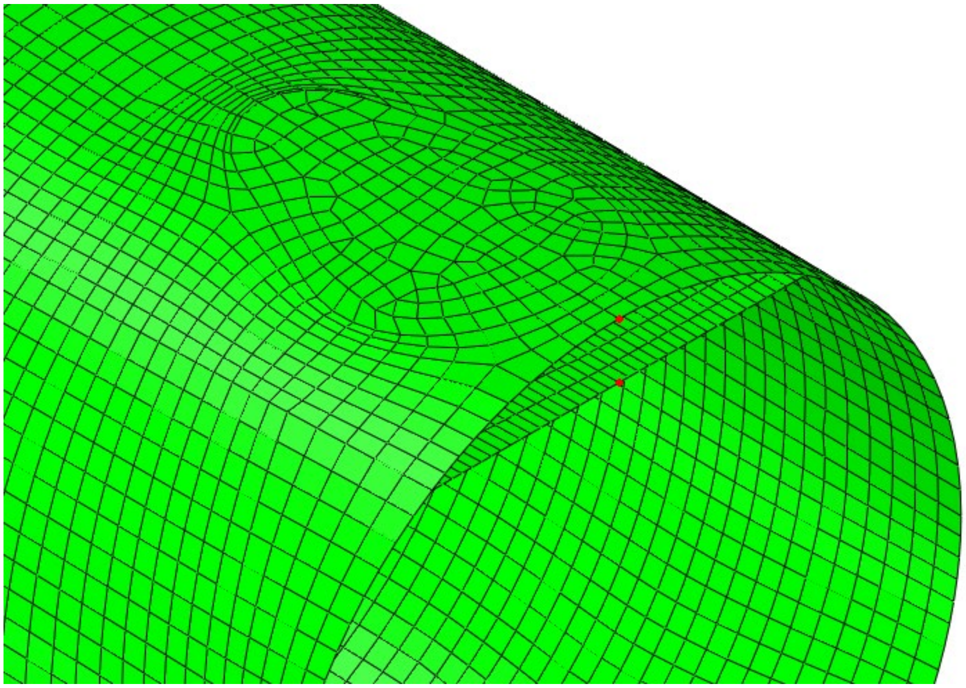

Figure D11. Reference Points for Outage Height within Membrane Part

The relationship between outage height and outage volume for this model is shown in Figure D12. This figure also includes a quadratic regression equation for the volume versus height relationship. For the desired outage of 5 percent, the model used an outage height of approximately 9.64 inches below the top of the membrane.

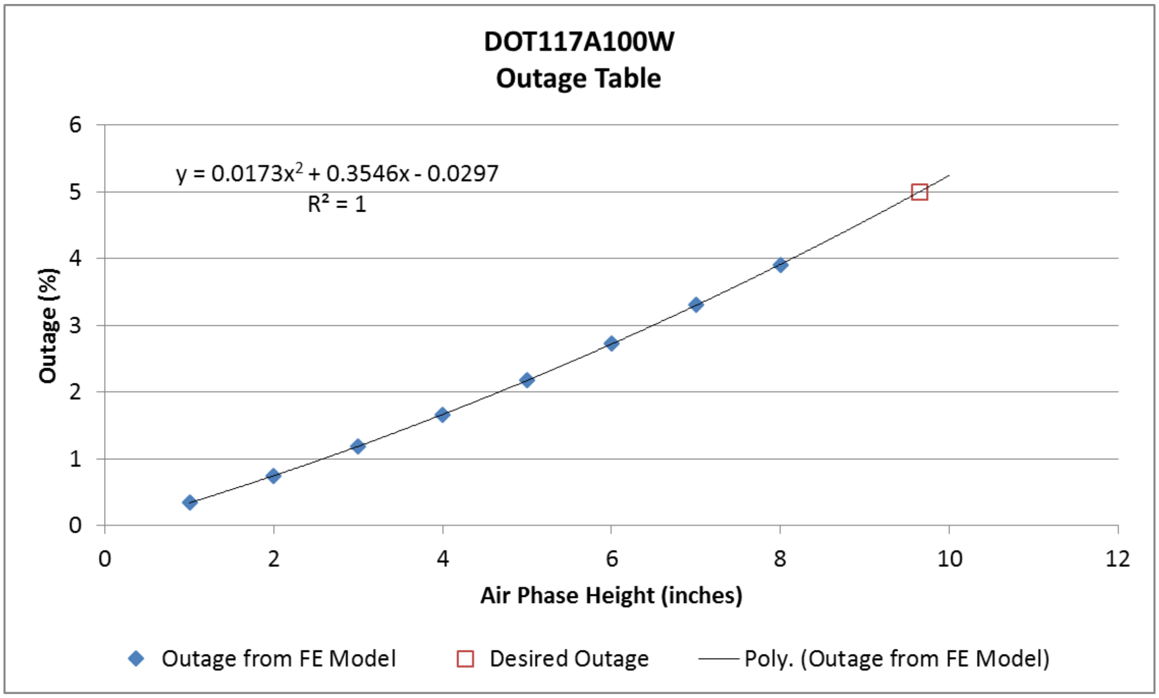

Figure D12. Outage Height versus Outage Volume for DOT-117 Model

The properties of the membrane part are summarized in Table D8 for the pre-test and post-test models.

Table D8. Properties of Membrane Mesh in FE Model

	Pre-test and Post-test Models
Type of Part	Deformable, Surface and Membrane
Material(s)	Membrane
Number of Elements	SFM3D3: 59 SFM3D4R: 10,935 M3D4R: 3,333
Part Weight	325.37 lbf

D8 – Ground

The rigid ground geometry was adjusted between the pre-test and post-test models to better approximate the test setup. The pre-test FE modeling used a rigid plane to represent the concrete slab. However, based on the actual test setup (discussed in Section 4.1), it was apparent that the bottom outlet protective housing would likely enter a cutout in the concrete slab with sufficient deformation of the tank. After the test, damage to the concrete pit confirmed that the housing had struck the edge of the pit. Thus, the post-test model featured the geometry of both the concrete slab and the pit. A second post-test model was created to examine the influence of modeling the ground as a deformable versus a rigid part.

For both the pre-test and post-test models, the rigid ground was modeled with all six degrees-of-freedom (DOF) fixed. For the post-test model using the deformable ground, the face of the ground on the symmetry plane had a symmetry boundary condition applied, and the bottom surface of the ground had all three displacement DOF fixed.

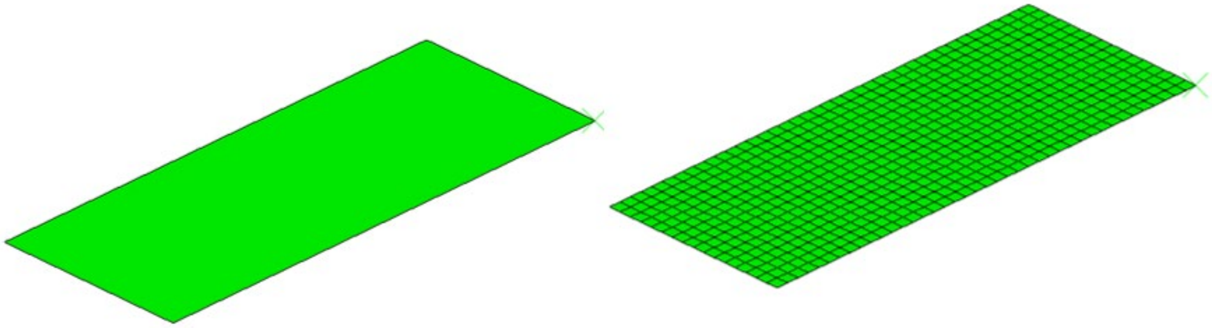

Figure D13. Pre-Test Rigid Ground Geometry (left) and Mesh (right)

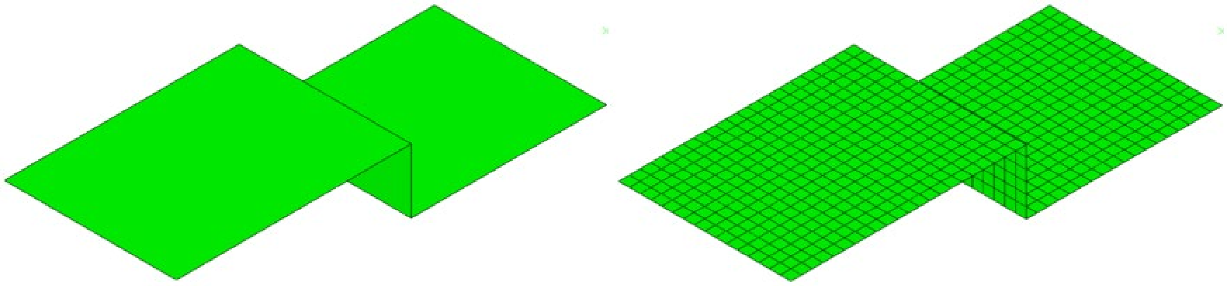

Figure D14. Post-Test Rigid Ground Geometry (left) and Mesh (right)

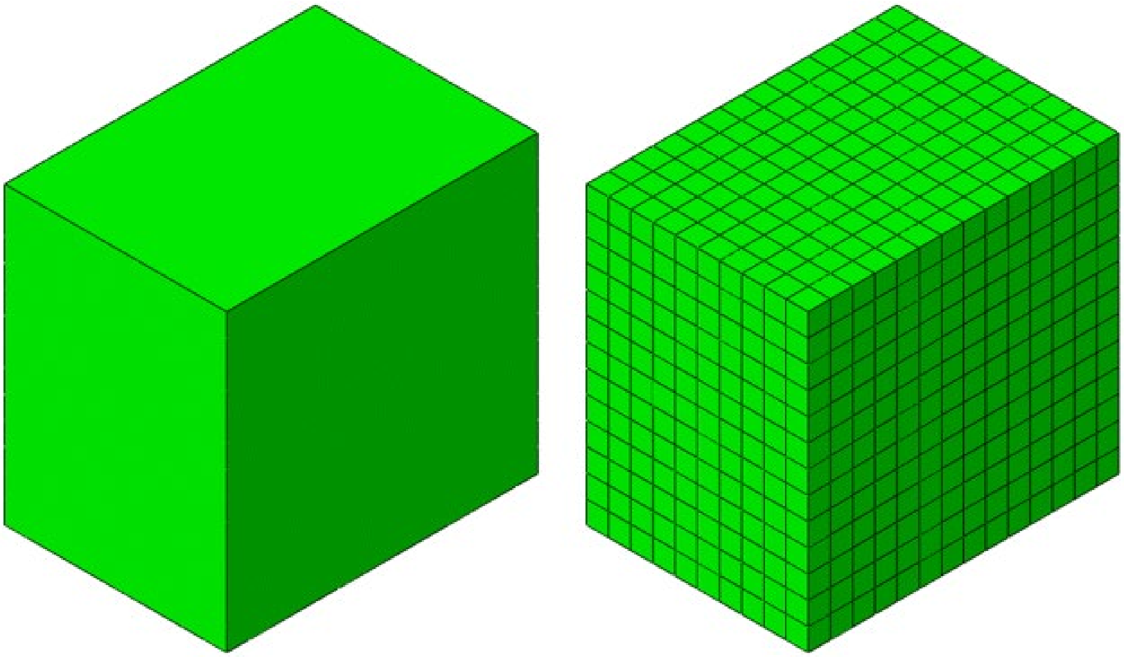

Figure D15. Post-Test Deformable Ground Geometry (left) and Mesh (right)

Table D9. Properties of Ground Meshes in FE Models

	Pre-test Model	Rigid Post-test Model	Deformable Post-test Model
Type of Part	Rigid Body	Rigid Body	Deformable
Number of Elements	R3D4: 640 RNODE3D: 3	R3D4: 736 RNODE3D: 4	C3D8: 1,820
Material(s)	-	-	Concrete
Part Weight	-	-	606.15 lb

D9 – Water

The water phase of the lading was modeled as a deformable Lagrangian part in both the pre-test and post-test FE models. The properties of the water material are defined in Section 5.3.3. The geometry of the water part and its mesh are shown in Figure D16.

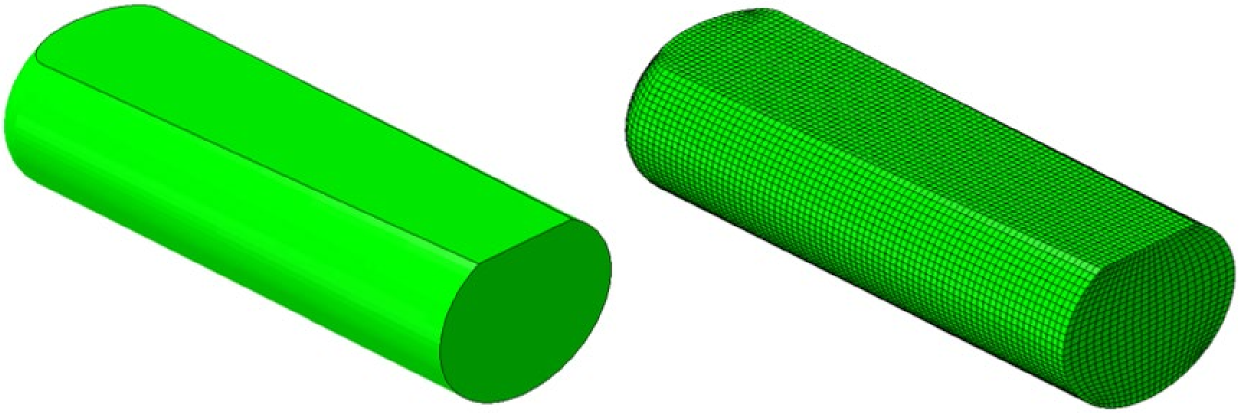

Figure D16. Water Geometry (left) and Mesh (right)

Table D10. Properties of Water Mesh in FE Model

	Pre-test and Post-test Models
Type of Part	Deformable
Material(s)	Water
Number of Elements	C3D8: 45,530
Part Weight	119,996.1 lbf

Appendix E. Modeling Techniques Common to Pre-test and Post-Test Finite Element Models

E1 – Symmetry Conditions

During the impact test, the test plan called for the impactor to strike the DOT-117 tank car at its longitudinal center. To facilitate computational efficiency, this permitted a half-symmetric model to be used to simulate the test. A symmetry boundary condition was applied to the tank (solid and shell element portions), the jacket, the water, and the internal surface dividing the two phases of the lading.

E2 – Rigid Impactor Boundary Conditions

The rigid impactor was constrained against all motion except for longitudinal displacement. The impactor was given an initial velocity corresponding to the simulated impact speed. The pre-test models were run at various speeds, and the post-test model was run at the measured test speed of 13.9 mph.

E3 – Rigid Wall Boundary Conditions

The rigid wall was constrained against motion in all degrees-of-freedom (DOF).

E4 – Ground Boundary Conditions

In the pre-test and post-test models using a rigid ground, the ground was constrained at all six DOF at its rigid body reference point.

In the post-test model using a deformable ground, two different boundary conditions were applied to the part. At the symmetry plane, a symmetry boundary condition was applied to the ground. At the bottom surface of the ground, all three displacement DOF were constrained. No boundary conditions were necessary on rotational DOF because the deformable ground was meshed using continuum elements, which only possess translational DOF. The boundary conditions on the deformable ground are shown in Figure E1.

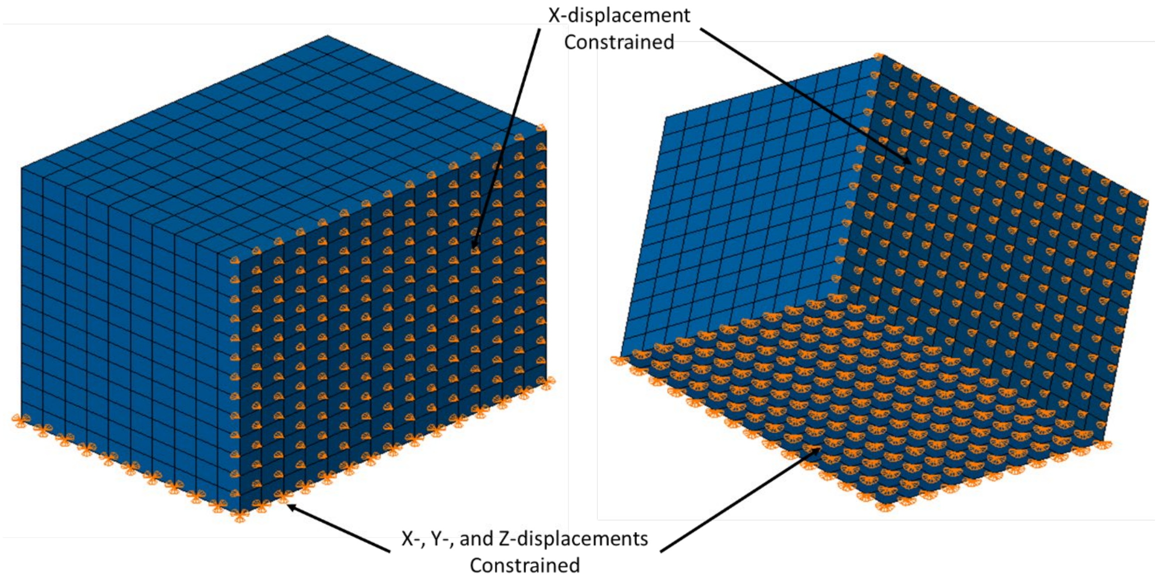

Figure E1. Boundary Conditions on Deformable Ground

E5 – Jacket-to-tank Tie

The jacket and tank were attached to one another using a tied constraint acting over the region of the bolster in the physical tank car. Standoffs between the tank and jacket were not included in this model, so this tied constraint represented the only connection between the tank and jacket. A "Tied Constraint" was defined between the arc representing the bolster on both the tank and the jacket parts. A position tolerance of 1 inch was used to account for the gap between the tank and jacket, where the thermal protection (not modeled) exists in the physical car.

E6 – Tank-to-surface Tie

The portion of the tank modeled using shell elements was tied to the surface representing the interior surface of the tank using a tied constraint. Although the meshes used on both parts were similar, because they were not identical, a position tolerance of 5 inches was used to minimize the likelihood that a surface node escaped being tied to the shell tank.

E7 – Tank-to-skid Coupling

The tank was connected to the rigid skid through a kinematic coupling. This coupling applied to all 6 DOF. The coupling was defined between the arc of nodes on the tank, which represent the bolster and the rigid body reference point of the skid, as shown in Figure E2.

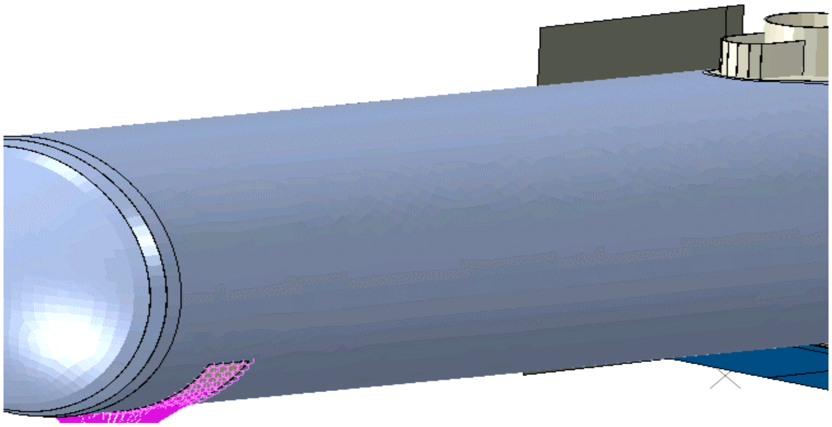

Figure E2. Tank-to-Skid Coupling

Additionally, a “Cartesian” type of connector was used to constrain the motion of the skid in both the vertical and the longitudinal (in the direction of impactor travel) directions. A nonlinear damper was defined between the skid and ground to constrain longitudinal motion. This damper defined the longitudinal resistance force as a function of skid speed, such that the skid had to overcome an initially high force when it was moving slowly. Once this initial peak was overcome, the resistance offered to skid motion diminished as the skid moved more quickly. This simplified model was intended to approximate the effect of static friction being overcome as the skid initially begins its motion, followed by a reduced resistance from kinetic friction. The longitudinal relationship used in the Cartesian connector is shown in Table E1 and plotted in Figure E3.

Table E1. Longitudinal Skid Behavior

Reaction Force (lbf)	Skid Velocity (in/s)
-100	-10
-38,000	-1
0	0
38,000	1
100	10

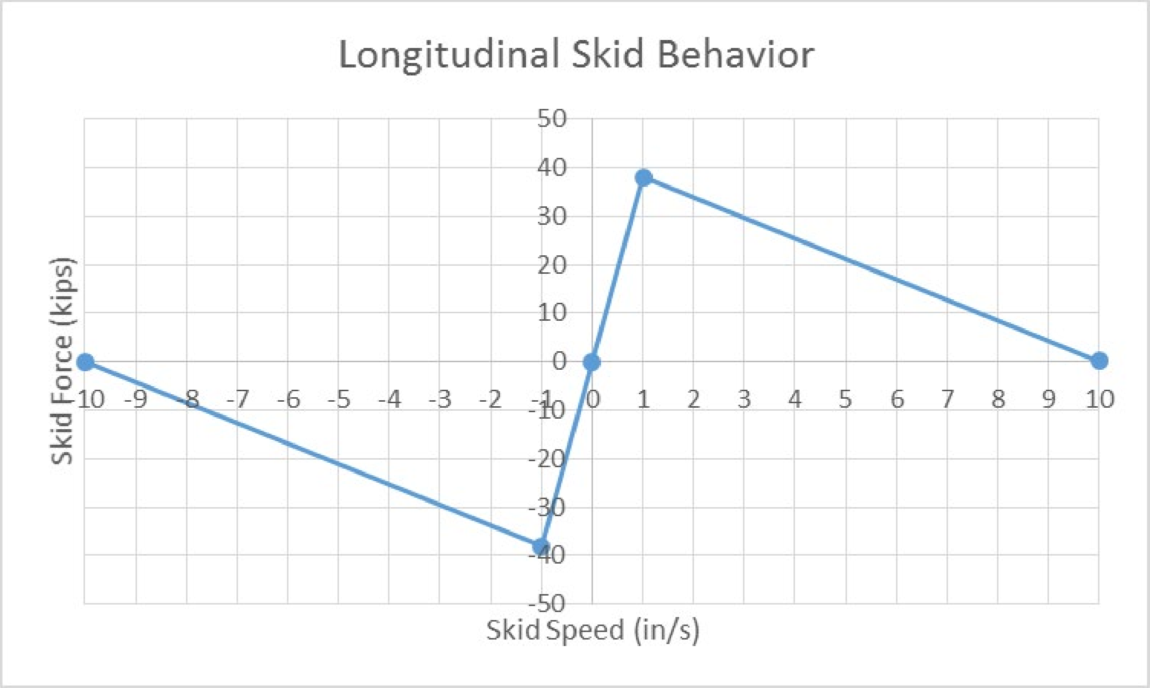

Figure E3. Longitudinal Skid Behavior

In the vertical direction, the skid used a "Stop" behavior assigned to a connector between skid and ground to limit its range of motion. In the vertical downward direction, the reference point of the skid was prevented from having any displacement. In the upward direction, a limit of 100 inches was used. This number is arbitrary, but was chosen to be larger than any anticipated vertical motion of the skid. These two vertical stops approximated the behavior of the skid on the ground during the physical test, where the skid was prevented from moving downward through contact with the ground but free to lift upward if sufficient lifting forces overcame the weight resting on it.

E8 – Shell-to-Solid Coupling

A shell-to-solid coupling constraint was used to attach the patch of solid elements in the vicinity of the impact zone to the rest of the shell-meshed tank. This type of constraint is necessary to ensure a smooth transition from solid elements, which possess only translational DOF, and shell elements, which possess translational and rotational DOF. The meshes on the solid part and the shell part were controlled such that every element on the shell edges involved in the coupling spanned two solid elements. Since the shell part corresponded to the mid-plane thickness of the tank, the shell part was aligned with the mid-plane of the solid patch. The interface between the solid patch and the shell tank is shown in Figure E4. The solid patch is shown in dark red, while the shell mesh of the tank is light.

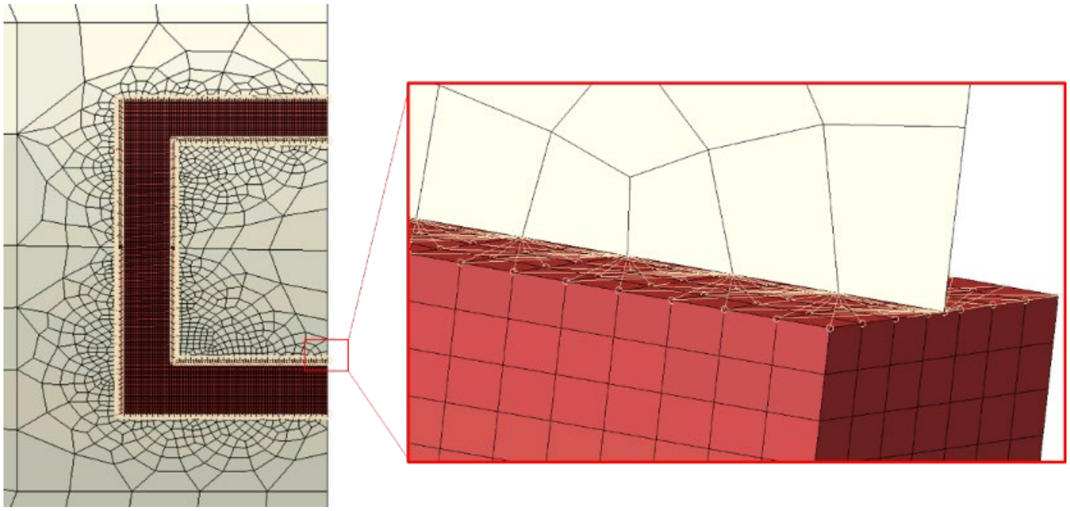

Figure E4. Shell-to-Solid Coupling Region

E9 – Internal Pressures and Temperatures

The lading within the tank was given an initial pressure of 12.3 psi [19], corresponding to atmospheric pressure at Pueblo, CO's, altitude of approximately 4,700 feet [20]. As the water and gas phases deformed, the pressure was free to change in response.

Using the fluid cavity approach of modeling the air phase required an initial temperature to be defined for the lading. Based on average historical climate data around the planned date of the DOT-117 test, an initial temperature of 70 °F was chosen for the models [21]. The initial temperature and pressure definitions were not adjusted between the pre-test and post-test models, as the actual test conditions were similar enough to what had been modeled. However, it should be noted that the pre-test model used water properties from a previous modeling effort. These properties had to be adjusted in the post-test model to correspond to properties at 70 °F.

E10 – Springs

Soft springs ($k=1 \times 10^{-6}$ lbf/inch) were placed within the model at locations corresponding to the string potentiometers installed within the tested tank (see Section 3.3). The use of springs allowed a direct comparison between the change-in-length of a string potentiometer during the test and the change-in-length of the corresponding spring in the FE model.

E11 – Pressure Relief Valve Modeling

The pressure relief valve (PRV) was approximated in the model as a fluid exchange between the pneumatic cavity representing the outage (see further description of outage modeling in Section 5.3.4) and ambient air, using a "Volume Rate Leakage" approach. The PRV in the test had a start-to-discharge pressure of 75 psi. The model used a prescribed pressure versus volumetric flow rate relationship to approximate the behavior of the PRV during the impact simulation.

The volumetric flow rate relationship used in the FE model was based on a PRV manufacturer's data sheet [22]. The flow rates were first converted from standard cubic feet per minute (SCFM) to actual cubic feet per minute to account for the test being conducted at an elevation of approximately 4,700 feet [23]. The flow rates were further converted into the unit system used by the model, so that the volumetric flow rates in the FE model were defined as actual cubic inches per second. The air pressure versus volumetric flow rate relationship input to the FE models is shown in Table E 2 and plotted in Figure E 5.

Table E2. Volumetric Flow Rate Relationship for PRV Modeling

Gage Pressure (psi)	Volumetric Flow Rate (in^3/s)
0	0
5	0
10	0
15	0
20	0
25	0
30	0
35	0
40	0
45	0
50	0
55	0
60	0
65	0
70	0
75	0
77.25	512,843
85	553,310
97.5	622,326

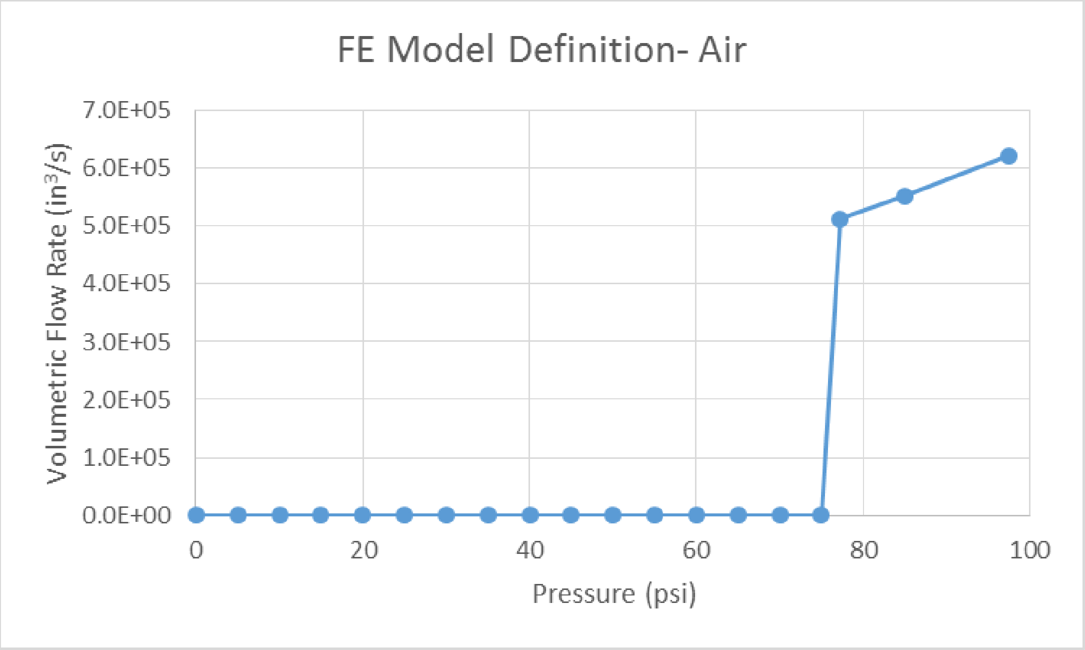

Figure E5. Volumetric Flow Rate Relationship for PRV Modeling

E12 – Mass Scaling

Variable mass scaling was used in both the coupon models and the puncture models. Because of the need for a refined mesh of solid elements in the impact zone, the puncture models feature a large number of very small elements. These two factors combine to create models with significant runtimes, even when executed on multiple-CPU workstations. Variable mass scaling was employed in the FE models to decrease the runtime without decreasing either the span or the resolution of the refined meshes. Variable mass scaling is a technique in which the user sets a target time increment for a set of elements within the model (up to and including all elements within the model) and the Abaqus solver increases the mass of each element to attempt to bring the minimum timestep up to the user-defined minimum. "Variable" refers to the software's ability to increase the mass of each element by a different amount, based on the material and geometry of each element. While mass scaling is an efficient way of reducing runtime without remeshing a model, care must be exercised when using this technique with highly-dynamic simulations. If an overly-aggressive mass scaling is applied, the amount of artificial mass added to the model in the refined mesh area can significantly affect both the overall dynamic response as well as the puncture behavior of the model.

The material coupon models used a mass scaling of 5 x 10^{-7} seconds. Mass scaling should have relatively little influence over the results of the coupon simulation, as the loading is chosen to be quasi-static.

The pre-test puncture FE models used a variable mass scaling of 1 x 10^{-6} seconds over the entire model. The mass scaling factors were recalculated at 20 intervals during the course of the simulation. This mass scaling factor is somewhat aggressive, and was chosen based on the need to perform the pre-test simulations in a timely manner, based on the planned test schedule.

The post-test puncture models used a variable mass scaling of 5 x 10^{-7} seconds over the entire model. The mass scaling factors were recalculated at 20 intervals during the simulation. A less aggressive mass scaling factor was chosen for the post-test simulations to bring the mass scaling factor down to the same factor as used in the material coupon models. Consequently, the post-test puncture models required more time to run than the pre-test models. However, the post-test model was run fewer times, as it was only necessary to run the puncture model at the measured test speed to establish model validity, whereas the pre-test puncture models were run at different speeds to estimate the impact response for different test conditions.

E13 – Contact

A general contact definition was used in this model. The global contact used frictionless contact, except for metal-on-metal contact. A coefficient of friction of 0.3 was defined between the impactor and jacket, between the jacket and tank, and between the rigid wall and jacket. A coefficient of 0.5 was used for contact involving the ground slab. Contact exclusions were defined between the jacket and itself, and between the shell tank and the solid tank patch.

Appendix F.
Material Behaviors in Finite Element Models

F1 – Introduction

Pre-test finite element (FE) models used TC128 (tank) and A1011 (jacket) material responses that were based on models developed during previous testing efforts [5, 6, 7]. A full description of the processes used to develop these material models can be found in these references.

Following the test, material coupons were cut from the tested DOT-117 and subjected to tensile coupon testing. The results of these material coupon tests were used to create a new TC128 material for post-test modeling. The processes used to create the pre-test and post-test material models are described in this appendix.

F2 – Simulation of Coupon Tests

For both the A1011 jacket material and the TC128 tank material, simulations of tensile coupon tests were used to develop the stress-strain responses, define a damage initiation envelope, and determine a reasonable damage progression once damage had been initiated. As the material responses developed using a coupon model were planned for implementation in the DOT-117 tank car model, modeling techniques for performing the coupon simulations were chosen to be deliberately similar to the modeling techniques planned for the DOT-117 tank car. The same solver (Abaqus/Explicit), element types, and mesh sizes were chosen for each coupon model and the corresponding material in the DOT-117 tank car model. This was done to attempt to minimize the uncertainty associated with developing a material response using one set of techniques, but using a different set of techniques to model puncture in the tank car impact simulation. If the tank car model was run using a different solver or different mesh size, it is expected that the material behaviors would need to be redeveloped using coupon simulations that used similar solvers and mesh density.

F3 – A1011

The A1011 material used in the jacket is based on the A1011 material response developed during a previous testing program. The appendix of Reference 6 contains a full description of the process used to develop the A1011 material [6], which is based on material data originally published in Reference 7. As the material behaviors for A1011 were previously developed for implementation in a 0.04-inch fully integrated shell element (S4) mesh, this same mesh formulation and element size were used in the DOT-117 model.

The plastic stress-strain behavior used in the DOT-117 model for the A1011 jacket is presented in Table F1 and shown in Figure F1. The damage initiation envelope used in the DOT-117 models is shown in Figure F2. The material used a 1,500 in-lbf/in^2 linear damage progression.

Table F1. A1011 True Stress and Plastic Strain Behavior

True Stress (psi)	Plastic Strain (in/in)
47,000	0
46,000	8.22E-04
46,200	1.20E-02
53,000	3.00E-02
58,000	6.00E-02
62,000	1.10E-01
68,000	1.95E-01
125,000	1.15E+00

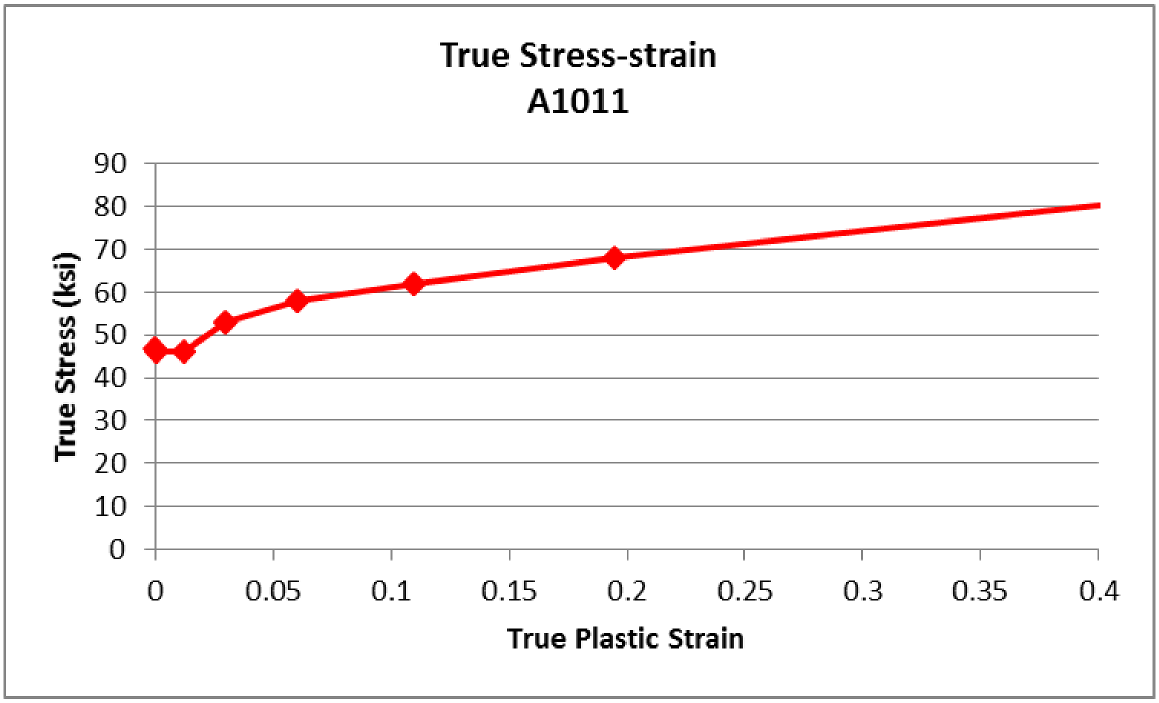

Figure F1. A1011 True Stress and Plastic Strain Behavior

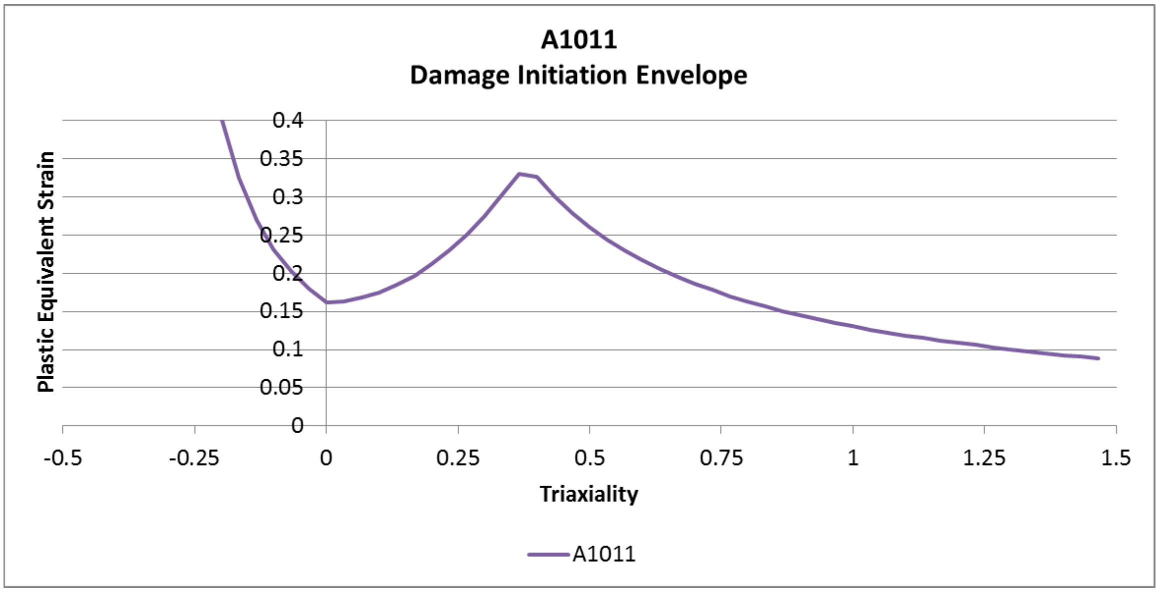

Figure F2. A1011 Damage Initiation Envelope

F4 – TC128

Two characterizations of TC128 were developed over the course of this project. Prior to the test, a characterization was developed based on mill data provided by the manufacturer of the DOT-117 for the plates used to construct the shells of several DOT-117 tank cars. After the test, a second characterization was developed based on the measured properties of the TC128 from the tested DOT-117. The TC128 coupon models are summarized in Table F2.

Table F2. TC128 Tensile Coupon Models

TC128 Model	Mesh and Elements	Mesh Size in Neck	Damage Initiation	Damage Progression
Pre-test	Bricks – C3D8I	0.081”	B-W Envelope from Reference 7	700 in-lbf/in^2 Exponential Progression
Actual Test Material	Bricks – C3D8	0.081”	Quick Calibration B-W Envelope based on coupon test and simulation results	1,500 in-lbf/in^2 Linear Progression

F.4.1 – Pre-Test Characterization

Prior to the test, the manufacturer of the DOT-117 tank car provided material data on the TC128 plates that were used to manufacture four cars, including the car to be tested. This data included the yield strength, ultimate strength, and elongation (in an 8-inch gage) for each of the plates used in the four cars. The average of each material behavior from the pool of plate data is provided in Table F3.

Table F3. Average Material Properties for Plates Used to Construct DOT-117 Shells

Average Yield Strength	62,062.5	psi
Average Ultimate Strength	88,854.17	psi
Average % Elongation in 8"	21.56667	%

While having the strength and elongation data from multiple plates across multiple cars provided some useful data, the manufacturer's data did not include the measured stress-strain responses for each plate. The piecewise true-stress true plastic strain behavior that is defined as an input to Abaqus needed to be approximated, based on the average material behaviors for the shell plates. Additionally, a reasonable damage initiation envelope needed to be estimated for the pre-test model.

One complication in comparing this data to TC128 behavior measured in previous tank cars tests concerns the use of an 8-inch gage for the DOT-117 plate material tensile tests. In previous material characterizations, a 2-inch gage cylindrical or rectangular coupon had been used. Because the DOT-117 plate material was tested using an 8-inch gage coupon, the results could not be directly compared to previous tests. As the gage length decreases, the effect of necking on the measured elongation increases, as the initial length of undeformed material is smaller. This is reflected in the TC128 material specification, which requires an elongation of 22 percent for 2-inch gage coupons, but 16 percent for 8-inch gage coupons [28].

In order to estimate the material response of the processed TC128 steel in the DOT-117 tank car, the plastic material behavior used in modeling a previously performed impact test (Test 2) was applied to an FE model of the 8-inch tensile coupons used to characterize the manufacturer's TC128 stock plate material [7]. The plastic true stress-strain data was then modified in an iterative process until the yield and ultimate strength output by the 8-inch tensile coupon FE model were in agreement with the measurements from the stock plate material. The plastic material behavior input that resulted in the best agreement is shown in Figure F3 and Table F4.

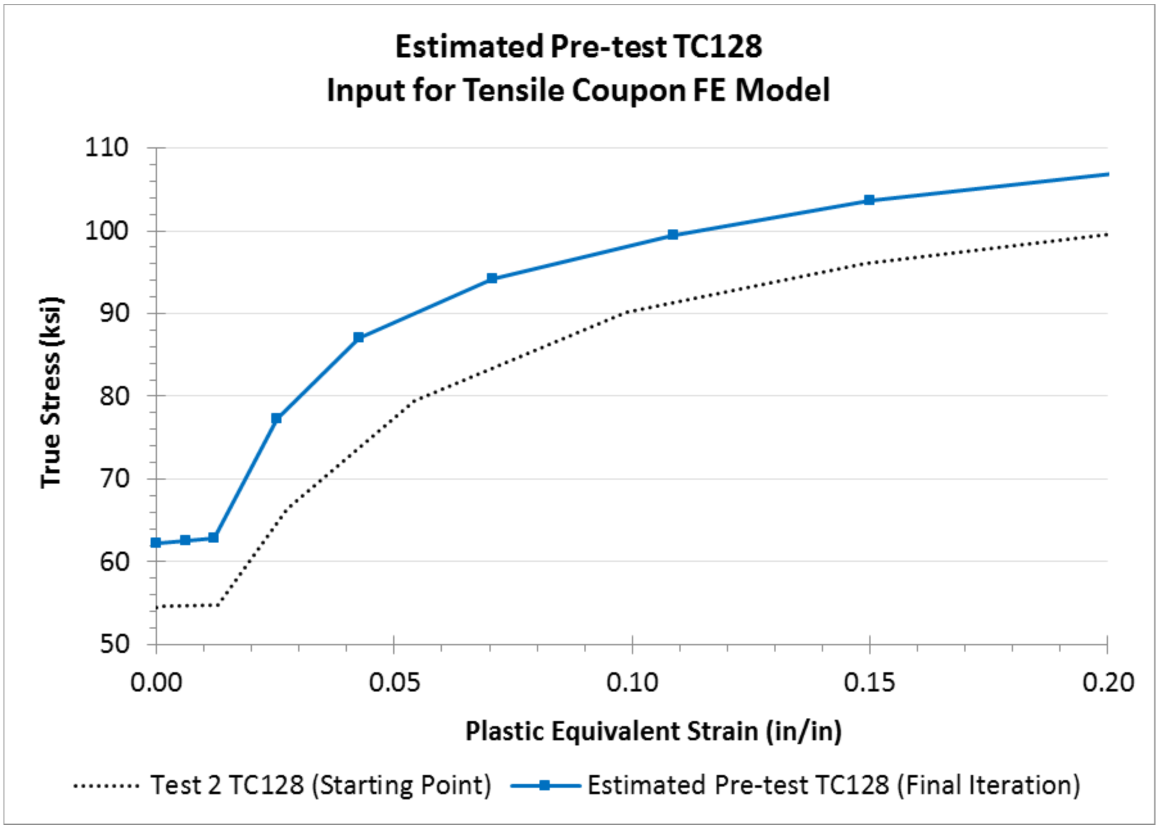

Figure F3. True Plastic Stress/Strain Responses for First and Last Iteration in Pre-Test Material Development

Table F4. True Stress/True Plastic Strain Inputs for Estimated Pre-Test TC128

True Stress (psi)	True Plastic Strain (in/in)
62,292.13125	0
62,592.13125	0.006080772
62,892.13125	0.012161544
77,281.86576	0.025467826
87,000.67102	0.042547672
94,211.12617	0.07063725
99,516.66667	0.108813683
103,700	0.15
167,500	1.15

The material data values that were provided by the manufacturer did not include the types of detailed measurements that are necessary to apply Lee and Wierzbicki’s “Quick Calibration” method of developing a ductile damage initiation model [18]. Because the material data indicated a ductility (21.56 percent) that was greatly in excess of the minimum required ductility (16 percent) for the 8-inch gage coupon, an existing ductile damage initiation model for a highly ductile sample of TC128 was sought. At the time of the pre-test modeling, the most ductile variety of TC128 with a developed damage initiation envelope was the material taken from Test 2 [7]. The damage initiation envelope shown in Figure F4 was used in the pre-test DOT-117 FE model [7]. An attempt was made to improve the agreement between the elongation output from the FE model and the measured elongation taken from the plate material by iteratively scaling the envelope, but no significant improvement in the agreement could be made because the output was already in good agreement. The lack of improvement after scaling resulted in Test 2 and the DOT-117 test using the same damage initiation envelope.

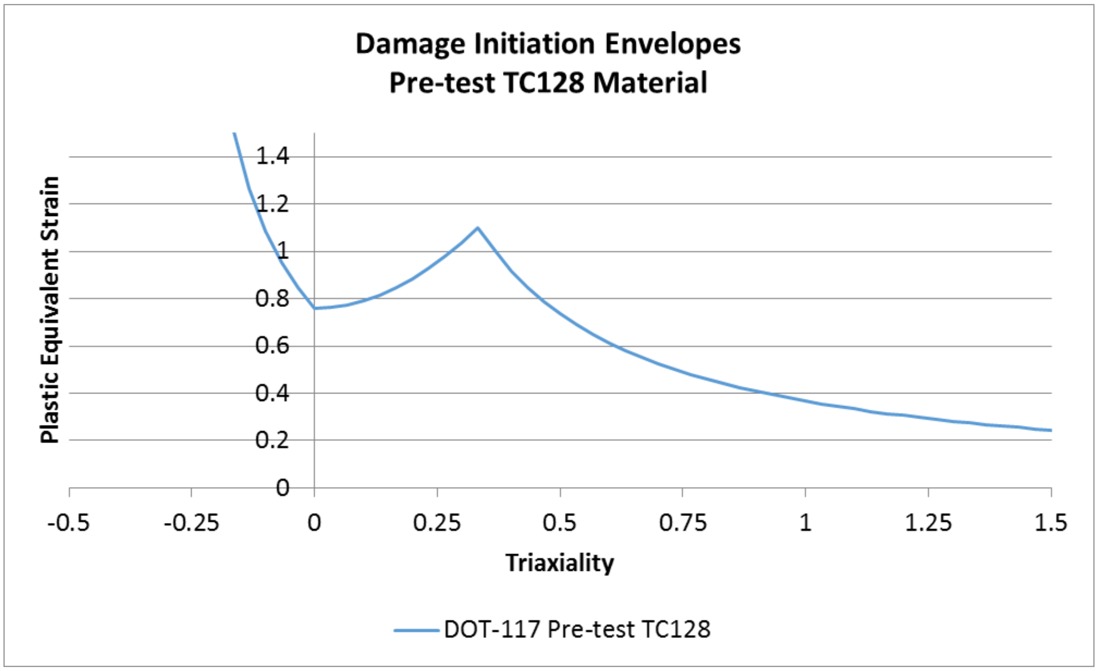

Figure F4. Damage Initiation Envelopes for Pre-Test TC128 Material

In addition to the plastic material properties and damage initiation properties described above, the pre-test tensile coupon FE model was assigned the material behavior parameters outlined in Table F5.

Table F5. Summary of Material Parameters for Pre-Test Tensile Coupon

Parameter	Value
Mass Density	7.35×10^{-4} lbf-s^2/inch
Modulus of Elasticity	3.26×10^7 psi
Poisson’s Ratio	0.3
Plasticity	Piecewise Linear (see Table 24)
Damage Initiation	B-W Envelope from Test 2 (see Figure F4)
Damage Progression	Exponential, 700 in-lbf/in^2

The pre-test tensile coupon FE model of the TC128 steel in the DOT-117 tank car was created with a mesh of incompatible mode 8-node brick elements (C3D8I) in the 8-inch gage section and reduced integration 8-node brick elements (C3D8R) in the remaining sections as shown in Figure F5. The coupon was meshed so that there were seven elements through the thickness, which corresponded to a 0.081-inch mesh size. A YZ-symmetry plane was applied at half the width. A linear displacement boundary condition was applied in the positive Y direction to the top surface at a rate of 4.5 in/s, while the bottom surface was fixed. The Abaqus/Explicit solver was used to run the model for 0.5 second while a quasi-static state was maintained. A linear spring with a negligible stiffness (1 x 10^{-6} lbf/inch) was attached across the 8-inch gage section in the Y direction to act as an extensometer measuring nominal strain. The reaction force in the Y direction was calculated at the lower boundary condition of the coupon model and divided by the initial gage cross-sectional area to calculate nominal stress.

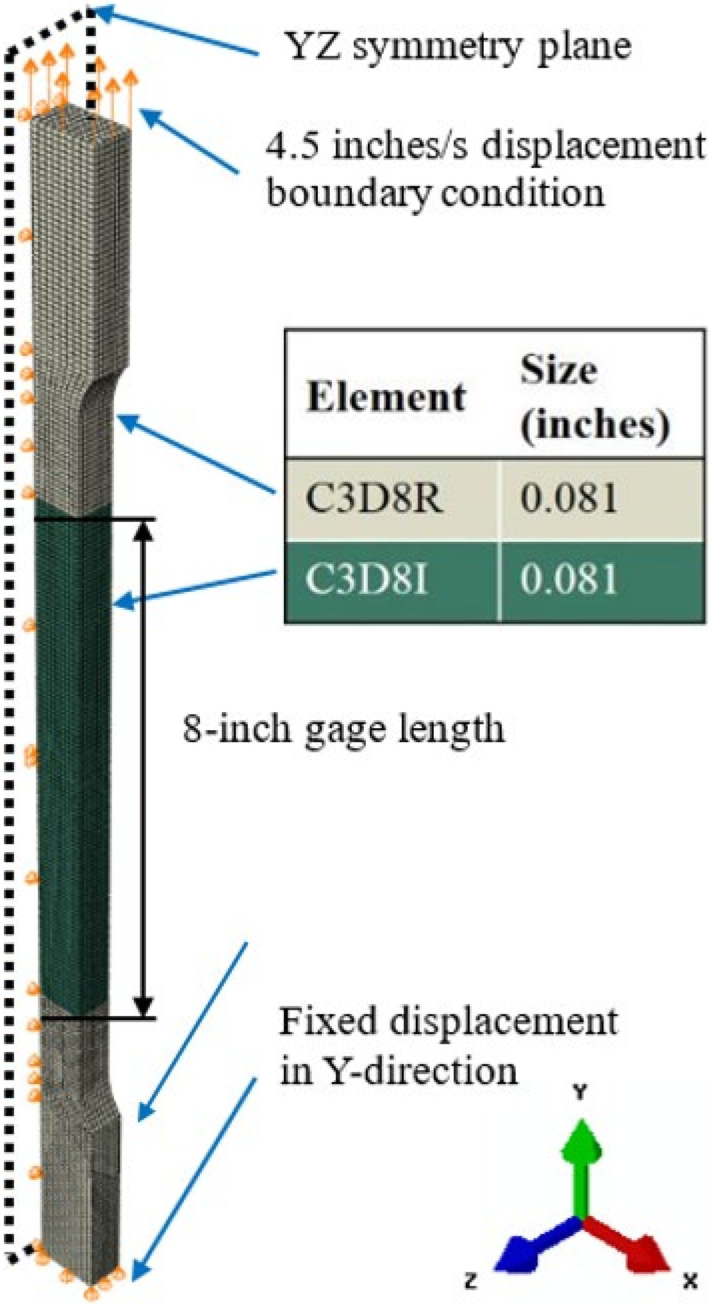

Element	Size (inches)
C3D8R	0.081
C3D8I	0.081

Figure F5. DOT-117 Pre-Test Tensile Coupon FE Model

The nominal stress-strain response output from this model is shown in Figure F6. This figure also includes dashed lines that represent the average yield strength, ultimate strength, and elongation taken from the material data on the TC128 plates used to manufacture several DOT-117 tank cars. Good agreement was observed in the comparison of the nominal stress-strain response of the pre-test tensile coupon FE-model and the manufacturer-provided measurements taken from the TC128 plates.

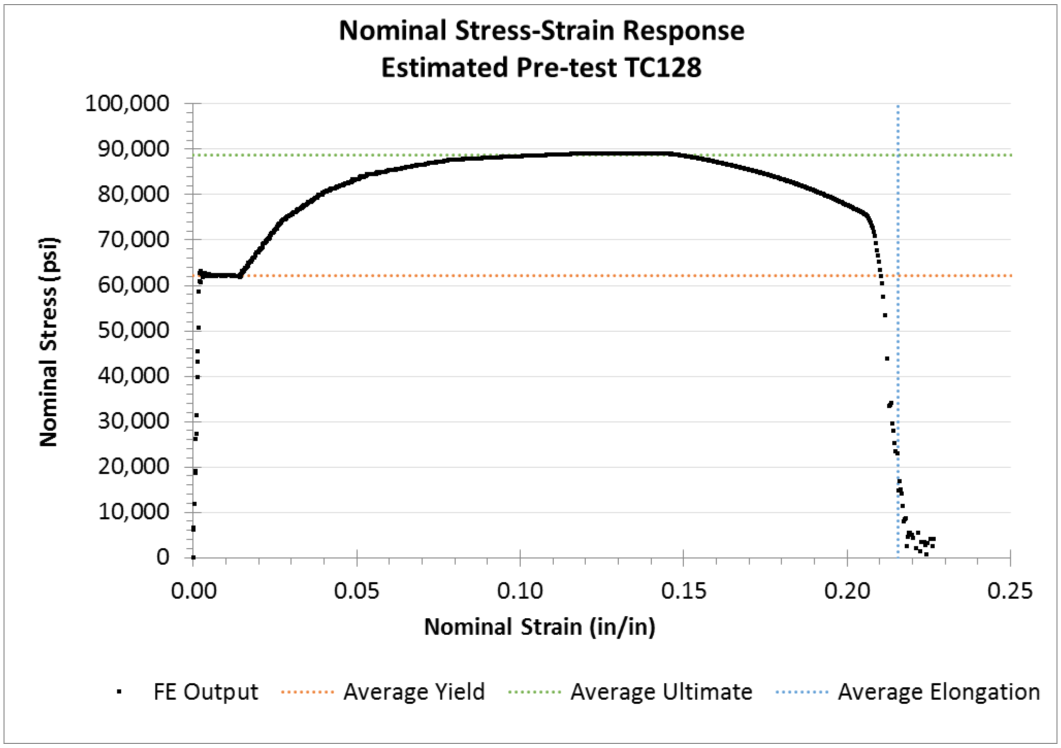

Figure F6. Nominal Stress-Strain Response from Estimated Pre-Test TC128 Behavior

F.4.2 – Post-Test Characterization

Following the test, material coupons were excised from the tested DOT-117 and sent off for tensile testing. The material was cut into 2-inch gage length rectangular coupons for tensile testing. The results of the tensile tests are included in Appendix B4. Additionally, the actual test data was provided to Volpe for use in developing a material response for the material in the tested tank car. Figure F7 contains a plot of the three nominal stress-strain responses from the tested tank car. The dashed lines at the end of each curve represent an extrapolation from the last data point made during the measurement to the zero-stress state.

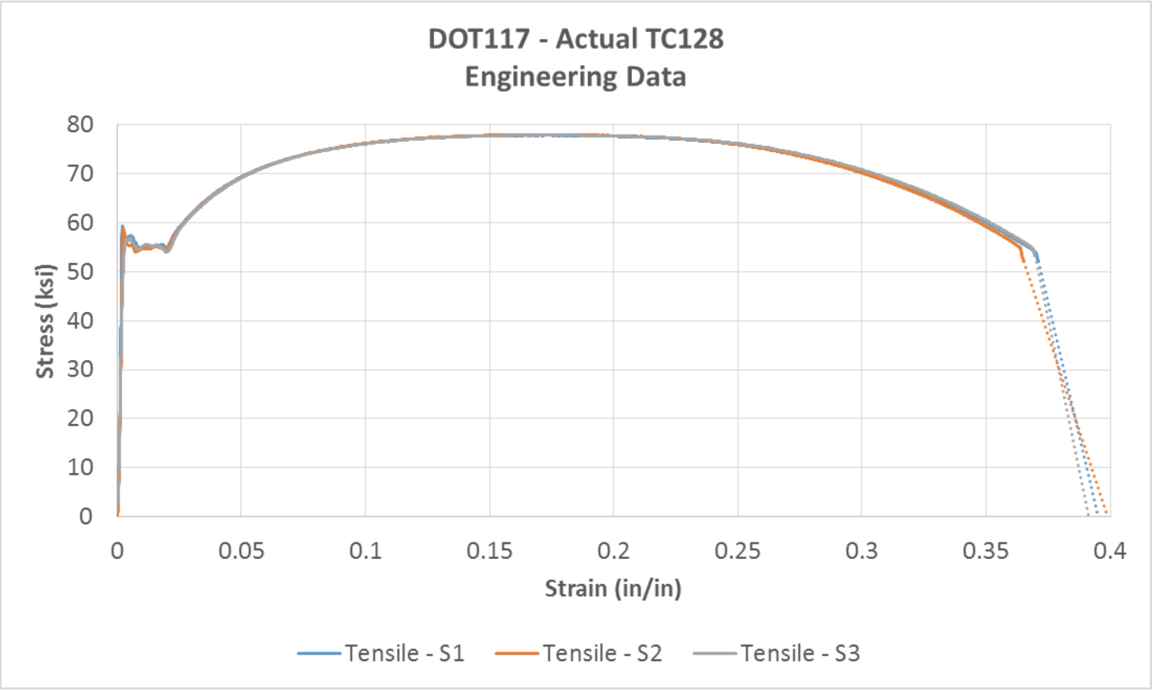

Figure F7. Measured Stress-Strain Responses of Three Samples from Tested Car

A summary of the DOT-117 material properties measured in the three coupon tests is provided in Table F6.

Table F6. Average Properties from TC128 Coupon Tests

Tested Sample		UTS	Yield	Elongation	RA	Initial Width	Final Width	Initial Thickness	Final Thickness	Initial Gage Length	Final Gage Length
		ksi	ksi	Percent	Percent	inches	inches	Inches	inches	inches	inches
S1	03973H	77.9	57.1	38	67	0.5018	0.291	0.5932	0.3342	2	2.76
S2	03974H	78	55.3	38	63	0.5014	0.3058	0.5934	0.3612	2	2.75
S3	03975H	77.9	56.8	39	66	0.5021	0.2992	0.5941	0.341	2	2.77
Average		*77.9*	*56.4*	*38.3*	*65.3*	*0.5018*	*0.2987*	*0.5936*	*0.3455*	*2*	*2.76*

The material behavior characterization developed for the Actual TC128 used in the test car was targeted to match one of the stress-strain responses in the middle of the range of responses observed from the tensile test results. An FE model of the 2-inch gage coupon was developed. Similar to the model used in the pre-test characterization, a mesh size of 0.081-inch was used in the gage, resulting in seven elements through the thickness of the sample. The post-test coupon model was meshed using 8-node hexahedral (C3D8) elements in the gage area, and C3D8R elements outside of this area. Using an iterative process, the test measurements were used to develop a true stress-true plastic strain response that showed good agreement with the tensile test results. The resulting true stress-true plastic strain behavior is shown in Table F7 and plotted in Figure F8.

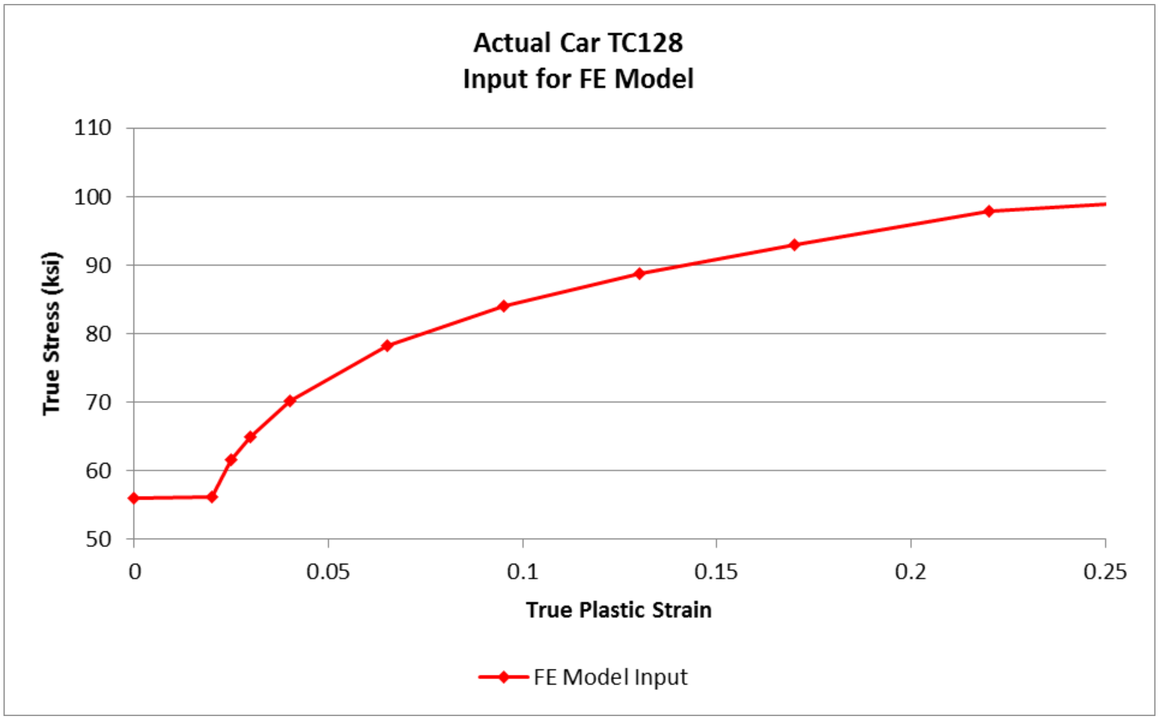

Figure F8. Actual TC128 from Test Car True Stress and Plastic Strain Behavior

Table F7. True Stress/True Plastic Strain Inputs for Actual TC128 from Test Car

True Stress (psi)	True Plastic Strain (in/in)
56,000	0
56,100	0.020
61,550	0.025
64,875	0.030
70,127	0.040
78,293	0.065
84,069	0.095
88,724	0.130
93,000	0.170
97,800	0.220
132,200	1.220

Using results from the tensile tests and simulations as inputs, a damage initiation envelope was developed with the quick calibration approach [18]. The damage initiation envelope is a series of plastic equivalent (PEEQ) strain values at different values of stress triaxiality (TRIAX) that are used to determine when an element has begun to take on damage. Since the measured nominal stress-strain behaviors for these samples exhibited a flat response near the ultimate strength of the material, the value used in the quick calibration method for "displacement at peak force" was iteratively adjusted until the coupon test simulations provided reasonable agreement with the test measurements. Using this approach, the cusp is not forced to occur at a triaxiality of one-third, but is calculated using the tensile test results. The envelope developed for actual TC128 is plotted next to the envelope used for the pre-test TC128 in Figure F9. The values used to define this envelope are provided in Table F8.

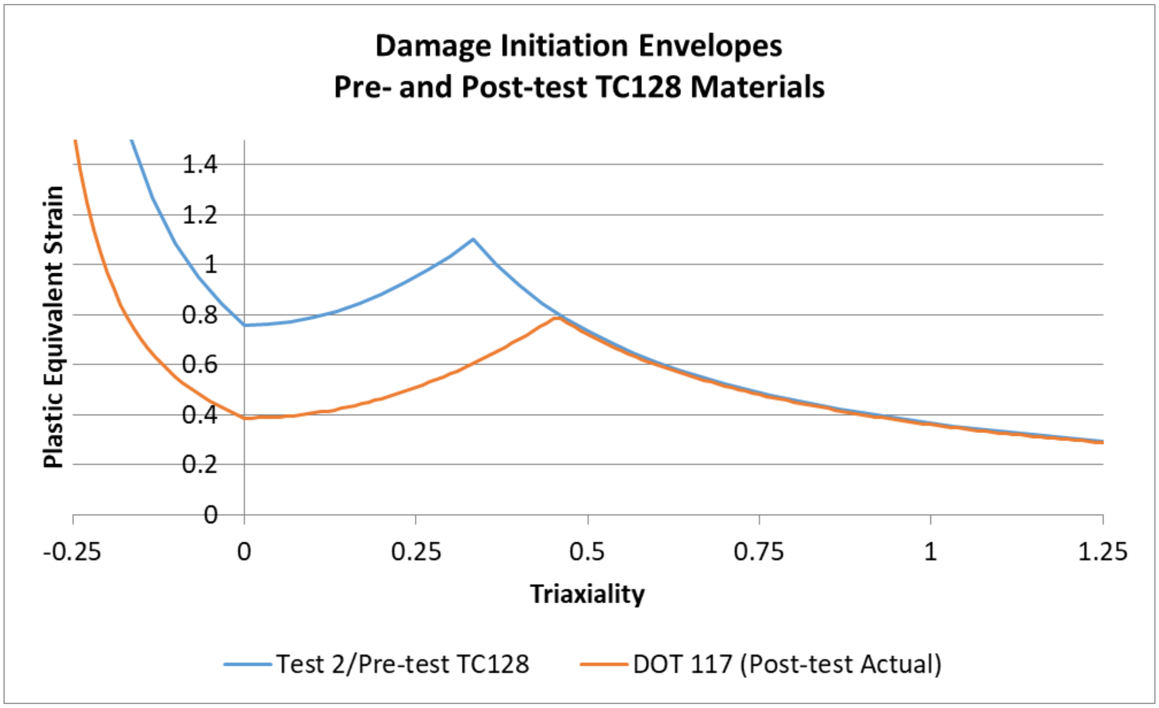

Figure F9. Damage Initiation Envelopes for Pre-Test and Post-Test TC128 Materials

Table F8. Damage Initiation Envelope for Post-Test Actual TC128

Triax.	PEEQ	Triax.	PEEQ	Triax.	PEEQ	Triax.	PEEQ	Triax.	PEEQ
-0.30	3.87	0.08	0.4	0.46	0.784	0.84	0.43	1.22	0.296
-0.29	2.977	0.09	0.403	0.47	0.768	0.85	0.425	1.23	0.293
-0.28	2.419	0.10	0.407	0.48	0.752	0.86	0.42	1.24	0.291
-0.27	2.037	0.11	0.411	0.49	0.736	0.87	0.415	1.25	0.289
-0.26	1.759	0.12	0.415	0.50	0.722	0.88	0.41	1.26	0.286
-0.25	1.548	0.13	0.42	0.51	0.708	0.89	0.405	1.27	0.284
-0.24	1.382	0.14	0.426	0.52	0.694	0.90	0.401	1.28	0.282
-0.23	1.248	0.15	0.431	0.53	0.681	0.91	0.397	1.29	0.28
-0.22	1.138	0.16	0.437	0.54	0.668	0.92	0.392	1.30	0.278
-0.21	1.046	0.17	0.444	0.55	0.656	0.93	0.388		
-0.20	0.967	0.18	0.451	0.56	0.644	0.94	0.384		
-0.19	0.9	0.19	0.458	0.57	0.633	0.95	0.38		
-0.18	0.841	0.20	0.466	0.58	0.622	0.96	0.376		
-0.17	0.79	0.21	0.474	0.59	0.612	0.97	0.372		
-0.16	0.744	0.22	0.482	0.60	0.601	0.98	0.368		
-0.15	0.704	0.23	0.491	0.61	0.592	0.99	0.364		
-0.14	0.667	0.24	0.501	0.62	0.582	1.00	0.361		
-0.13	0.634	0.25	0.51	0.63	0.573	1.01	0.357		
-0.12	0.605	0.26	0.52	0.64	0.564	1.02	0.354		
-0.11	0.578	0.27	0.531	0.65	0.555	1.03	0.35		
-0.1	0.553	0.28	0.542	0.66	0.547	1.04	0.347		
-0.09	0.53	0.29	0.553	0.67	0.539	1.05	0.344		
-0.08	0.509	0.30	0.564	0.68	0.531	1.06	0.34		
-0.07	0.49	0.31	0.576	0.69	0.523	1.07	0.337		
-0.06	0.472	0.32	0.589	0.70	0.515	1.08	0.334		
-0.05	0.455	0.33	0.602	0.71	0.508	1.09	0.331		
-0.04	0.44	0.34	0.615	0.72	0.501	1.10	0.328		
-0.03	0.425	0.35	0.629	0.73	0.494	1.11	0.325		
-0.02	0.412	0.36	0.643	0.74	0.488	1.12	0.322		
-0.01	0.399	0.37	0.657	0.75	0.481	1.13	0.319		
0	0.387	0.38	0.672	0.76	0.475	1.14	0.317		
0.01	0.387	0.39	0.687	0.77	0.469	1.15	0.314		
0.02	0.388	0.40	0.702	0.78	0.463	1.16	0.311		
0.03	0.389	0.41	0.718	0.79	0.457	1.17	0.308		
0.04	0.39	0.42	0.735	0.80	0.451	1.18	0.306		
0.05	0.392	0.43	0.752	0.81	0.445	1.19	0.303		
0.06	0.394	0.44	0.769	0.82	0.44	1.20	0.301		
0.07	0.397	0.45	0.786	0.83	0.435	1.21	0.298		

The damage progression value was determined iteratively by comparing the results of the FE simulation of the coupon test to the actual test results. Best agreement was obtained using a linear damage progression of 1,500 in-lbf/in^2. The nominal stress-strain response for the Actual TC128 material used in post-test modeling is shown in Figure F10 alongside the measured stress-strain responses from the coupon tests.

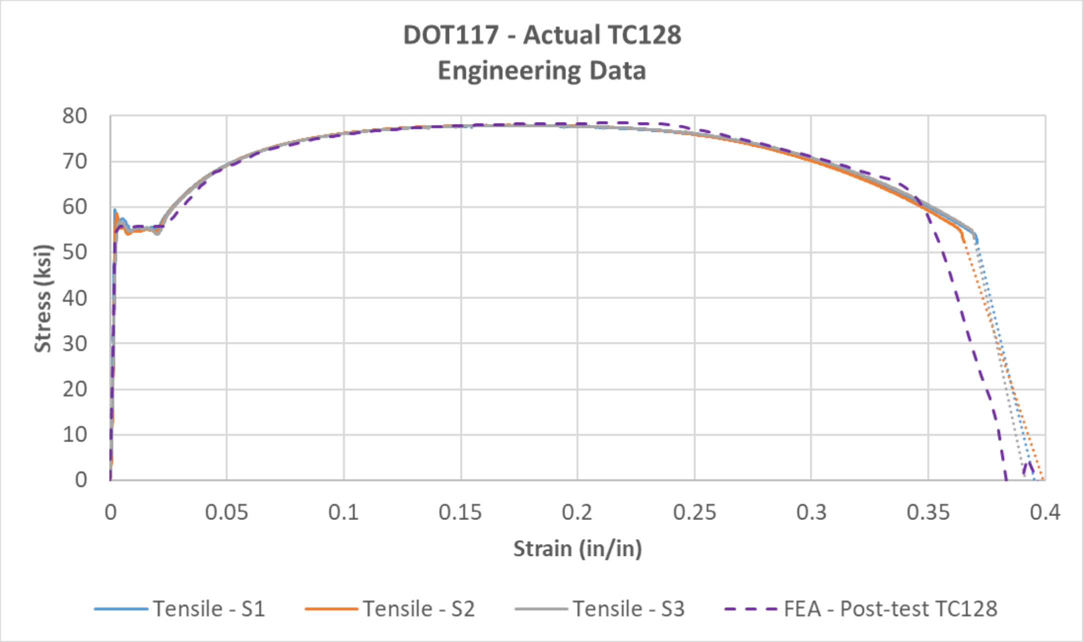

Figure F10. Engineering Stress-Strain Results from Actual TC128

Key values compared between the coupon simulation and the average test measurements include the change in width and thickness of the sample, the reduction in area, and the toughness of the material. The toughness was determined through numerical integration of the nominal stress-strain curve from its first point through the point at which the curve was extrapolated to have zero stress post-fracture. The comparisons shown in Table F9 indicate that the FE model of the coupon test exhibits excellent agreement for each of these parameters.

Table F9. Comparison of Key Results from Coupon Tests and Coupon Simulations

Parameter	Value	Units	Percent Difference (FEA-Measured)/Measured
Final Width (FEA)	0.295	inches	-1.1%
Final Width (Measured)	0.299	inches	-
Final Thickness (FEA)	0.334	inches	-3.3%
Final Thickness (Measured)	0.346	inches	-
%RA (FEA)	66.9	%	2.3%
%RA (Measured)	65.3	%	-
Toughness (FEA)	26.4	in-kip/in^3	-2.0%
Toughness (Measured)	26.9	in-kip/in^3	-

The post-test model exhibited agreement within 5 percent for each of the parameters that were compared between the average test data and the FE results.

F5 – Water

The water was explicitly modeled using a mesh to account for its actual initial geometry within the tank. Prior to executing the puncture model, a series of non-puncture models were executed to evaluate the effects of using different meshing techniques and element sizes on the water mesh. This effort looked at the qualitative behaviors of different techniques, the quantitative influences on both the global force-time response and the pressure-time history, and looked at the effect on computational time. The non-puncture model used in this study featured simplified geometry, no material failure behavior, and a coarse mesh. This model featured runtimes of several hours, compared to several days for the puncture model. Due to the computational demand associated with the fine mesh patch in the puncture model, a fluid modeling approach that provided reasonable results without requiring an unreasonable increase in computational cost was sought.

F5.1 – Mesh Size – C3D8 "Brick Elements"

Two non-puncture models were run to investigate the influence of mesh size on a C3D8 "brick" element representation of the water. Both models were run at 18 mph. The force-time history responses from both models are shown in Figure F11, and the air pressure-time responses from both models are shown in Figure F12. A summary of key results from each model is shown in Table F10. The 3-inch mesh did not exhibit a major difference in any key result from the 4-inch mesh, except that the 3-inch mesh had a runtime that was more than 3.6 times that of the 4-inch mesh.

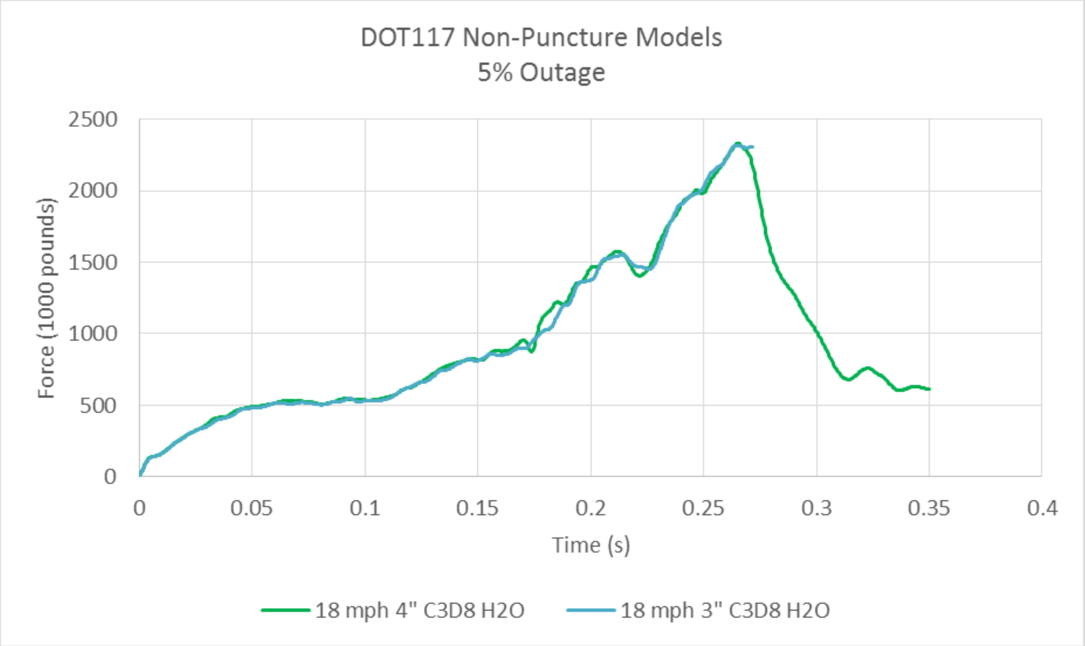

Figure F11. Force Versus Time for 18 mph Impacts Using 3-Inch and 4-Inch C3D8 Water Meshes

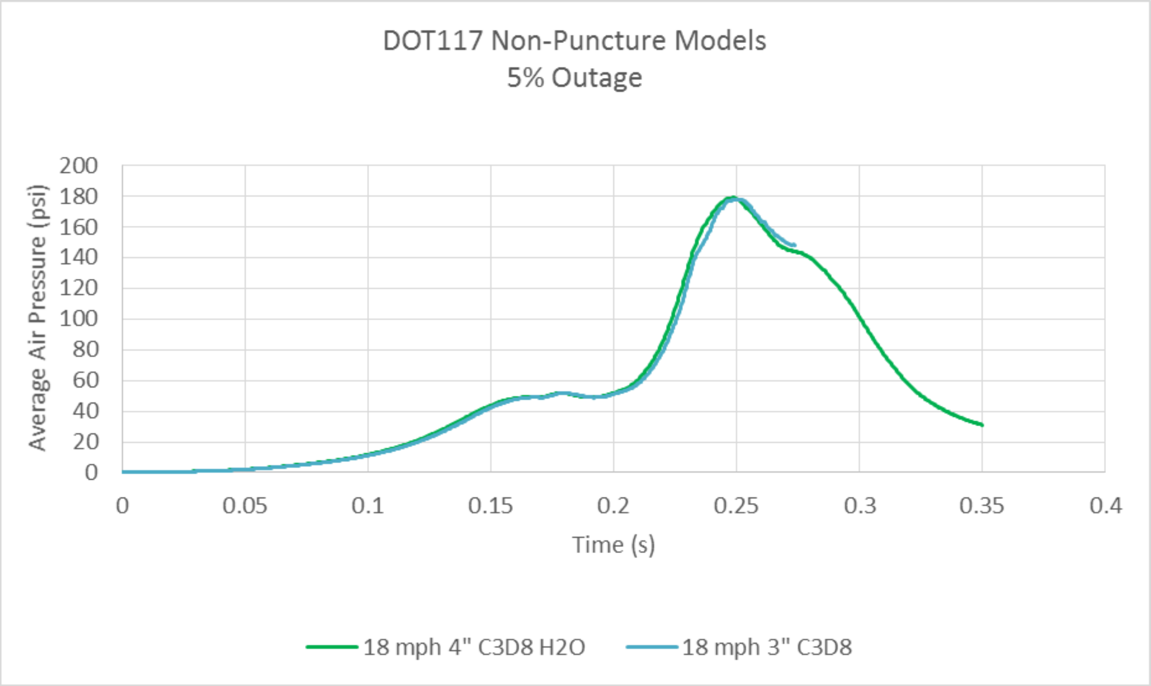

Figure F12. Average Air Pressure Versus Time for 18 mph Impacts Using 3-Inch and 4-Inch C3D8 Water Meshes

Table F10. Comparison of Results from 18 mph Impacts Using 3-Inch and 4-Inch C3D8 Water Meshes

Impact Speed	Water Mesh Technique	Water Mesh Size	Venting?	Max Force	Max Displacement	Max Air Pressure	Runtime
mph	-	Inches	-	kips	Inches	psi	hours
18	C3D8	3	No	2317.8	56.5	177.9	2.9
18	C3D8	4	No	2331.6	56.3	178.8	0.8

F5.2 – Mesh Size—PC3D Particles

One of the material modeling techniques offered by Abaqus is a smoothed particle hydrodynamic (SPH) approach. This technique does not use conventional elements, but uses discrete particles to represent a body. This approach was previously used in the test of a DOT-112 tank car to model the air in the outage [5]. One advantage offered by the SPH approach, compared to a Lagrangian approach, is the ability to model large deformations without mesh distortion resulting in a model slowdown or termination. Thus, SPH was considered as an option for modeling the water within the tank that would capture the complex sloshing and not be prone to distortion.

Three non-puncture models were run at 15 mph to investigate the influence of mesh size on a PC3D SPH particle representation of the water. The force-time history responses from the models are shown in Figure F13, and the air pressure-time responses from the models are shown in Figure F14. A summary of key results from each model is shown in Table 30. As the particle spacing becomes smaller, the model becomes stiffer. This results in a higher peak force, a larger peak pressure, and a smaller maximum indentation. The increase in particle density also comes with an increase in the runtime of the model.

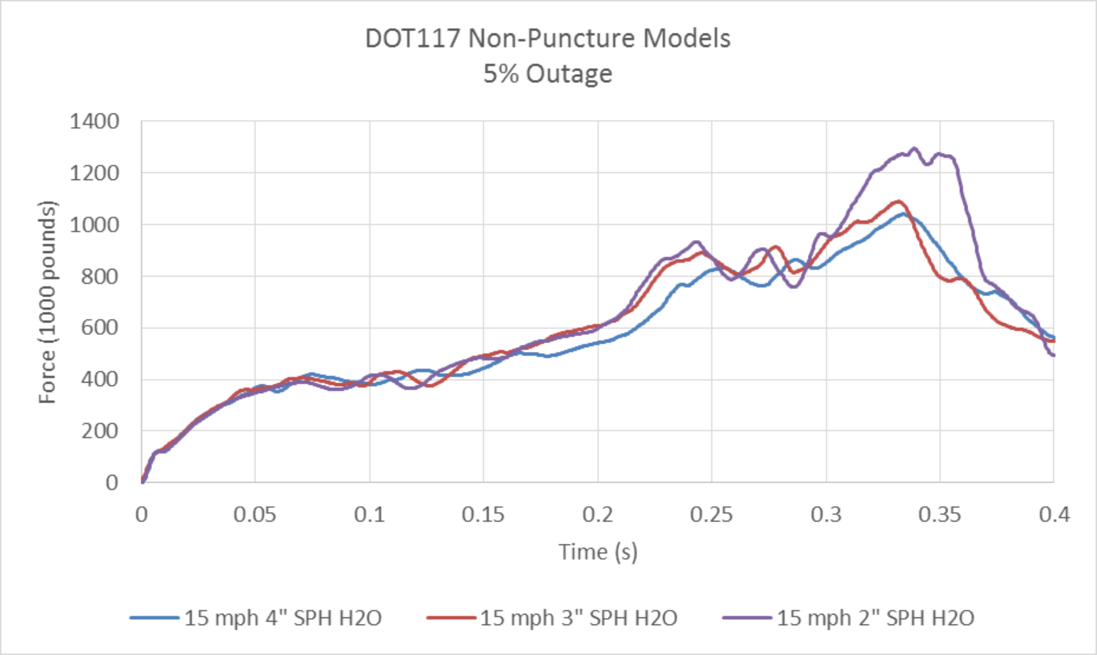

Figure F13. Force Versus Time for 15 mph Impacts Using 2-Inch, 3-Inch, and 4-Inch SPH Water Meshes

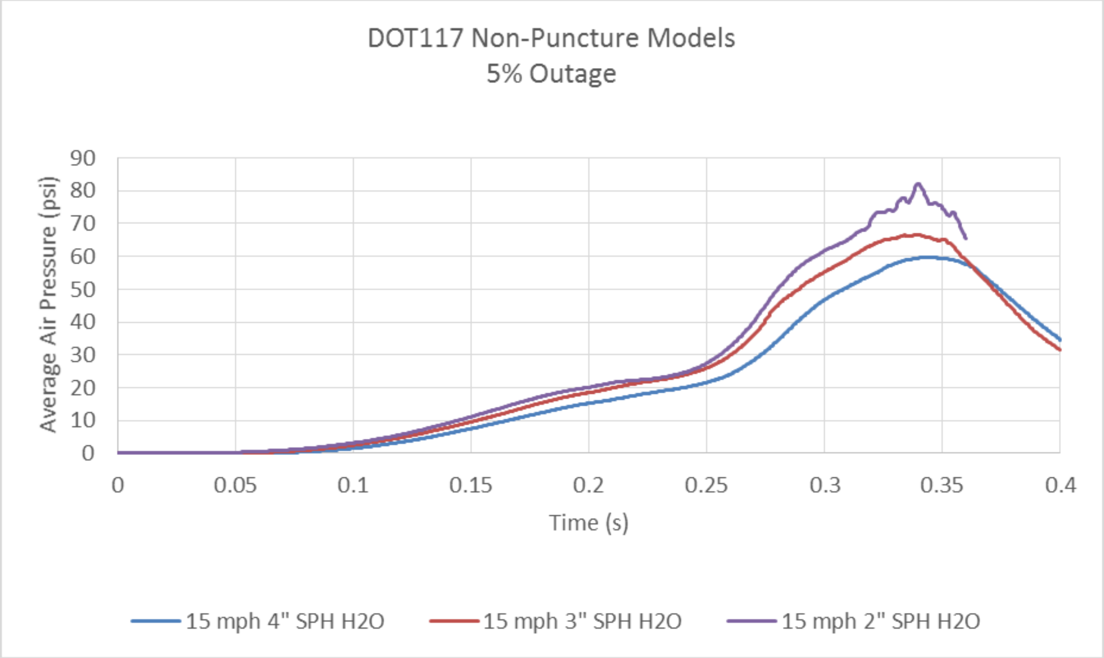

Figure F14. Average Air Pressure Versus Time for 15 mph Impacts Using 2-Inch, 3-Inch, and 4-Inch SPH Water Meshes

Table F11. Comparison of Results from 15 mph Impacts Using 2-Inch, 3-Inch, and 4-Inch SPH Water Meshes

Impact Speed	Water Mesh Technique	Particle Spacing	Venting?	Max Force	Max Displacement	Max Air Pressure	Runtime
mph	-	inches	-	kips	inches	psi	hours
15	SPH	4	No	1,040.0	58.2	59.6	2.1
15	SPH	3	No	1,089.5	56.5	66.7	8.2
15	SPH	2	No	1,295.1	56.8	82.1	14.5

From these results, it appears that the SPH technique exhibits some mesh dependence in this range of particle spacing. Additionally, the computational cost of refining the mesh was deemed to be too great to be implemented in a puncture model, owing to the high computational demand of the refined impact zone mesh necessary for the puncture modeling techniques applied. Thus, the SPH approach was discarded in favor of a Lagrangian mesh technique for the water.

F6 – Concrete (Post-Test Model Only)

An elastic-plastic concrete behavior was defined for the ground slab, using concrete properties from Abaqus Example Problem 2.1.15, “Seismic Analysis of a Concrete Gravity Dam” [17]. The mechanical properties were converted into the unit system used in the DOT-117 tank car model. The properties input to the post-test FE model are summarized in Table F12 through Table F14.

Table F12. Properties of Concrete for Post-Test FE Model with Deformable Ground

Density	0.000249	$(\text{lbf-s}^2/\text{in})/\text{in}^3$
Modulus of Elasticity	4.50×10^6	psi
Poisson’s Ratio	0.2	-
Dilation Angle	36.31	degrees

Table F13. Concrete Tension Stiffening Behavior for Post-Test FE Model with Deformable Ground

Psi	inches
420.61	0.00E+00
281.94	2.61E-03
188.99	4.84E-03
126.69	6.83E-03
84.92	8.67E-03
56.92	1.04E-02
38.16	1.21E-02
25.58	1.38E-02
17.14	1.55E-02
11.49	1.72E-02
7.70	1.90E-02

Table F14. Concrete Compression Hardening Behavior for Post-Test FE Model with Deformable Ground

Psi	**strain**
1,885.49	0.00E+00
3,495.42	0.001

Abbreviations and Acronyms

Abbreviations & Acronyms	Definition
AAR	Association of American Railroads
B-W	Bao-Wierzbicki
CFC	Channel Frequency Class
DOF	Degrees-of-Freedom
EOS	Equations of State
FRA	Federal Railroad Administration
FE	Finite Element
FEA	Finite Element Analysis
HD	High Definition
HHFT	High-Hazard Flammable Trains
HS	High Speed
NDT	Non-Destructive Testing
PEEQ	Plastic Equivalent
PHMSA	Pipeline and Hazardous Materials Safety Administration
PRV	Pressure Relief Valve
SSC	Shell-to-Solid Coupling
SAE	Society of Automotive Engineers
SCFM	Standard Cubic Feet per Minute
SPH	Smoothed Particle Hydrodynamics
TRIAX	Stress Triaxiality
TIH	Toxic by Inhalation
TC	Transport Canada
TTC	Transportation Technology Center (the site)
TTCI	Transportation Technology Center, Inc. (the company)
DOT	United States Department of Transportation
Volpe	Volpe National Transportation Systems Center